UNIONE EUROPEA
Fondo Sociale Europeo

Ministero dell'Istruzione, dell'Università e della Ricerca

PON RICERCA E INNOVAZIONE 2014 - 2020

PhD in Chemical Science and Technology

Cycle XXXIV

Development of "lead-free" piezoceramics based on potassium sodium niobate (KNN) from mechanochemically activated precursors

PhD Student: Antonio Iacomini

Coordinator of the PhD Program: Prof. Carla Cannas

Supervisors: Prof. Stefano Enzo

Prof. Sebastiano Garroni

Prof. Lorena Pardo

Final exam. Academic Year 2020 – 2021

Thesis defense: June 2022 Session

Summary

1 Introduction

1.1 Problem statement

Materials always had a great influence on society. Man's evolution is parallel to the use of new type of material for various purposes. This was obvious in the Stone Age, Bronze Age and Iron Age. We have named these eras by the most advanced material in that period because these materials determine the state of technology at that time. Today, the influence of materials is still present and technological development has enabled the use of increasingly sophisticated materials adapt to more and more specific function. For example, smart and functional materials have become quite common in our daily life. By definition, smart or intelligent materials are materials that have the intrinsic and extrinsic capabilities, first, to respond to stimuli and environmental changes and, second, to activate their functions according to these changes.**[1]** Some examples of smart materials are:

- Piezoelectric material
- Electrostrictive materials
- Magnetostrictive materials
- Shape memory materials
- Electrochromic materials
- Phase change materials

Among them, piezoelectric materials are one of the largest groups and have become a key technology for a wide range of industrial and consumer products. Current technology includes applications on actuators, ultrasonic motors, transformers, micro-energy harvesting devices, hydrophones, high-resolution ultrasonic medical imaging, and accelerometers in mobile phones, notebooks and so on.**[1]** In the last two decades, piezo- devices market has seen a tangible growth. The current market was

estimated approximately at € 4 billion in 2015 and forecasts indicate that it would double (€ 8 billion) by 2024.**[2]**

With exceptional electromechanical properties and mild processing conditions, highly dense PZT (lead, zirconate, titanate), with a general formula $Pb(Zr_xTi_{1-x})O_3$, is the most commonly used compound in the manufacturing of piezoceramics-based devices.**[3]** However, the toxic nature of lead oxide, which is the main component in PZT systems (~60 wt.%), has raised concern about its environmental impact during all stages of its "life-cycle".**[4]** For this reason, the European Union has adopted measures regarding the restriction of the use of substances harmful to health in electronic devices including mercury, cadmium, hexavalent chromium and lead.**[5]** Nevertheless, there are some exceptions where the "lead free" alternative is not yet available; piezoceramics fall into this category.**[6]** Currently, there are four large family of highly promising lead-free systems which are: $(K, Na)NbO_3$ (KNN)-based, $(Bi_{0.5}, Na_{0.5})TiO_3$ (BNT)-based, $BaTiO_3$ (BT)-based, and $BiFeO_3$ (BF)-based piezoceramics.**[7]** Among the many lead-free based candidates, KNN (potassium, sodium, niobate), with a general formula of $K_xNa_{1-x}NbO_3$, has received great interest in the recent past, due to its promising electromechanical properties coupled with a high Curie temperature (217–304 °C).**[8]** These promising properties, combined with the ever-increasing restrictions adopted against the use of lead in the manufacturing of costumer objects, have promoted fervent research into these systems. However, their extensive penetration into the commercialized devices is still hampered by their scarce reproducibility, poor sinterability and as yet unclarified impact on human health.

The processing of the KNN-based system results affected by many open issues. Firstly, alkali loss during the calcination and sintering steps, usually performed at high temperatures (700 °C and 1150 °C, respectively), contributes to an incorrect stoichiometry with the further formation of undesired secondary phases which drastically reduce the performance of the system and its reproducibility.**[9]**

Likewise, KNN-based powders with excessively large particles and grain sizes result in it being difficult to sinter under mild conditions. These processes-related problems can be overcome by increasing the reactivity of the powders by mechanical processing or introducing specific dopants.**[10]** In particular, the mechanochemical activation through high energy ball milling has received considerable interest for the processing of complex perovskite materials with good compositional homogeneity.**[11]** Nevertheless, this technique requires a further effort of study and deepening.

Concerning the toxicological aspect of KNN-based materials, few tangible results have been published to the best of our knowledge. There are few works focusing on the environmental impact and sustainability of KNN, which is expected to be less hazardous than PZT, but the mining of the starting reagents (Nb_2O_5) has been evaluated as being more environmentally deleterious if compared with lead oxide.**[12]** A toxicological experimental assessment and information about the safety of KNN materials are then of primary importance, together with their processing optimization.

Low cytotoxicity, reproducibility and scalability of the manufacturing process are fundamental requirements to make the KNN a serious candidate to replace PZT. In any case, this is not enough as the performance of the "lead free" system should be, at least, comparable with that of PZT. The electromechanical properties of a piezoceramic depends on various parameters including density, grain size and crystal structure. The X-ray diffraction (XRD) is the main technique for investigating the crystalline structure of solid-state materials, and it certainly plays a fundamental role in the study of piezoceramics. Recently, *in-situ* diffraction characterizations are increasingly used to monitor the change of the crystal structure of the piezoceramic as a function of the applied poling electric field.**[13,14]** The useful information obtained from these experiments allows to understand how to further optimize the poling process, the microstructure and therefore the electromechanical properties

of the ceramic. However, these kinds of experiments are particularly difficult to perform and are mostly carried out in synchrotron facilities.

Within this context, the main objectives that this thesis work aims to do are summarized below:

1. Optimize the manufacturing process of KNN-based systems prepared by high energy ball milling. Particular attention will be paid to the effect of milling on crystallite and particles sizes and their correlation with the reactivity and sinterability of the as prepared samples.
2. Provide an assessment on the toxicological potential of KNN-based systems employing two widely used human and environmental cellular models (A549 cell line and *Saccharomyces cerevisiae*).
3. Understand the role of some dopants on the structure, microstructure and electromechanical properties of KNN ceramics.
4. Develop an innovative device to perform *in-situ* poling/temperature diffraction experiments for piezoceramics, suitable for common laboratory diffractometer.

1.2 Structure of the thesis

This thesis work will be divided into the following chapters:

- **Chapter 2**: theoretical and mathematical introduction on piezoelectric effect and their coefficients. Brief introduction on the main piezoelectric materials with perovskite structure.
- **Chapter 3:** State of the Art on KNN-based compositions prepared through Solid State Route (SSR).
- **Chapter 4:** description of the experimental procedure and characterisation techniques used in this thesis work.

- **Chapter 5, 6 and 7:** analysis and comments of the experimental results obtained on the KNN-based systems prepared through the mechanochemical activation method. Particular emphasis was given to the optimization of the milling process and to the structure / electrical properties relationship.
- **Chapter 8:** description of an innovative device to perform *in-situ* poling/temperature diffraction experiments suitable for common laboratory diffractometer.
- **Chapter 9:** general conclusions of the work and future perspective.

1.3 Bibliography

[1] J. Holterman, P. Groen. An introduction to Piezoelectric Materials and Applications, *Stichting Applied Piezo*, 1st edn, **2013**.

[2] Market Report, Global Piezoelectric Device Market. *Acmite Market Intelligence*, **2017**.

[3] J. Rödel, J. Li. *Mater. Res. Bull*. **2018**, 43, 576–580.

[4] M. Kosec, B. Malic, W. W. Wolny, A. S. James, C. Alemany and L. Pardo. *J. Korean Phys. Soc.* **1998**, 32 S1163-S1166.

[5] EU-Directive 2002/95/EC: Restriction of the use of certain hazardous substances in electrical and electronic equipment (RoHS), Offic. J. Europ. Union. **2003**, 46-L37, 19-23.

[6] A. J. Bell, O. Deubzer. *MRS Bulletin.* **2018**, 43(8), 581-587.

[7] H. Thong, C. Zhao, Z. Zhou, C. Wu, Y. Liu, Z. Du, J. F. Li, W. Gong, K. Wang. *Mater. Today*. **2019**, 29, 37–48.

[8] J. Wu, D. Xiao, and J. Zhu. *Chem. Rev*. **2015**, 115, 2559-2595.

[9] N. Senes, A. Iacomini, N. Domingo, S. Enzo, G. Mulas, S. Cuesta-Lopez, S. Garroni. *Phys. Status Solidi A* **2018**, 215, 1700921.

[10] B. Malič, J. Koruza, J. Hreščak, J. Bernard, K. Wang, J. G. Fisher, and A. Bencan. *Materials.* **2015**, 8, 8117-8146.

[11] T. Rojac, A. Benčan, H. Uršič, B. Malič, M. Kosec, *J. Am. Ceram. Soc*. **2008**, 91, 3789–3791.

[12] T. Ibn-Mohammed,T. S. C. L. Koh, I. M. Reaney, D. C. Sinclair, K. B. Mustapha, A. Acquaye, D. Wang, *MRS Commun.* **2017**, 7, 1–7.

[13] B. Li, M. C. Ehmke, J. E. Blendell, K. J. Bowman. *J. Eur. Ceram. Soc*. **2013**, 33, 3037–3044.

[14] P. Li, J. Zhai, B. Shen, S. Zhang, X. Li, F. Zhu, X. Zhang. *Adv. Mater*. **2018**, 1705171.

2 Theoretical background

2.1 Basis of piezoelectricity

The word piezoelectricity finds its etymological origin in the Greek words “piézein” which means to press, and electron, which in ancient times were the name of the amber, a material known for being capable to develop electrostatic charge. The first discovery of this phenomenon dates back to 1824 in Rochelle salt, but the first documented experiment was published in 1880 by the Curie brothers. They observed the formation of electric polarisation in a quartz single crystal subjected to mechanical stress.**[1]** This is what is called *direct piezoelectric effect* and is identified with the phenomenon whereby electrical charge (polarization) is generated from a mechanical stress, whereas the *converse piezoelectric effect* is, on the contrary, the strain appearing when an external electric field is applied.**[2]** In **Figure 2.1**, these two effects are schematized.

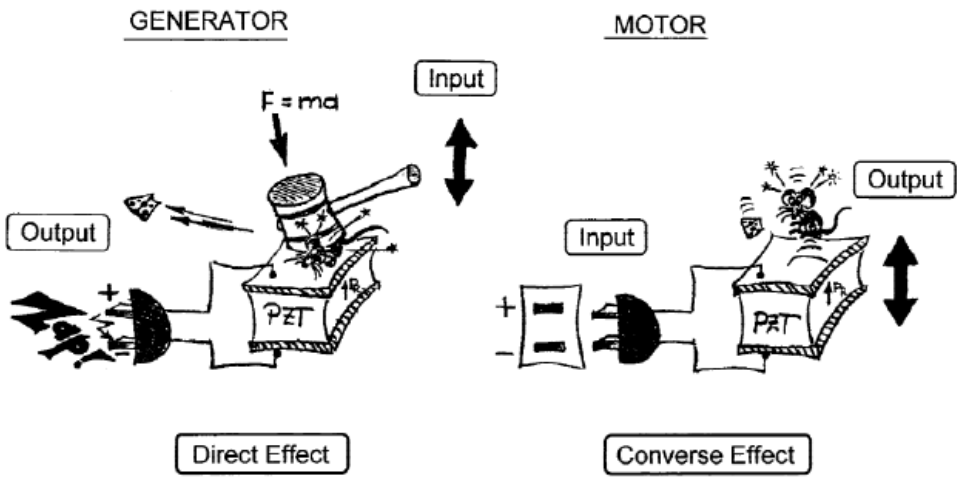

Figure 2.1. Piezoelectric effect in ferroelectric ceramics: (left) direct and (right) inverse piezoelectric effect.**[1]**

The equations that describe the direct and converse piezoelectric effect with regard to electric and elastic properties are:

$$D = dT + \varepsilon^T E \tag{2.1}$$

$$S = s^E T + dE \tag{2.2}$$

Where D is the dielectric displacement (consider it equal to polarisation), T the stress, E the electric field, S the strain, d a piezoelectric coefficient, s the material compliance and ε the dielectric permittivity. The superscripts indicate the physical quantity held constant. Piezoelectric ceramics are anisotropic; therefore, all physical constants are tensorial quantities, making necessary the use of tensor notation.**[3] Equations 2.1** and **2.2** describe a set of equations that relate these properties along different orientation of the material. The complete (linearised) description of the electric, elastic, and piezoelectric behaviour in matrix notation then reads (**Equation 2.3**):

$$\begin{pmatrix} S_1 \\ S_2 \\ S_3 \\ S_4 \\ S_5 \\ S_6 \\ D_1 \\ D_2 \\ D_3 \end{pmatrix} = \begin{bmatrix} s_{11}^E & s_{12}^E & s_{13}^E & 0 & 0 & 0 & 0 & 0 & d_{31} \\ s_{12}^E & s_{22}^E & s_{23}^E & 0 & 0 & 0 & 0 & 0 & d_{32} \\ s_{13}^E & s_{23}^E & s_{33}^E & 0 & 0 & 0 & 0 & 0 & d_{33} \\ 0 & 0 & 0 & s_{44}^E & 0 & 0 & 0 & d_{24} & 0 \\ 0 & 0 & 0 & 0 & s_{55}^E & 0 & d_{15} & 0 & 0 \\ 0 & 0 & 0 & 0 & 0 & s_{66}^E & 0 & 0 & 0 \\ 0 & 0 & 0 & 0 & d_{15} & 0 & \varepsilon_{11}^T & 0 & 0 \\ 0 & 0 & 0 & d_{24} & 0 & 0 & 0 & \varepsilon_{22}^T & 0 \\ d_{31} & d_{32} & d_{33} & 0 & 0 & 0 & 0 & 0 & \varepsilon_{33}^T \end{bmatrix} \begin{pmatrix} T_1 \\ T_2 \\ T_3 \\ T_4 \\ T_5 \\ T_6 \\ E_1 \\ E_2 \\ E_3 \end{pmatrix} \tag{2.3}$$

By convention, it is assumed that the polarization direction coincides with the Z-axis. Direction X, Y and Z for convenience of notation are indicated as 1, 2 and 3, respectively, while rotations cutting around these axes are indicated as 4, 5 and 6, respectively. The first subscript indicates the direction of polarization generated in the piezoelectric element by direct piezoelectric effect or the direction of the field intensity applied by inverse piezoelectric effect; the second represents the direction of the

applied stress or that of the strain induced. Many elements of the matrix in **Equation 2.3** are zero or not independent due to the symmetry of the crystal which reduces the number of independent constants considerably. For example, the poled ferroelectric ceramic PZT has a $C\infty = C_{6v}$ crystal class. The symmetric reduced matrix in **Equation 2.3** has 2 independent free dielectric permittivity (ε^T_{33}, $\varepsilon^T_{11} = \varepsilon^T_{22}$), three independent piezoelectric constant (d_{33}, d_{31}, d_{15}) and 5 independent elastic constants under short circuit boundary conditions, which are $s^E_{11} = s^E_{22}$, s^E_{33}, $s^E_{44} = s^E_{55}$, $s^E_{12} = s^E_{21}$, $s^E_{13} = s^E_{23}$ and $s^E_{66} = 2(s^E_{11} - s^E_{12})$.**[4,5]** In the light of this, some of the most relevant electric, dielectric, mechanical and piezoelectric coefficients will now be presented and described in detail.

- **Piezoelectric charge (or strain) coefficient d_{ij}**

It represents the mechanical strain produced by an applied electric field (**Equation 2.4**) or the charge detected on the electrodes due to the applied mechanical stress (**Equation 2.5**).

$$d = \frac{strain\ development}{applied\ electric\ field}\left[\frac{m}{V}\right] \tag{2.4}$$

$$d = \frac{short\ circuit\ charge\ density}{applied\ mechanical\ stress}\left[\frac{C}{N}\right] \tag{2.5}$$

According to the various directions where the stress or the electric field can be applied on piezoelectric ceramics, it is possible to have three main different operation modes:

- Longitudinal operation: d_{33}-mode

In the longitudinal operation mode (d_{33}), the deformation and electric field are in Z (3) direction, thus parallel to the polarization. Following the restrictions of the analysis of this operation mode, **Equation 2.3** simplifies considerably and becomes:

$$\begin{pmatrix} S_3 \\ D_3 \end{pmatrix} = \begin{bmatrix} s^E_{33} & d_{33} \\ d_{33} & \varepsilon^T_{33} \end{bmatrix} \begin{pmatrix} T_3 \\ E_3 \end{pmatrix} \tag{2.6}$$

- Transverse operation: d_{31}-mode

In the transverse mode, the electric field is parallel to the polarization (3) and the deformation is perpendicular to the polarization direction (1). According to this operation mode, the matrix equation becomes:

$$\begin{pmatrix} S_1 \\ D_3 \end{pmatrix} = \begin{bmatrix} s_{11}^E & d_{31} \\ d_{31} & \varepsilon_{33}^T \end{bmatrix} \begin{pmatrix} T_1 \\ E_3 \end{pmatrix} \tag{2.7}$$

- Shear operation: d_{15}-mode

The shear mode implies that the electric field is perpendicular to the polarization direction (1), and the relevant deformation is shear deformation around the other perpendicular axis. The relevant two-port equation become:

$$\begin{pmatrix} S_5 \\ D_1 \end{pmatrix} = \begin{bmatrix} s_{55}^E & d_{15} \\ d_{15} & \varepsilon_{11}^T \end{bmatrix} \begin{pmatrix} T_5 \\ E_1 \end{pmatrix} \tag{2.8}$$

- **Piezoelectric voltage constant g_{ij}**

It represents the electric field produced at open circuit by a mechanical stress (**Equation 2.9**) or it can be seen as the strain developed over the applied charge density (**Equation 2.10**).

$$g = \frac{open\ circuit\ electric\ field}{applied\ electric\ field} \left[\frac{V/m}{N/m^2}\right] \tag{2.9}$$

$$g = \frac{strain\ developed}{applied\ charge\ density} \left[\frac{m^2}{C}\right] \tag{2.10}$$

As in the case of the piezoelectric charge coefficient *d*, it is possible to have three different g coefficient (g_{33}, g_{31} and g_{15}) according to the different operation modes. The relationship between *d* and *g* coefficient is described by the following relation:

$$g = \frac{d}{\varepsilon^T} \tag{2.11}$$

The g coefficient is the measure of the sensitivity of the piezoelectric material, therefore high g coefficient is needed for sensor. As it merges from **Equation 2.11**, g is proportional to d and it is inversely proportional to permittivity. High permittivity is required in order to overcome the losses associated with the cables; however, an excessive value affect the g coefficient and thus, the sensitivity of the material.

- **Electromechanical coupling coefficient**

The electromechanical coupling coefficient (k_{ij}) is a measure of the fraction of the electric energy that is converted into mechanical energy (**Equation 2.12**) or vice versa (**Equation 2.13**). It represents a sort of piezoelectric efficiency of the material and provides important information about the coupling between the vibration mode and the excitation.

$$k^2 = \frac{mechanical\ energy\ converted\ into\ electric\ energy}{supplied\ mechanical\ energy} \quad (2.12)$$

$$k^2 = \frac{electric\ energy\ converted\ into\ mechanical\ energy}{input\ electric\ energy} \quad (2.13)$$

As previously seen for the piezo coefficients, it is possible to recognize various coupling coefficient on the basis of the modes of operation under examination. Their expression and relationship with the piezoelectric charge coefficient, permittivity and elastic compliance are listed below.

$$k_{33}^2 = \frac{d_{33}^2}{s_{33}^E \varepsilon_{33}^T} \quad (2.14) \qquad k_{31}^2 = \frac{d_{31}^2}{s_{11}^E \varepsilon_{33}^T} \quad (2.15) \qquad k_{15}^2 = \frac{d_{15}^2}{s_{55}^E \varepsilon_{11}^T} \quad (2.16)$$

Since the piezoceramics are often characterized as thin disk, two other coupling coefficients are often reported which are the planar coupling coefficient (k_p) and the thickness coupling coefficient (k_t). The planar coupling coefficient refers to uniform radial tension or compression of the disk in the plane normal to the poling axis, and it is related to the other coefficient by the following equation:

$$k_p^2 = \frac{2d_{31}^2}{(s_{11}^E + s_{12}^E)\varepsilon_{33}^T} = \frac{2}{1 - \nu_{12}^E} k_{31}^2 \quad (2.17)$$

Where ν^E_{12} is the Poisson's ratio under short circuit conditions. It is necessary to point out that all the parameters presented above describe the quasi-static behaviour of the piezoceramics. In the case of dynamic conditions, the situation become more complex due to dissipative phenomena of both electrical and mechanical nature caused by energy losses. For simplicity, we will take as an example two simple models that describe the dielectric and mechanical losses of piezoelectric materials.

- **Dielectric loss ($\tan\delta_e$)**

Dielectric losses are due to dielectric hysteresis, that is to say, the phase difference between the applied electric field and the resulting polarization. Considering the phase lag, the dielectric permittivity is expressed in complex form as follow:

$$\varepsilon = \varepsilon' - i\varepsilon'' \quad (2.18)$$

The dielectric loss is often expressed in terms of the dielectric loss tangent ($\tan\delta_e$) which is the ratio between the imaginary and the real part of the dielectric permittivity.

$$tan\delta_e = \frac{\varepsilon''}{\varepsilon'} \quad (2.19)$$

Alternatively, can be expressed as electric quality factor (Q_e), which is essentially the reciprocal of the dielectric loss tangent:

$$Q_e = \frac{1}{tan\delta_e} \quad (2.20)$$

- **Mechanical loss**

Compared to dielectric losses, mechanical losses are often expressed in terms of the mechanical quality factor Q_m. In analogy with the dielectric permittivity, the elastic coefficients can be expressed in complex form as follow:

$$s = s' - is'' \tag{2.21}$$

Therefore, the corresponding quality factor is:

$$Q_m = \frac{1}{tan\delta_m} = \frac{s'}{s''} \tag{2.22}$$

One of the most common ways to perform an accurate characterisation of a piezoceramic material is the resonance method.**[6]** The IEEE standard on piezoelectricity reported a well-established method to describe the piezoelectric behaviour of a material at the resonance frequencies. However, the equations provide information only on the real part of the material coefficients. An important breakthrough in this sense was made in 1994 by Alemany et al.**[7]** The authors described the development of an automatic iterative method for the accurate determination of the real and imaginary parts of the material coefficients involved in the operational modes of piezoelectric resonance of ceramic materials. Details on this method, widely used in this thesis work, will be provided in the experimental part.

2.2 Crystal structure and ferroelectricity

As known from crystallography, crystals are classified into 32-point groups based on their symmetry as shown in **Table 2.1**.**[1]** A first classification can be done by dividing the 32 crystallographic classes into 11 centro-symmetric and 21 non-centro-symmetric. According to the Neumann's principle, the symmetry element of any physical properties of a crystal must include the

symmetry elements of the point group of the crystal.**[3]** This implies that when a material group point includes a centre of symmetry, the piezoelectric effect is forbidden. Therefore, only the non-centro symmetrical classes can show piezoelectric effects, with the only exception of the class 432 that does not show piezoelectricity due to other crystallographic constraints.

Table 2.1. Centro-symmetric and non-centro-symmetric point groups in crystals with different symmetries.

Crystal system	**Symmetry element**	**Centro symmetric**	**Non-centro symmetric**
Triclinic	Center	$\bar{1}$	1
Monoclinic	Center, axis, plane	2/m	2, m
Orthorhombic	Center, axis, plane	mmm	222, mm2
Tetragonal	Center, axis, plane	4/m; 4/mmm	4, $\bar{4}$, 442, 4mm, $\bar{4}$2m
Trigonal	Center, axis, plane	$\bar{3}$, $\bar{3}$m	3, 32, 3m
Hexagonal	Center, axis, plane	6/m, 6/mmm	6, $\bar{6}$, 622, 6mm, $\bar{6}$m2
Cubic	Center, axis, plane	m3, m3m	23, $\bar{4}$3m, 432

Of the 20-point groups, 10 of the crystal classes contain a unique axis where the dipole moment is oriented in the unstrained condition, and they exhibit spontaneous polarization. The total polarisation vector is influenced by the application of a mechanical stress and temperature. Materials that have this temperature dependence are called pyroelectric. Ferroelectric materials represent a sub-group of pyroelectric materials, and they have the peculiarity that the spontaneous polarisation can be switched from one crystallographic orientation to others following the application of an external electric field. The spontaneous polarisation of these materials exists only in a specific temperature range. Below the so-called Curie temperature T_c, all the ferroelectric materials show the typical spontaneous polarisation. Above this temperature the crystal is in the paraelectric form, with no spontaneous

polarisation. For example, **Figure 2.3** shows the case of Barium Titanate ($BaTiO_3$). Above its Curie temperature $BaTiO_3$ is arranged in the paraelectric cubic phase with zero net polarisation.

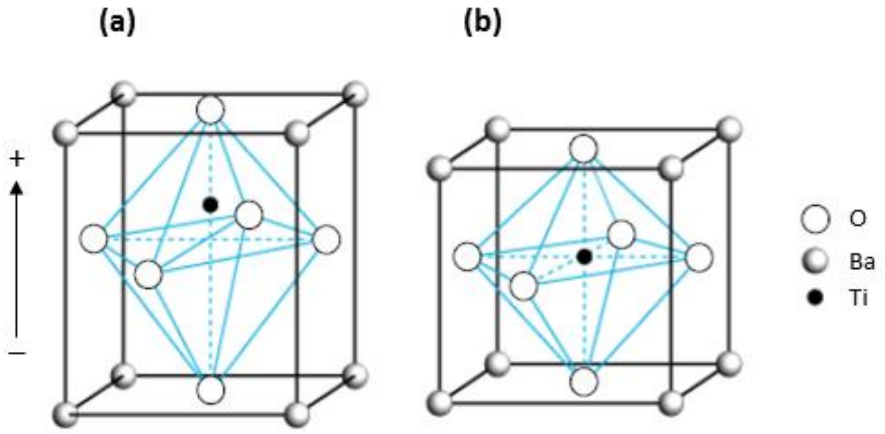

Figure 2.3. Crystal structure of $BaTiO_3$. (a) non-centrosymmetric tetragonal lattice (T < Tc) and (b) centrosymmetric cubic lattice (T>Tc).**[8]**

A ferroelectric polycrystalline ceramic is composed of crystalline domains, which are randomly oriented in all directions, thus, at a macroscopic level, the total net polarisation is equal to zero. To confer piezoelectric properties on the ferroelectric material it is necessary to align these randomly oriented domains. The alignment process is called *poling process* and requires the application of a direct current electric filed. It is mainly applied at relatively high temperature, below the Curie's temperature of the material, to enhance the alignment of the domains in the field direction. When the applied field is removed, most of crystallites remain in their aligned direction (**Figure 2.4**). After the poling process, the polycrystalline ceramic material is assimilable, for the effects of electrical behaviour, to a piezoelectric crystal; in fact, it has a moment of net dipole in the absence of deformation that responds linearly to an applied electric field or mechanical stress. A characteristic property of these materials is the non-linearity between the polarization (P) and the applied electrical field (E) which is shown in the hysteresis curves of various ferroelectric materials in **Figure 2.5**.

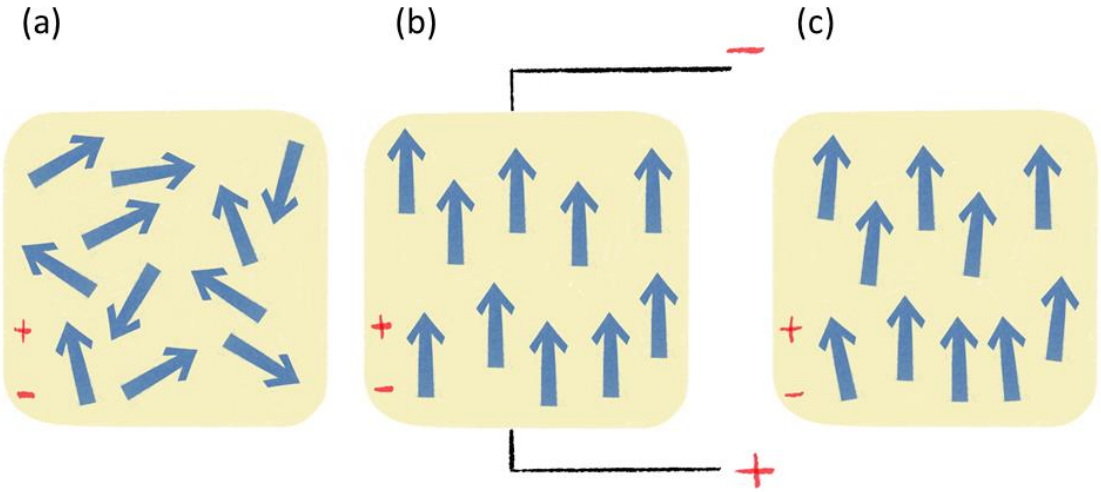

Figure 2.4. Poling process. (a) Randomly oriented dipoles, (b) polarisation in DC electric field, (c) oriented dipoles.

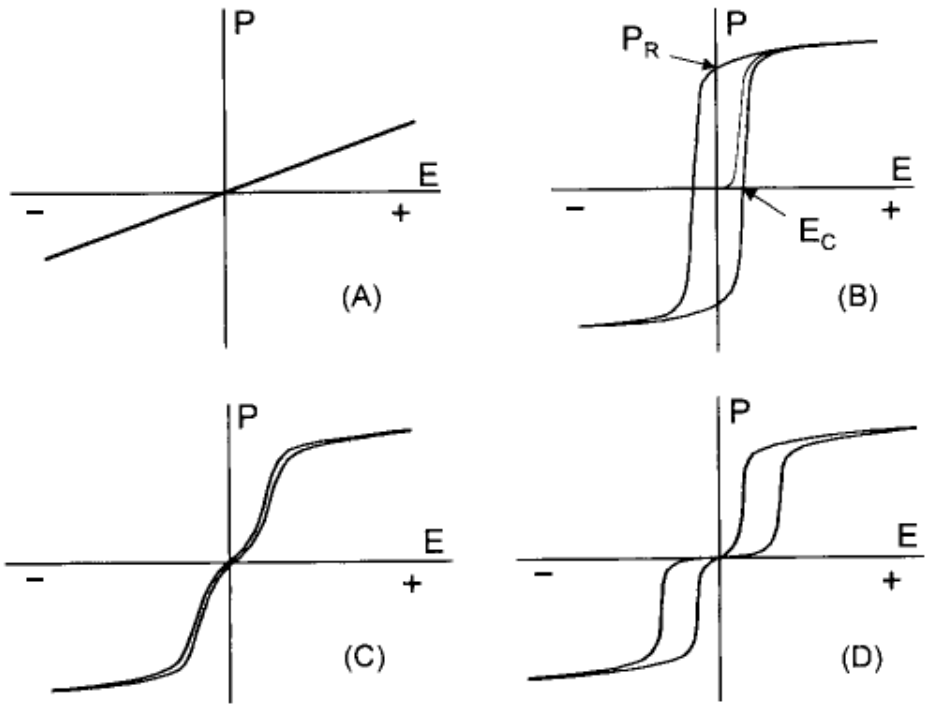

Figure 2.5. Typical hysteresis loops from various ferroelectric ceramics: (A) $BaTiO_3$ capacitor (no hysteresis), (B) soft (easily switchable) PZT, (C) PLZT 8.6/65/35 relaxor, and (D) PSZT antiferroelectric material.**[1]**

Hysteresis loops come in all sizes and shapes and, similar to fingerprint, identify the material in a very special way. The most common polarization-filed hysteresis curve is that one in **Figure 2.5b**. When an electric field is applied, the dipole begins to align with the field and the value of polarization (P) increases along with the electrical field until it reaches a saturation value. Reversing the direction of the electric field, the polarization decreases but will not fall down to zero. The remanent polarization (Pr) is the polarization value when the electrical field is equal to zero. To reduce the value of polarization to zero it is necessary to apply a field in the opposite direction. The field at which polarization is zero is called the coercitive field (Ec). If the field is further increased in the opposite direction, we observe the same phenomenon but in the negative direction. The hysteresis loop can be explained by the potential energy of the central cation of the perovskite unite cell that has the form of a double well as shown in **Figure 2.6**.

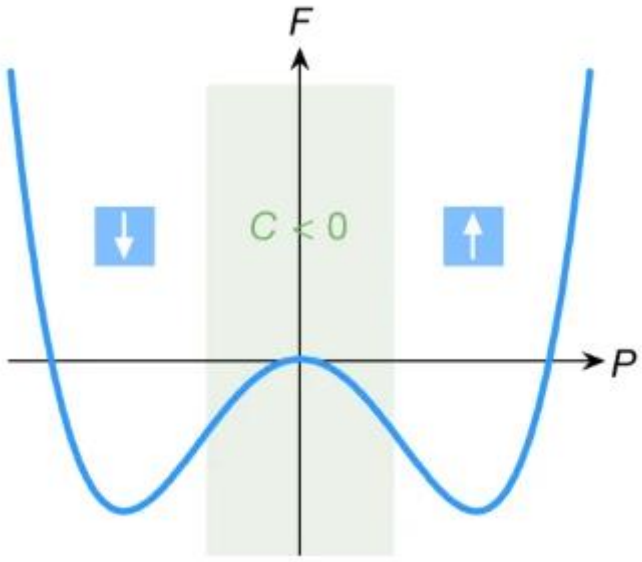

Figure 2.6. Variation of the free energy (F) of central cation of perovskite unit cell along c axis as a function of the polarization P. The grey zone represents the area with negative capacitance.**[9]**

The external field in the opposite direction of polarization moves the central cation from the potential minimum to the saddle point. The polarization is reversed after the field reaches its threshold value. When the field is removed, the cation stays in this well. However, many ferroelectric materials such as $BaTiO_3$, $PbTiO_3$ and $PbZrO_3$ experiment the ferroelectric fatigue, which is the loss of switchable polarization by repeated polarization reveals.**[10]** This phenomenon is due mainly to domain-wall pinning and microcracking and in fact represents a major drawback in applications like actuation, non-volatile ferroelectric random-access memory (NVFRAM), optical data storage and microelectromechanical systems (MEMS).

2.3 Ferroelectric perovskite ceramic materials

Figure 2.7 schematically shows the classification of piezoelectric materials. The vast majority of piezoelectric devices are based on ferroelectric polycrystalline ceramics due to their high performance and ease of manufacture. Among them, ferroelectric ceramics with perovskite ABO_3 crystal structure are the most studied because of their superior electrical properties due to their larger spontaneous polarization vector. Some of the main ones will be discussed below.

- **Lead zirconate titanate (PZT)**

The lead zirconate titanate $Pb(Zr_{1-x}Ti_x)O_3$ (PZT) is the most commercially exploited systems due to their large dielectric, piezoelectric and electromechanical coupling coefficients suitable for a wide number of classical technological applications such as buzzers, gas ignitors, sensors, ultrasonic motors and so on.**[11]** The compositional range in which the piezoelectric properties are optimized is close to the composition at $x \sim 0.5$. Around this composition, it is observed the coexistence of two ferroelectric phases (tetragonal and rhombohedral) that it takes the name of Morphotropic Phase Boundary (MPB). The explanation of the excellent piezoelectric properties around the MPB is related

to the increased ease of reorientation of the ferroelectric domains during the poling process due to the larger number of polar states.

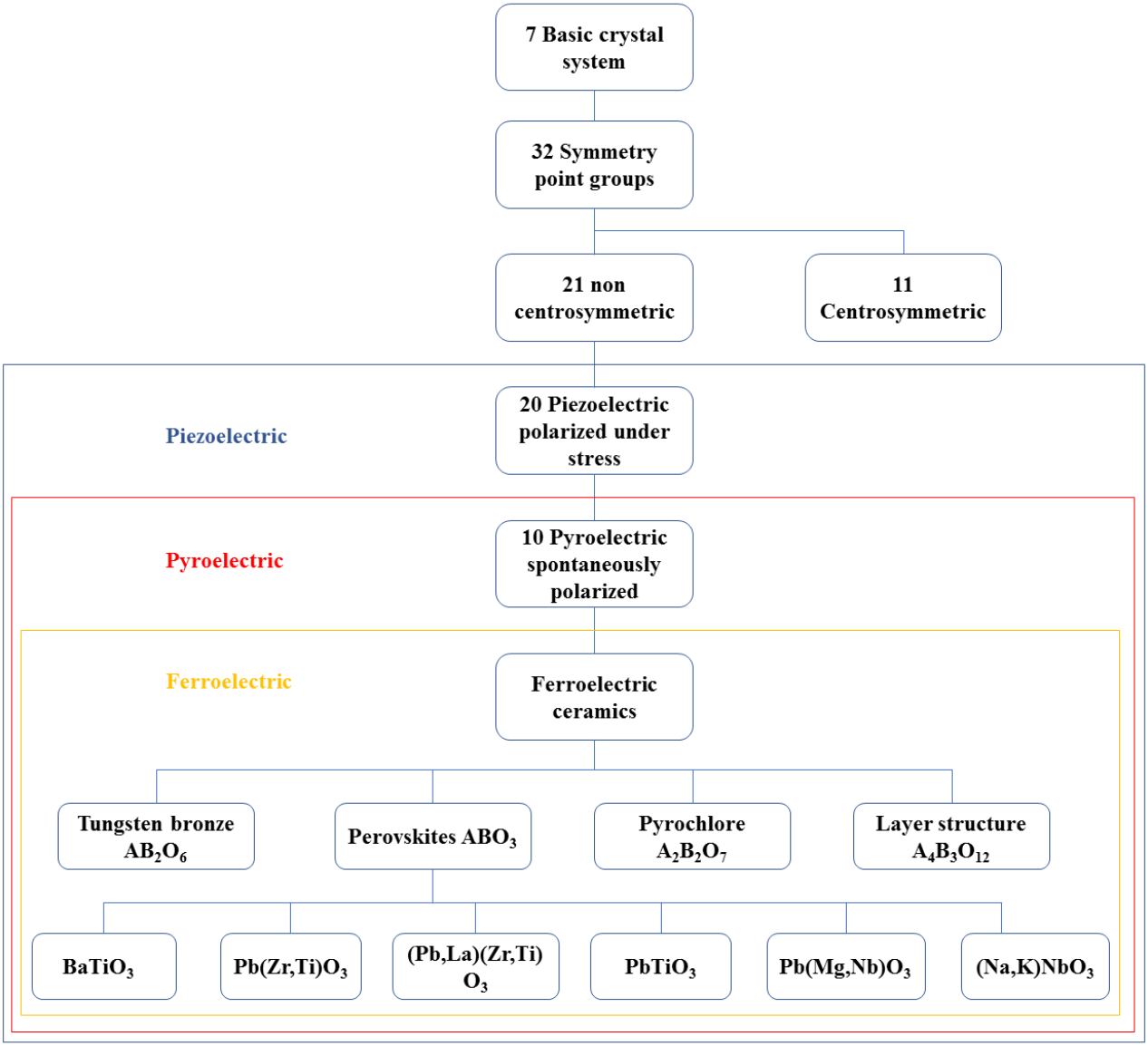

Figure 2.7. Schematic representation of the crystal systems classification for piezoelectric materials.

- **Barium Titanate (BT) and BT-based materials**

$BaTiO_3$ (BT) is the first piezoelectric ceramics that has been studied and used since 1940s.**[12]** The crystal structure of BT between, 5-120°C, is characterized by a tetragonal symmetry with P4mm space group. Over the Curie point (~120°C) the BT assumes a cubic centrosymmetric structure with Pm-3m space group. The cubic structure of BT certainly does not exhibit piezoelectric properties but it possesses an interesting isotropic dielectricity with a high dielectric constant. Below the Curie point, the tetragonal non-centrosymmetric structure causes a spontaneous polarization which confers ferroelectric and piezoelectric behaviour to the material. Regarding its piezoelectric properties, the d_{33} and k_{33} coefficients frequently reported are about 190 pC/N and 50% respectively.**[13]** Despite the electromechanical properties are fairly good, the low Curie point represent a problem for practical applications. A new modified BT system as the $(1–x)Ba(Zr_yTi_{1-y})O_3–x(Ba_{1–z}Ca_z)TiO_3$ (BCZT) shows improved piezoelectric properties (d_{33} ~620 pC/N); however, the problem related to the low Curie point still remains (~90°C).**[14]** For this reason**,** different additives as the $LiTaO_3$ or $Ba(Mg_{1/3}Nb_{2/3})O_3$ were used in order to increase the Curie point of this system without altering too much its electrical properties.**[15,16]**

- **Potassium sodium niobate (KNN) and KNN-based materials**

Potassium sodium niobate family (KNN) is the most promising and widely studied "lead free" system.**[13]** The 50/50 composition ($K_{0.5}Na_{0.5}NbO_3$) is characterized by improved dielectric and piezoelectric properties due to the Morphotropic Phase Boundary between a monoclinic and an orthorhombic phase.**[17]** Compared to BT and BT-based systems, the KNN exhibits a relatively high Curie temperature (~ 420°C) which makes it particularly attractive for practical applications.**[18]** The pure KNN presents several disadvantages which are mainly related to the poor densification, off-stoichiometry induced by volatilization during sintering and lower electromechanical properties

compared to PZT (d_{33} = 80 pC/N; k_p = 0.36-0.4; Q_m = 130).**[19]** For these reasons, over the years many additives have been successfully tested on KNN in order to improve these aspects. The state of the art presented in the next chapter will provide an insight on this topic.

2.4 Bibliography

[1] G. H. Haertling, *J. Am. Ceram. Soc*. **1999**, 82, 797–818.

[2] J. Tichý, J. Erhart, E. Kittinger, and J. Přívratská. Fundamentals of Piezoelectric Sensorics. Berlin, Heidelberg: Springer Berlin Heidelberg, **2010**.

[3] J. F. Nye. Physical properties of crystals: their representation by tensors and matrices. Oxford Science Publications **1985**.

[4] J. Holterman, P. Groen. An Introduction to Piezoelectric Materials and Applications. Stichting Applied Piezo, **2013**.

[5] F. Lionetto, A. Licciulli, F. Montagna, A. Maffezzoli. Piezoceramics: an introductive guide to their practical applications, Materials & Processes, **2004**, 3-4, 107-127.

[6] A. M. González, A. García, C. Benavente-Peces, L. Pardo. *Materials*. **2016**, 9, 72.

[7] C Alemany, L Pardo, B Jimenez, F Carmona, J Mendiola, A. M. Gonzalez. *J. Phys. D: Appl. Phys*. **1994**, 27, 148-155.

[8] E. Mercadelli, Università Degli Studi Di Bologna Alma Mater Studiorum. PhD thesis. **2013**.

[9] M. Hoffmann, F. P. G Fengler, M. Herzig, T. Mittmann, B. Max, U. Schroeder, R. Negrea, P. Lucian, S. Slesazeck, T. Mikolajick. *Nature*. **2019**, 565, 464–467.

[10] C. S. Hwang, R.M. McMeeking. *Ferroelectrics.* **1998**, 211, 177–194.

[11] S. Troyler McKinstry. *Am. Ceram. Soc. Bull*. **2020**, 99(1), 22–23.

[12] A. Von Hippel. *Rev. Mod. Phys.* **1950**, 22, 221.

[13] L. Pardo, M. E. Villafuerte-Castrejón, E. Morán, A. Reyes-Montero, R. Vivar-Ocampo, A. M. Gonzalez. Ecological, lead-free ferroelectrics. Magnetic, *Ferroelectric, and Multiferroic Metal Oxides*, **2017**, 201-219.

[14] W. Liu, X. Ren. *Phys. Rev. Lett.* **2009**, 103. 257602.

[15] M. Zhoua, R. Liang, Z. Zhou, C. Xua, X. Nie, X. Dong. *Mater. Res. Bull*. **2018** 106, 213–219.

[16] Z. Huang, Y. Lai, W. Guan, Y. Zeng, Y. Wei, S. Wu, J. Han, Y. Mao, Y. Xiang. *Mater Lett.* **2016**, 178, 163–165.

[17] D. W. Baker, P. A. Thomas, N. Zhang, and A. M. Glazer. *Appl. Phys. Lett*. **2009** 95, 091903.

[18] S. Garroni, N. Senes, A. Iacomini, S. Enzo, G. Mulas, L. Pardo, and S. Cuesta-Lopez. *Phys. Status Solidi A* **2018**, 215, 1700896.

[19] L. Egerton and D. M. Dillon. *J. Am. Ceram. Soc*. **1959**, 42, 438-442.

3 State of the Art

3.1 Introduction

Solid State Route (SSR) is an easy and cheap way to synthesize piezoelectric ceramics. In this context, potassium and sodium niobate (KNN) ceramics are not an exception, however some drawbacks are still present which can significantly affect the performance and the reproducibility of this material. Difficulties to obtain a dense product and control the stoichiometry are some of the main obstacles that prevent the large-scale production of this promising "lead free" system.**[1-3]** These main problems are actually closely related, and they depend mainly on the volatility of the sodium and potassium ions at the common sintering temperatures, which are typically higher than 1100 °C.**[4,5]**. This processing easily leads to deviations from stoichiometry and sometimes to the formation of unwanted secondary phases, which negatively affect the properties of the piezoceramic.**[6]** Therefore, the impossibility of using high temperature during the sintering process often involves some difficulty to obtain dense ceramics which is reflected in low electric properties.**[7,8]** Excellent results were obtaining using Hot Pressing (HP), Hot Isostatic Pressing (HIP) and Spark Plasma Sintering technique (SPS) that was possible to obtain with high density and excellent electrical properties.**[9-12]** However, common air sintering remains the simplest method, most widespread and economical, to prepare compacted products.**[13,14]**

Over the years various additives have been tested in order to limits these drawbacks; copper and zinc-based compounds such as CuO, $K_4CuNb_8O_{23}$, $CuNb_2O_6$, $K_{5.4}Cu_{1.3}Ta_{10}O_{29}$, ZnO and $K_{1.94}Zn_{1.05}Ta_{5.19}O_{15}$ have proved to be very efficient to improve the densification of the material through the insertion of acceptor cations (Cu^{2+}, Zn^{2+} etc ...) by replacing the Nb^{5+} ions in the crystalline lattice.**[15-20]** This occurred via the formation of a liquid phase during the sintering process as well as an increase of the "hard" behaviour. Basically, the main contribute of these doping

agents is the increase of the density with a lowering of the sintering temperature and a lowering of the mechanical losses. However, the increase of the electric and piezoelectric response is often marginal. Another class of doping agents of the ABO_3 perovskite-type are, for example, $LiBO_3$ (B = Nb^{5+}, Ta^{5+}, Sb^{5+}), $Bi_{0.5}A_{0.5}TiO_3$ (A = Na^+, Li^+, K^+), $CTiO_3$ (C = Ba^{2+}, Sr^{2+}, Ca^{2+}) and $DZrO_3$ (D = Ba^{2+}, Sr^{2+}, Ca^{2+}), $BiEO_3$ (E = Sc^{3+}, Al^{3+}, Fe^{3+}, Co^{3+}). The related multicomponent systems shall result in an improvement of “soft" properties which translates into better dielectric and piezoelectric properties often at the cost of mechanical losses.**[21]** Between these, bismuth ferrite ($BiFeO_3$; BF) is a quite promising doping agent. BF is a multiferroic material with a perovskite type structure and rhombohedral symmetry at room temperature; it has a high Curie temperature (810°C) and a high spontaneous polarization (about 100 $\mu C/cm^2$) and it can be easily introduced into the KNN matrix.**[22]**

Since a large part of this thesis work has been devoted to the study of the “pseudo-binary” KNN-BF system, the *State of the Art* here presented will be focused on KNN-based system with an emphasis on BF modified systems. After a first part dedicated on the processing method through the solid state route (SSR) and the electrical properties of KNN-BF composition, we will go on to illustrate various multicomponent systems trying to understand the reasons behind the choice of each modifying agent. Finally, the last section will be dedicated to some promising KNN-based systems prepared using the Spark Plasma Sintering technique.

3.2 KNN-BF: fabrication method and electrical properties

The synthesis procedure through solid state route foresees various steps summarized in **Figure 3.1**. Sodium Carbonate (Na_2CO_3), potassium carbonate (K_2CO_3), niobium (V) oxide (Nb_2O_5), iron (III) oxide (Fe_2O_3) and bismuth (III) oxide (Bi_2O_3) are generally used as a starting reagent.**[23-28]**

Due to their high hygroscopicity, sodium and potassium carbonate are subjected to an anhydrification process before being manipulated. Milling is necessary to decrease the average particle size, obtain a more homogeneous mixture and therefore to increase the reactivity of the powders and thus facilitate the solid-state reaction and the sintering process.

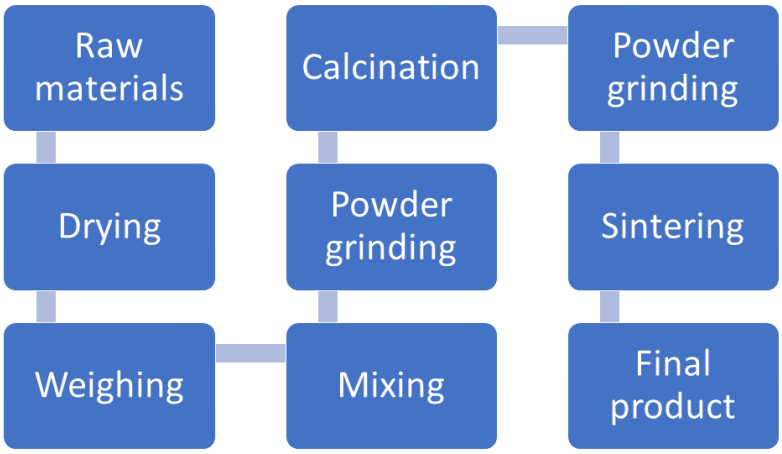

Figure 3.1. Flow diagram of the main steps used to manufacture compacted ceramic products by solid state route (SSR).

Grinding is generally conducted with ethanol as a medium and using plastic, agate, zirconia or yttria-stabilized zirconia jars and balls.**[23-28]** The reaction temperature used for calcination is generally between 800-900 °C; sodium and potassium carbonates, iron oxide and bismuth oxide react with niobium oxide to form the perovskite phase. The reaction in the general case of (1-x)KNN-xBF is shown below (**Equation 3.1**):

$$a\,K_2CO_3 + a\,Na_2CO_3 + b\,Nb_2O_5 + c\,Bi_2O_3 + c\,Fe_2O_3 \rightarrow (1-x)K_{0.5}Na_{0.5}NbO_3 - x\,BiFeO_3 + b\,CO_2 \quad (3.1)$$

Where **a**, **b**, **c** and **x** are stoichiometric coefficients that depend on the desired composition. The only waste product is the carbon dioxide which is easily removed during the heat treatment. The

calcination reaction is generally followed by the consolidation process of the powders which takes the name of sintering.

Sintering is a widely used technique to make useful part from metal or ceramic powders. During this process, the powder particles bond to each other and matter transport occurs. In this way it is possible to eliminate micro-pores and the sample becomes denser and stronger.**[29]** A widely used variant is the liquid phase sintering (LPS). Generally, an additive (sintering aid) is added before sintering. The additive, in the liquid state at the sintering temperature, wet the solid matrix providing a capillary force that pulls the grain together, moreover the liquid improves transport rates responsible for grain coarsening and densification.**[30]** For KNN ceramics it has been found that density increased greatly within a narrow temperature range around 1120 °C but it tends to decrease when the sintering temperature exceeds this narrow limit.**[31]**

Table 3.1. Main parameters involved in the synthesis and manufacturing of KNN-BF systems through solid state route.

System	Milling condition	Calcination temperature °C	Sintering temperature °C	Ref.
(1-x)KNN-xBF ($0 \leq x \leq 0.10$)	Planetary ball mill - alcohol (12h)	850-900	1000-1130	**[23]**
(1-x)KNN-xBF ($0 \leq x \leq 0.06$)	Ball milling - ethanol (12h)	880	1135	**[24]**
(1-x)KNN-xBF ($0 \leq x \leq 0.018$)	Ball milling - ethanol (24h)	850	1085-1100	**[25]**
(1-x)KNN-xBF ($0 \leq x \leq 0.07$)	Planetary ball mill - alcohol (10h)	900	1100	**[26]**
(1-x)KNN-xBLF ($0 \leq x \leq 0.04$)	Ball milling - ethanol (12h)	800	1100-1150	**[27]**
(1-x)KNN-xBF ($0 \leq x \leq 0.03$)	Attrition mill - isopropanol (1h)	850	1100-1140	**[28]**

In principle, piezoelectric properties follow a similar trend however a deviation from this behaviour was observed when volatility of alkaline ions becomes significant. All of this leads to the formation of unwanted secondary phases which result in deterioration of piezo properties. The volatilization is obviously accentuated with the increase of temperature but also by the presence of liquid phases. In the specific case of (1-x)KNN-xBF system (with $0<x<0.10$), the best sintering conditions were found between 1000-1150°C. In **Table 3.1** are included some of the main parameters involved in the synthesis and manufacturing of KNN-BF system.

Table 3.2. Summary table with some of the most important electric and piezo coefficients of KNN-BF systems prepared through solid state route.

System	d_{33} (pC/N)	k_p (%)	P_r (μC/cm²)	ε_r	tanδ	Q_m	Ref.
(1-x)KNN-xBF (x =0.01)	185	46	23.3				**[23]**
(1-x)KNN-xBF (x=0.006)	146	51		432	0.046	107	**[24]**
(1-x)KNN-xBF (x=0.013)	173	40	26	905	0.04		**[25]**
(1-x)KNN-xBF (x=0.01)	145	31	11.3			80	**[26]**
(1-x)KNN-xBLF (x=0.01)	144	34	22.5	500	0.1		**[27]**
(1-x)KNN-xBF (x=0.01)	182	50	26				**[28]**

Concerning electrical properties, Zuo et al. have obtained interesting properties in the composition around the phase boundary between 1-2 mol% of $BiFeO_3$. In particular the 0.99KNN-0.01BF possess the best properties of P_r = 23.3 μC/cm², d_{33} = 185 pC/N and k_p = 46% using a sintering temperature of 1100 °C.**[23]** Xu et al. found optimized parameters in the compositional range between 0.6 and 1 mol% of BF. In particular they found good properties of d_{33} = 146 pC/N, k_p = 51%, T_c = 405 °C, To-

t = 185°C, ε_r = 432, and tanδ = 4.60% for the sample doped with 0.6 mol% of BF.**[24]** Li et al. have studied a composition range of 0.009<x<0.018 adding 1 mol% of Fe_2O_3 as a fluxing medium to improve sinterability. They found maximal properties of d_{33} = 173 pC/N, k_p = 0.40, tanδ = 0.04, ε_r = 905, P_r = 26 μC/cm^2, E_c = 11.2 kV/cm for the KNN doped with 1.3 mol% of BF.**[25]** Sun et al. explored a wider composition up to 7 mol% of BF however, according with the works mentioned above, they found optimum piezoelectric properties of d_{33} = 145 pC/N, k_p = 0.31, Q_m = 80, Pr = 11.3 μC/cm^2 and E_c = 16.5 kV/cm for the sample doped with 1 mol% of BF.**[26]** Zhang et al. have studied a similar system with small amount of lanthanum in KNN-BF [(1-x)$K_{0.5}Na_{0.5}NbO_3$- x$Bi_{0.8}La_{0.2}FeO_3$ (BLF)]; in particular they studied a compositional range between 0.5 and 4 mol% of BLF and they found optimized parameters of P_r = 22.5 μC/cm^2, d_{33} = 144 pC/N, and k_p = 0.34 by adding 1 mol% of BLF.**[27]** No particular differences in terms of properties are observed between this work and the classic BF doped systems. Recently, Khesro and co-workers have shown very promising results of d_{33} = 182 pC/N, and k_p = 0.50 with the addition of BF around x~1 mol%. In this case, they opted for an excess of sodium in the KNN matrix, as it has been demonstrated that the composition x= 0.6 (Na^+ rich) have lower T_{O-T} compared to x = 0.5.**[28]** In **Table 3.2** a summary table with the main electric and piezo coefficients of these systems. Summarizing is quite clear that the best properties are achieved when 1 mol% of BF is added to the KNN matrix (d_{33} = 144-185 pC/N; k_p = 0.31-0.5; Q_m = 75-107). This increase of piezoelectric response, compared to undoped KNN (d_{33} = 80 pC/N; k_p = 0.36-0.4; Q_m = 130), is attributed to the co-presence of two different ferroelectric phases which guarantee a large number of thermodynamically equivalent states and therefore a high degree of alignment of ferroelectric dipoles.**[32]** In addition, BF seems to have benefits also as a sintering aid when it is added in small doses (below 2 mol%), and this determines a remarkable improvement of the quality of microstructure, as it can be appreciated in **Figure 3.2**.

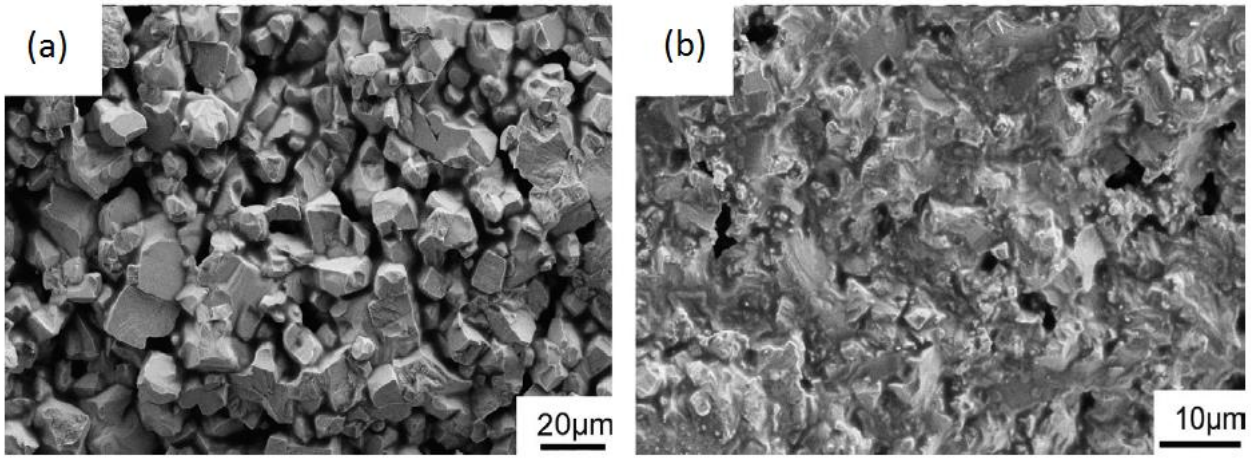

Figure 3.2. SEM micrograph of fractured surface of (a) pure KNN and (b) KNN modified with 1 mol% of BF.**[26]**

3.3 KNN-BF + ABO_3

The 50:50 composition of KNN (**Figure 3.3**) is characterized by three main phase transitions. A rhombohedral-orthorhombic (R-O) phase transition at ~ -120 °C, an orthorhombic-tetragonal (O-T) at ~ 200°C and a tetragonal-cubic (T-C) at ~ 420°C which also represent the Curie temperature of this system. The crystal structure at room temperature of the 50:50 composition is often described to be composed of two orthorhombic phases where the dielectric and piezoelectric properties are maximized.**[34]** However, the true nature of the crystalline structure near this composition is still unclear and is subject of debate. For example, Tellier et al. proposed a monoclinic Pm structure with a β angle close to 90°.**[35]** Baker et al. suggest a coexistence of an orthorhombic Amm2 and a monoclinic Pm phase (**Figure 3.4**). The phase transition as a function of the composition was studied by measuring the full width at half maximum (FWHM) of the 200/002 peaks in the region between $0.4<x<0.9$. They observed that between 0.4 and 0.5 the FWHM decrease rapidly until it reaches a constant value beyond 0.5, which indicates that the structure has completely entered to the orthorhombic phase and confirming the change of structure.**[36]**

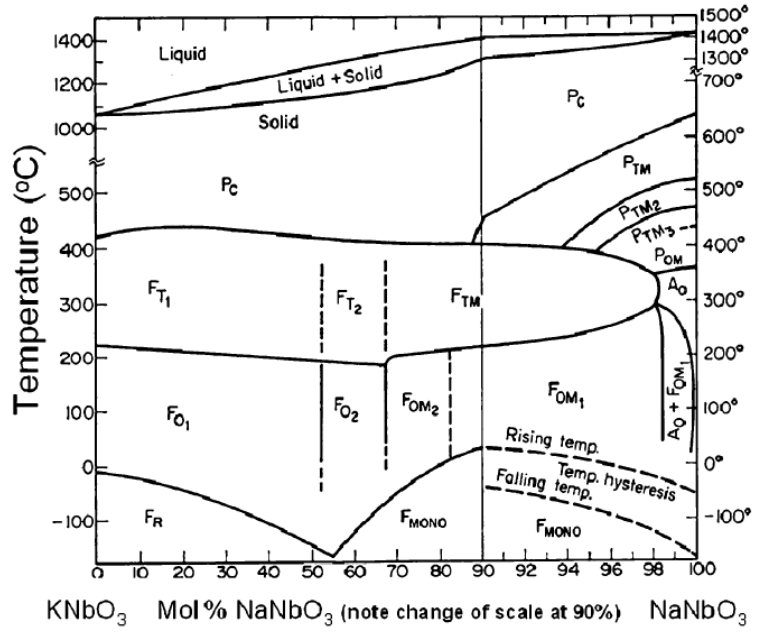

Figure 3.3. The original phase diagram of the binary system $KNbO_3$-$NaNbO_3$.**[33]**

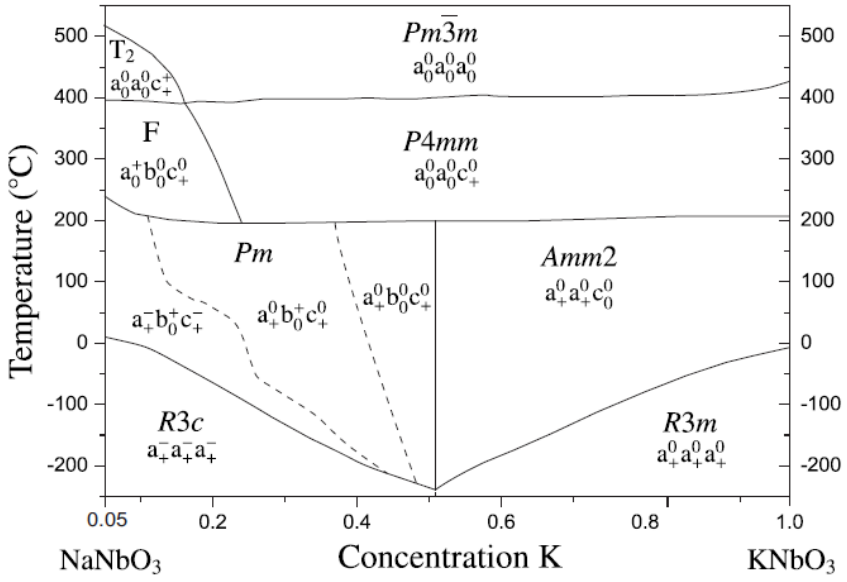

Figure 3.4. Phase diagram of KNN proposed by Baker et al.**[36]** In this case the 50:50 composition is characterized by an orthorhombic-monoclinic phase boundary.

This claim was supported by the works of Dai and Kumar, which confirm the co-presence of an orthorhombic and monoclinic phases at x ~ 0.5.**[37, 38]** Another point of view provides for the co-

existence between an orthorhombic symmetry and monoclinic ABO_3 primary cell as shown in **Figure 3.5** As the β angle of the monoclinic cell is very close to 90°, the structure is often described simply as orthorhombic, especially in all of those papers that are focused mainly on materials properties. For the sake of simplicity, from this point we will refer to this structure as an orthorhombic structure with Amm2 space group. It is well known that the optimization of piezoelectric properties of a polycrystalline ceramic depends on the choice of a very restricted composition that takes the name of Morphotropic Phase Boundary (MPB). This particular range is characterized by the co-presence of two different ferroelectric phases where dielectric, piezoelectric and electromechanical coupling coefficients are maximized. Many discussions have arisen concerning the reasons that explained the underlying mechanisms of the enhanced piezo properties along the MPB, however it is widely accepted that this effect is due to the optimal domain orientation during the poling process caused by a larger number of thermodynamically equivalent states, represented by the oriented dipolar sites inside the unit cells.

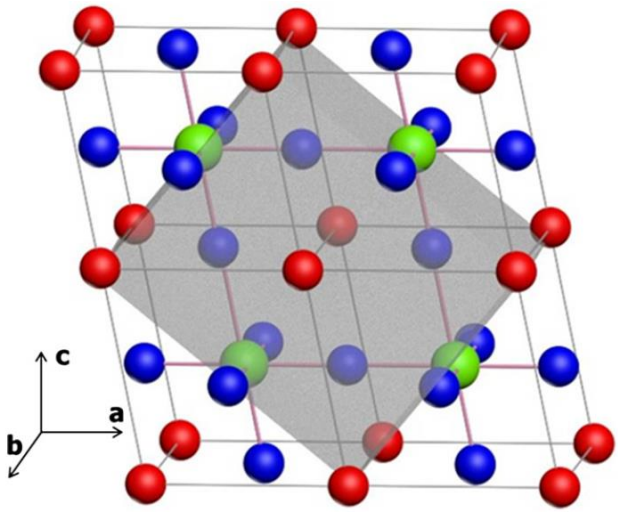

Figure 3.5. Orthorhombic Amm2 structure (grey area) with 4 monoclinic ABO_3 primary cell. The β angle is exaggerated for a clearer view of the structure.**[39]** The red balls are the A-site occupied by alkali elements, green balls are B-site of Niobium oxide (V) and blue balls are the oxygen atoms.

Strictly speaking, the MPB is referred to a structural change, that depends on the variation of the composition, and it is almost independent from the temperature. A well-known example is represented in **Figure 3.6** by the PZT ($Pb(Zr_{1-x}Ti_x)O_3$) in which the co-existence of tetragonal and rhombohedral phases is reached to a specific composition around x ~ 0.48.

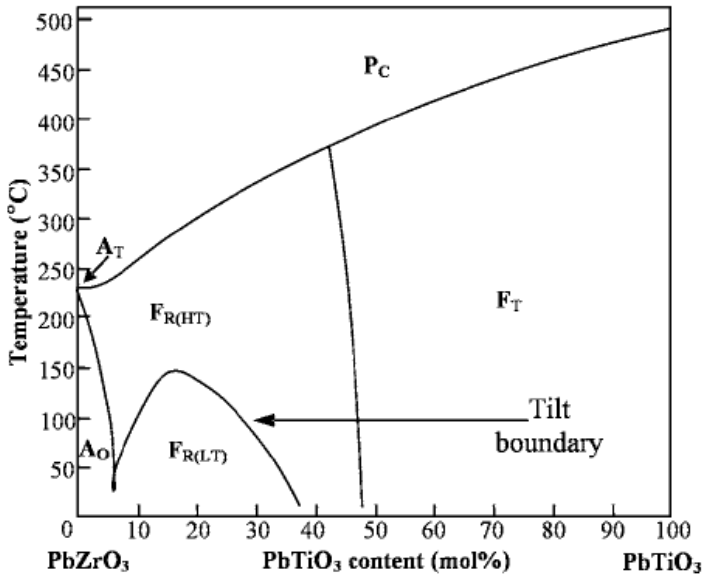

Figure 3.6. PZT phase diagram. The MPB is almost independent from the temperature (note the slight slope to the left in the part of the phase diagram rich in Zr^{4+}) and in happens when x ~ 0.48.**[40]**

As we have seen previously, KNN materials have three kind of phase boundaries with a dependence on both composition and temperature. In this case we properly speak of Polymorphic Phase Transition (PPT) and the main difference with MPB is the strong dependence of the temperature, as can be appreciate in a schematic way in **Figure 3.7**. MPB-piezoceramics have the characteristic of having a negligible dependence on temperature which allows a wide range of operating temperatures (~ 1/2 T_c). Instead, PPT-piezoceramics generally exhibit a large temperature dependence of the piezo properties which translates to a rapid degradation of the piezo coefficients when the PPT temperature is exceeded.

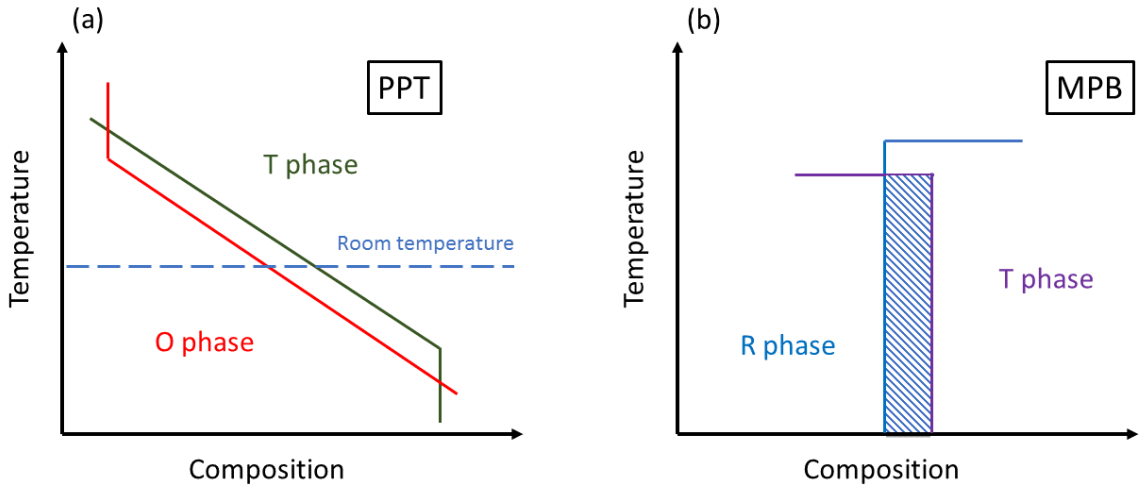

Figure 3.7. Difference between PPT (a) and MPB (b). Note the dependence of the temperature in the PPT case.

This fact certainly constitutes an additional limit to KNN-based systems and therefore the engineering of new dopants requires a greater attention towards the stabilization of the working temperatures. Ample proof has now been provided that piezoelectric properties of a piezoceramic can be enhanced through the formation of phase boundaries by chemical modification. Regarding KNN-based materials, three kind of phase boundaries (O-T, R-O and R-T) can be "shifted" to room temperature by adding an appropriate amount of modifying agents. The number and type of dopants tested on KNN matrix is really huge and constantly increasing **[21]**, but since this review is interested particularly on KNN-BF based systems, only the latter will be analysed. It is widely accepted that KNN-BF system has an orthorhombic-tetragonal (O-T) phase transition at room temperature when ~ 1 mol% of BF is added to KNN matrix.**[24-26, 41]** Since most of the works are much more interested in the material properties of the ceramics, an accurate crystallographic study is often missing. In any case, some powerful tools like high-resolution synchrotron X-ray powder diffraction, neutron diffraction, Raman spectroscopy and Rietveld refinement are very useful to identify the true nature

of these mixed systems.**[42-45]** In order to evaluate the transformation of the crystal structure as a function of the composition, the approach that is generally used provides for a comparison between the diffraction peaks around 46°. A clear example is provided by Li et al. in **Figure. 3.9**. Pure KNN is characterized by an orthorhombic crystal structure, easily recognizable because the signal at ~ 46° is made up of two distinct peaks corresponding to the crystal planes (202) and (020) among which the (202) is much more intense. With the progressive addition of BF, a change in the relative intensity of these two peaks is observed. This phenomenon is justified by the change from orthorhombic to tetragonal symmetry. The PPT is located around x~0.01, easily recognizable because the two split peaks have nearly the same intensity. With further addition of BF (x>0.015) the system completely assumes a pseudocubic structure with **a** and **c** cell parameters very similar to each other.

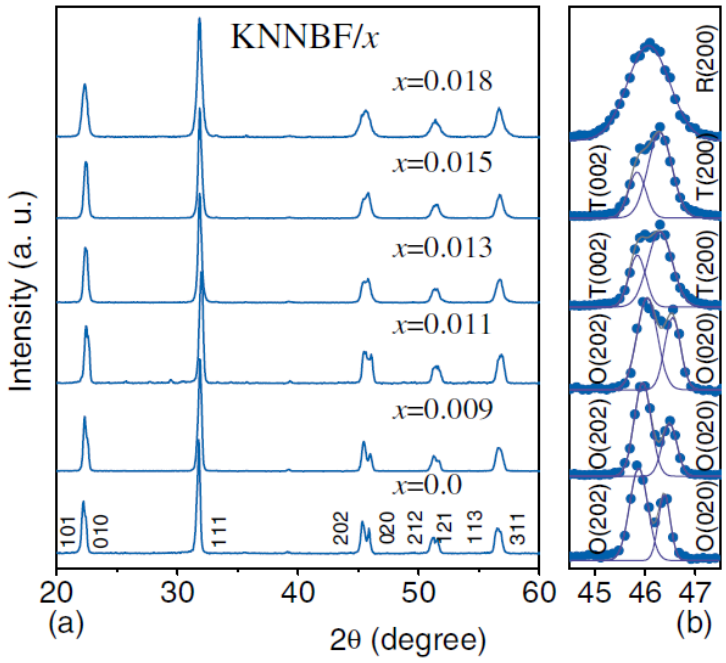

Figure 3.8. (a) XRD patterns of (1-x)KNN-xBF with 0<x<0.018. (b) Magnification of the diagnostic peak around 45°.**[25]**

A net improvement in terms of electrical properties was achieved with KNN-BF + ABO_3 systems. Generally, these systems are characterized by complex chemical compositions with three or more ABO_3 type compounds. $K_{0.5}Na_{0.5}NbO_3$-$LiSbO_3$-$BiFeO_3$ (KNN-LS-BF) is one of them with very promising electrical properties (d_{33} ~ 260-285 pC/N; k_p ~ 0.48-0.54).**[46-49]** In order to explore the electrical properties of the composition, generally, the ratio between two components is kept fixed and the third component is added with different concentration. For example, Jiang et al. studied the (1-x)(0.95$K_{0.5}Na_{0.5}NbO_3$-0.05$LiSbO_3$)-x$BiFeO_3$ solid solution (0<x<0.01); they found optimum properties of d_{33} = 260 pC/N, k_p = 51.5%, ε_r = 1561 and tanδ = 0.02 attributing the enhancement of properties to the formation of the PPT between orthorhombic and tetragonal phases at x ~ 0.004.**[46]** Comparable results of d_{33} = 280 pC/N, k_p = 53.3%, ε_r = 1613 and tanδ = 0.027 were obtained for (0.996-x)$K_{0.5}Na_{0.5}NbO_3$-0.004$BiFeO_3$-x$LiSbO_3$ with x=0.05 which is essentially the same nominal composition as the previous work.**[47]** Also this time, the PPT plays an important role in the enhancement of the piezoelectric properties, however this view is not always accepted. For example, Zhu proposed a single tetragonal structure with optimum properties of d_{33} =285 pC/N, k_p = 54.3%, ε_r = 2185 and tanδ = 0.0192 for 0.937KNN-0.06LS-0.003BF composition. In this case best properties have been attributed to a better densification and to a better microstructure rather than to PPT.**[48]** A small addition of Co^{3+} as a substitute for Fe^{3+} in $BiFeO_3$ for KNN-LS-BF was investigated by Zhao et al. They found optimum piezo properties of d_{33} = 276 pC/N, k_p = 48%, ε_r = 1284 and tan = 0.0195.**[49]** The role of cobalt is to improve the growth of the grains and the densification process, moreover it seems to have no influence on the crystalline symmetry of the solid solution, which remains tetragonal throughout the range of composition investigated. Another equally promising systems is the (K, Na, Li,)(Nb,Ta)O_3-x$BiFeO_3$ (KNLNT-BF). In this case, the third component is virtually represented by Lithum Tantalate ($LiTaO_3$) but since lithium and tantalum are not in 1:1 stoichiometric ratio, as a formality, they are inserted as substituents within the KNN formula. The

KNLNT shows different phase transition behaviour which depend on the difference in terms of the amount of lithium ions within the solid solution. For example, Zhou et al. studied the $Li_{0.03}(Na_{0.53}K_{0.48})_{0.97}Nb_{0.8}Ta_{0.2}O_3$–$xBiFeO_3$ with $0 \leq x \leq 2$ mol%. At room temperature, KNLNT shows the prevalence of the orthorhombic phase but the introduction of the BF inside the solid solution causes a progressive transformation in favour of the tetragonal phase which becomes single phase for high levels of BF (**Figure 3.9**). The pure KNLNT ceramics show a To-t around 50°C, this is the reason why the ceramic has an orthorhombic symmetry at room temperature. After the addition of BF, the To-t is progressively shifted towards lower temperatures until the tetragonal phase becomes predominant. The best electrical properties of d_{33} = 238 pC/N, k_p ~47.0% and Q_m ~75 have been found for KNLNT with 0.5 mol% of BF, attributing this improvement to the coexistence of the orthorhombic and tetragonal ferroelectric phases.**[50]**

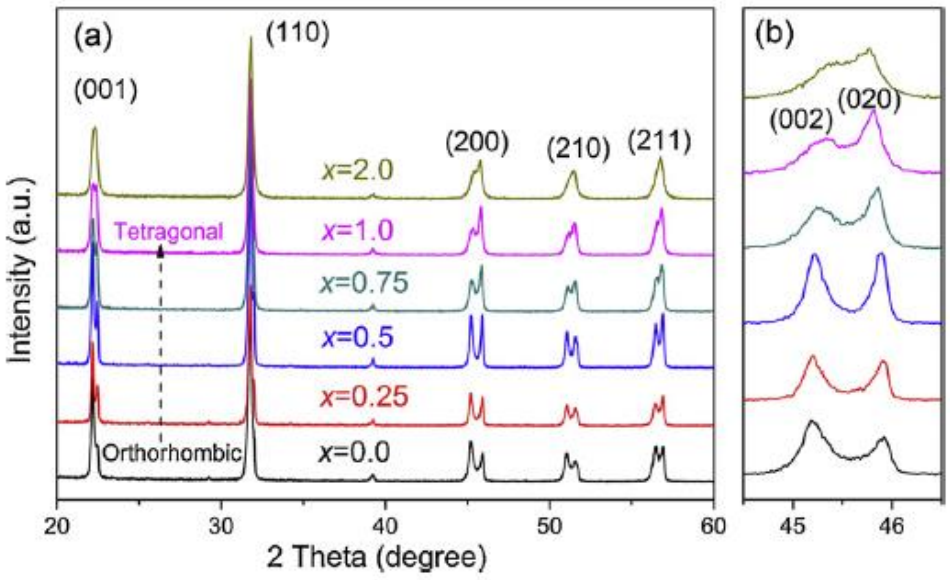

Figure 3.9. (a) XRD patterns of KNLNT-xBF.**[50]**

A similar system with composition $(1\text{-}x)[(K_{0.458}Na_{0.542})_{0.96}Li_{0.04}](Nb_{0.85}Ta_{0.15})O_3$–$xBiFeO_3$ ($0<x<0.008$) was studied by Chao et al. In this case, the higher amount of Li^+ compared to the previous case, determines that To-t of KNLNT is already around room temperature, a further addition

of BF causes a further shift towards lower temperature, this justifies the constant presence of the tetragonal phase throughout the range of composition explored. The 0.4 mol% BF doped KNLNT exhibited excellent electrical properties of d_{33} = 261 pC/N, k_p = 0.58, P_r = 23.7 μC/cm^2. This time, the optimal electrical properties are attributed to the denser and more uniform microstructure; in addition, the lattice deformation generated by A-site vacancy makes the reorientation of the ferroelectric domains easier during electrical poling and leads to the enhancement of the piezoelectric properties.**[51]** A similar system with the addition of small amount of Sb^{5+} (1-x)($K_{0.44}Na_{0.52}Li_{0.04}$)($Nb_{0.84}Ta_{0.1}Sb_{0.06}$)$O_3$-x $BiFeO_3$ was studied by Jiang et al. The ease of domain wall movement around the MPB due to the co-existence of the orthorhombic and tetragonal phases allows to obtain the optimized electrical properties of d_{33} = 246 pC/N, k_p = 43% ε_r = 1871, tanδ = 0.0196 and Q_m = 94.**[52]** These results seems to be in good agreement with that found by Chao et al with the composition (1-x)[($K_{0.458}Na_{0.542}$)$_{0.96}Li_{0.04}$]($Nb_{0.85}Ta_{0.15}$)O_3–x$BiFeO_3$, in addition they have shown that the addition of BF could also improve the time and temperature stability of KNLNT based ceramics.**[53]** The good electrical properties of KNN-LS-BF and KNLNT-BF have been recently further improved by new solid solution based on $K_{0.5}Na_{0.5}NbO_3$-$Bi_{0.5}Na_{0.5}ZrO_3$-x$BiFeO_3$ (KNN-BNZ-BF). The obtained excellent piezoelectric properties (d_{33} > 400 pC/N) are ascribed to the new R-O-T phase coexistence which is considered to resemble the classical morphotropic phase boundary (MPB) observed in lead zirconate titanate (PZT). The mechanism of formation of this new phase boundary involves the simultaneous use of Bi^{3+} and Zr^{4+}. Is well known that Bi^{3+} can shift the To-t through room temperature, instead Zr^{4+} increase the Tr-o to room temperature. Therefore, Bi^{3+} and Zr^{4+} could be used to tune the $T_{R–O}$ and $T_{O–T}$ of KNN forming the R−T phase boundary by simultaneously shifting $T_{R–O}$ and $T_{O–T}$ at room temperature. BNZ can be used for this purpose, however Zr^{4+} has a strong influence in lowering the Curie Temperature of KNN ceramics which results in a disadvantage in terms of electrical stability. In this context, BF plays an important role in

maintaining a relatively high T_c and at the same time to favour the formation of the R-T phase transition at room temperature. This process can be clearly monitored by measuring the variation of dielectric permittivity as a function of temperature according to different compositions (**Figure 3.10**).

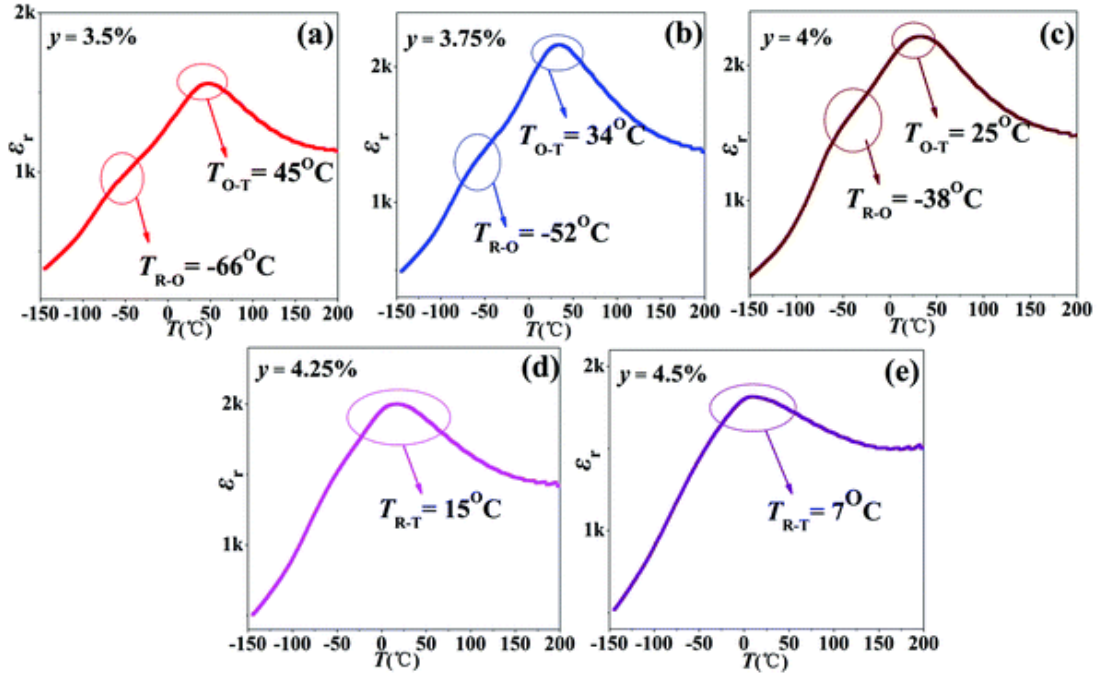

Figure 3.10. ε_r–T (−150–200 °C) curves of KNN–yBNZ–0.006BF ceramics with different y contents: (a) y = 0.035, (b) y = 0.0375, (c) y = 0.040, (d) y = 0.0425, and (e) y = 0.045.**[54]**

Important results have been achieved in terms of piezoelectric response. Wu et al. have studied (1-x-y)KNN-xBF-yBNZ solid solution and they took over a giant d_{33} of 428 pC/N with a relatively high Curie temperature of ~ 318°C with x = 0.006 and y = 0.04.**[54]** Ma and co-workers obtained similar results of d_{33} = 438 pC/N ad T_c ~ 320°C with a very similar nominal composition.**[55]** A decisive step forward was made by Yao et al. with a small addition of Sb^{5+} as a substituent of Nb^{5+} to KNN-BF-BNZ system. The KNNS-BF-0.03BNZ ceramic was found to show a giant d_{33} piezoelectric coefficient of 550 pC/N at room temperature.**[56]** In **Table 3.3** are summarized some of the main electrical and piezoelectric coefficients of KNN-BF + ABO_3 compounds.

Table 3.3. Summary table with some of the most relevant electric and piezoelectric coefficients of KNN-BF+ ABO3 systems prepared through solid state route.

System	d_{33} (pC/N)	k_p (%)	ε_r	tanδ	Q_m	Ref.
(1-x)(0.95KNN-0.05LS)-xBF (x=0.004)	260	51.5	1561	0.02	44.48	**[46]**
(1-x)(0.996KNN-0.004BF)-xLS (x=0.05)	280	53.3	1613	0.027		**[47]**
0.937KNN-0.06LS-0.003BF	285	54.3	2185	0.0192	66	**[48]**
KNN–LS–BF(1-x)Cx (0<x<0.8)	276	48	1284	0.0195		**[49]**
KNLNT + 0.5mol% $BiFeO_3$	238	47			75	**[50]**
KNLNT + 0.4mol% $BiFeO_3$	261	58				**[51]**
KNLNTS + 0.6mol% $BiFeO_3$	246	43	1871	0.0196	94	**[52]**
KNLNT + 0.4mol% $BiFeO_3$	261	58	1116	0.016		**[53]**
(1-x-y)KNN-xBF-yBNZ (x=0.006 and y=0.04)	428	52				**[54]**
0.954K(1-x)NxN–0.04BNZ–0.006BF	438	51	2304	0.029	50	**[55]**
KNNS-BF-xBNZ (x=0.03)	550	52	3490	0.043	51	**[56]**

3.4 KNN-ABO_3 + sintering aids

Another well-known class of modifying agents extensively tested on KNN systems are the sintering aids. It is important to immediately point out that this modifying strategy is not alternative to the use of ABO_3 agents, but it could be complementary, as we will see later. The ABO_3 agents act by modifying the crystal structure of KNN that causes the shift of the phase transitions at room temperature which determines the multiple ferroelectric phase coexistence. This produces an increase of the "soft" behaviour of the ceramics which translates into an improvement of the piezoelectric properties of KNN. However, the sintering temperatures of these systems still remain high (typically >1100°C)**[46-56]** and this can easily lead to problems related to volatility of the alkaline ions and reproducibility. Furthermore, the mechanical quality factor (Q_m) is strongly compromised (**Table 3.3**) and this precludes the use of these materials in high-power acoustic applications like ultrasonic devices and sonar technologies.

In this context, the sintering aids proved to be very efficient in improving both densification and, in some cases, the "hard" characteristic of KNN ceramics. In particular, copper-based additives have proved to be very effective for both purposes. For example, Ahn et al. obtained good electrical properties of d_{33} = 100 pC/N; k_p = 0.36% and Q_m = 1200 adding 1.5 mol% of CuO to pure KNN. Despite the extremely low sintering temperature of 950°C, the sample reached a relatively high density of 91% of TD. The excellent sintering behaviour has been attributed to the liquid phase formation at low temperature while the large mechanical quality factor (Q_m = 1200) was explained with the Cu-substitution on the Nb-site which causes the formation of oxygen vacancy that pin the domain boundary.**[15]** Matsubara et al. developed a new additive based on copper with formula $K_4CuNb_8O_{23}$ (KCN). They obtain an excellent density value of 4.40 g/cm^3 (97.5 % of TD) and good electrical properties of d_{33} = 180 pm/V; k_p = 0.39; Q_m = 1200 with the addition of 0.5 mol% of KCN.

They also found a decrease in the sintering temperature as a function of the addition of KCN, in particular the optimum sintering temperature of KNN ceramics, at which the density is maximized, decreased from 1140°C to 1060°C by varying the composition from 0 to 1.5 mol% of KCN.**[16]** Yang et al. tested a columbite-type modified agent as $CuNb_2O_6$ (CN) with the aim of improving the sinterability of KNN as CuO but also to decrease the A/B ratio. They found good piezoelectric properties (d_{33} = 92.5 pC/N; k_p = 40%) and excellent "hard" characteristic (E_c = 25.5 kV/cm and P_r = 22.63 μC/cm^2 and Q_m = 1933) for the sample modified with 1 mol% of CN.**[17]**

Zinc based compounds are another class of sintering additives widely studied on KNN system. Zn^{2+} has the same valence and similar ionic radius (88 pm) to copper (87 pm), therefore it is expected to act as an acceptor doping by substituting Nb^{5+} in the crystal lattice. However, the large "hardening" behaviour is not observed.**[19,20]** For example, Chen et al. studied the pure KNN modified with increasing amount of ZnO.**[19]** They found that ZnO promotes the growth of grain and the density of KNN which it is reflected in a significant improvement in the piezoelectric response of the material (KNN = 85 pC/N; KNN:0.2ZnO = 110 pC/N). Through XRD investigation the presence of ZnO secondary phase emerged already at low concentrations (0.1 molar ratio), furthermore SEM/EDX investigation confirms the massive presence of this phase which recrystallize preferentially at the grain boundaries. No "hardening" effect is mentioned in this work which means that the mechanical quality factor probably doesn't undergo major changes. Another zinc-based compound tested as a sintering additive is $K_{1.94}Zn_{1.06}Ta_{5.19}O_{15}$ (KZT).**[20]** The apparent density of the KNN ceramics was increased with KZT addition to a relative density of approximately 96.3% for KZT levels of over 0.5 mol%. Higher KZT addition (> 0.5 mol%) reduces the size of grains probably due to the excess of liquid phase. The optimum piezoelectric and dielectric properties of $\varepsilon^T_{33}/\varepsilon_0$ = 590, d_{33} = 126 pC/N, k_p = 0.42, and P_r = 18 μC/cm^2 were obtained for 0.5 mol% of KZT. The enhancement of the electrical

properties has been attributed to the high density (96.3 % of TD) and to the larger grain size of KNN-0.5KZT composition. The mechanical quality factor undergoes an increase depending on the addition of KZT. Pure KNN shows Q_m ~ 60 which increases up to ~ 100 for KNN-2KZT. The increase of Q_m is attributed to the domain pinning effect at the grain boundary due to the decrease of the grain size with the addition of KZT. In any case, the reported Q_m value of ~ 100 is much lower than copper-based systems (Q_m > 1000) and this reflect the minor "hardening" effect of Zn-based compounds. In **Table 3.4** are summarized some of the main information related to KNN modified with Cu and Zn-based compounds discussed in this section.

Table 3.4. Summary table with some of the most relevant information on pure KNN modified with Cu and Zn compounds.

System	Sintering temperature (°C)	Density (g/cm^3)	d_{33} (pC/N)	k_p (%)	Q_m	Ref.
KNN + 1.5 mol% CuO	950	91 (TD %)	100	0.36	1200	**[15]**
KNN + 0.5 mol % KCN	1095	4.40	-	0.39	1200	**[16]**
KNN + 1 mol% CN	1075	4.47	92.5	0.40	1933	**[17]**
KNN:0.2ZnO	1100	4.21	110	-	-	**[19]**
KNN + 0.5 mol % KZT	1070	96 (TD %)	126	0.42	~ 50	**[20]**

As already mentioned, the use of sintering aids is not an alternative strategy to ABO_3-type agents. Indeed, they have often been used together, with success, in several works in order to improve some deficient aspects of KNN. In principle, sintering aids are added to KNN+ABO_3 compounds to decrease the sintering temperature. In the specific case of copper-based agents, the addition of these additives also determines a significant increase in the hard properties of the ceramic, and this is

particularly interesting since the mechanical quality factors of KNN+ABO_3 systems is very low (**Table 3.3**). Therefore, obtain a material with high piezoelectric response and at the same time good "hard" characteristics, is a compelling goal for many applications. However, the addition of CuO to KNN modified with Sb, Ta, and/or ABO_3-type compounds doesn't cause the same huge increment in the "hard" characteristics of the ceramic as observed in the case of pure KNN. An attempt to explain this behaviour has been proposed by Liao et al.**[57]** The authors examined the composition $K_{0.5}Na_{0.5}Nb_{1-x}Sb_xO_3$ + 1 mol% CuO ($0<x<0.16$). In particular, they found that the EPR signal of the dimeric and trimeric defect combinations DC1 ($Cu''_{Nb} - V_o^{\bullet\bullet}$) and DC2 ($V_o^{\bullet\bullet} - Cu'' - V_o^{\bullet\bullet}$) progressively decreases with the addition of Sb. This means that there is a significant decrease of the content of these two defect combinations which are responsible of the "hard" characteristic of the ceramic. At the same time, the XPS spectroscopy revealed that almost all Cu^{2+} ions have been converted to Cu^{+} ions after the addition of Sb. This implies that the Cu^{+} ions preferentially settle in the A-sites thus preventing the formation of the oxygen vacancy and the defect dipoles. The reason why Cu^{2+} is reduced to Cu^{+} is not mentioned, but it is probably due to some redox reaction in which Sb is involved. This proposed explanation fits well with the experimental evidence and most likely can be considered valid for similar systems. For example, Li et al studied the composition $(1-x)(K_{0.5}Na_{0.5})NbO_3-xBiScO_3$ doped with 1 mol% CuO. The addition of $BiScO_3$ ($0.005<x<0.025$) lowers the mechanical quality factor from 537 (x = 0.005) to 105 (x = 0.025) but increase the piezoelectric response, which is optimized around x = 0.018 (d_{33} = 224 pC/N, kp = 0.402; ε_r = 1217; tanδ = 0.0174; Q_m = 288). Despite the addition of the ABO_3 component, the presence of copper oxide guarantees a relatively high mechanical quality factor (Q_m = 288).**[58]** A similar composition with 2 mol% of $BiScO_3$ and 1 mol% of CuO shows equally promising electrical properties of d_{33} ~ 207 pC/N, k_p ~ 0.421 and Q_m ~ 285.**[59]** Another quite promising ABO_3 modifying agent is $SrTiO_3$ (ST). The binary systems based on KNN and ST present difficulties in the sintering phase due to the lack of

liquid phase formation even at high temperatures (>1000°C) leading to poor sinterability and low piezoelectric properties. In this case the addition of CuO is also justified to help the densification process. For example, Seo et al. have added 1.5 mol% of CuO to $0.95(Na_{0.5}K_{0.5})NbO_3–0.05SrTiO_3$. The addition of CuO helps the densification of KNN-ST by lowering the sintering temperature below 1000°C and also significantly improve Q_m which reaches the optimized value of 288.**[60]** Copper oxide has been tested also on ternary systems such as KNN-LS-BF or KNN-LN-LS. However, in both cases, the addition of CuO does not involve an appreciable improvement in the mechanical quality factor. In particular, Wang et al have tested small amount of CuO (0-0.6 mol%) on KNN-LS-BF composition.**[61]** They found optimum electrical properties of d_{33} = 243 pC/N, k_p = 0.40, ε_r = 1506, tanδ = 2.85 % with 0.15 mol% of CuO, however Q_m is still low (21.87) and remain low even with larger addition of CuO (Q_m = 30). Similarly, the KNNLS-BF composition modified with 0.8 mol% of CuO shows interesting electrical properties of d_{33} = 172 pC/N, k_p = 42%, = ε_r = 417 but the mechanical quality factor results to be still low (158.75). An outstanding result was achieved by Zhao et al. which they have obtained excellent piezo coefficients (d_{33} = 207 pC/N; k_p = 0.44) and, at the same time, good "hard" characteristics (Q_m = 320) in the KNN-based ceramic with nominal composition $0.95(K_{0.5}Na_{0.5}NbO_3)–0.05Li(Nb_{0.5}Sb_{0.5})O_3$ doped with 0.8 mol% of CuO.**[63]** In **Table 3.5** are summarized the main electrical coefficients of KNN modified with ABO_3 compounds and CuO.

Copper oxide it is the additive that most of all has a positive influence both on the sintering process and on the "hard" characteristics of the ceramics. However, many other additives have been tested as well on KNN-based systems whose effects differs from copper-based systems. For example, zinc oxide (ZnO) has been successfully tested on pure KNN system and its effect as a sintering aid has

been widely proved. In the case of pure KNN systems, the zinc oxide appeared to have a weak "hardening" effect; on the contrary, in complex KNN-based systems it has a clear "softening" effect.

Table 3.5. Summary table with some of the most relevant electric and piezoelectric coefficients of KNN + ABO_3 systems modified with CuO.

System	d_{33} (pC/N)	k_p (%)	ε_r	tanδ	Q_m	Ref.
0.982KNN−0.018BS + 1 mol% CuO	224	0.402	1217	0.0174	288	**[58]**
0.98KNN-0.02BS + 1 mol% CuO	207	0.421	1278	0.018	285	**[59]**
0.95KNN–0.05ST + 1.5 mol% CuO	200	0.35	1235		288	**[60]**
0.95KNN-0.05LS-0.02BF+ 0.15 mol% CuO	243	0.40	1506	0.0285	22	**[61]**
0.998KNNLS-0.002BF + 0.8 mol% CuO	172	0.42	417		158	**[62]**
0.95KNN–0.05LNS + 0.8 mol% CuO	207	0.44	340	0.0137	320	**[63]**

For instance, Li et al found a remarkable donor doping effect of ZnO in the ceramic with composition $0.92(K_{0.5}Na_{0.5})NbO_3$-$0.02(Bi_{0.5}Li_{0.5})TiO_3$-$0.06BaZrO_3$ (0.92KNN-0.02BLT-0.06BZ). The authors prove that Zn^{2+} can compensate for the volatilization of A-site elements and suppress the formation of the oxygen vacancies, while the formation of A-site vacancies might account for the enhanced domain wall mobility. This leads to an improvement of the soft characteristics of the ceramic and thus to an enhancement of the piezoelectric coefficients.**[64]** Wang et al investigated the sintering performance of KNN-LS-BF system modified with ZnO. Dense ceramic can be obtained at the relatively low temperature of 1010 °C. The electrical coefficients are optimized at around 1020°C while further increase of the sintering temperature (>1020°C) determines a drastic reduction of the coefficients.**[65]** Li et al. have obtained excellent soft properties (d_{33} = 320 pC/N, k_p = 0.484) in the

composition $0.95(K_{0.5}Na_{0.5})NbO_3–0.05(Bi_{0.5}Na_{0.5})ZrO_3$ (0.95KNN-0.05BNZ) modified with 1 mol % of ZnO.**[66]** Manganese oxide (MnO_2) has been successfully tested as a sintering aid, but the main benefit seems to be related with the reduction of the dielectric losses and the increase of the dielectric behaviour. For example, Cheng et al studied $0.98(K_{0.5}Na_{0.5})NbO_3–0.02LaFeO_3$ composition (KNN-LF) modified with small amount of MnO_2. The addition of 1.5 mol% of MnO_2 improve the density and decrease the sintering temperature of KNN-LF ceramic. At the same time, the dielectric permittivity ε_r is increased approximately up to 2000 and dielectric loss ($\tan\delta$) is reduced below 3%.**[67]** The MnO_2 seems to have a positive effect also on the piezoelectric properties of KNN-based ceramics, which is mainly due to an improvement of the density of the material. For example, Lin et al. studied the composition $(Na_{0.5}K_{0.5})(Nb_{1-y}Sb_y)O_3$ modified with small amount of MnO_2 (0-1.5 mol%). They found that without using the sintering aid, the ceramic with composition $(Na_{0.5}K_{0.5})(Nb_{0.94}Sb_{0.06})O_3$ possess poor density (4.11 g/cm^3) and relatively low piezo coefficient (d_{33} =146 pC/N, $k_p = 0.33$, and $k_t = 0.40$). After the addition of MnO_2 (0.5-1.5 mol%) the density of KNNS significantly increases up to 4.41 g/cm^3 with a consequent improvement of the piezoelectric response (d_{33} ~ 175 pC/N; k_p ~ 0.5, k_t ~ 0.5).**[68]** Similarly, the MnO_2 has a beneficial effect also for the composition $0.94(K_{0.5}Na_{0.5})NbO_3–0.06Ba(Zr_{0.05}Ti_{0.95})O_3$ (0.94KNN-0.06BZT). The electrical insulation and the densification are improved after the addition of 1 mol% of MnO_2 with a considerable improvement also of the dielectric and piezoelectric response (d_{33} = 234 pC/N, k_p = 49%, k_t = 48%, ε_r = 1191, $\tan\delta$ = 1.20%) which are optimized around this composition.**[69]** The vanadium oxide (V_2O_5) helps the sintering process and improve the temperature stability and the electrical properties of KNN-based ceramic. For example, Wang et al. investigated the composition $Na_{0.5}K_{0.5}NbO_3$-$LiSbO_3$-$BiFeO_3$ (KNN-LS-BF) modified with 0.3 mol% of V_2O_5. The addition of V_2O_5 significantly improve the temperature stability in the temperature range of 30°C to 420°C and cause a shift in the orthorhombic–tetragonal phase transition to below room temperature. At the same

time, the V_2O_5 modified ceramic possess good dielectric and piezoelectric properties ($\varepsilon_r > 1066$, $\tan\delta < 4\%$, $d_{33} > 185$ pC/N, $k_p > 0.25$).**[70]** Zhai et al. found that V_2O_5 decrease the sintering temperature of KNN-LS-BF ceramic. The optimized amount of V_2O_5 is included within 0.45 mol%. Further addition of sintering aid determines the formation of secondary phases such as KVO_3 and $NaNbO_3$ which will degrade the piezoelectric properties. The optimized electrical coefficients were found for 0.3 mol% of V_2O_5 and the relating constants are $d_{33} = 183$ pC/N, $k_p = 0.25$, $\varepsilon_r = 638.83$, $\tan\delta = 0.7$ %, $Q_m = 53.87$.**[71]** It can be appreciated that the mechanical quality factor of the ceramic still remain low, and this could be related to the oxidation state of V^{5+} which is isovalent with Nb^{5+}, therefore this substitution does not promote the formation of the oxygen vacancy. The magnesium oxide has been little explored on both KNN and KNN-based systems. The work by Meng and co-authors is one of the few reports where this element is used to modify the KNN.**[72]** The authors studied the composition $0.96(K_{0.5}Na_{0.5})NbO_3–0.04LiTaO_3$ (0.96KNN-0.04LT) modified with small amount of MgO (0-1 mol%). They found that the addition of MgO improve the sintering performance and the dielectric properties of KNN-LT system. The optimized coefficients of $d_{33} = 128$ pC/N, $k_p = 33.4\%$, $\varepsilon_r = 611$, $\tan\delta = 2.84\%$ were found for 0.96KNN-0.04LT + 0.25 mol% of MgO sintered at the relatively low temperature of 1060°C. The lithium fluoride (LiF) is the only additive on this list that is not an oxide. It is commonly used as a sintering aid in other perovskite materials such as $KTa_{1-x}Nb_xO_3$ (KTN), $BaTiO_3$ (BT), and PMNT and recently it has also been tested on KNN-based ceramics.**[73,74]** For instance, Shi et al. tested LiF on $0.996(0.95K_{0.5}Na_{0.5}NbO_3\text{-}0.05LiSbO_3)\text{-}0.004BiFeO_3$ composition. They found that LiF causes structural changes from a coexistence of tetragonal with orthorhombic phases into a single orthorhombic phase with the increase of LiF. This also determines a greater thermal stability as the orthorhombic-tetragonal phase transition is shifted at higher temperature (from 30°C to 110°C) causing a decay of the electrical properties, which is also partially due to a worsening of the density of the material.**[73]** Taking into account that the samples

were sintered at relatively high temperatures (1060-1100°C) and considering that an ideal sintering aid should effectively lower the sintering temperature while maintaining the piezoelectric properties as much as possible, LiF addition seems to be only detrimental to KNN systems. However, Zhou et al. obtained interesting results in the composition $0.95Li_{0.02}(Na_{0.53}K_{0.48})_{0.98}Nb_{0.8}Ta_{0.2}O_3{-}0.05AgSbO_3$ modified with small addition of LiF (0-0.06 mol%). They managed to obtain a dense ceramic (about 90% of TD) at the extremely low sintering temperature of 900°C with the small addition of LiF (0.06 mol%). This result has been attributed to the low melting point of LiF (845°C) which forms a liquid phase that penetrates the local particles and significantly speeds up the grain growth as well as the densification process. The sample sintered at 900°C shows a relatively high converse piezoelectric coefficient (d_{33}*) of 375 pm/V.**[74]** In **Table 3.6** are summarized some of the most important electric coefficients of KNN+ABO_3 system modified with other less common sintering aids. Summarizing, copper oxide is the sintering aid that has been mostly tested both on pure KNN and KNN-based materials. This is due to its great potential as a densifying agent but also as a doping to increase the "hard" behaviour of KNN ceramics. Instead, zinc oxide has a "softening" effect on KNN-based ceramics due to the replacement of Zn^{2+} on the A-site of the perovskite structure. The manganese oxide is a good sintering aid; in addition, promotes the dielectric characteristics of the ceramic and reduces the dielectric losses. Other additives such as V_2O_5, MgO and LiF seem to be promising. However, to fully understand their potential, further studies are needed in this regard.

Table 3.6. Summary table with some of the most relevant electric and piezoelectric coefficients of KNN + ABO_3 systems modified with some sintering aids.

System	d_{33} (pC/N)	k_p (%)	ε_r	tanδ	Q_m	Ref.
0.92KNN-0.02BLT-0.06BZ + 0.3 wt.% ZnO	350	50	2176	0.024	68	**[64]**
0.95KNN-0.05LS-0.004BF + 2 mol% ZnO	278	45	1236	0.027	37	**[65]**
0.95KNN-0.05BNZ + 1 mol% ZnO	320	48	1763	0.029		**[66]**
0.98KNN–0.02LF + 1.5 mol% MnO_2			1749	0.023		**[67]**
KNNSx + z MnO_2 (x = 0.06-0.08) (z = 0.5-1)	204	51	1053	0.030		**[68]**
0.94KNN-0.06BZT + 1 mol% MnO_2	234	49	1191	0.012		**[69]**
KNN-LS-BF + 0.3 mol% V_2O_5	185	25	1066	0.040		**[70]**
KNN-LS-BF + 0.3 mol% V_2O_5	183	25	638	0.007	54	**[71]**
0.96KNN-0.04LT + 0.25 mol% MgO	135	36	600	0.037		**[72]**
KNN-LS-BF + 1.5 mol% LF	173	35	1157	0.033	64	**[73]**
LKNNTAS-0.06LiF	375 (pm/V)	29	1000			**[74]**

3.5 KNN-based ceramics prepared by Spark Plasma Sintering (SPS)

The Spark Plasma Sintering (SPS) is a highly efficient sintering technique that involves the contemporaneous use of uniaxial pressure and high intensity pulsed current. The SPS is considered as a modification of the Hot-Pressing (HP) technique, and it differs from the latter in the way the

sample is heated. In HP the sample is heated inside the furnace, while in SPS the heating take place by an electric current flowing directly thought the mold that contain the powders. This technique presents several advantages including shorter times and lower temperatures compared to conventional sintering methods. Moreover, allows to densify materials hard to sinter such as refractory materials, metastable phases or nanomaterials.**[75]** As known, one of the problems related to KNN systems is the difficult to obtain high dense ceramics due to the high volatility of the sodium and potassium ions at the common sintering temperature. In this context, the SPS offers a great advantage because it allows to obtain a highly dense product (~ 99% of TD) in a very short time and using low sintering temperatures (900-970°C).**[12,76]**

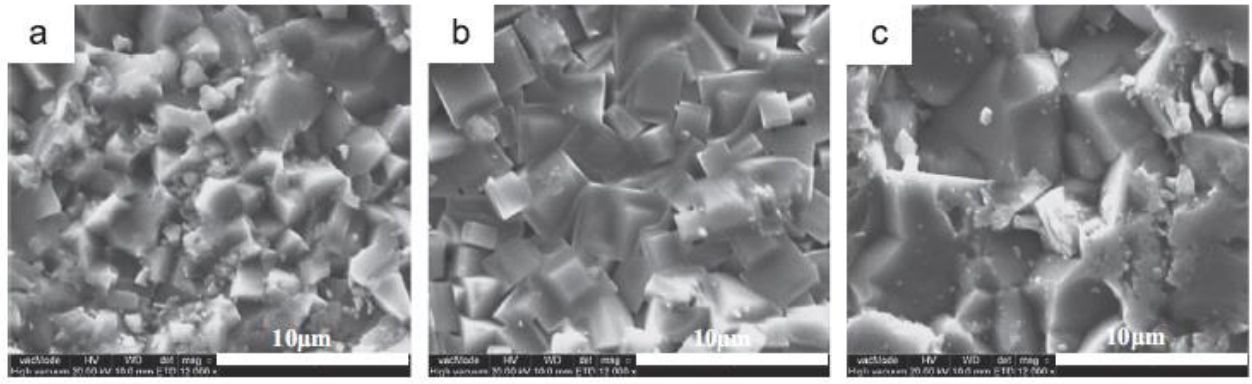

Figure 3.11. Microstructures of KNN prepared via SPS sintered at (a) 925, (b) 950 and (c) 975°C.**[12]**

The sintered product is characterized by an extremely dense microstructure (**Figure 3.11**), very close to the theoretical density of the material. Due to the very fast sintering and low temperatures, the grain sizes are small (**Figure 3.11)**. For this reason, an annealing treatment is then carried out in air in order to increase the size of the grains and decrease the oxygen vacancies, which are inevitably formed due to the anaerobic conditions of the SPS process.

The electrical properties of KNN-SPS are often better compared to those prepared by common sintering (d_{33} = 80 pC/N; k_p = 0.36-0.4; Q_m = 130).**[32]** For example, Bah et al. have obtained an

excellent planar coupling factor (k_p) of 48% for the undoped KNN sintered at 920°C.**[12]** This result has been attributed to the optimized grain size (~ 2 μm) and density (96% of TD). A relatively high d_{33} coefficient of 148 pC/N was obtained by Li et al. The high piezo response is due to the high density (~ 99% of TD), however the planar coupling factor is lower compared to the work of Bah et al. and this could be attributed to the very small grain size of 200-500 nm.**[76]** KNN modified with Ta, Li/Ta, Li/Ta/$CaZrO_3$ and $BaTiO_3$ have also been tested with this technique and they exhibit interesting properties.**[77-79]** For instance, Jean et al. studied the $K_{0.5}Na_{0.5}Nb_{1-x}Ta_xO_3$ composition (KNNT). They found significant improvement of the relative density over 96% for all the compositions sintered between 920 and 960 °C, under 50 MPa, for 5–10 min with heating rates of 100 °C/min. Optimized dielectric and piezoelectric coefficients (ε_r = 1027; d_{33} = 160 pC/N; k_p = 46%) are obtained in spark plasma sintered $K_{0.5}Na_{0.5}Nb_{1-x}Ta_xO_3$ ceramics, for x ranging between 0.10 and 0.30.**[77]** The addition of another element (i.e, Li) further improve the electrical properties of KNNT modified systems. For example, Zhen et al. investigated the composition with nominal formula $(Li_{0.04}K_{0.44}Na_{0.52})(Nb_{0.85}Ta_{0.15})O_3$ (LKNNT). Their work, in particular, highlights the importance of the post annealing treatment. When post-annealing temperature was fixed at 900 °C, all LKNNT samples show high dielectric permittivity >800, but relatively low d_{33} values of 135–162 pC/N. Through the optimization of the post annealing temperature, the piezoelectric coefficient was enhanced from 156 to 225 pC/N. This is mainly due to an increase of the size of grains as well as the orthorhombic-tetragonal phase boundaries.**[78]** Despite the good properties listed above, KNN fabrication via SPS is very challenging and requires particular attention in the process. As reported by Malic et al., the as-sintered samples were dark coloured and electrically conductive as a result of partial reduction of Nb^{5+} to Nb^{4+} and formation of oxygen vacancies.**[79]** Furthermore, the grain sizes are extremely small due to the rapid sintering conditions. The air annealing following the sintering is important specially to reduce the oxygen vacancy and to re-oxidize Nb^{4+} to Nb^{5+}, but also to increase

the average grain size and thus to facilitate the poling process. If the annealing temperature is not optimized, and therefore the grain size does not increase appreciably, the piezo properties are modest and, in some cases, even lower than that obtained by normal sintering.**[79]** Complex compositions are avoided with this technique because it often involves several compositional segregations that do not allow an improvement of the piezoelectric response, to the point that the electrical properties are lower than the pure KNN system. An example is provided by the work by Zhou et al., who have studied the complex composition with nominal formula $0.95(Na_{0.49}K_{0.49}Li_{0.02})(Nb_{0.8}Ta_{0.2})O_3–0.05CaZrO_3$. The small piezoelectric signal is only 124 pm/V; in addition, the phase angle is – 1.8°, that is very far from the ideal value of 90°. This means that the domain wall motion is probably inhibited.**[80]** An interesting alternative to SPS sintering have been recently proposed by Vilarinho et al., which is the Spark Plasma Texturing (SPT).**[81]**

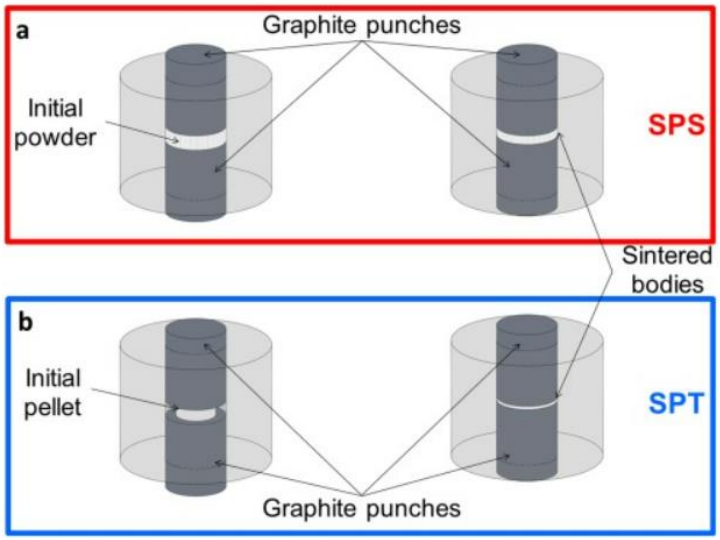

Figure 3.12. Schematic representation of (a) SPS and (b) SPT.

In SPT a uniaxial pressure is applied in an edge-free configuration, allowing ceramics to deform in the radial direction, as schematically shown in **Figure 3.12**. The SPT sample showed an improvement in terms of density (99 % of TD) and electrical properties (d_{33} = 108 pC/N) compared to the sample sintered by conventional SPS (96 % of TD; d_{33} = 95 pC/N). The resultant compressively stressed

lattice enhances the dielectric and piezoelectric performance while the higher density and lower grain size obtained have been attributed to phenomena related to neck destruction, particle rearrangement, and destruction of agglomerates, typical of the SPT process. In **Table 3.7** are summarized some fabrication parameter and electrical properties of the KNN-based materials prepared by Spark Plasma Sintering discussed in this section.

Table 3.7. Summary table with some of the most relevant fabrication parameter, electric and piezoelectric coefficients of KNN-based systems prepared with Spark Plasma Sintering method.

System	SPS temperature (°C)	Annealing temperature (°C)	d_{33} (pC/N)	k_p (%)	ε_r	Ref.
KNN	920	900		48	288	**[12]**
KNN	920	900	148	39	584	**[76]**
KNNT	920-960	900	155	46	1027	**[77]**
LKNNT	970	900-1100	225	44	960	**[78]**
KNNS	1300	950	88			**[79]**
LKNNT-CZ	1050	850	124 (pm/V)			**[80]**
KNN (SPT)	1000	900	108		576	**[81]**

3.6 Conclusions

This chapter has revised some recent works on KNN-based systems prepared by solid state route and Spark Plasma sintering. The formation of the Polymorphic Phase Transition (PPT) through the addition of ABO_3 modifying agent allows to significantly increase the electrical properties of KNN ceramics. In this context, KNN-BF based systems such as KNNS-BF-BNZ show very large piezoelectric coefficient (d_{33} ~ 550 pC/N) which are comparable to some of the most performing

"soft" PZT systems. However, the extremely complex chemical composition as well as the low reproducibility due to the volatility of the alkaline ions, makes these systems unattractive for large-scale production. Moreover, the low mechanical quality factor ($Q_m < 100$) does not allow the use of these materials for "high power" applications. For this reason, some promising binary systems such as KNN-BS or KNN-LNS are modified with CuO in order to decrease the sintering temperature and to increase the mechanical quality factor. CuO is a well-known sintering aids which improve the densification of KNN, but it is also an excellent "hard" dopant. The mechanical quality factor of pure KNN is extremely enhanced by the addition of CuO ($Q_m > 1000$), however the same noticeable behaviour is not observed in binary or ternary KNN systems. This is probably due to a partial reduction of Cu^{2+} into Cu^{+} which preferentially settles in the A-site of the perovskite structures, thus preventing the formation of the oxygen vacancy. The Spark Plasma Sintering is a very efficient technique which allows to carry out fast sintering (5-10 minute) using low temperatures (900-1000 °C). KNN-SPS ceramics exhibit high densities (~ 99% of TD). KNN modified systems with one or two doping elements exhibit increased piezoelectric properties, but more complex systems are difficult to prepare as it often involves several compositional segregations which causes a deterioration of the electrical properties. The air annealing treatment is usually necessary to reduce oxygen vacancies, increase the electrical resistance and increase the grain size of the ceramics. The Spark Plasma Texturing (SPT) is an interesting variant which allows to obtain even higher densities and improved electrical properties compared to classic SPS sintering.

3.7 Bibliography

[1] S. Garroni, N. Senes, A. Iacomini, S. Enzo, G. Mulas, L. Pardo, and S. Cuesta-Lopez. *Phys. Status Solidi A.* **2018**, 215, 1700896.

[2] B. Malic, J. Koruza, J. Hrescak, J. Bernard, K. Wang, J. G. Fisher, and A. Bencan. *Materials.* **2015**, 8, 8117-8146.

[3] J. Acker, H. Kungl, and M. Hoffmann. *J. Am. Ceram. Soc.* **2010**, 93(5), 1270-1281.

[4] S. Gupta, D. Maurya, Y. Yan, S. Priya, Development of KNN-Based Piezoelectric Materials, *Springer New York,* **2012**, 89-119.

[5] H. Du, Z. Li, F. Tang, S. Qu, Z. Pei, and W. Zhou. *Mater. Sci. Eng. B.* **2006**, 131, 83-87.

[6] F. Hussain, I. Sterianou, A. Khesro, D. C. Sinclair, and I. M. Reaney. *J. Eur. Ceram. Soc*. **2018**, 38, 3118-3126.

[7] J. Ji, X. Li, B. Fang, X. Zhao, S. Zhang, J. Ding, and H. Luo. *Ferroelectrics.* **2018**, 526, 33-45.

[8] J. Zhang, Y. Qin, Y. Gao, W. Yao, and M. Zhao. *J. Am. Ceram. Soc*. **2014**, 97, 759-764.

[9] R. Jaeger and L. Egerton. *J. Am. Ceram. Soc*. **1962**, 45, 209-213.

[10] L. Egerton and C. Bieling. *Ceram. Bull*. **1968**, 47, 1151-1156.

[11] L. Jing-Feng, K. Wang, B. Zhang, and L. Zhang. *J. Am. Ceram. Soc*. **2006**, 89, 706-709.

[12] M. Bah, F. Giovannelli, F. Schoenstein, G. Feuillard, E. L. Clezio, and I. Monot-Laffez. *Ceram. Int*. **2014**, 40, 7473-7480.

[13] F. Rubio-Marcos, J. J. Romero, and J. F. Fernandez. *J. Nanopart. Res*. **2010**, 12, 2495-2502.

[14] F. Rubio-Marcos, J. Romero, M. Martin-Gonzalez, and J. Fernandez. *J. Eur. Ceram. Soc*. **2010**, 30, 2763-2771.

[15] C. Ahn, M. Karmarkar, D. Viehland, D. H. Kang, K. S. Bae, and S. Priya. *Ferroelectr. Lett. Sec*. **2008**, 35, 66-72.

[16] M. Matsubara, T. Yamaguchi, K. Kikuta, and S. Hirano. *Jpn. J. Appl. Phys*. **2004**, 43, 7159-7163.

[17] M. R. Yang, C. C.Tsai, C. S. Hong, S. Y. Chu, and S. L. Yang. J. Appl. Phys. **2010**, 108, 094103.

[18] R. Wang, S. Shibusawa, N. Miura, H. Bando, and M. Itoh. *Ferroelectrics* **2009**, 385, 6141-6148.

[19] Z. Pan, J. Chen, L. Fan, J. Zhang, S. Zhang, Y. Huang, L. Liu, L. Fang, and X. Xing. *J. Am. Ceram. Soc.* **2015**, 98, 3935-3941.

[20] J. Ryu, J. Choi, B. Hahn, D. Park, W. Yoon, and K. Kim. *IEEE Trans. Ultrason. Ferroelectr. Freq. Control* **2017**, 54, 2510-2515.

[21] J. Wu, D. Xiao, and J. Zhu. *Chem. Rev.* **2015**, 115, 2559-2595.

[22] D. Alikin, A. Turygin, A. Kholkin, and V. Shur, *Materials* **2017**, 10 (2017).

[23] R. Zuo, C. Ye, and X. Fang. *J. Phys. Chem. Solids*. **2008**, 69, 230-235.

[24] P. Xu, M. H. Jiang, and X. Y. Liu, in Advanced Materials and Structures, volume 335 of *Advanced Materials Research*, p. 968-975, Trans Tech Publications Ltd, **2011.**

[25] X. Li, L. Wu, D. Xiao, J. Zhu, P. Yu, Y. Jiang, and J. Wu. *Phys. Stat. Sol. A* **2008**, 205, 1211-1214.

[26] X. Sun, J. Chen, R. Yu, X. Xing, L. Qiao, and G. Liu, *Sci. Technol. Adv. Mater*. **2008**, 9, 025004.

[27] C. Zhang, Z. Chen, W. j. Ji, L. Wang, Y. B. Chen, S. Yao, S. T. Zhang, and Y. F. Chen. *J. Alloys Compd.* **2011**, 509, 2425-2429.

[28] A. Khesro, D. Wang, F. Hussain, R. Muhammad, G. Wang, A. Feteira, and I. M. Reaney. *Front. Mater.* **2020**, 7, 140.

[29] X. Kuang, G. Carotenuto, and L. Nicolais. *Adv. Perform. Mater*. **1997**, 4, 257-274.

[30] R. M. German, P. Suri, and S. J. Park. *J. Mater. Sci*. **2009**, 44, 1-39.

[31] K. Wang and J. F. Li. *J. Adv. Ceram.* **2012**, 1, 24-37.

[32] L. Egerton and D. M. Dillon. *J. Am. Ceram. Soc*. **1959**, 42, 438-442.

[33] T. R. Shrout and S. J. Zhang. *J. Electroceram.* **2017**, 19, 113-126.

[34] H. Birol, D. Damjanovic, and N. Setter. *J. Eur. Ceram. Soc*. **2006**, 26, 861-866.

[35] J. Tellier, B. Malic, B. Dkhil, D. Jenko, J. Cilensek, and M. Kosec. *Solid State Sci* **2009**, 11, 320-324.

[36] D. W. Baker, P. A. Thomas, N. Zhang, and A. M. Glazer. *Appl. Phys. Lett*. **2009**, 95, 091903.

[37] Y.-J. Dai, X.-W. Zhang, and K.-P. Chen. *Appl. Phys. Lett*. **2009**, 94, 042905.

[38] P. Kumar, M. Pattanaik, and Sonia. *Ceram. Int.* **2013**, 39, 65-69.

[39] J.-F. Li, K. Wang, F.-Y. Zhu, L.-Q. Cheng, and F.-Z. Yao. *J. Am. Ceram. Soc.* **2013**, 96, 3677-3696.

[40] D. I. Woodward, J. Knudsen, and I. M. Reaney. *Phys. Rev. B* **2005**, 72, 104110.

[41] U. Nuraini, N. A. Triyuliana, M. Mashuri, and S. Suasmoro, *IOP Conf. Ser. Mater. Sci. Eng.* **2019**, 496, 012043.

[42] B. Noheda, J. A. Gonzalo, L. E. Cross, R. Guo, S.-E. Park, D. E. Cox, and G. Shirane. *Phys. Rev. B* **2000**, 61, 8687-8695.

[43] Y. Uesu, M. Matsuda, Y. Yamada, K. Fujishiro, D. E. Cox, B. Noheda, and G. Shirane. *J. Phys. Soc. Jpn.* **2002**, 71, 960-965.

[44] B. Noheda, D. E. Cox, G. Shirane, R. Guo, B. Jones, and L. E. Cross. *Phys. Rev. B* **2000**, 63, 014103.

[45] A. K. Singh and D. Pandey. *Phys. Rev. B* **2003**, 67, 064102.

[46] M. Jiang, X. Liu, and G. Chen. *Scr. Mater*. **2009**, 60, 909-912.

[47] M. H. Jiang, X. Y. Liu, G. H. Chen, J. F. Ma, G. S. Zhu, and J. W. Xu. in Materials Science and Nanotechnology, I, volume 531 of *Key Engineering Materials*, p. 632-635, Trans Tech Publications Ltd, **2013**.

[48] H.-W. Zhu, X.-J. Wang, D.-Y. Zheng, Z.-H. Peng, L. Yang, and C. Fang. *J. Mater. Sci. Mater. El*. **2018**, 29.

[49] X. Zhao, H. Wang, C. Yuan, J. Xu, Y. Cui, and J. Ma. *J. Mater. Sci. Mater. El*. **2017**, 24, 1480-1484.

[50] J.-J. Zhou, J.-F. Li, L.-Q. Cheng, K. Wang, X.-W. Zhang, Q.-M. Wang. *J Eur Ceram Soc* **2012**, 32, 3575–3582.

[51] X. Chao, J. Wang, C. Kang, Zhao Li, Z. Yang. *Ceram. Int.* **2015**, 41, 12887–12895.

[52] M. Jiang, X. Liu, C. Liu. *Mater. Res. Bull* **2010**, 45, 220–223.

[53] X. Chao, Z. Yang, Z. Li, Y. Li. *J Alloys. Compd* **2012**, 518, 1– 5.

[54] B. Wu, J. Wu, D. Xiao, J. Zhu. *Dalton Trans.* **2015**, 44, 21141-21152.

[55] J. Ma, Bo Wu, W. Wu, M. Chen. *J Mater Sci: Mater Electron*. **2017**, 28, 4458–4466.

[56] W. Yao, J. Zhang, C. Zhou, D. Liu, W. Su. *J Eur Ceram Soc* **2020**, 40(4) 1223-1231.

[57] Y. Liao, D. Wang, H. Wang, T. Wang, Q. Zheng, J. Yang, K.W. Kwok, D. Lin. *Ceram. Int.* **2019**, 45, 13179–13186.

[58] X. Li, M. Jiang, J. Liu, J. Zhu, X. Zhu, L. Li, Y. Zhou, J. Zhu, D. Xiao. *Phys. Status Solidi A.* **2009**, 206(11), 2622–2626.

[59] J. Liu, J. Zhu, X. Li, M. Wang, X. Zhu, J. Zhu, D. Xiao. *Mater Lett* **2011**, 65, 948–950.

[60] I.-T. Seo, K.-H. Cho, H.-Y. Park, S.-J. Park, M.-K. Choi, S. Nahm, H.-G. Lee, H.-W. Kang, H.-J. Lee. *J. Am. Ceram. Soc*. **2008**, 91(12), 3955–3960.

[61] H. Wang, X. Zhai, J. Xu, X. Zhao, L. Yang. *J Mater Sci: Mater Electron* **2016**, 27, 5016–5019.

[62] Y. Zhao, Y. Zhao, R. Huang, R. Liu, H. Zhou. *Mater Sci Forum.* **2011**, 687, 228-232.

[63] Y. Zhao, Y. Zhao, R. Huang, R. Liu, H. Zhou. *J. Am. Ceram. Soc.* **2011**, 94(3), 656–659.

[64] J.-W. Li, Y.-X. Liu, H.-C. Thong, Z. Du, Z. Li, Z.-X. Zhu, J.-K. Nie, J.-F. Geng, W. Gong, K. Wang. *J. Alloys Compd*. **2020**, 847, 155936.

[65] H. Wang, Xiayan Zhao, J. Xu, X. Zhai, L. Yang. *J Mater Sci: Mater Electron.* **2016**, 27, 2036–2041.

[66] F. Li, D. Xiao, J. Wu, Z. Wang, Chao Liu, J. Zhu. *Ceram. Int.* **2014**, 40, 14601–14605.

[67] H. Cheng, W. Zhou, H. Dua, F. Luo, D. Zhu, B. Xu. *Ceram Int* **2014**, 40, 5019–5023.

[68] D. Lin, K. W. Kwok, H. Tian, H. W. L. Chan. *J. Am. Ceram. Soc*. **2007**, 90(5), 1458–1462 .

[69] D. Lin, K.W. Kwok, H.L.W. Chan. *Mater Chem. Phys.* **2008**, 109, 455–458.

[70] H. Wang, X. Zhai, J-W. Xu, C.-L. Yuan, L. Yang. *J. Electr. Mater.*, **2013**, 42(8), 2556-2559.

[71] X. Zhai, H. Wang, J. Xu, C. Yuan, X. Zhang, C. Zhou, X. Liu. *J Mater Sci: Mater Electron,* **2013**, (24) 687–691.

[72] H. Meng, Y. Yang, Y. Wang, D. Wan, Q. Li, Y. Cheng. *Ferroelectrics*, **2010**, 404, 105–111.

[73] D. Shi, L. Liu, Y. Huang, L. Fang, C. Hu. *Ferroelectrics*, **2014**, 467(1), 99-109.

[74] J.-J. Zhou, L.-Q. Cheng, K. Wang, X.-W. Zhang ,J.-F. Li, H. Liu, J.-Z. Fang. *J. Eur Ceram Soc.* **2014**, 34, 1161–1167.

[75] U.A Tamburini. Encyclopedia of Materials: Technical Ceramics and Glasses, *Elsevier*, **2021**, 294-310.

[76] J.-F. Li, K. Wang, B.-P. Zhang and L.-M. Zhang. *J. Am. Ceram. Soc*. **2006**, 89(2), 706–709.

[77] F. Jean, F. Schoenstein, M. Zaghrioui, M. Bah, P. Marchet, J. Bustillo, F. Giovannelli, I. Monot-Laffez. *Ceram Int.* **2018**, 44, 9463–9471.

[78] Y. Zhen, J.-F. Li, K. Wang, Y. Yan, L. Yu. *Mater. Sci. Eng. B*. **2011**, 176, 1110– 1114.

[79] D. Kuscer, A. Kocjan, M. Majcen, A. Meden, K. Radan, J. Kovač, B. Malič, *Ceram. Int.* **2019**, 45, 10429–10437.

[80] J.-S. Zhou, F.-Z. Yao, K. Wang, Q. Li, X.-M. Qi, F.-Y. Zhu, J.-F. Li. *J Mater Sci: Mater Electron.* **2015**, 26, 9329–9335.

[81] R. Pinho, A. Tkach, S. Zlotnik, M. E. Costa, J. Noudem, I. M.Reaney, Paula M.Vilarinho. *Appl. Mater Today*. **2020**, 19, 100566.

4 Experimental procedure

In this chapter, the methods and the experimental procedure used through this thesis are discussed. Each paragraph describes both the method and the instruments used for the synthesis and characterisation of each composition explored and discussed along the **Chapters 5, 6** and **7**. Some recurring methodologies, such as the piezoelectric characterisation, are described in detail only once.

4.1 Processing, electrical properties and cytotoxic effect of potassium sodium niobate (KNN) modified with magnesium niobium oxide (MN)

4.1.1 Synthesis and sintering of KNN-xMN ceramics

KNN powders were prepared through solid-state reaction, starting from a mixture of K_2CO_3 (Sigma Aldrich, ≥ 99.995 %), Na_2CO_3 (Sigma Aldrich, ≥ 99.5 %) and Nb_2O_5 (Alfa Aesar, 99.9985 %), in a molar ratio 1:1:2, respectively. Manipulations of the starting reagents have been conducted in an Ar Glove box machine (MBraun) (**Figure 4.1**) with level of oxygen and moisture below 2 ppm in order to prevent hydration, contamination and side reactions.

Figure 4.1. Glove Box used to handle reagents.

8 grams of powders were transferred into a stainless-steel vial together with 1 ball (stainless steel) of 10 g. The powders were mechanically treated up to 24 hours at 875 rpm by using a Spex 8000M Mixer/Mill (**Figure 4.2**) and then transferred into an alumina crucible. The calcination step was conducted from room temperature to 825 °C for 4 hours using a heating rate of 3 °C/min and then cooled up to 25°C with a cooling rate of 10 °C/min. $MgNb_2O_6$ powders were synthesized through solid-state reaction exploiting a similar procedure reported in the current literature.**[1]**

MgO (Sigma Aldrich, ≥99 %) and Nb_2O_5 (Alfa Aesar, 99.9985 %) weighted in a stoichiometric molar ratio 1:1, were mixed by high energy ball-milling (Spex 8000M Mixer/Mill), for 24 hours at 875 rpm, and then thermally treated up to 1000°C (dwell time: 1 hour) by using a heating rate of 5°C/min (the cooling step was realized with a rate of 10°C/min).

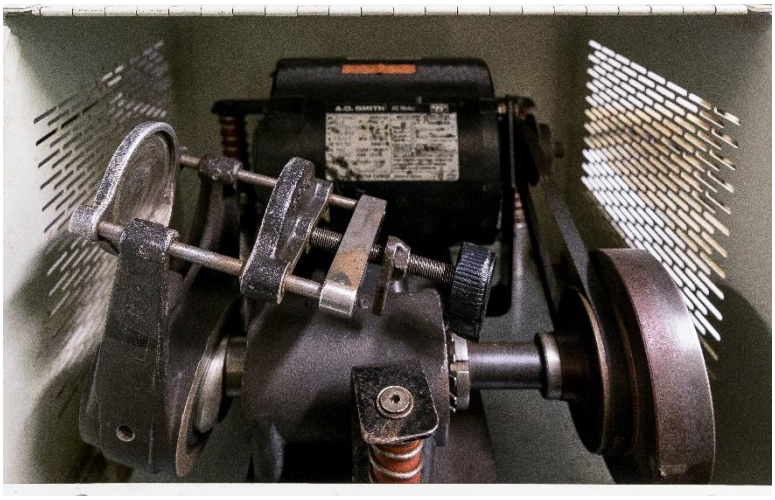

Figure 4.2. SPEX 8000M Mixer/Mill used for sample preparation

The modification process of KNN powders, was made by mixing appropriate amount of KNN and MN: four samples were prepared with increasing weight percentage of MN (0, 0.5, 1, 2 and 4 wt.%, respectively). KNN and MN were milled, with 5 ml of ethanol (Sigma Aldrich, purity >95 %), for 24 hours at 875 rpm. The as-obtained slurry was then transferred in a beaker and heated in an oven at 150°C for 4 hours to eliminate the solvent. The powders were finely ground in a mortar to obtain a

fine particulate and mixed with few drops of polyvinyl alcohol (PVA) solution (3 wt.%) before compacting into a disk by means of a hydraulic press (220 kg/cm^2 for 30 minutes). The pellets were thermally treated for 10 hours at 550°C to eliminate all traces of PVA. Sintering was conducted at 1100°C for 3 hours using a heating rate of 5 °C/min and cooling rate of 10 °C/min. Finally, bulk densities were measured by geometric method using the common formula $\boldsymbol{\rho = m / V}$; where m is the mass of the pellet and V is the volume of the cylinder calculated as $\boldsymbol{V = \pi * r^2 * t}$; where **r** is the radius and **t** is the thickness of the pellet.

4.1.2 Structural, Microstructural and Morphological Characterization

Structural investigations were conducted using a SMARTLAB diffractometer (**Figure 4.3**) with a rotating anode source of copper (λ=1.54178 Å) working at 40 kV and 100 mA. The spectrometer is equipped with a graphite monochromator and a scintillation tube in the diffracted beam. The patterns were collected in the angular range from 18° to 110° with a step size of 0.05° and a fixed counting time of 4 seconds per point.

Figure 4.3. Rigaku SmartLab diffractometer.

Quantitative analysis of the crystalline phases and structure determinations were performed with the MAUD software (Materials Analysis Using Diffraction), a Rietveld extended program.**[2]** Lattice parameters of the constituent phases were refined from the line peak positions after allowing a correction for the zero-offset, while crystallite size and lattice disorder contributions to the peak broadening were separated because of the wide angular range explored. Microstructure and morphology of the samples have been characterized by Quanta FEI 200 Scanning Electron Microscope (**Figure 4.4**). Grain size distributions of the sintered pellets, evaluated on 100 grains, were estimated using the ImageJ software. Thermogravimetric were performed with Labsys TGA/DTA and DSC instrument from room temperature to 1000 °C using a heating rate of 5 °C/min and cooling rate of 30 °C/min under argon atmosphere.

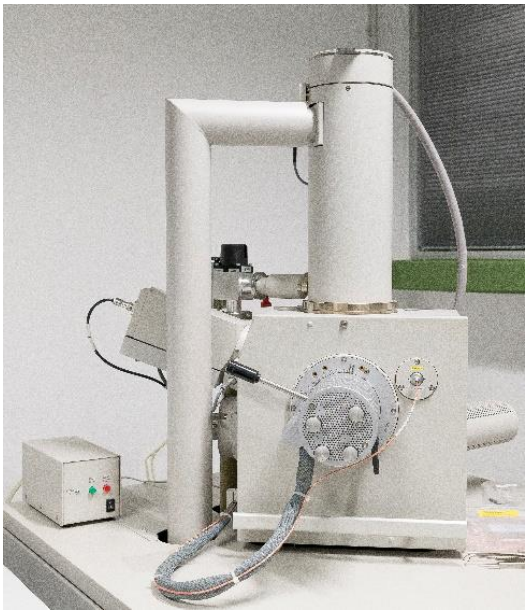

Figure 4.4. Quanta FEI 200

4.1.3 Piezoelectric, Dielectric and Elastic Characterization at Resonance

To measure electric properties, pellets were reduced in thickness by polishing to the proper thickness/diameter aspect ratio. Silver paste was attached on both surfaces of the thin disks and

welded at 400 °C for 30 minutes. After that, samples were increasingly poled in thickness under 10-35 kV/cm at 130°C for 15 minutes in a silicone oil bath, followed by field cooling (FC). Permittivity vs. temperature curves at frequencies above 1 kHz were measured using an automatic temperature control and capacitance-loss tangent data acquisition from an impedance analyzer (HP 4194 A) (**Figure 4.5**). The quasi-static d_{33} piezoelectric charge coefficient, which characterizes the sensor performance of the ceramic in the poling field direction, was measured with a Berlincourt d_{33}-meter at 100 Hz. Complex impedance as a function of the frequency was measured with an impedance analyzer (HP 4192 A-LF) at the radial extensional resonance of the thickness poled thin disks (**Figure 4.6**). The related piezoelectric, dielectric and elastic material coefficients, including all the losses, were determined using the software for automatic iterative analysis of the complex impedance vs. frequency curves.

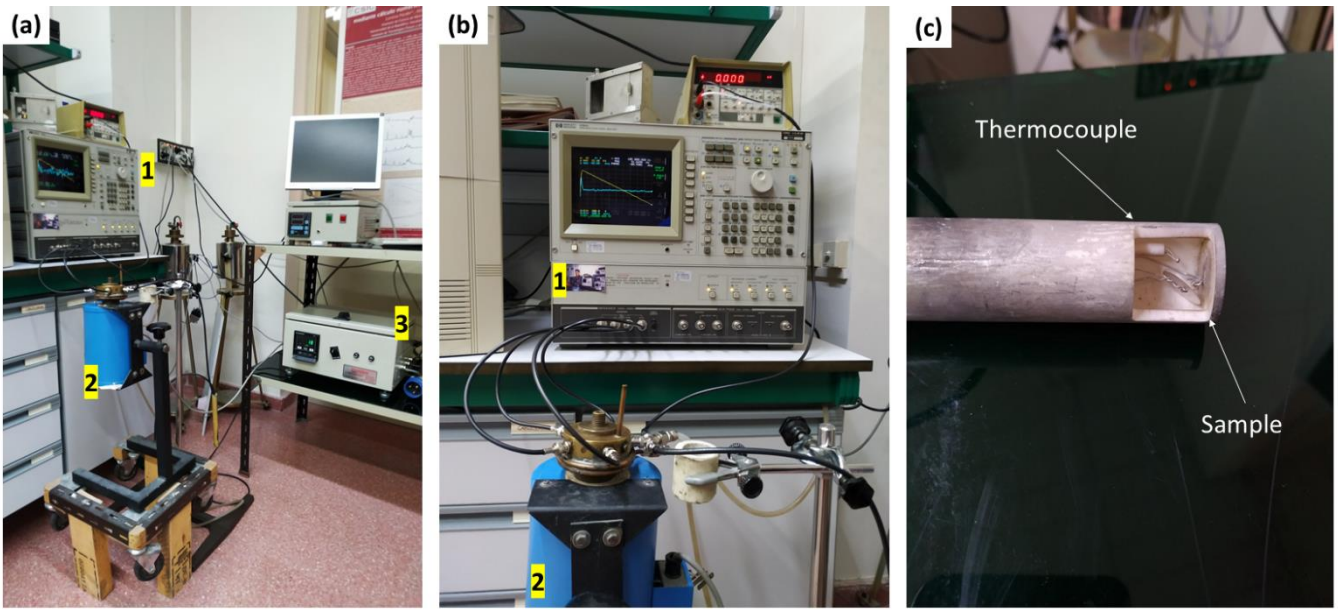

Figure 4.5. (a) Complete setup for dielectric permittivity measurements Vs temperature: 1) HP 4194 A impedance analyser (100 Hz - 40MHz), 2) furnace and 3) temperature controller. **(b)** Front detail of the impedance analyser (1) and the furnace with the connection cables (2). **(c)** Detail of the sample holder. It can be seen the sample (thin disk) between the electric contact and the thermocouple.

The numerical method used was developed by Alemany et al.**[3,4]** A set of non-linear equations, which result when experimental data of complex impedance (Z*) or admittance (Y*=1/Z*) at specific frequencies are introduced into the appropriate analytical solution of the wave equation, is solved iteratively until a convergence criterion is fulfilled. This set of equations is established for as many frequencies, which are automatically selected by the program, as unknown material coefficients. For the automatic determination of these frequencies, the program uses an alternative representation to the classical plots for Z* or Y* of modulus and phase as a function of the frequency.

Figure 4.6. HP4192A LF Impedance analyser (5Hz-13MHz) for measurements and calculations in planar and thickness mode.

Instead, the peaks of resistance (R) and conductance (G) values are plotted vs. frequency, being Z*=R+iX and Y*=G+iB. The two main frequencies, f_s and f_p, used to establish the set of four equations to solve, are determined as those corresponding to the maximum values in the R and G peaks, respectively. For each iteration, the other two values of frequency are also determined automatically. The reconstruction of the R and G peaks is carried out once the material coefficients are calculated. An example is provided in **Figure 4.7**.

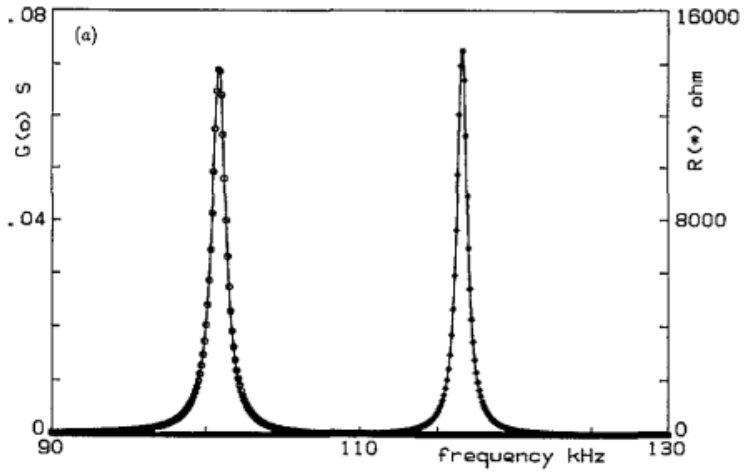

Figure 4.7. Radial resonance and anti-resonance profiles of the PZ27 sample. Dots are the experimental data, while full lines are the reconstructed curves.**[4]**

The calculated coefficients are inserted in the analytical expression of the resonance and calculation of the complex admittance is performed by this model as a function of the frequency and the reconstructed peaks plotted. The residuals for these reconstructed R and G peaks to the experimental ones, quantified by the regression factor ($\Re^2$) accounts with the validity of the model for the resonance mode. The closer is the model to the experimental curves; the closer is $\Re^2$ to 1. For the planar mode, the complex material coefficients (P*=P′<M->iP′′) directly determined in this analysis are the piezoelectric charge coefficient, d_{31}, the dielectric permittivity, ε^T_{33}, and the elastic compliances, s^E_{11} and s^E_{12}. The value of d_{31} allows analyzing the sensor performance in the perpendicular plane to the applied field, and the ratio d_{33}/d_{31} gives an insight of the anisotropy of the material. Besides, a number of other material coefficients are determined by the software from those, using well known relationships.**[4]** These allow us to analyze the performances of the ceramics as generator (piezoelectric voltage coefficient g_{31}) and energy transducer (electromechanical coupling factors and frequency number k_p, k_{31}, $N_p=f_s(kHz)D(mm)$, where D is the diameter of the disk). For anisotropic materials, as the piezoelectric ceramics, the Poisson's ratio (σ) depends on the direction of extension

and transverse deformation. Ceramics have two σ values, for planes parallel and perpendicular to the poling direction. From the radial mode of resonance, we can calculate the latter as $\sigma P = <M-> s^E_{12}/s^E_{11}$. A perfectly incompressible isotropic material deformed elastically at small strains would have a Poisson's ratio of exactly 0.5. Most piezoceramics exhibit values of about 0.3. In piezoceramics, σ allows also to quantify the in-plane anisotropy, the higher the σ the lower the anisotropy and the higher the mechanical coupling between various vibrational modes. Losses can be expressed for each material complex coefficient as loss tangent factor ($\tan\delta = P''/P'$), commonly used for the dielectric coefficients, or as a quality factor ($Q <C=> P'/P''$), commonly used for the elastic coefficients. The mechanical Q factors (Q_m) calculated by the iterative method here used was compared with that calculated according to international standard methods. The latter was considered very accurate for both low and high loss materials, as well as for low and high electromechanical coupling factor materials.**[5]** The calculation of piezoelectric coefficients in complex form allows obtaining piezoelectric losses, not so commonly reported, but equally important for the design of devices.

4.1.4 Human Alveolar A549 Cells Viability Assay

The cell line A549 (ATCC, CCL-185) was grown and maintained in a humidified incubator (37 °C and 5% CO_2) with DMEM (Dulbecco's Modified Eagle Medium, a basal medium for supporting the growth of many different mammalian cells), supplemented with 10% FCS (Fetal Calf Serum) and 1% penicillin/ streptomycin (Sigma-Aldrich). To assess the potential toxicity of KNN powders, human lung carcinoma A549 cells were exposed to different concentrations, for a period of 24 h. First, cells (approximately $3*10^4$) were incubated in culture media with 5% CO_2, for 24 h at 37 °C. Subsequently, they were seeded in 96-well plates, and exposed to the KNN powders, diluted in DMEM 1% FCS. Once the cells were exposed for 24 h, they were washed and incubated for 2.5 h, with 100 μL of a Neutral Red solution, prepared as follows: a 1:100 dilution (in treatment media)

from the Neutral Red stock (4 mg/mL) was incubated for 24 h at 37 °C, protected from light. Afterwards, cells were washed with DPBS (Dulbecco's phosphate-buffered saline, a balanced salt solution used for washing cells) and fixed with formaldehyde 4%. Cells were washed again with DPBS, and an extraction solution, containing 50% ethanol 96°, 49% distilled H_2O and 1% acetic acid, was added to each well. After a moderate shaking step of 10 min, the extraction solution was transferred to an opaque 96-well plate, and fluorescence was measured employing a microplate reader (BioTek Synergy HT, excitation: 530/25; emission: 645/40). Results were expressed a percentage of the average values obtained in the negative control condition.

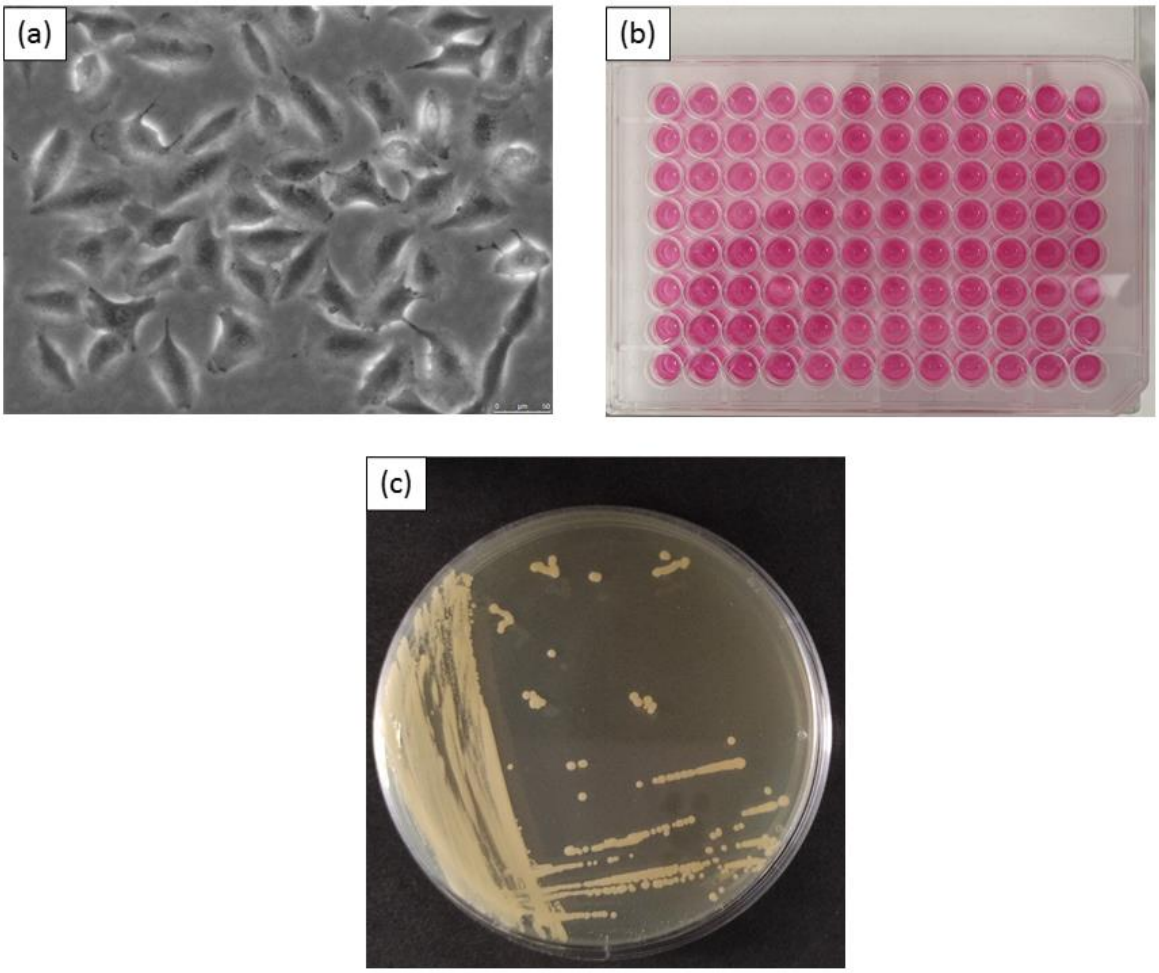

Figure 4.8. (a) A549 cells (human lung cells) observed with an optical microscope, (b) 96 well plate where cells are cultured and (c) agar plate where colonies of S. cerevisiae are isolated.

4.1.5 Saccharomyces cerevisiae Viability Assay

The S. cerevisiae BY4741 strain was grown and maintained in standard liquid YPD medium (1% yeast extract, 1% yeast bacto-peptone, 2% glucose). Cell cultures in liquid media were done on a rotary shaker at 185 rpm at 30 °C. Yeast cells viability after exposure to different KNN concentrations was determined by performing the colony forming units (CFUs) assay, through the following steps: Yeast cells at OD600 = 1 (exponential growth phase) were exposed to 1000 µg/mL of KNN and KNN-based powders for 2 and 24 h, in 1 mL cultures, using 24-well plates. To determine CFUs at both sampling times, 100 µL of cells aliquots, previously diluted 10^4 times, in the case of 2 h exposure, and 10^5 times, in the case of 24 h exposure, were spreaded on solid YPD medium (6% agar), employing disposable Digralsky spatula. Subsequently, agar plates were incubated at 30 ºC for 48 h. Afterwards, colony forming units were counted for each condition tested.

4.2 Processing optimization and electrical properties of KNN-BF-CuO system

4.2.1 Synthesis and sintering of KNN-BF-CuO ceramics

$0.99K_{0.5}Na_{0.5}NbO_3$-$0.01BiFeO_3$ (abbreviated as KNN-BF) powders were prepared through solid-state reaction, starting from a mixture of K_2CO_3 (Sigma Aldrich, ≥ 99.995%), Na_2CO_3 (Sigma Aldrich, ≥ 99.5%) and Nb_2O_5 (Sigma Aldrich, monoclinic polymorph 99.9985%), Bi_2O_3 (Sigma Aldrich, ≥ 99.9%) and Fe_2O_3 (Sigma Aldrich, ≥ 99%). Manipulations of the starting reagents have been conducted in an Ar Dry Box machine (MBraun), in order to prevent hydration of the carbonates. Raw materials were weighted according to the desired stoichiometry and transferred into a stainless-steel vial together with 1 ball (stainless steel) of 10 g. The powders were mechanically treated up to 24 hours by using a Spex 8000M Mixer/Mill at 875 rpm in 5ml of ethanol as a medium. The as-obtained slurry was then transferred in a beaker and heated in an oven at 150°C for to eliminate the

solvent. The calcination step was conducted from room temperature to 900 °C for 5 hours using a heating rate of 5°C/min and cooling rate of 10°C/min. The calcined powders were milled with 0, 0.5 and 1 wt.% of CuO (Sigma Aldrich, 99+%) (henceforth abbreviated as KNN-BF, KNN-BF+0.5CuO and KNN-BF+CuO) up to 24 hours in 5 ml of ethanol. The powders were finely ground in a mortar to obtain a fine particulate and mixed with few drops of polyvinyl alcohol (PVA) solution (3 wt.%) before compacting into a disk by means of a hydraulic press (220 kg/cm^2 for 30 minutes). The pellets were thermally treated for 2 hours at 600 °C to eliminate all traces of PVA. Sintering was conducted between 1000-1150°C, based on the amount of copper oxide, for 2 hours using a heating rate of 4 °C/min and cooling rate of 10 °C/min. Bulk densities were measured by geometric method.

4.2.2 X-Ray diffraction analysis and microstructural characterization

Structural investigations were conducted using a Rigaku D-MAX diffractometer (**Figure 4.9**) with an anode source of copper (λ = 1.54178 Å) working at a power of 40 kV and 40 mA. The spectrometer is equipped with a graphite monochromator and a scintillation tube in the diffracted beam. Quantitative analysis of the crystalline phases and structure determinations were performed with the MAUD program (Multiple Analysis Using Diffraction), within the Rietveld approach.**[2]**. Microstructure characterization of the fractured surface and pellet surface of the samples has been evaluated by Quanta FEI 200 scanning electron microscope (SEM). Thermogravimetric were performed with Labsys TGA/DTA and DSC instrument from room temperature to 1000 °C using a heating rate of 5 °C/min and cooling rate of 30 °C/min under argon atmosphere.

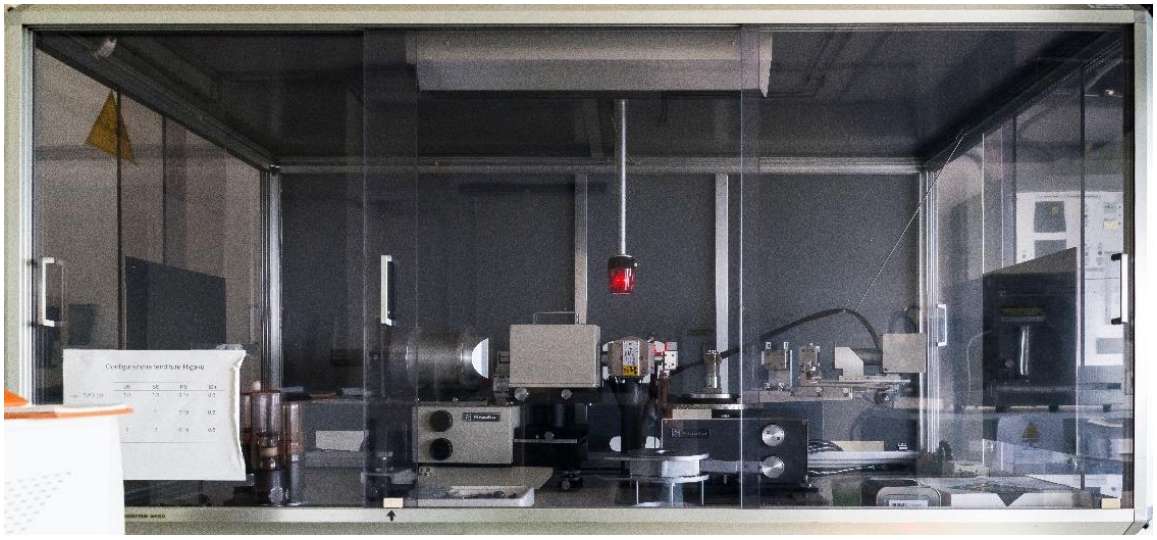

Figure 4.9. Rigaku D-MAX diffractometer.

The Energy Dispersive X-Ray Spectrometry (EDS) analysis were performed with EDAX equipment working at 30 kV and accumulating about 20k counts. Particle Size distribution was obtained via Dynamic Light Scattering measurements (DLS) with Malvern Zetasizer Nano S90 with 633 nm "red" laser at room temperature.

4.2.3 Piezoelectric, dielectric and elastic characterization at resonance

In order to measure electric properties, pellets were reduced in thickness by polishing to the proper thickness/diameter aspect ratio. Silver paste was attached on both surfaces of the thin disks and welded at 400°C for 30 minutes. After that, samples were increasingly poled in thickness under 10-30 kV/cm at 100°C for 15 minutes in a silicone oil bath, followed by field cooling (FC). Permittivity vs. temperature curves at frequencies above 1 kHz were measured using an automatic temperature control and capacitance-loss tangent data acquisition from an impedance analyser (HP 4194A). The quasi-static d_{33} piezoelectric charge coefficient was measured two hours after poling with a Berlincourt d_{33}-meter at 100Hz. Complex impedance as a function of the frequency was measured with an impedance analyser (HP 4192A-LF) at the radial extensional resonance of the

thickness poled thin disks. The related piezoelectric, dielectric and elastic material coefficients, including all the losses, were determined using the software for automatic iterative analysis of the complex impedance vs. frequency curves. The numerical method, used was developed by Alemany et al.**[4,5]**

4.3 Spark Plasma Sintering (SPS) and electrical properties of KNN-BF system

4.3.1 Fabrication of SPS KNN-BF ceramics

The processing of particles follows a similar procedure as described in the **paragraph 4.2.1**. Sintering experiments were conducted in vacuum using SPS equipment (515S model, Fuji Electronic Industrial Co., Ltd., Kanagawa, Japan; **Figure 4.10a**) under the following conditions: dwell temperature (T_D), heating rate, dwell time (t_D), and mechanical pressure (P) of 940, 100 °C/min, 5 min, and 50 MPa, respectively. The temperature was measured using a K thermocouple placed inside the diameter dye (**Figure 4.10b**). After sintering, four different samples were annealed in air for 2 hours at 950, 1000, 1050 and 1100°C named respectively Sh2, Sh3, Sh4 and Sh5. The as sintered SPS samples was named Sh1. Bulk densities were measured with the Archimedes' method as an average of four measurements.

4.3.2 X-Ray diffraction analysis and microstructural characterization

Structural investigations were conducted using a SMARTLAB diffractometer (**Figure 4.3**) with a rotating anode source of copper (λ=1.54178 Å) working at 40 kV and 100 mA. The patterns were collected in the angular range from 18° to 110° with a step size of 0.05° and a fixed counting time of 15 seconds per point (high resolution). Microstructure and morphology of the samples have been characterized by Quanta FEI 200 Scanning Electron Microscope (**Figure 4.4**). Raman analyses

were performed by a Senterra confocal Raman microscope (Bruker) with a 632 nm laser excitation, 1 mW power, and 10× objective.

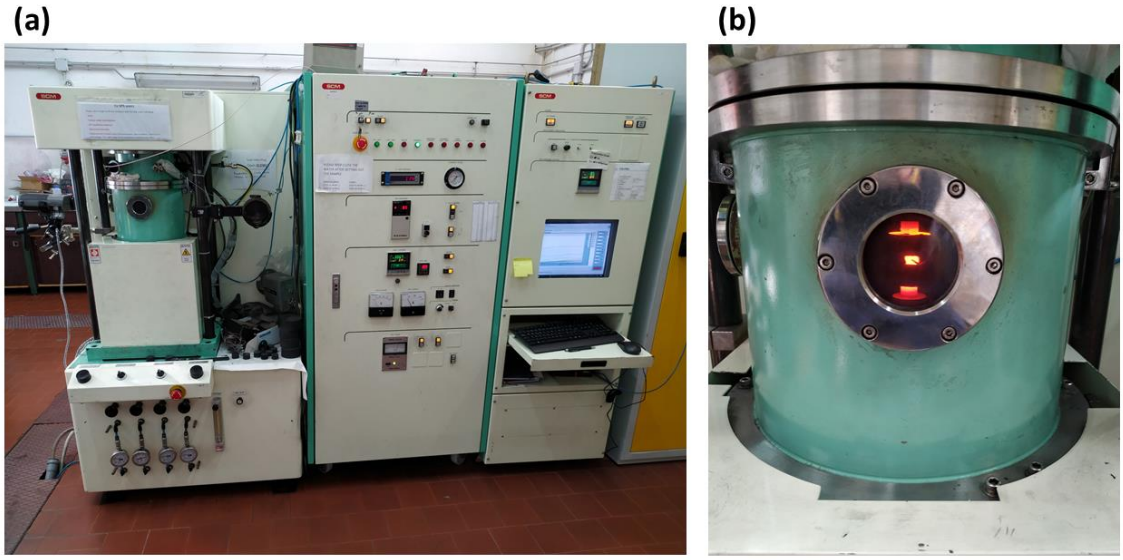

Figure 4.10. **(a)** Spark Plasma Sintering furnace (Fuji Electronic Industrial Co.). **(b)** Detail of the furnace during an SPS experiment. It can be seen the diameter dye with the thermocouple placed inside.

4.3.3 Piezoelectric, dielectric and elastic characterization at resonance

In order to measure electric properties, pellets were reduced in thickness by polishing with a sandpaper up to a thickness of about 1mm. Silver paste was attached on both surfaces of the thin disks and welded at 400°C for 1 hour. After that, samples were increasingly poled in thickness under 20 kV/cm at 50-100°C for 15 minutes in a silicone oil bath, followed by field cooling (FC). Permittivity vs. temperature curves at frequencies above 1 kHz were measured using an automatic temperature control and capacitance-loss tangent data acquisition from an impedance analyser (HP 4194A) from room temperature to 420 °C. The quasi-static d_{33} piezoelectric charge coefficient was measured two hours after poling with a Berlincourt d_{33}-meter at 100Hz. Complex impedance as a function of the frequency was measured with an impedance analyser (HP 4192A-LF) at the radial extensional

resonance of the thickness poled thin disks. The method to acquire the material coefficients has been already described previously.

4.4 Bibliography

[1] Y. C. Liou, Y. L. Sung. *Ceram. Int.* **2008,** 34(2), 371–377.

[2] M. Bortolotti, L. Lutterotti, G. Pepponi. *Powder Diffr*. **2017**, 32, S225–S230.

[3] C. Alemany, L. Pardo, B. Jiménez, F. Carmona, J. Mendiola, A. M. Gonzalez. *J. Phys. D*. **1994**, 27(1), 148–155.

[4] C. Alemany, A. M. González, L. Pardo, B. Jiménez, F. Carmona, J. Mendiola. *J. Phys. D.* **1995**, 28(5), 945–956.

[5] L. Amarande, C. Miclea, C. Tanasoiu, *Ferroelectrics*. **2007**, 350(1), 38–47.

5 Processing, electrical properties and cytotoxic effect of potassium sodium niobate (KNN) modified with magnesium niobium oxide (MN)

5.1 Introduction

As emerged from **Chapter 3**, low reproducibility and the difficulty to obtain dense product are some of the main aspects that afflict KNN ceramics. Great effort was devoted to the search for additives capable of improving the densification and, at the same time, to lower the sintering temperature of this system. KNN ceramics have a very narrow sintering range around 1120° C that is very close to the solidus-liquidus line (Chapter 3, **Figure 3.3**). This means that, at those temperatures, the volatility of the alkaline ions is extremely high and very hard to control. Excellent results have been obtained with copper or zinc-based compounds (**Table 3.4**) which allow to obtain high KNN densities using relatively low sintering temperatures while keeping, at the same time, good piezoelectric properties. With the aim of exploring new additives, over the years some new compounds have been tested as a sintering aid on KNN and KNN-based materials, some of them have been listed in the State of the Art (Chapter 3, **Table 3.6**). In this context, it has been reported that Mg-based compounds could improve the sintering behaviour of KNN ceramics while maintaining good electrical properties. However, this element has been little explored and its effect on the densification and electrical properties of KNN is still unclear.**[1]** For these reasons, the lead-free system based on potassium sodium niobate (KNN), opportunely modified with a novel additive as $MgNb_2O_6$ (MN), was prepared through a combination of the mechanochemical activation method and air sintering. The effect of the mechanical processing on the microstructure refinement of the processed powders was established by X-ray diffraction and the average crystallite size content of the Nb_2O_5 species was evaluated. The experimental evidence was rationalized using a phenomenological model which permitted us to obtain the amount of powder processed at each collision and to optimize the activation

step of the pre-calcined reagents. After that, the effect of MN on sintering behaviour, structure, microstructure, and piezoelectric, elastic and dielectric properties at resonance have been evaluated. With the aim to shed further light on possible hazard of KNN-based ceramics, the toxicological potential of the as-processed KNN pellets and commercial PZT were determined by in vitro screening employing two model organisms that were selected as representatives of human (A549 cell line) and environmental exposures (Saccharomyces cerevisiae).

5.2 Ball milling effect on mixed powders

Figure 5.1 shows the analysis investigation referring to the as-mixed powders prior to any mechanical treatment (0h BM). The integral agreement factor calculated from the residual curve amounts to R_{wp} = 14.88%, which is assumed satisfactory, given the complex phase composition in the pattern and the narrow peaks, mainly from the Nb_2O_5 monoclinic phase, dominating the pattern.

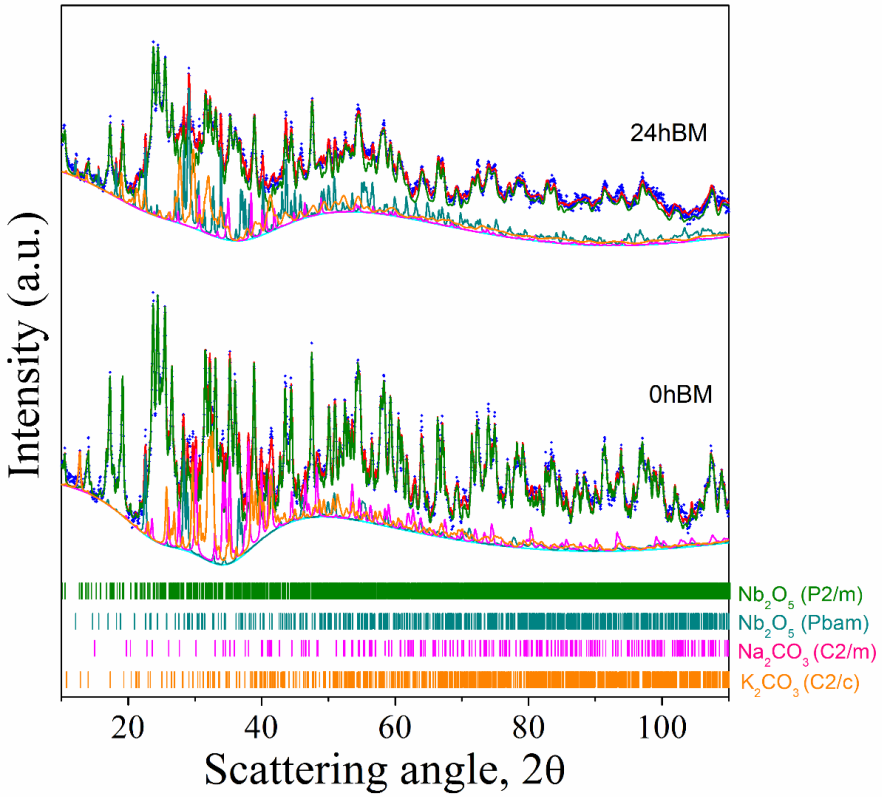

Figure 5.1. XRD pattern of the reaction mixture before (0 h BM) and after (24 h BM) the mechanical treatment. Blue dots are experimental data points, cyan lines are the background, red lines are the full calculated pattern and colored lines represent the contribution of each phase to the theoretical model used for the calculation.

In this fit, the instrument function, determined separately with a well-crystallized LaB_6 specimen, is considered. The specimen appears to be composed of both monoclinic (68 wt.%) and orthorhombic

(1 wt.%) polymorphs of Nb_2O_5, with net prevalence of the first. despite its lower electron density with respect to niobia. The graph also shows (orange curve) the presence of hydrated potassium carbonate (16 wt.%) (the X-ray data collection was conducted under air). The average crystallite size of monoclinic niobia, after correction for the instrument function, is ca 1050 Å.

Concerning the 24h BM sample, from rapid spectrum analysis it is possible to deduce that no substantial new phase was formed during mechanical grinding. Moreover, a broadening of the peaks was observed. This broadening could be caused by microstrain introduced by mechanical stress during the milling and/or by fragmentation and decrease in the average crystallite size down to the nanometer range.**[2]** The average crystallite size for monoclinic niobia is 400 Å, and the amount of the orthorhombic polymorph of niobia is increased in this specimen (about 11% wt., to compare with 1% wt. in the 0 h BM min specimen). The increase in the orthorhombic polymorph after the milling step is consistent with previous work.**[3]** The total amount of the niobia monoclinic polymorph is roughly the same (71 wt.%); this is mainly due to the lower detectability of sodium and potassium carbonates after the milling process, which were detected with a percentage by weight, respectively, of 8 and 10%. The perovskite phase of KNN was not detected in this sample, or at least, its concentration is below the detection limit of the instrument.

Considering the direct relation between crystallite sizes and powders' reactivity, the refinement of the former represents an important aspect that needs to be properly investigated. To this regard, the evolution of the microstructure of the starting powders submitted to BM was then evaluated from the sequence of XRD patterns, not shown here for brevity, acquired for selected times up to 24 h of mechanical processing. The values of the coherent diffraction domains are then shown in **Figure 5.2** as a function of the milling time (**Figure 5.2a**). The increasing milling time was accompanied by the progressive decrease in crystallite size <L>. The monotonic change reached an asymptotic value after

about 11 h of milling: the average crystallite size <L> varied from an initial value L_0 of about 1050 Å (0 h BM) to a final one L_f of 400 Å (12-24 h BM).

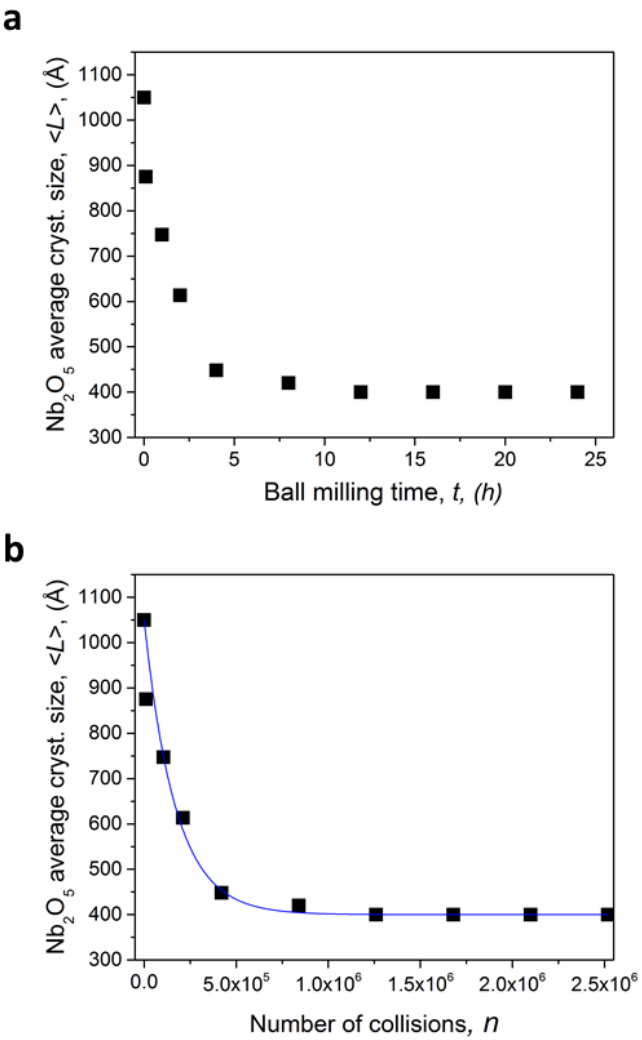

Figure 5.2. Average crystallite size <L> of coherent diffraction domains as a function of the milling time t_m (**a**) and total number *n* of collisions (**b**).

Taking in consideration the experimental approach adopted for this work (8 g of powders, 1 ball, 875 rpm), an inelastic regime of collisions was assumed during the mechanical process, which should provide a regular milling dynamic. Under such conditions, the milling time, t_m, and the number of impacts, n, show a direct proportionality, as also indicated in **[4]**, and the variation of the average crystallite size can be also reported as a function of the total number of collisions (**Figure 5.2b**). It is

in fact well established that mechanochemical processing occurs during each collision and the powders involved in this event are only a subvolume V* of the trapped powder. The stochastic model previously elaborated and discussed in detail in **[4]**, can be applied to the variation of physical properties, such as the refinement of crystallite size during a series of impacts. The kinetic of microstructural refinement can be described by the **Equation 5.1**:

$$< \mathrm{L} > = L_0 \exp(-Kn) + L_f[1 - \exp(-Kn)] \qquad \textbf{(5.1)}$$

where n, L_0 and L_f have been previously introduced, while K is the apparent rate constant of the process which corresponds to the volume fraction effectively processed at collision ($K = V^*/V_{tot}$). The mathematical function **Equation 5.1** describes almost perfectly the experimental values reported in **Figure 5.2b** (full blue line and black squares, respectively). The fit provides a K value of 5.92×10^{-6}, which indicates that a mass of 34.6 μg is processed per collision. According to the model used it is then possible to rationalize that the energy transferred to the trapped powders at first collision is enough to provide the change of the initial L_0 grain size to the final L_f grain size in the 34.6 μg of mass processed. Further collisions do not cause any noticeable change. Furthermore, it is possible to establish that operating with an impact energy, E_{imp}, of 0.088 J, the reduction of Nb_2O_5 crystallize size is accomplished after $1.20*10^6$ collisions (≈12 h BM). This allowed us to optimize this processing step, significantly reducing the milling time and preventing any contaminations induced by prolonged ball milling. These milling parameters were then adopted for producing the KNN-based powders for being densified and then tested. Further characterization on the as processed powders was performed to confirm the influence of the milling processing.

Representative micrographs of sample, a mixture of K_2CO_3, Na_2CO_3 and Nb_2O_5 prepared before and after mechanical treatment of 12 h, are reported in **Figure 5.3**. In **Figure 5.3a** the sample appears only as a simple mixture of Nb_2O_5 and carbonates. In **Figure 5.3b** these structures have been reduced

in size by the mechanical grinding and the mixture appears as an aggregate of fine particulate matter. The mechanical treatment induces important morphological and structural changes to the reaction mixture, and this may affect the solid-state reaction.

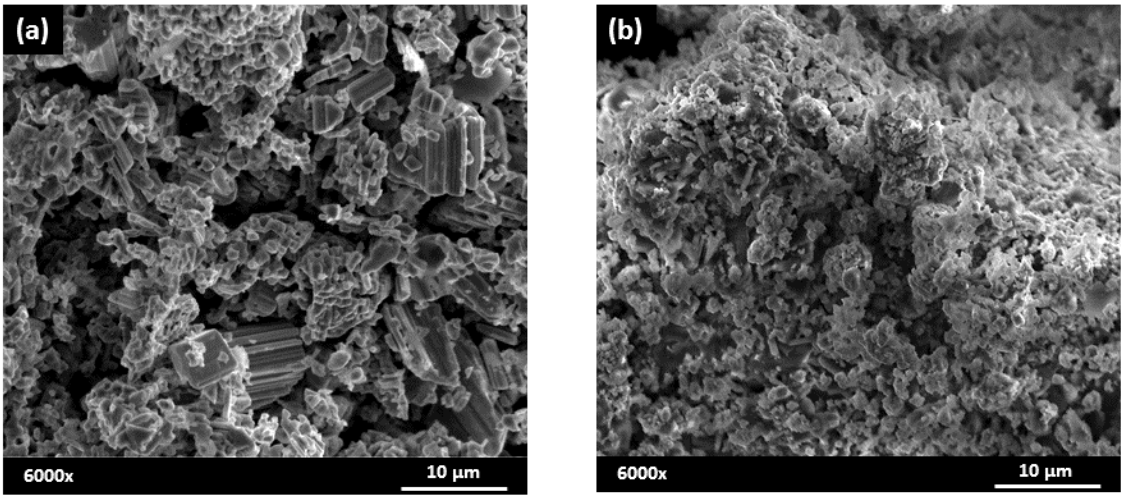

Figure 5.3. SEM micrograph of mixture powders: (**a**) 0 h BM and 12 h BM (**b**).

Thermogravimetric and DSC signals have been acquired on the samples under consideration to further investigate any reactivity differences of the powder mixture (**Figure 5.4**). All the experiments were carried out from room temperature up to 1000 °C. It can be seen from **Figure 5.4a** the powder mixtures of the unmilled specimen go through two stages of thermal decomposition from room temperature to about 125 °C, which are accompanied by two small endothermic peaks. According to Farooq et al., the first weight loss is due to the evaporation of physically adsorbed water, while the second may be due to the removal of chemically adsorbed water.**[5]** Between 150 °C and 190 °C there is another weight loss of ~ 1 wt.%, which could be related to the decomposition of some residuals of the hydrogen carbonates.**[6]** Between 470 and 800 °C it can be seen that a large weight loss of about 10.5% occurs, which is due to the decomposition of the alkali carbonates. The thermogravimetric profile of the milled sample (**Figure 5.4b**) is quite different from the previous one.

From room temperature to ~ 170 °C it is possible to see two clear weight losses of about 7.8 wt.% accompanied by two endothermic peaks correlated to the removal of water. After that, two distinct thermal phenomena take place, between 240–500 °C and 600–700 °C, respectively, which are responsible for a relative weight loss of 10.7 wt.% due to the decomposition of the alkali carbonates. Considering the reaction that takes place between the carbonates and niobium oxide, it is possible to calculate the theoretical weight loss which occurs during the heating treatment:

$$K_2CO_3 + Na_2CO_3 + 2Nb_2O_5 \rightarrow 4(K_{0.5}Na_{0.5})NbO_3 + 2CO_2 \uparrow (g) \qquad (5.2)$$

From **Equation 5.2** it can be deduced that the weight loss is due to the formation of two moles of carbon oxide. Therefore, the estimated weight loss is 88.018 g/mol (CO_2 M.W = 44.009 g/mol), which corresponds to about 11.3 wt.%. In the experimental case, the contribution of the weight loss of the adsorbed water must also be considered. In both samples, the weight loss due to the decomposition of the carbonates is in good agreement with the theoretical calculation. The different reactivity is well highlighted by the different trends of the two thermograms. Indeed, the decomposition of the carbonates, in the case of the milled sample, begins relatively early at around 240 °C and is completed at 700 °C, while for the unmilled sample this range is between 470–800 °C. Therefore, the milling process considerably increases the reactivity and lowers the calcination temperature of the reaction.

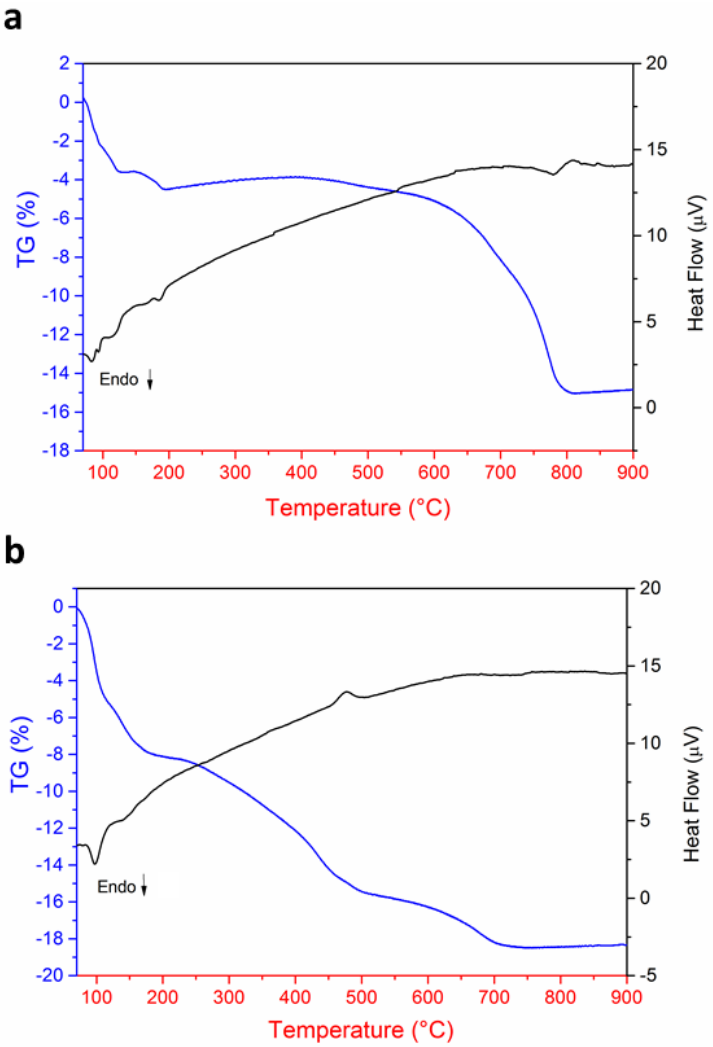

Figure 5.4. Thermogravimetric analyses and DSC of mixed powders mechanically treated for (**a**) 0h BM and (**b**) 12h BM. The blue line is the thermogram and the black line is the DSC signal.

The powders from thermogravimetric analyses were preserved and analyzed by XRD. The results are shown in **Figure 5.5**. The pattern of the 0h BM sample can be decomposed, according to Rietveld, as it is made by three phases: orthorhombic potassium niobate (s.g. Amm2), orthorhombic sodium niobate (s.g. Pbcm) and tetragonal $K_6Nb_{10.8}O_{30}$, with a weight percentage about of 66%, 17% and 17%, respectively. The low matching value reached (R_{wp} = 5.51%) highlights the excellent approach of the model to the experimental data. The tetragonal P4/mbm phase has the tungsten–bronze type structure with the formula $K_6Nb_{10.8}O_{30}$. This phase is formed in case of alkaline ions deficiency, and

it is an intermediate phase during the solid-state reaction.**[7]** It is also frequently reported in KNN sintered samples as it is formed during the sintering step due to the volatilization of the alkaline ions.**[8]**

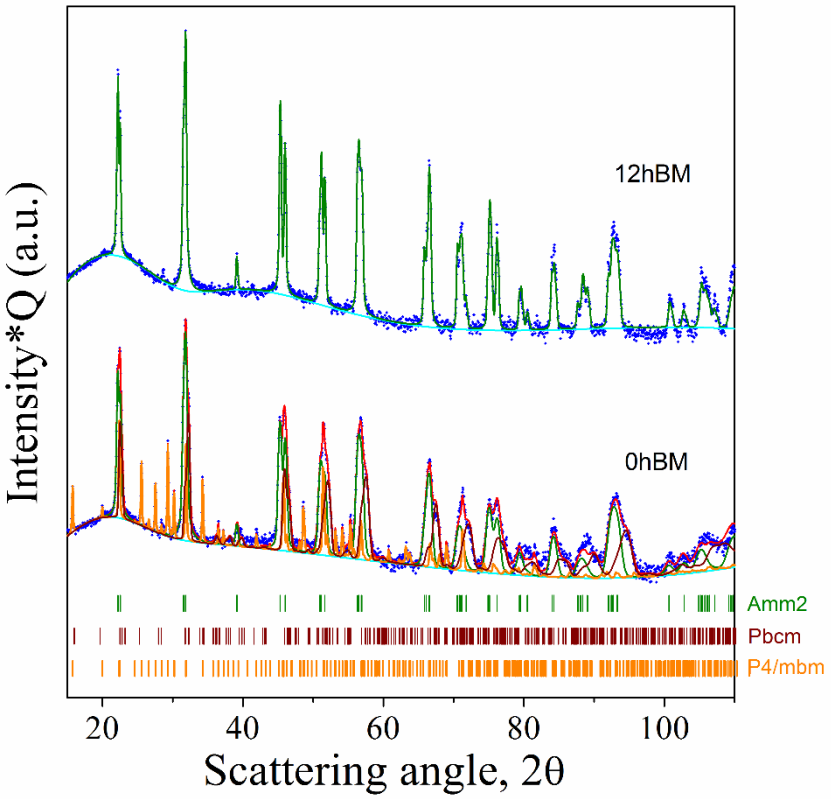

Figure 5.5. XRD patterns of KNN powders collected from thermogravimetric experiments. The logarithmic intensity is multiplied times Q ($2\pi/d_{hkl}$) to emphasize the high angle peaks.

The orthorhombic Pbcm is an antiferroelectric phase with formula $NaNbO_3$, while the orthorhombic Amm2 phase is the well-known ferroelectric phase commonly reported for pure KNN systems.**[9]** Otherwise, the 12h BM sample shows a single-phase structure with orthorhombic symmetry (s.g Amm2). A small peak has been detected around 28° which is most probably related to some residue of the tetragonal tungsten bronze phase. The cell parameters (**a** = 3.9444 Å; **b** = 5.6408 Å; **c** = 5.6723 Å) and volume of the cell (**V** = 126.206 $Å^3$) are in good agreement with those reported for pure

stoichiometric $K_{0.5}Na_{0.5}NbO_3$ (**a** = 3.9436 Å; **b** = 5.6510 Å; **c** = 5.6726 Å; **V** = 126.415 $Å^3$).**[8]** The lack of homogenization and low reactivity of the starting powders determine the presence of a niobate mixture, even after a high temperature (1000 °C). The milling step increases the reactivity, lowers the calcination temperature and allows us to obtain a single-phase powder product.

5.3 Structural, microstructural and electrical characterization of KNN-xMN ceramics

The magnesium niobium oxide (here and after abbreviates as MN) was synthesized with the solid-state method starting from Nb_2O_5 and MgO and according to the following chemical reaction (**Equation 5.3**).

$$MgO + Nb_2O_5 \rightarrow MgNb_2O_6 \quad (5.3)$$

The XRD pattern and the Rietveld analysis of the synthesised MN is reported in **Figure 5.6**. Blu data points are experiment, red full line is the contribution from the Rietveld analysis for the $MgNb_2O_6$ phase (96 wt.%). The green line refers to traces of unreacted Nb_2O_5 (4 wt.%), while the full cyan line refers to the background. Tics at the bottom mark the hkl peak positions expected based on the lattice parameters for the orthorhombic Pbcn space group, while the black line refers to the curve of residuals. The good matching of the model with the experimental data is highlighted by the low R_{wp} achieved by the analysis (R_{wp} = 8.61%). The density of the as-prepared KNN ceramics, sintered at 1100°C, as a function of MN concentration (wt.%) is summarized in **Figure 5.7**. With the increasing of MN content, the density firstly increased from 4.02 g cm^{-3} (pure KNN) to 4.10 g cm^{-3} (MN 0.5 wt.%), until reaching an optimal value of 4.28 g cm^{-3} for the sample modified with 1 wt.%, corresponding to 94.9 % of the theoretical density (TD) of pure KNN (4.51 g cm^{-3}).**[10]**

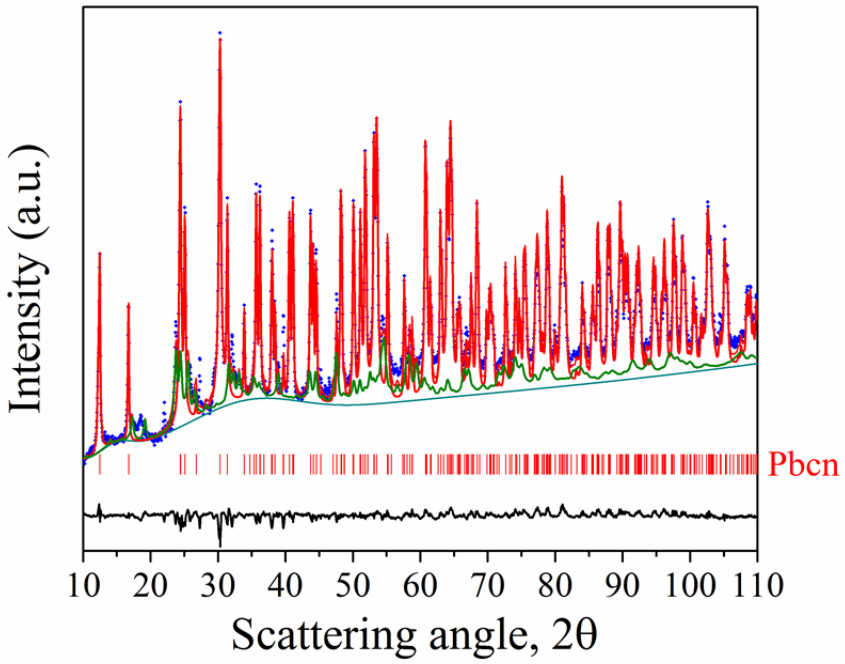

Figure 5.6. XRD pattern and Rietveld refinement of the $MgNb_2O_6$ used to modify KNN ceramics.

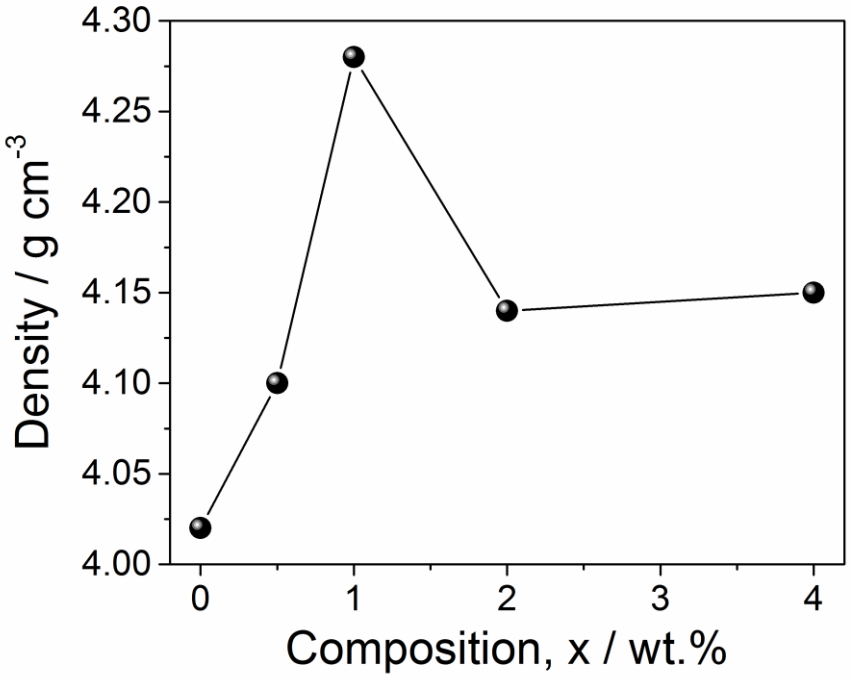

Figure 5.7. Density Vs composition of KNN-xMN series.

For higher amount of MN (2 wt.%), the density decreased to 4.14 g cm^{-3}, in accordance with trends reported in the current literature for other KNN-modified systems.**[11-12]** The system with 4 wt.% of MN, exhibits a similar density with respect to 2 wt.%, but it resulted too conductive for determining its electromechanical properties, most probably due to the presence of secondary phases segregated at the grain boundaries.**[13]** For this reason, the structural and microstructural characterization has been carried out only for the 0.5, 1 and 2 wt.% modified systems, together with the pure KNN for comparison purposes. Starting from the crucial point that the structures of piezoceramics significantly influence their properties, the XRD patterns of calcined KNN and sintered KNN-xMN (x=0, 0.5, 1, 2 wt.%), at room temperature, were recorded to get light on their structure. The as-calcined pure KNN pattern appears as a complex multiphase mixture (**Figure 5.8**).

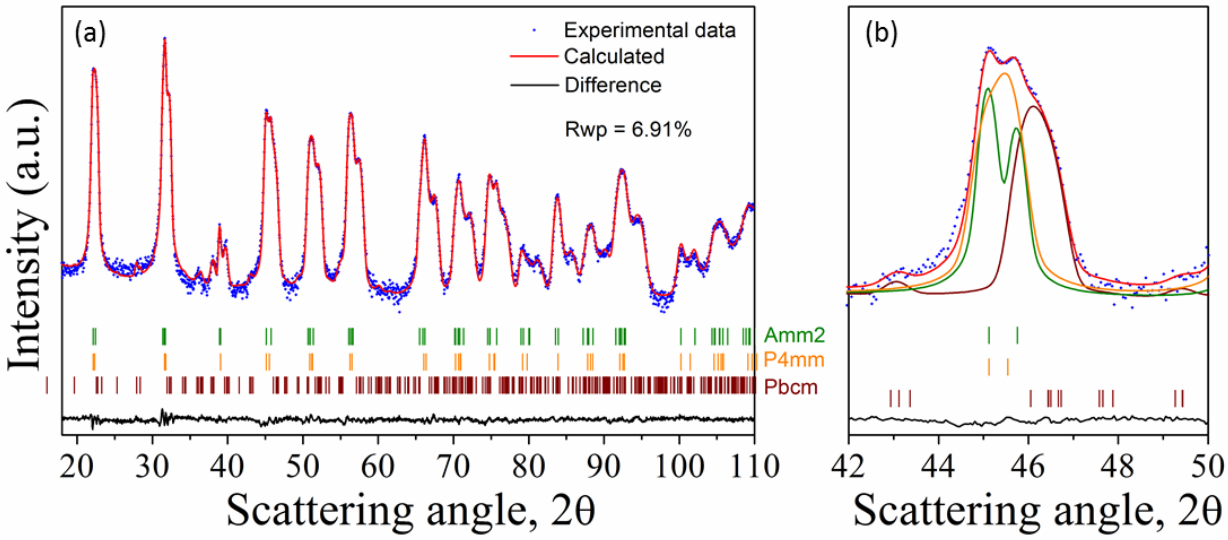

Figure 5.8. XRD pattern and Rietveld refinement of calcined KNN powders. (b) Magnification of the diffraction peak between 42 and 50°.

The Rietveld refinement were performed using the orthorhombic Amm2 $KNbO_3$, the tetragonal P4mm $K_{0.3}Na_{0.7}NbO_3$ and the orthorhombic Pbcm $NaNbO_3$ as a starting model, according to what reported by other authors (**Figure 5.8a**).**[14-15]** The good agreement between the model and the

experimental data was established by the low R-factor (R_{wp}=6.91 %) achieved by this analysis. Shoulders on the right side of the peaks are attributable to the orthorhombic Pbcm phase of the $NaNbO_3$ (**Figure 5.8b**). The presence of mixed phases was due to the monoclinic polymorph of Nb_2O_5 used as starting reagent in the solid-state reaction, in agreement with what was observed by Hreŝĉak et al.**[2]** The milled monoclinic Nb_2O_5 formed an inhomogeneous mixture of solid solutions with various Na : K ratios.

Table 5.1. Results of Rietveld analysis of calcined KNN powders with comparison with literature.

Phase	**a (Å)**	**b (Å)**	**c (Å)**	**V (Å^3)**	**Cryst. Size (Å)**	**R.m.s strain**	**Wt. %**
Amm2 $KNbO_3$	3.9660	5.6676	5.6996	128.114	1115	$1.9*10^{-3}$	24
P4mm KNN	3.9836		4.0187	63.773	1175	$4.0*10^{-3}$	48
Pbcm $NaNbO_3$	5.5484	5.601	15.6408	486.063	>2000	$4.6*10^{-3}$	28
Amm2 $KNbO_3$ **[16]**	3.9807	5.6880	5.7111	129.312	-	-	-
P4mm KNN **[17]**	3.9509		4.0085	62.572	-	-	-
Pbcm $NaNbO_3$ **[15]**	5.5071	5.5698	15.5245	476.190	-	-	-

The estimated cell volumes here evaluated for the orthorhombic Amm2, the tetragonal P4mm and the orthorhombic Pbcm phases (**Table 5.1**) are slightly different compared to the corresponding values reported in the literature for purely stoichiometric compounds. In particular, we observed a shrinkage of $KNbO_3$ and an expansion of $NaNbO_3$ and $K_{0.3}Na_{0.7}NbO_3$ unit cell volumes. This evidence suggests that a partial diffusion of Na^+ and K^+ into $KNbO_3$ and $NaNbO_3$ respectively take place during calcination. This may be justified by the smaller Na^+ radius (rNa=1.02 Å) compared to K^+ (rK=1.38 Å). Since the reaction rate of Na_2CO_3/Nb_2O_5 is one order of magnitude higher than K_2CO_3/Nb_2O_5, it is reasonable to expect that the average crystallite size dimensions will be larger for $NaNbO_3$ (2000

Å vs 1115 Å). At the same time, the micro-strain generated by the presence of K^+ in the $NaNbO_3$ unit cell is about twice compared to $KNbO_3$ (**Table 5.1**). The tetragonal P4mm, which is the majority phase in the powder mixture, shows a slightly larger cell volume (63.773 $Å^3$) compared to the stoichiometry composition (62.572 $Å^3$), suggesting that this phase probably contain a larger amount of potassium than the nominal composition.

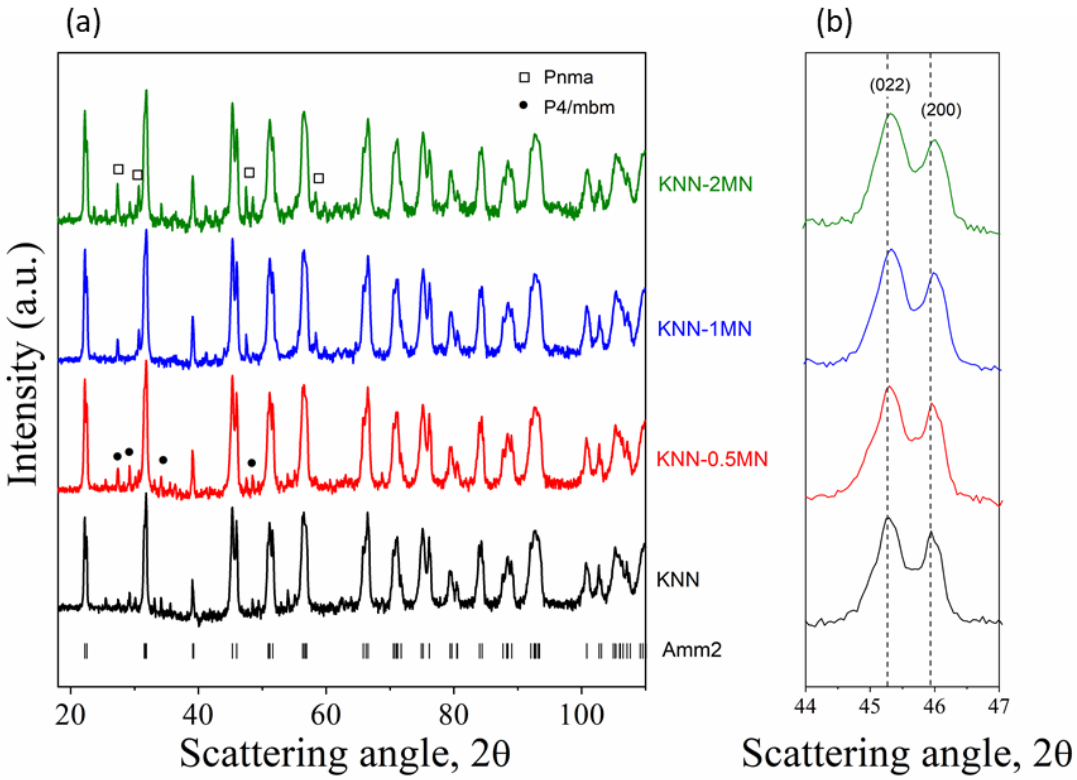

Figure 5.9. XRD pattern of KNN-xMN sintered pellets. (b) Magnification of the (022) and (200) reflection peaks between 44 and 47°.

The XRD analyses of sintered pellets are reported in **Figure 5.9**. All ceramics possessed the typical perovskite-type structure. For x<1 a tetragonal tungsten-bronze type phase has been detected in trace which was formed during sintering due to the volatilization of alkaline ions.**[8]** A secondary phase, with orthorhombic symmetry and s.g Pnma, was also detected for x>1. Since this impurity phase

appears for the high concentration of MN, it is reasonable to relate it to the addition of dopant, which reaches the solubility limit around x~1. The diffraction peaks of MN could not be observed for any pattern. This seems in apparent contrast with the post calcined KNN-xMN patterns, which presented the Bragg reflections ascribable to MN phase (see **Figure 5.10**). The disappearance of the MN peaks is then related to the full reaction between KNN and MN, which took place during the sintering process.

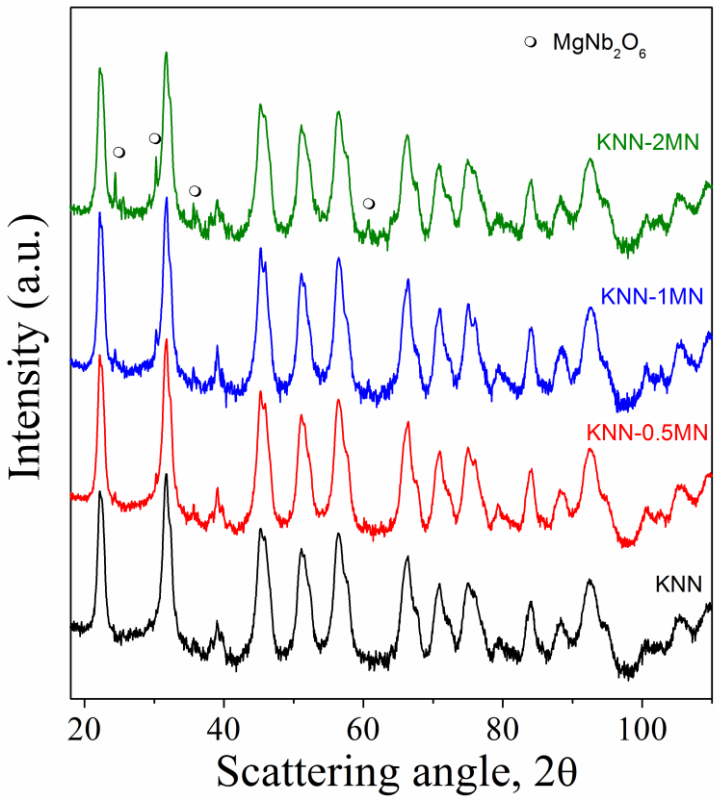

Figure 10. XRD patterns of KNN-xMN series after 24 hours of mechanical grinding as a function of the $MgNb_2O_6$ loading expressed in wt.%.

The patterns of sintered samples have been analysed by the Rietveld method and the results are shown in **Table 5.2**. As it can be surmised, the single-phase homogeneity was obtained during the subsequent sintering step at 1100 °C, with the formation of a with formula $K_{0.5}Na_{0.5}NbO_3$. Cell parameters and cell volume turn out to be in good agreement with the literature data (**Table 5.2**). The system with

0.5 wt.% of MN (KNN-0.5MN) showed a similar crystalline structure with a dominant orthorhombic Amm2 phase, while the Rietveld analysis performed on the KNN-1MN pattern, revealed the presence in trace (~ 3 wt.%) of the orthorhombic Pnma secondary phase. This still unknown phase possesses a $KTiNbO_5$-type structure, also observed in other ceramics such as $Rb(Mg_{0.34}Nb_{1.66})O_5$ and $K(Fe_{0.43}Nb_{1.57})O_5$ and, as already mentioned above, its presence is probably related to the solubility limit of MN in KNN ceramics and/or volatilization and segregation of alkali elements during the thermal treatment.**[18]** Increasing the content of MN (KNN-2MN), a further increase of this second phase has been detected (~ 5 wt.%). The results show that the crystallographic parameters of the Amm2 phase are roughly similar for all samples (**Table 5.2**). However, as it can be better visualized in the magnification in **Figure 5.9b** for the (022) and (200) reflection peaks, a slight shift toward higher two theta angles, for increasing amount of MN, has been observed. Since the ionic radius of Mg^{2+} (0.72 Å, 6 CN) is larger than Nb^{5+} (0.64 Å, 6 CN), the addition of a low amount of Mg^{2+} inside the KNN matrix is expected to produce an expansion of the unit cell, as observed by Li and co-authors.**[19]** For higher amount of Mg^{2+} this effect is limited by the high oxygen vacancy concentration which produces a reverse tendency and thus a shrinkage of the unit cell. In this case, a decrease in the cell volume is observed with an increasing concentration of MN. This phenomenon could be explained by the formation of A-site vacancy in the ABO_3 perovskite formula, due to the addition of an excess of Nb^{5+} ions (B-site) which causes an overall decrease in the cell volume. Similar behaviour was found for KNN modified with another columbite-type structure dopant as $CuNb_2O_6$.**[20]** The equivalent cell volume for KNN-1MN and KNN-2MN, further confirms that the solubility limit of MN in the KNN matrix is roughly x~1. Furthermore, the root-mean-square strain (r.m.s strain), which is a measure of the lattice distortion, for the Amm2 phase increases as a function of the amount of MN. Pure KNN shows a strain of about $6.0*10^{-4}$ (**Table 5.2**) while KNN-2MN has a strain of about $1.8*10^{-3}$, which is one order of magnitude higher than pure KNN.

Table 5.2. Structural parameters estimated by Rietveld analysis on sintered KNN powders XRD patterns. In [8] the Bmm2 settings are interchanged with Amm2 for comparison purposes.

Sample	Phase (SG)	a (Å)	b (Å)	c (Å)	V (Å^3)	r.m.s strain	wt. (%)	Rwp (%)
KNN	*Amm2*	3.9476	5.6439	5.6755	126.449	$6.0*10^{-4}$	98	10.27
	P4/mbm	12.5866		3.9729	629.397	$5.4*10^{-4}$	2	
KNN-0.5MN	*Amm2*	3.9466	5.6422	5.6744	126.355	$1.4*10^{-3}$	97	10.85
	P4/mbm	12.5925		3.9714	629.749	$2.1*10^{-4}$	3	
KNN-1MN	*Amm2*	3.9451	5.6406	5.6719	126.215	$1.5*10^{-3}$	97	10.25
	Pnma	6.5279	3.8250	18.6057	464.570	$8.7*10^{-4}$	3	
KNN-2MN	*Amm2*	3.9453	5.6410	5.6711	126.213	$1.8*10^{-3}$	95	10.38
	Pnma	6.5313	3.8255	18.6145	465.092	$7.0*10^{-4}$	5	
KNN **[8]**	*Amm2*	3.9436	5.6510	5.6726	126.415			

The SEM micrographs of the surfaces and the cross sections of the KNN-xMN ceramics sintered at 1100 °C, are illustrated in **Figure 5.11**. The images show that the pure KNN and KNN-0.5MN (**Figure 5.11a-b**) reveal a similar microstructure characterized by cubic-shape grains.**[21]** The KNN-1MN (**Figure 5.11c**) presents a well-packed microstructure characterized by a more homogeneous grain size. An evident limit of the grain growth was reached for the KNN-2MN sample, which showed a less compact microstructure, an increase of porosity and roundish grain morphology (**Figure 5.11d**). This evidence suggests that an excess of the orthorhombic Pnma secondary phase, most probably located at grain boundaries, inhibits the growth of the grains, also preventing the formation of the cubic-shaped grains. The statistical calculation of the grain size reveals that KNN and KNN-0.5MN have a lognormal grain distribution with an average grain size of 3.38 μm and 3.25 μm, respectively. For a high amount of MN (x > 1) large particles of > 6 μm are not detected anymore and the grain

size distributions, both for KNN-1MN and KNN-2MN, are characterized by a narrower, quasi-Gaussian curve, with an average grain size of 2.72 μm and 2.48 μm, respectively. A similar behaviour for higher amount of the impurity phase, has been observed in other ceramics systems, such as Mn-doped $BiFeO_3$ and $KCuTa_3O_9$-modified KNN.**[22]**

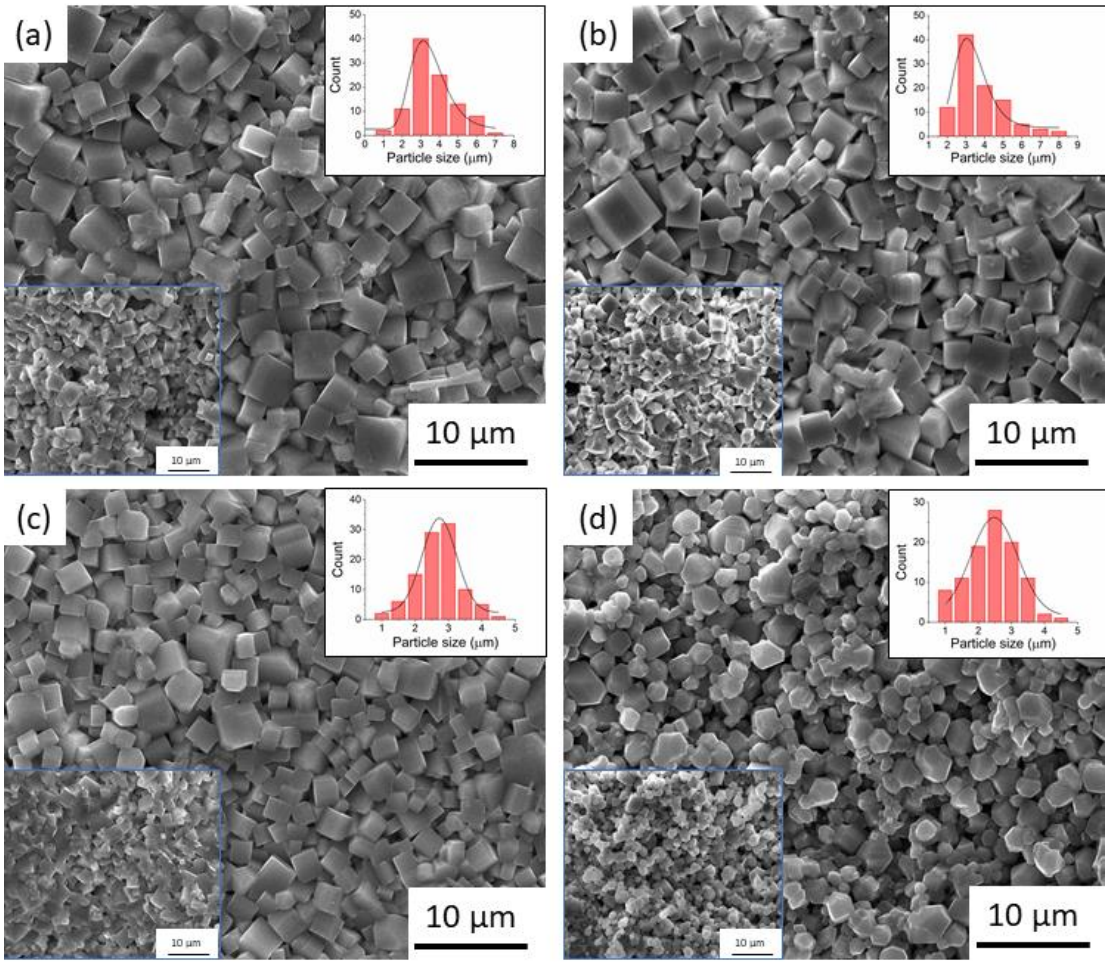

Figure 5.11. SEM micrographs of selected areas for grain size analysis (a) KNN, (b) KNN 0.5MN, (c) KNN-1MN and (d) KNN-2MN sintered at 1100 °C for 3 h. Insets shows the grain size distributions and the fractured surface of the samples.

Figure 5.12 shows the dielectric permittivity and losses of KNN-1MN and KNN-2MN as a function of the temperature for increasing frequency from 1 kHz. The low temperature (T1) dielectric anomaly

corresponds to the orthorhombic to tetragonal (O-T) polymorphic phase transition, whereas the high temperature (T2) corresponds to the phase transition to the paraelectric cubic phase (T-C).

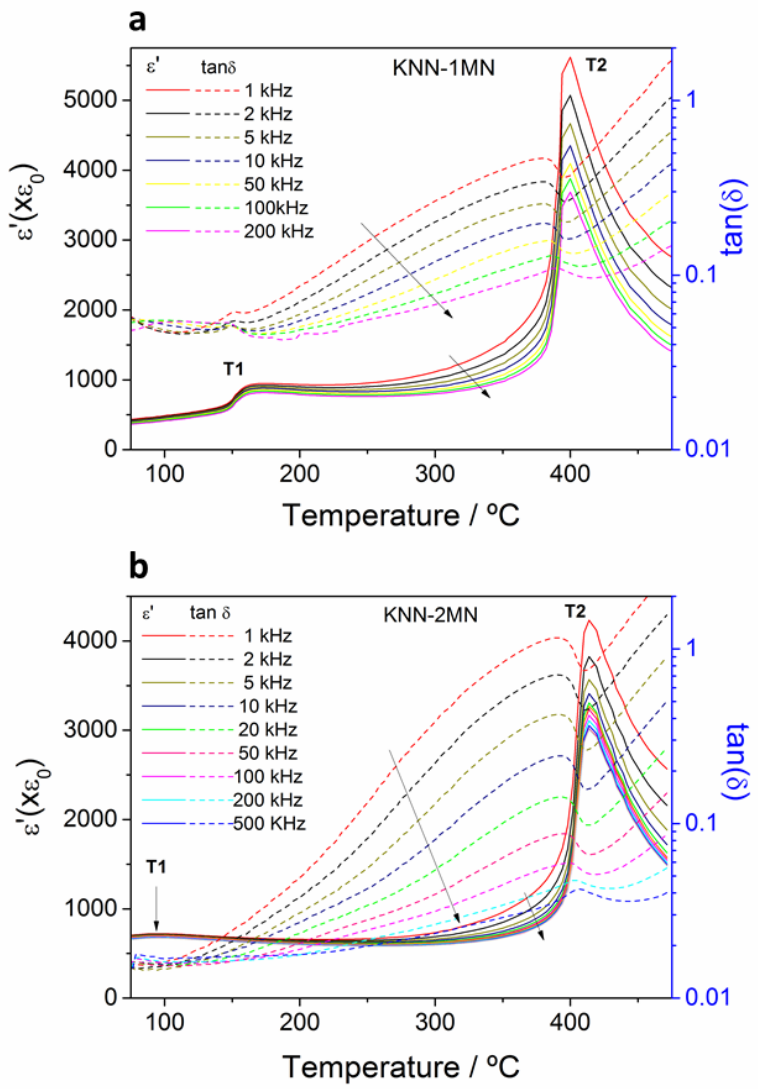

Figure 5.12. Dielectric permittivity ε^{T}_{33} and losses vs. temperature for (a) KNN-1MN and (b) KNN-2MN ceramics. Arrows indicate increasing frequency.

KNN-0.5MN ceramic has similar temperature dependence as KNN-1MN one (**Figure 5.12a**) with well-defined anomalies. T1 takes place at 175.7, 175.8 and 94.4 °C, for KNN-0.5MN, KNN1-MN and KNN-2MN at 1 kHz, respectively, and is always lower than the one for pure KNN (200 °C).**[9]**

Thus, the decrease of T1, as the amount of MN increases, is not linear. For KNN-2MN this low-temperature anomaly is much wider. This diffuse phase transition could reflect the crystal disorder confirmed by XRD analysis, in turn reflected in the distinct morphology of the grains in this ceramic (**Figure 5.11d**). T2 for the maximum permittivity is 396.1, 400.0 and 413.8 °C at 1 kHz, for 0.5, 1 and 2 % of MN, respectively. All temperatures are also lower than that for pure KNN (420 °C).**[9]** This reduction of temperatures is also found for other dopants.**[23]** The higher porosity of the KNN-2MN ceramic gives place to a lower value of the maximum permittivity at T2.

Figure 5.13 shows d_{33} as a function of the electric poling field. We can see that the KNN-0.5MN sample shows the highest d_{33} value for 20 kV cm^{-1}. The threshold value, beyond which the d_{33} starts to decrease due to the mechanical deterioration of the sample, seems to be 20 kV cm^{-1} for the pure KNN and KNN-0.5MN. The KNN-1MN shows endurance against degradation by electric field until 30 kV cm^{-1}, though the saturation of d_{33} is reached at 20 kV cm^{-1}.

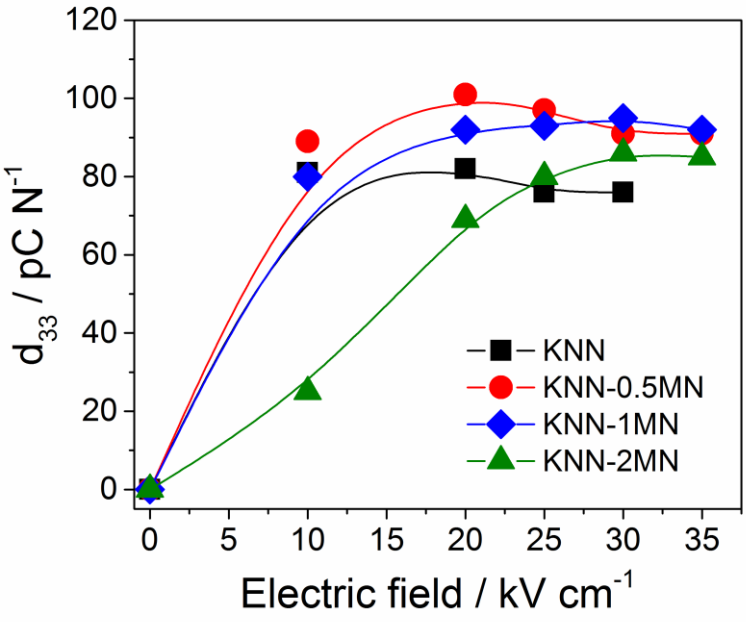

Figure 5.13. Piezoelectric coefficient d_{33} Vs Electric field.

This behaviour is most probably related to the increase in the amount of additive, which results in better densification and optimized microstructure for KNN-1MN (**Figure 5.11c**). The pure KNN and KNN-0.5MN continue to worsen while KNN-2MN undergoes the degradation only after the maximum d_{33} is achieved at 30 kV cm^{-1}. In **Figure 5.13** is apparent that the increase of MN content above 1 % makes it necessary to use higher poling fields to achieve similar, slightly lower, d_{33}. This slightly lower value is most likely a microstructural effect of the higher porosity of the ceramic (**Figure 5.11d**). In KNN-2MN, the need of a higher field to get almost similar d_{33} is mainly due to the lower grain size of this sample. It is well-known that the ferroelectric domain width is proportional to the grain size. The more complex domain configuration and the higher surface pinning of domain walls, causing their reduced mobility, results in higher energy needed for their reorientation, thus higher electric fields.**[24]** The inhibition of grain growth, as already explained, is a compositional effect.

Table 5.3. Comparison of properties between ceramics in our work and of some KNN ceramics modified with common oxide.

Property/Sample	**KNN-0.5MN**	**KNN-1MN**	**KNN-$K_4CuNb_8O_{23}$**	**KNN-CuO**	**KNN-CuO**	**KNN-ZnO**
d_{33} (pC N^{-1})	97	92	90	82	86	97
k_p (%)	27.4	29.1	36	39	38	30.4
$\boldsymbol{\varepsilon_{33}^{T}}$	267	282	292	240	231	371
$\tan\delta_e$	0.015	0.043	0.006	0.005	0.003	0.068
Q_m	158	116	1500	2523	2280	143
[Ref]	This work	This work	**[23]**	**[25]**	**[26]**	**[27]**

Table 5.3 shows a comparison between some properties of the ceramics in our work with the higher d_{33} values and ceramics of KNN doped with common sintering aids, such as Cu and Zn based

compounds. Cu-doped ceramics show a much higher mechanical quality factor (Q_m) than the ceramics here studied due to what appears to be a major electromechanical "hardening" effect of Cu-based compounds, however Q_m values are comparable with those of Zn-based compounds.**[23,25-27]** However, the piezoelectric coefficient (d_{33}), planar coupling factor (k_p), relative dielectric permittivity (ε^T_{33}) and dielectric losses ($\tan\delta_e$) are comparable.

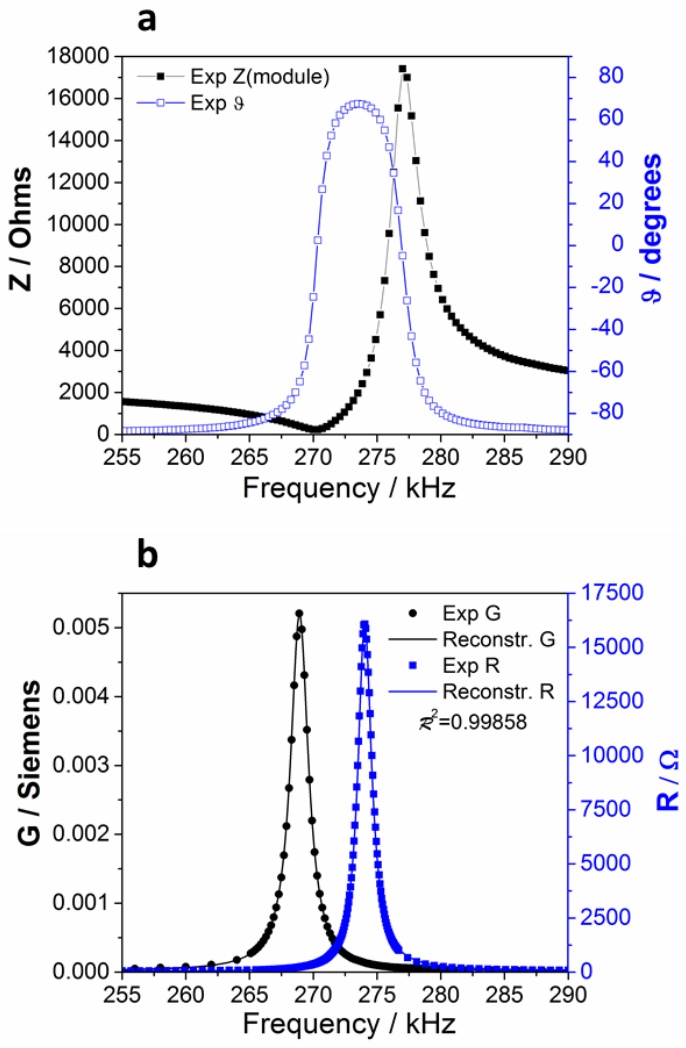

Figure 5.14. Equivalent representations of the complex impedance spectrum at the fundamental radial mode of resonance of a thin disk of KNN-0.5MN ceramic: (a) experimental modulus and phase plot and (b) R and G plot that is used in the iterative analysis, where symbols represent the experimental data and lines the reconstructed peaks.

Table 5.5. Room temperature piezoelectric, dielectric and elastic complex material properties of KNN-xMN ceramics.

Property/ Sample	**KNN**	**KNN-0.5MN**	**KNN-1MN**	**KNN-2MN**
d_{33} (pC N^{-1})	78	97	92	85
$\Re^2$	0.99995	0.99858	0.99976	0.99782
d_{31} (pC N^{-1})	-19.32	-36.99	-31.90	-29.60
$Q_p(d_{31})$	105	76	47	107
d_{33}/d_{31}	4.03	2.62	2.88	2.93
g_{31} (10^{-3} mV N^{-1})	-8.85	-14.04	-10.8	-8.47
$Q_p(g_{31})$	416	69	45	141
N_p (kHz mm)	3320	2399	3071	3298
k_p (%)	21.60	27.36	29.06	26.42
k_{31} (%)	13.34	15.72	17.25	14.79
ε^T_{33}	247	297	334	395
$\tan\delta_e$	0.012	0.028	0.043	0.016
s^E_{11} (pm^2 N^{-1})	9.61	21.02	11.52	11.45
$Q_m(s^E_{11})$	307	158	118	261
s^E_{12} (pm^2 N^{-1})	-2.30	-7.14	-3.41	-4.27
$Q_m(s^E_{12})$	307	158	118	261
s^D_{11} (pm^2 N^{-1})	9.44	20.50	11.18	11.00
$Q_m(s^D_{11})$	312	154	114	259
s^D_{12} (pm^2 N^{-1})	-2.47	-7.65	-3.75	-4.52
$Q_m(s^D_{12})$	283	172	131	267

s^E_{66} (pm^2 N^{-1})	23.82	56.30	29.85	31.44
$Q_m(s^E_{66})$	307	158	118	261
c^E_{11p} (10^{10} N m^{-2})	11.04	5.38	9.51	10.14
$Q_m(c^E_{11p})$	307	158	118	261
c^D_{11p} (10^{10} N m^{-2})	11.37	5.67	10.08	10.67
$Q_m(c^D_{11p})$	319	148	110	256
Poisson's ratio (σ^P)	0.239	0.339	0.296	0.373
Q_s(calc)	308	152	120	249
Q_p(calc)	323	147	108	256

All piezoelectric, elastic and dielectric complex parameters obtained from the radial resonance of the ceramics studied in this work are shown in **Table 5.5**. As a representative example, **Figure 5.14a** shows the measured complex impedance curves (modulus and phase) for the fundamental mode of the extensional radial resonance of a thin disk of KNN-0.5MN ceramic. **Figure 5.14b** also shows the equivalent plot of R and G, both the experimental and reconstructed peaks, used for the calculation of parameters in **Table 5.5**. It is apparent that the model used is accurate and reproduces well the experimental curves (**Figure 5.14b**) as quantified by a $\Re^2$ factor close to 1. This happens to all ceramics (**Table 5.5**). Instead, the losses commonly reported are restricted to one dielectric ($\tan\delta_e$) and one mechanical (Q_m) factor. Piezoelectric losses arise from the friction of the vibration or strain that result as a response to an electric field or from the dielectric losses associated with the voltage or charge generated as a response of a mechanical stress. They are an important parameter in the design of devices as they emerge as undesired hysteresis of the piezoelectric response and heat generation. What clearly emerges from **Table 5** is that the addition of the doping agent increases the piezoelectric response with respect to the undoped composition. In particular, the enhancement of the charge

coefficients, d_{33} and d_{31}, and coupling factors, k_p and k_{31} has been proved in the compositional range between 0.5-1 % of MN. The addition of MN also reduces the piezoelectric anisotropy as quantified by the ratio d_{33}/d_{31}. The wide low temperature dielectric anomaly of KNN-2MN (**Figure 5.12b**) influences the room temperature values of ε^T_{33}, also at the frequency of planar resonance. Permittivity at room temperature otherwise should be lower for this ceramic, since it contains higher porosity (**Figure 5.11d**), but, nevertheless, is the highest of the modified ceramics. All ceramics have higher compliances (s_{ij}), as well as lower stiffness (c_{ij}) and frequency number (N_p) than pure KNN, but also than the KNN-$K_4CuNb_8O_{23}$ doped ceramic, favoring the sensor performance.**[23]** All modified ceramics are less stiff at resonance than pure KNN. Losses are also calculated by the ratio between the frequency of the maximum of the recalculated R and G peaks and their width at half height, Q_s and Q_p, respectively, as losses affect the shape of these peaks. In this way the R, G peak plots are the fingerprint of the losses of the ceramic. Noticeably, Q_s correlates very well with the $Q_m(s^E_{ij})$ mechanical quality factors. The KNN-0.5MN sample shows the best piezoelectric activity and relatively low piezoelectric losses (d_{33} = 97 pC N^{-1}; d_{31} = -36.99 pC N^{-1} and g_{31}= -14.04×10^{-3} mV N^{-1}; $Q_p(d_{31})$ = 76 (or $\tan\delta_p(d_{31})$ = 0.013) and $Q_p(g_{31})$ = 69 (or $\tan\delta_p(g_{31})$ = 0.015), which results in the best sensor performance for charge and voltage generation. KNN-0.5MN ceramic is also the most compliant. KNN-1MN shows the best coupling factors (k_p = 29.06 % and k_{31} = 17.25 %), which means the best energy conversion efficiency, which is related with the best microstructure achieved.

5.4 Toxicology Assessment of KNN-xMN ceramics

To assess the potential cytotoxic effects of the different piezoelectric ceramics under study, the human lung carcinoma cell line (A549) was selected as a cellular model, to study possible adverse effects in human health via inhalation exposure of the selected piezoceramic powders. To determine

the percentage of living cells after the exposure to different lead-free KNN systems (KNN, KNN-0.5MN and KNN-1MN) and to a commercial system (PZT, 3N-99.9%, provided by American Elements), the Neutral Red assay (one of the viability tests most widely used in nanotoxicological studies) was performed. A549 cells were exposed to different concentrations (6.4, 32, 160, 800 μg/mL) of the different samples for a period of 24 h. As shown in **Figure 5.15**, after A549 cells exposure to KNN, KNN-0.5MN, KNN-1MN, and commercial PZT, the viability of the cells was not reduced in the presence of any of the concentrations tested, indicating the absence of cytotoxicity in the employed conditions. Previous studies have reported the good biocompatibility of PZT piezoelectric ceramics, despite the risk of PB release into the environment after their preparation and disposal.**[28]** Additionally, the cytotoxicity of KNN has been reported to be low.**[29]** In fact, the biocompatibility of KNN ceramics has also been verified by employing MC3T3-E1 osteoblasts, being suggested as an appropriate biomaterial with electroactivity for bone tissue regeneration.**[30]** Therefore, the obtained results in the present work are in line with those previously reported in similar studies.

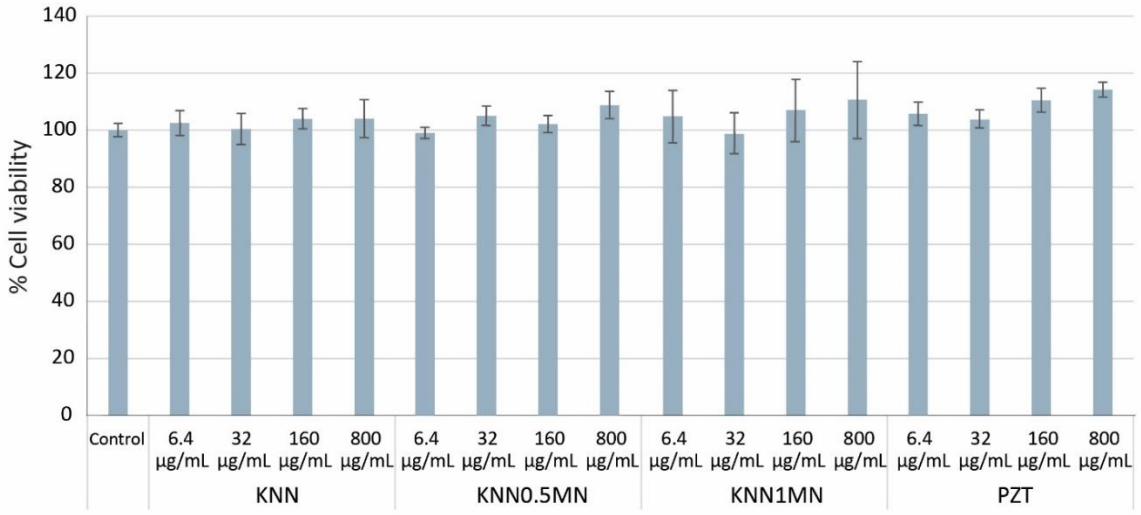

Figure 5.15. A549 cells viability after exposure to different concentrations of KNN, KNN-0.5MN, KNN-1MN, and PZT. "Control" corresponds to non-exposed cells.

The yeast S. cerevisiae is a eukaryotic model that is extensively used to comprehend fundamental molecular mechanisms and biological processes, which is also used as a tool for the toxicological evaluation of substances. Therefore, to evaluate the potential environmental impact of BN, yeast cells were exposed to 1000 µg/mL of KNN, KNN-0.5MN, KNN-1MN, and PZT, at two exposure times (2 and 24 h), and subsequently their viability was assessed through colony forming units' (CFUs) determination. As shown in **Figure 5.16**, no significant cells' viability changes were observed after 24 h, amongst different exposure conditions. The antimicrobial properties of KNN ceramics are scarce, although they have been previously explored employing nosocomial bacteria.**[31]** However, data on their antifungal potential are not available. In contrast to the reported significant antibacterial effect of KNN piezoceramics against Staphylococcus aureus, the present study indicates that the materials under study do not have antifungal capacity. In any case, more studies are necessary to clarify the potential toxicity of KNN-based materials against different fungal species.

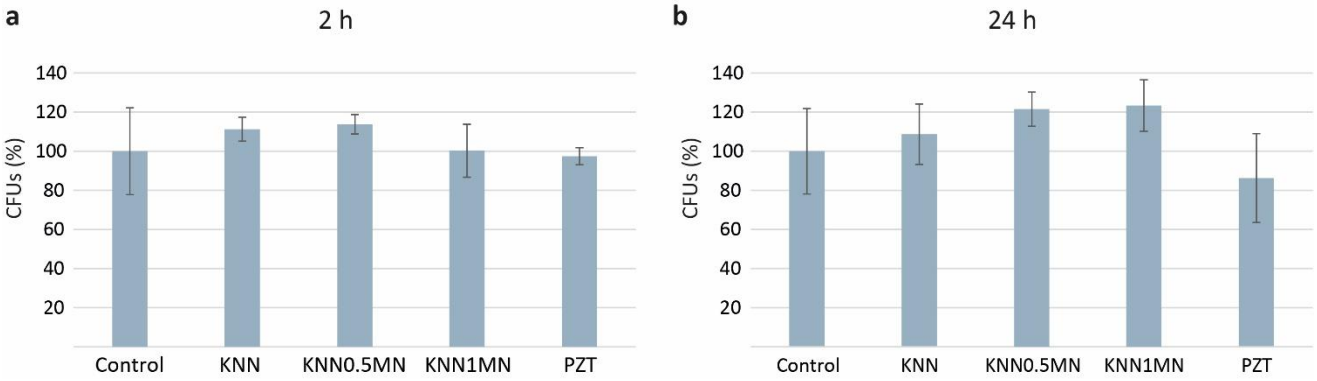

Figure 5.16. Determination of S. cerevisiae cells CFUs after exposure to 1000 µg/mL of KNN, KNN-0.5MN, KNN-1MN, and PZT, for 2 h (a) and 24 h (b). "Control" corresponds to non-exposed cells.

5.5 Conclusions

Summarizing, KNN and KNN-MN ceramics were successfully synthesized through the mechanical activation of the starting reagents conducted with a shaker ball mill (Spex) under a regime of inelastic collisions and energy impact of 0.088 J. It was shown that the methodological approach adopted allows us to rationalize the microstructural refinement processes in the Nb_2O_5 species. The phenomenological model was able to describe the kinetics of crystallite size variation and the value of the kinetic constant indicates that 34.6 μg of powder are processed in a single collision. It was also established that only one collision event was enough to refine the crystallite size of the fraction of powder processed. Controlling these parameters makes possible the synthesis with a proper stoichiometry of KNN and significant reproducibility; at the same time, they could be useful for an upscaling of the process. The effect of MN on KNN ceramics has been evaluated on the structure microstructure and electrical behaviour. The sintered pellets show a perovskite structure with orthorhombic symmetry and Amm2 space group. An orthorhombic Pbcm secondary phase appears for concentration of MN higher than 1.0 wt.%. Furthermore, the addition of MN causes an increase of the lattice distortion of the Amm2 phase. Experimental results show that the densification of KNN ceramics can be significantly improved by adding an appropriate amount of MN (1 wt.%). KNN-1MN also shows a better microstructure, characterized by well packed grains with narrower, quasi-Gaussian, size distribution. The Pnma secondary phase seems to act as an inhibitor of the grain growth: in fact, the KNN-2MN sample shows smaller particle size and different particle shape characterized by roundish grains. A non-linear dependence of the phase transition temperatures T1 (O-T) and T2 (T-C) with the amount of MN was found. The addition of MN reduces both temperatures with respect to those of pure KNN. The best properties were obtained in the compositional range between 0.5–1 wt.% of MN. KNN-0.5MN shows the highest charge and voltage

coefficients with relatively lower anisotropy and piezoelectric losses (d_{33} = 97 pC N^{-1}; d_{31} = −36.99 pC N^{-1} and g_{31} = −14.04×10^{-3} mV N^{-1}; Qp(d_{31}) = 76 and Qp(g_{31}) = 69), while KNN-1MN possess the best electromechanical coupling factors (k_p=29.06 % and k_{31}=17.25 %), which can be correlated with the best microstructure achieved. This work provides a positive evaluation of the addition of MN on KNN ceramics. The simple manufacturing method is easily scalable and suitable for medium-large scale productions. Finally, the toxicological test performed on KNN-xMN ceramics by exposing all the systems to two human and environmental cellular models, suggests that KNN-based materials are not cytotoxic and, in contrast with previous studies, that they do not have antifungal capacity.

5.6 Bibliography

[1] H. Meng, Y. Yang, Y. Wang, D. Wan, Q. Li, Y. Cheng. *Ferroelectrics*. **2010**, 404, 105–111.

[2] R. Singh, P. K Patro, A. R. Kulkarni; C. S. Harendranath. *Ceram. Int*. **2014**, 40, 10641–10647.

[3] J. Hrešcak, A. Bencan, T. Rojac, B. Malic. *J. Eur. Ceram. Soc*. **2013**, 33, 3065–3075.

[4] S. Garroni. *J. Phys. Chem. Solids.* **2012**, 73, 770–776.

[5] M. U. Farooq, J. G. Fisher, J. H. Kim, D. Kim, E. C. Shin, Y. H. Kim, J. H. Kim, S. H. Moon, J. S. Lee, X. Lin, et al. *J. Ceram. Process. Res.* **2016**, 17, 304–312.

[6] H. Tanaka. *J. Therm. Anal.* **1987**, 32, 521–526.

[7] B. Malic, D. Jenko, J. Holc, M. Hrovat, M. Kosec. *J. Am. Ceram. Soc.* **2008**, 91, 1916–1922.

[8] F. Hussain, I. Sterianou, A. Khesro, D. C. Sinclair, I. M. Reaney. *J. Eur. Ceram. Soc.* **2018**, 38, 3118–3126.

[9] S. Garroni, N. Senes, A. Iacomini, S. Enzo, G. Mulas, L. Pardo, S. Cuesta-Lopez. *Phys. Status Solidi A.* **2018** 215, 1700896.

[10] H. Birol, D. Damjanovic, N. Setter. *J. Eur. Ceram. Soc*. **2006**, 26, 861–866.

[11] D. Gao, K. W. Kwok, D. Lin, H. L. W. Chan. *J. Mater. Sci.* **2009**, 44, 2466–2470.

[12] S. Su, R. Zuo, X. Wang, L. Li. *Mater. Res. Bull.* **2010**, 45(2), 124–128.

[13] C.-C. Tsaietal, S.-Y. Chu, C.-S. Hong, S.-L. Yang. *Ceram. Int.* **2013**, 39, S165–S170.

[14] R. Beltrami, E. Mercadelli, C. Baldisserri, C. Galassi, F. Braghin, N. Lecis. *Powder Technol*. **2020**, 375, 101–108.

[15] H. C. Thong, C. Zhao, Z. X. Zhu, X. Chen, J. F. Li, K. Wang, *Acta Mater*. **2019**, 166, 551–559.

[16] W. Sugimoto, K. Mimuro, Y. Sugahara, K. Kuroda. *J. Ceram. Soc. Jpn*. **1999** 107(4), 318-321

[17] D. W. Baker, P. A. Thomas, N. Zhang, A. M. Glazer. *Acta Crystal. B*, **2009,** 65, 22-28

[18] N. Kumada, E. Iwase, N. Kinomura. *Mater. Res. Bull*. **1998**, 33, 1729–1738.

[19] T. Li, H. Fan, C. Long, G. Dong, S. Sun. *J. Alloys Compd*. **2014**, 609, 60–67.

[20] M.-R. Yang, C.-C. Tsai, C.-S. Hong, S.-Y. Chu, S.-L. Yang. *J. Appl. Phys.* **2010**, 108(9), 094103.

[21] D. Jenko, A. Benčan, B. Malič, J. Holc, M. Kosec. *Microsc. Microanal.* **2005**, 11, 572–580.

[22] T. Wang, L. He, Y. Deng, Q. Zheng, Q. Li, N. Jiang, C. Xu, X. Cao, D. Lin. *Ceram. Int*. **2017**, 43(17), 15666–15677.

[23] S. Zhang, J. B. Lim, H. J. Lee, T. R. Shrout. *IEEE Trans Ultrason Ferroelectr Freq Control*. **2009**; 56(8): 1523–1527.

[24] Z. Cen, Y. Yu, P. Zhao, L. Chen, C. Zhu, L. Lia, X Wang. *J. Mater. Chem. C*. **2019**, 7, 1379–1387.

[25] D. Lin, K. W. Kwok, H. L. W. Chan. *J. Phys. D* **2008**, 41, 045401.

[26] H. Takao, Y. Saito, Y. Aoki, K. Horibuchi. *J. Am. Ceram. Soc*. **2006**, 89(6) 1951–1956.

[27] K. Chen, J. Zhou, F. Zhang, X. Zhang, C. Li, L. An. *J. Am. Ceram. Soc*. **2015**, 98, 1698–1701.

[28] T. Sakai, S. Hoshiai, E. J. Nakamachi. *Optoelectron. Adv. Mater.* **2006**, 8, 1435–1437.

[29] S. Yu, S. Kuo, W. Tuan, Y. Tsai, S. Wang. *Ceram. Int.* **2012**, 38, 2845–2850.

[30] W. Chen, Z. Yu, J. Pang, P. Yu, G. Tan, C. Ning. *Materials.* **2017**, 10, 345.

[31] T. Yao, J. Chen, Z. Wang, J. Zhai, Y. Li. *Colloids Surf. B.* **2019**, 175, 463–468.

6 Processing optimization and electrical properties of KNN-BF-CuO system

6.1 Introduction

One of the deficit aspects found in the previous chapter concerns the low values of the coupling factors of KNN-xMN ceramics (**Table 5.5**). This important parameter describes the piezoelectric efficiency of the material. In other words, it measures how strong the coupling is between vibration mode and the excitation. In this context, the microstructure of the material plays an important role; in particular, ceramics characterized by homogeneous and well welded grains are able to convert the energy more efficiently. As known, the microstructure is closely related to the sintering process which is affected by several parameter including heating rate, temperature, sintering atmosphere, dwell time and particle size distributions. Among them, the particle size and the particle size distribution are one of the most important parameters that influences the sintering behaviour of the ceramic.**[1]** It is often reported that the starting reagents are first milled separately in order to obtain small and narrow particle size distribution which ensure a homogeneous mixing of the components. After that, A-site and B-site reagents are mixed and ball milled separately before being milled together. Moreover, to enhance the compositional homogeneity, the milled product is generally calcined at least twice.**[2]** However, this method required several steps from the preparation of the precursors, and their mixing, to multi-calcinations with intermediate wet milling. Compared to conventional milling route, the High Energy Ball Milling technique allows to obtain homogeneous nano powders using a simpler procedure that involves few steps. In **Chapter 5** particular attention has been focused on the optimization of the milling process of the pre-calcination step. That study provided useful information regarding the refinement of the crystallites correlated with the reactivity of the starting reagents which allows to obtain the minimum milling time required to maximize the

reactivity of the starting powders. However, the second milling step, (i.e, post calcination) has been little explored and requires much more attention to further improve the microstructure of the sintered product. For all these reasons, the first part of this chapter will be dedicated to an accurate study on the optimization of the milling step for the fabrication of a promising system based on potassium sodium niobate (KNN) modified with small amount (1 mol %) of bismuth ferrite (BF). The powders were prepared through the mechanochemical activation method by High Energy Ball Milling. The effect of the mechanical milling will be discussed not only from the point of view of the refinement of crystallites, but also on the particle size distribution of both milling step and their effect on the sintered product. The modification of KNN with BF was carried out with the "traditional method"; Bi_2O_3 and Fe_2O_3 were added in the desired composition to the mixture of carbonates and niobium oxide and milled and then calcined together. This method differs from the "two step powder synthesis" where the two components, i.e., KNN and BF, are firstly synthetized separately and then milled together before sintering. Finally, the electrical properties of KNN-BF will be evaluated as well as the effect of small addition of copper oxide (CuO) as a sintering aid and an "hardening" dopant.

6.2 Ball milling optimization of KNN-BF system

In order to find the best milling conditions for the calcination process, the starting powders have been treated for different milling times (0, 6, 12, 24h) and the powders were analysed in their structure and morphology. XRD analyses were carried out using few mg of material, finely deposited on an adhesive polymeric support (Scotch Magic®).

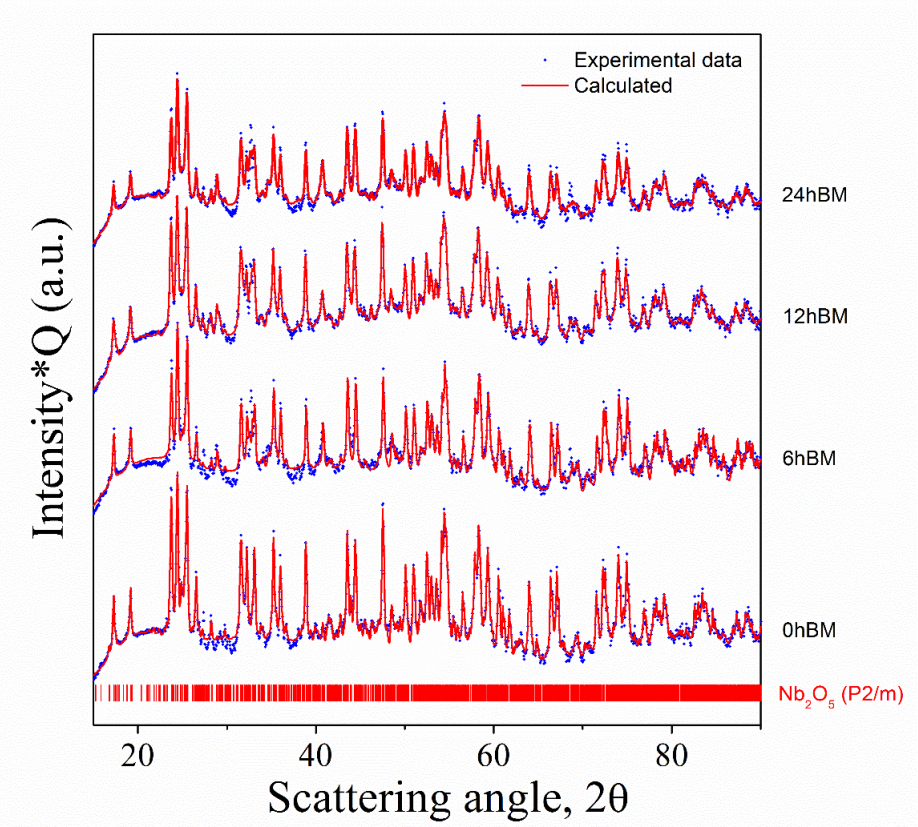

Figure 6.1. XRD pattern of the reaction mixture milled for different milling times.

Figure 6.1 shows the XRD patterns of the sample milled for different milling times. The diffraction patterns are characterized by the dominant presence of the monoclinic phase (P2/m s.g) of the niobium oxide, in agreement with what seen in the previous chapter (**Figure 5.1**). Sodium and potassium carbonates are difficult to spot probably for the low angle contribution of the polymeric support which cover the intensity of the two carbonates. For the same reasons, iron and bismuth

oxides were not identified. In **Figure 6.1** it is clear that the diffraction peaks of niobia undergo to a decrease in intensity and a slight broadening which is caused by micro-strain induced by mechanical stress during the milling and/or by fragmentation and decrease of the average crystallite. This assumption is confirmed by the measurement of the average crystallite size carried out with the Rietveld method (isotropic model). **Figure 6.2** shown the average crystallite size of niobia as a function of the milling time.

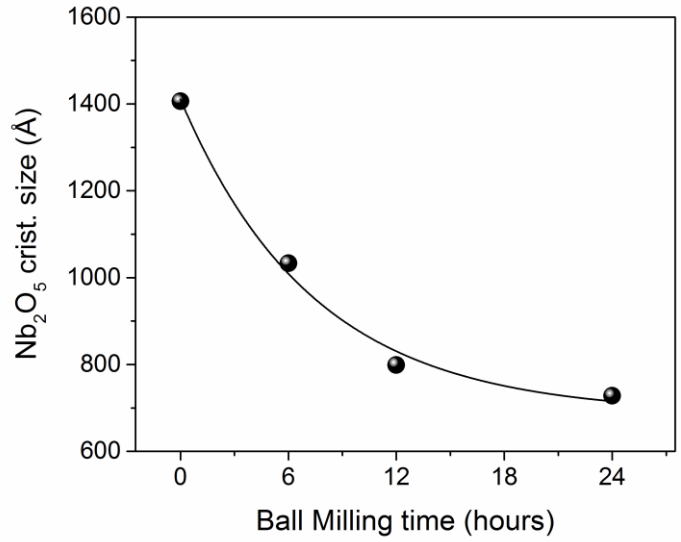

Figure 6.2. Average crystallite size of niobium oxide as function of the milling time.

In **Figure 6.2** it can be seen that the average crystallite size decreases exponentially from ~ 1400 Å (0h BM sample) to ~700 Å of the (24h BM sample). The value obtained for the 24 hours milled sample (~700 Å) is higher to that found for the mixed powders milled in dry condition for the same milling time (420 Å). This effect could be related to the presence of ethanol in the milling media which dampens the impact energy of the ball with the powders.**[3]** As a consequence, the dry milled sample have a larger amount of strain and defects compared to the wet milled sample. However, the presence of ethanol in this step favours a better recovery of the powders inside jar. In dry ball milling

condition the powders are often stucked to the walls and much more difficult to remove. This inevitably causes a large loss of material. The effect of milling time was also observed in terms of the variation in the average particle size by using the dynamic light scattering technique (DLS). In **Figure 6.3** are shown the distribution curves of the particles. In all the samples the particle sizes have a bimodal distribution. It is interesting to note that the bimodal shape is maintained regardless of the milling time as well as roughly the ratio between the two distribution peaks.

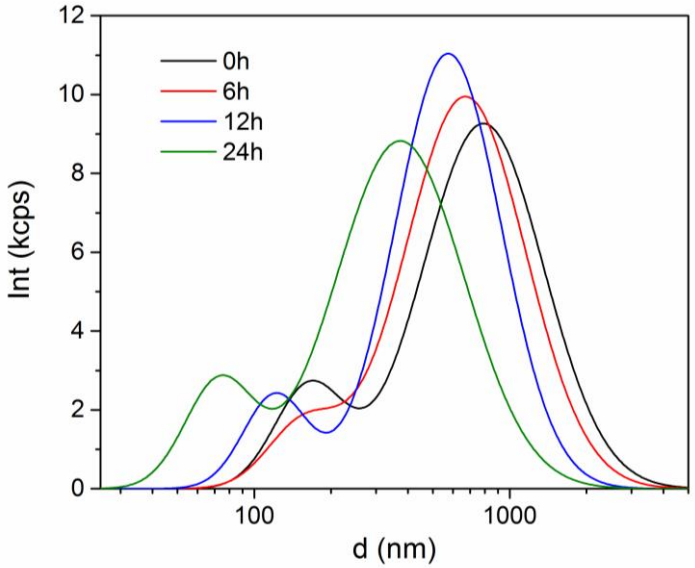

Figure 6.3. Particle size distribution of mixed reagents milled for different milling times. The particles dimensions axis is expressed in logarithmic scale.

The mechanical treatment produces a progressive decrease in the average particle size. The un-milled sample (black line) has two maxima at 1060 nm and 181 nm. After 6 hours of ball milling (red line) the sample presents a sub-micron particle size at 900 nm and 164 nm. The sample milled for 12 hours (blue line) has two peaks at 721 nm and 131 nm while the 24 hours milled sample (green line) reveals a further decrease of the particles with two maxima at 521 nm and 80 nm. The morphologies of the starting powders have been observed by means of scanning electron microscope.

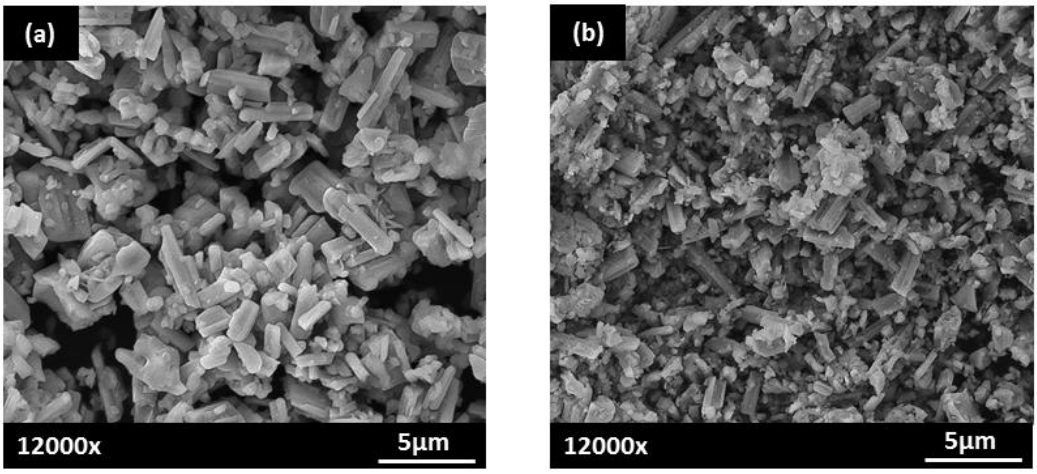

Figure 6.4. SEM picture of starting powders milled for **(a)** 0h BM and **(b)** 24h BM.

For representative purpose, in **Figure 6.4** are shown the two extreme cases (0h BM and 24h BM). The mechanical milling strongly reduces the particle dimensions from micrometric order down to manometer size (**Figure 6.4b**). Most probably, large particles (> 3µm) visible at microscope were not detected with DLS technique due to its instrumental limit. It is noticeable that the shape of the particles remains the same even after a prolonged mechanical treatment. It is well known that the milling process increases the reactivity of the starting powders.**[4]** The loss of the crystalline structure produced by the distortion and accumulation of defects is the driving force that cause the decrease of the activation barrier for the reaction. For this reason, the mechanochemically activated precursors have a lower calcination temperature than the non-activated counterpart. **Figure 6.5** shown the thermogravimetric curves of the samples where this effect is clearly highlighted. The experiments were made from room temperature up to 1000°C using a heating rate of 5°C/min and a cooling rate of 30°C/min. Considering first the thermogravimetric pattern of the un-milled sample (**Figure 6.5a**), the first weight loss of ~ 1.5 %, is due to the removal of adsorbed water. The second thermal event is located between 510°C and 840°C and involves a major relative weight loss of 10.5 %, which is due to the decompositions of the alkali carbonates.

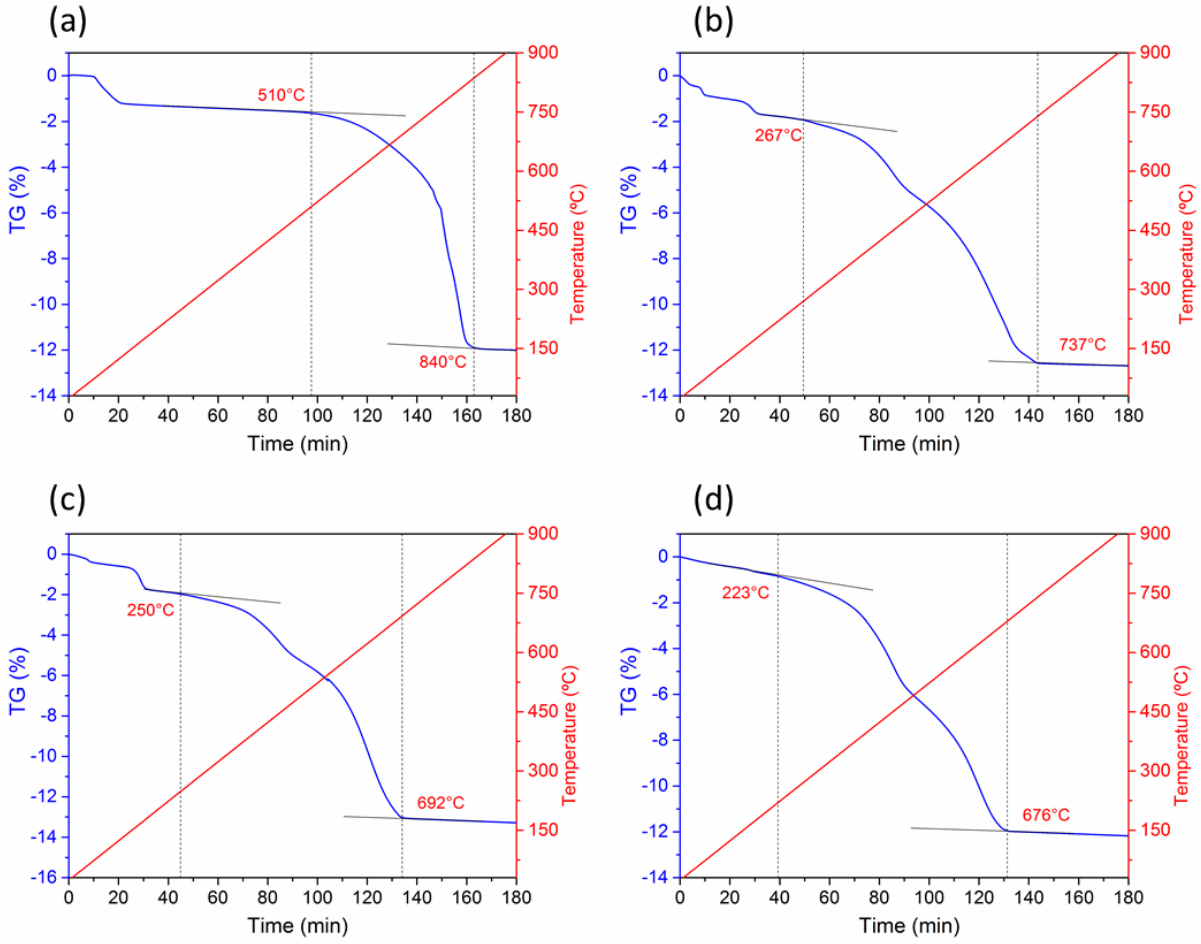

Figure 6.5. Thermogravimetric experiments of **(a)** 0h BM, **(b)** 6h BM,**(c)** 12h BM and **(d)** 24h BM. The onset of each thermal phenomena was detected as a deviation from the linear trend of the thermogram.

After 160 minutes (840°C) no other thermal phenomena were observed and most probably the reaction has been completed. The thermograms of the milled samples are reported in **Figure 6.5b-d**. In this case, the decomposition of the carbonates seems to be divided into two steps and they take place at much lower temperatures. This observation agrees with what seen previously for pure KNN system (**Figure 5.4**), however compared to the previous case, the reactivity of the powders is much lower, and this further confirm the role of the crystallite size in the evaluation of the reactivity of the powders. The decomposition of carbonates in the 6 hours milled sample (**Figure 6.5b**) starts at 270°C

and ends at 737°C after 144 minutes. In the 12 hours milled sample (**Figure 6.5c**), the same phenomenon occurs between 250°C and 692°C and the reaction is completed thereafter 134 minutes. In the 24 hours milled sample a further shift towards lower temperatures (223°C and 676°C) is observed. It is important to note that, for all the samples, the relative weight loss due to the decomposition of carbonates is around 11% and this suggests that the reaction was successful in each case. From an overall analysis it emerges that the most significant transformations take places between 0 and 6 hours of milling.

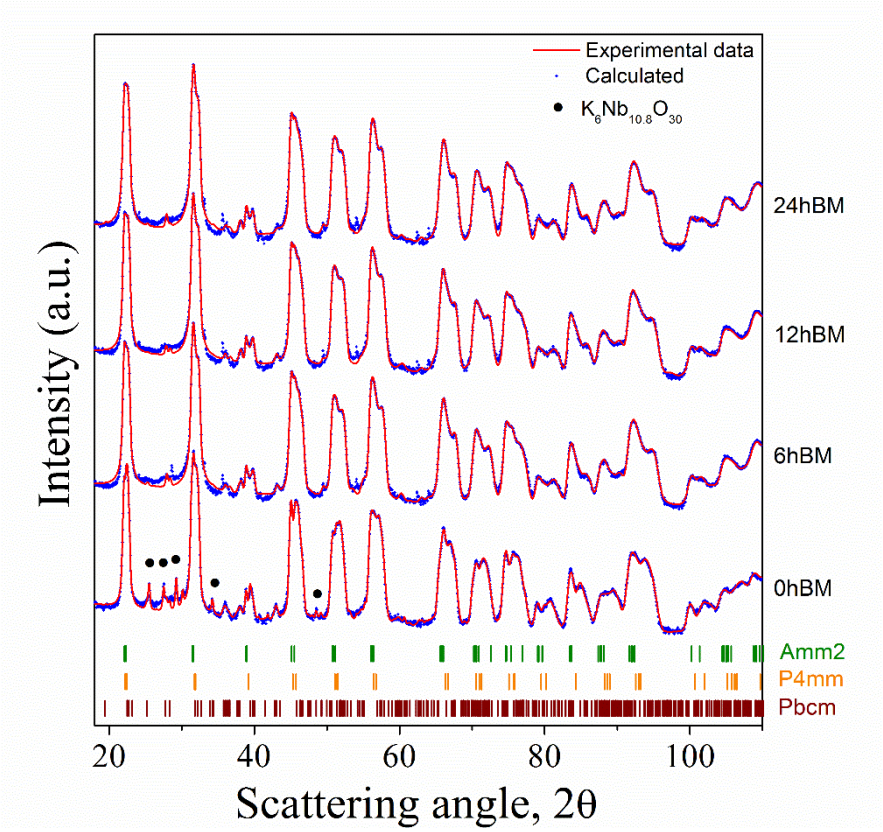

Figure 6.6. (a) XRD patterns of KNN-BF calcined powders obtained from different milling times.

A longer milling time significantly improves the reactivity of the powders (12h BM), however after 24 hours this improvement can be considered marginal. The powders from each milling batch were then calcined at 900 °C for 5 hours and the diffraction patterns are shown in the **Figure 6.6**. All the

samples have a crystalline structure characterized by a complex mixture of various niobates. The Rietveld refinement were performed using the orthorhombic Amm2 $KNbO_3$, the tetragonal P4mm $K_{0.3}Na_{0.7}NbO_3$ and the orthorhombic Pbcm $NaNbO_3$, according to our previous observation.**[5]** From a rapid spectrum analysis, it is possible to observe that the main differences can be found between the un-milled (0hBM) sample and the 6 hours milled sample. A further mechanical treatment (12 and 24h BM) does not seems to make noticeable differences. Considering first the un-milled sample (0h BM), the powders are composed of a mixture of orthorhombic Amm2, tetragonal P4mm and an orthorhombic Pbcm in a percentage by weight respectively of 42, 11 and 44%. The presence in trace (3 wt.%) of the tetragonal tungsten-bronze-type phase was also identified, which is no longer detected in the milled samples. The 6 hours milled sample is composed of the Amm2, P4mm and Pbcm in percentage by weight of 36, 40 and 24% respectively, whose composition is roughly the same also for the samples milled for longer milling times. **Table 6.1** summarize the quantitative information obtained from Rietveld analysis.

Table 6.1. Quantitative information about the phases that constitute the calcined KNN-BF powders obtained for different milling times. In the last column is reported the discrepancy index (R_{wp} %).

Sample/phases	Amm2 (wt.%)	P4mm (wt.%)	Pbcm (wt.%)	P4/mbm (wt.%)	R_{wp} (%)
0h BM	42	11	44	3	6.2
6h BM	36	40	24	--	5.7
12h BM	34	40	26	--	5.4
24h BM	38	40	22	--	5.9

From the XRD analysis it clearly emerges that the results of the calcination reaction are a complex mixture of niobates. However, the mechanical treatment causes a slight difference in terms of quantitative presence of the phases that constitute the mixture, which is roughly independent of the

milling time. First of all, the tetragonal tungsten-bronze type phase is no longer detected and this can be related to a better homogenization of the starting powders and to an increase of reactivity, as confirmed by the thermogravimetric experiments (**Figure 6.5**).

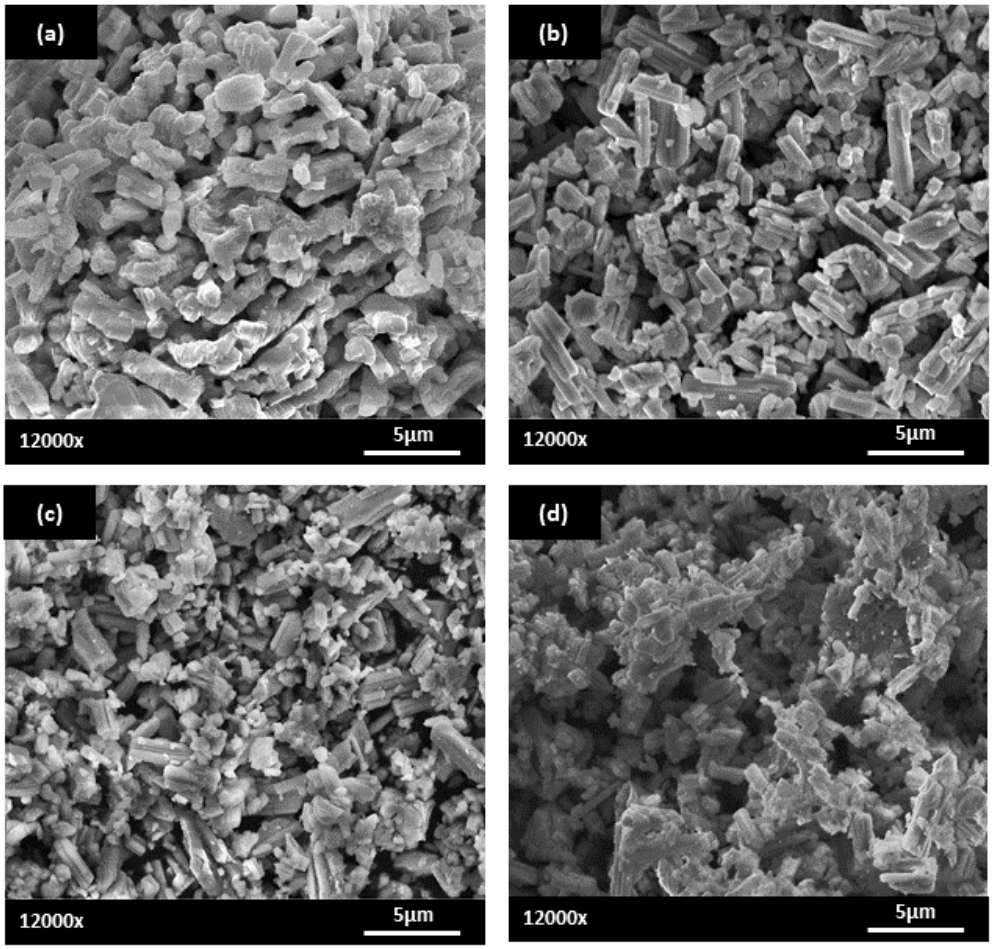

Figure 6.7. SEM picture of KNN-BF calcined at 900°C and prepared with different milling times: (a) 0h BM, (b) 6h BM, (c) 12h BM and (d) 24 hours.

Furthermore, the Pbcm phase seems to decrease from 30 to 22-26 wt.%. At the same time, the P4mm doubles its presence from ~ 21 to ~ 40 wt.% while the orthorhombic Amm2 phase undergoes to a slight decrease from 46 to 34-38 wt.%. No trace of Bi_2O_3, Fe_2O_3 or $BiFeO_3$ were detected in the sample analysed. It could be that iron and bismuth oxides are diffused within the crystalline structure

of the niobates or their amount is too low to be identified. Despite similar crystal structure, the calcined samples shown remarkable differences in terms of particle size **(Figure 6.7)**. The un-milled sample **(Figure 6.7a)** is characterized by large and coarse particles, while the milled sample **(Figure 6.7b-d)** have a finer and more homogeneous particle size, whose effect seems to be related to the milling time. Summarizing, the mechanical milling is beneficial for increasing the reactivity of the starting powders and obtaining a finer and homogeneous calcined product. This effect seems to be proportional to the milling time, at least in the range of times explored (0-24h). However, it is also important to keep in mind that a prolonged milling time increases the risk of iron contamination from the jar. Considering all the above results, we set this milling step at 12 hours.

The milling procedure following calcination is crucial to obtain dense ceramic with good electromechanical properties. For example, Cheng et al found that physical properties of KNN-based materials such as morphology of the bulk, phase structure, dielectric and ferroelectric properties were all affected by the particle size of the powders, which could be controlled by variation of ball milling time of the calcined powders.**[1]** Furthermore, the reduction of particle size it also determines a decrease of the sintering temperatures, and this is certainly an important aspect to take into consideration for those systems, such as KNN, which suffer of the high volatility of the A-site components during the sintering. For this reason, the calcined powders have been treated for different milling times (0, 6, 12 and 24 hours) and they have been analysed in their morphology, size and structure. In **Figure 6.8** are shown the distribution curves of KNN-BF calcined powders milled for different milling times. The particle size strongly decreases from micrometric order down to nanometer size. The un-milled KNN-BF shows an average particle size of ~ 1 μm. The sample milled for 6 hours presents submicron particle size of 748 nm; further increase of the milling time (12 and 24 hours) causes a slight decrease of the average particle size (621 and 631 nm respectively) however

the 24h BM sample has a wider distribution. In **Figure 6.9** are shown the SEM images of the particles milled for different times. The microscope images confirm what observed with the light scattering technique; however, some important additional information can be obtained. First of all, as previously seen, large particles of > 3 μm were not detected with DLS since the detention limit of the instrument is set at 3 μm, however their presence is clearly visible in **Figure 6.9a**. This means that, most probably, the average particle size is even higher compared to that measured with DLS. Furthermore, the sample milled for 24 hours presents very fine particulate together with large agglomerates of the order of few microns.

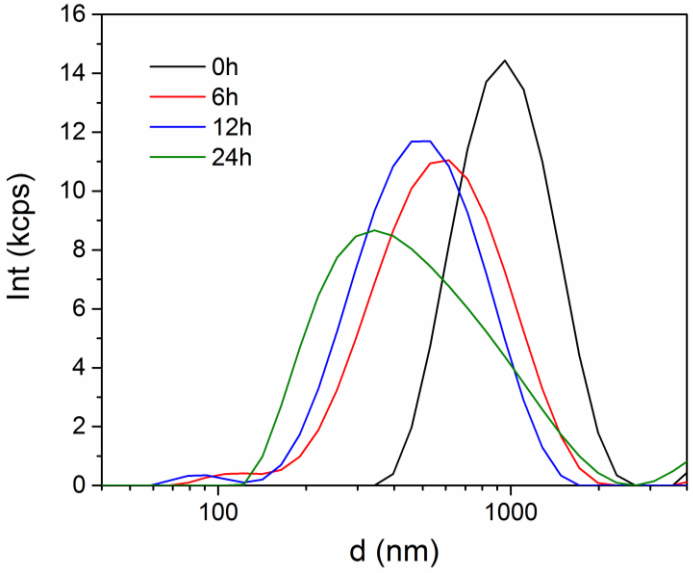

Figure 6.8. Particle size distribution of KNN-BF calcined powders milled for different milling times. The particles dimensions axis is expressed in logarithmic scale.

The homogeneity of the calcined powders plays an important role in affecting the grain growth and resultant grain size and density of the sintered pellet. Therefore, the presence of those large agglomerate together with small particle could be deleterious for the optimal densification process. Based on experimental observation, it seems that the particle size decreases up to 12 hours of milling. After that, as the milling time increases, the cold-welding mechanism predominates over the expected

fracturing mechanism. A schematic representation of this phenomenon is reported in **Figure 6.10**. The cold-welding is a well-known process that occurs to due to heavy plastic deformation experienced by the powders during the milling and happens especially if the material is ductile.**[3]** Generally, a Process Control Agent (PCA) is added to the powder mixture to reduce this mechanism. Despite the addition of ethanol as a PCA agent, the cold-welding mechanism was observed for long milling times. As reported by Suryanarayana**,** the time of milling is the most important parameter and it is chosen in order to achieve a steady state between the fracturing and the cold welding of the particles.

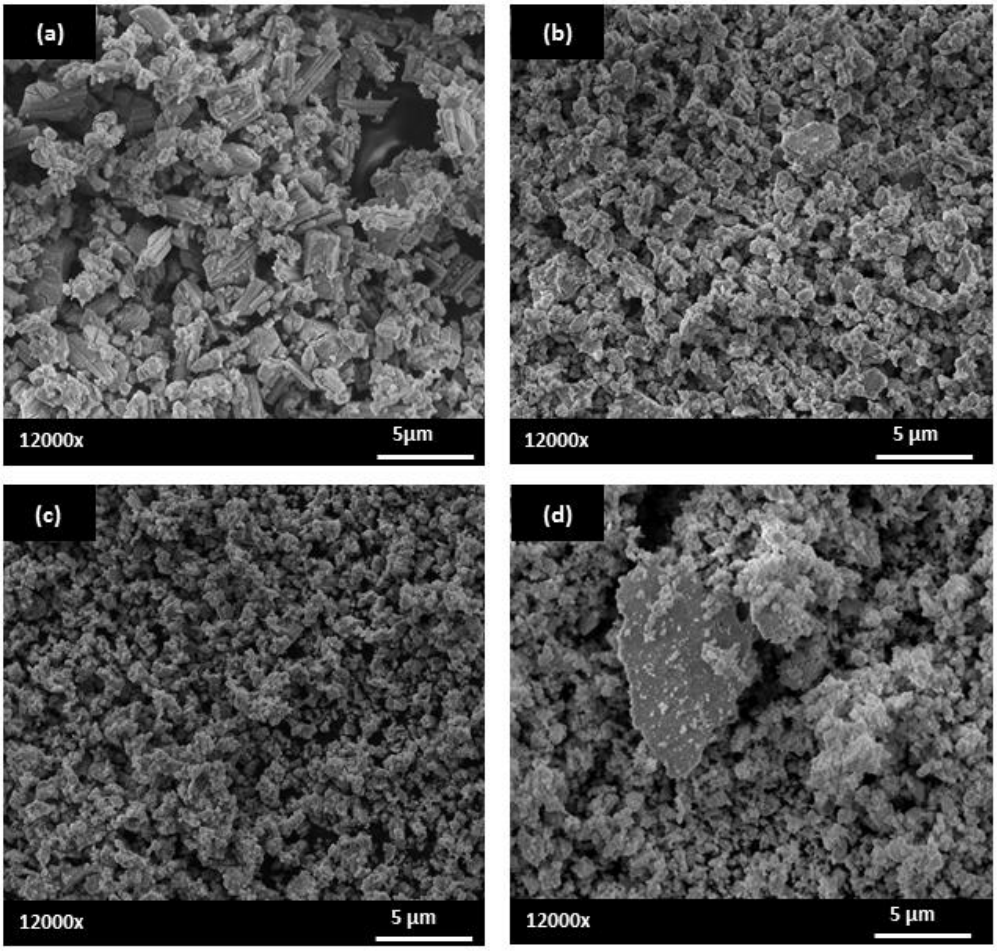

Figure 6.9. SEM picture of KNN-BF calcined powders milled for **(a)** 0h BM, **(b)** 6h BM, **(c)** 12h BM and **(d)** 24 hours. In the 24 hours ball milled sample can be seen the presence of large agglomerates.

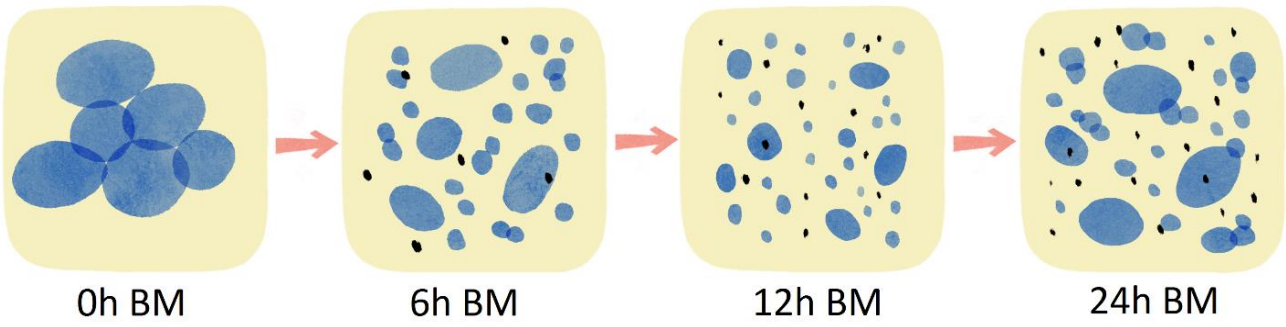

Figure 6.10. Schematic representation of the particle size evolution of calcined KNN-BF powders as a function of the ball milling time.

The required milling time depends on many variables including the type of milling, the intensity of milling, the ball-to-powders ratio and the temperature due to the heat that is released inside the jar. It also important to highlight that the danger of contamination inevitably increases together with the milling time. Therefore, it is preferable that the powders are milled for the necessary time and no longer. Considering the above results, it seems that 12 hours of milling are sufficient to obtain a homogeneous and small particle distribution.

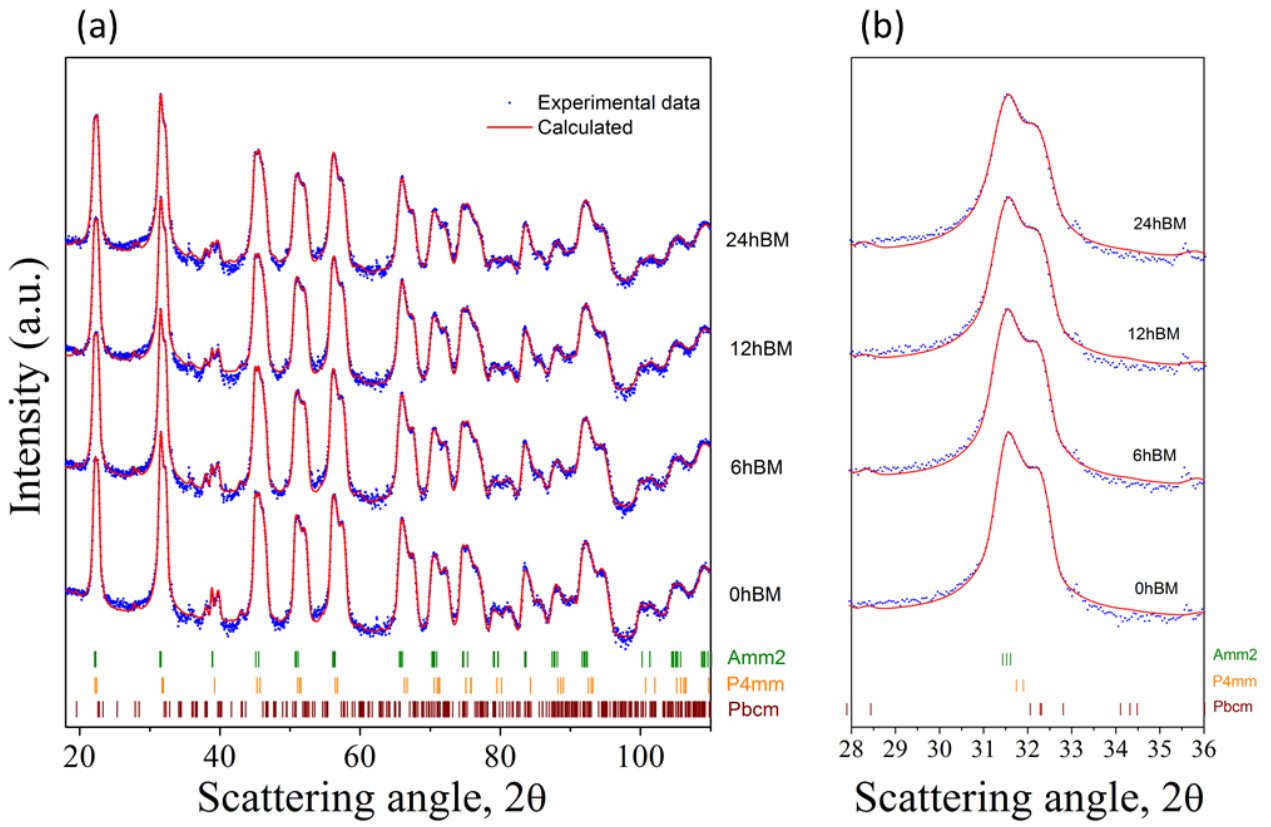

Figure 6.11. (a) XRD patterns of calcined KNN-BF milled for different milling times. (b) Magnification between 28° and 36°.

The crystal structure of the KNN-BF calcined samples was analysed as well and the results are shown in **Figure 6.11**. All the samples show a complex mixture of the same niobates previously seen. The percentage by weight of the Amm2, P4mm and Pbcm remains almost constant as the milling times increase (approximately 30, 40 and 30 wt.% respectively). The main differences concern the noticeable decrease in intensity of the diffraction peaks and the line broadening, as can be appreciate in detail in **Figure 6.11b**. These two effects are generally related and they depend on the mechanical deformation introduced into the powders that generates lattice strain and crystallite size in the nanometer range.

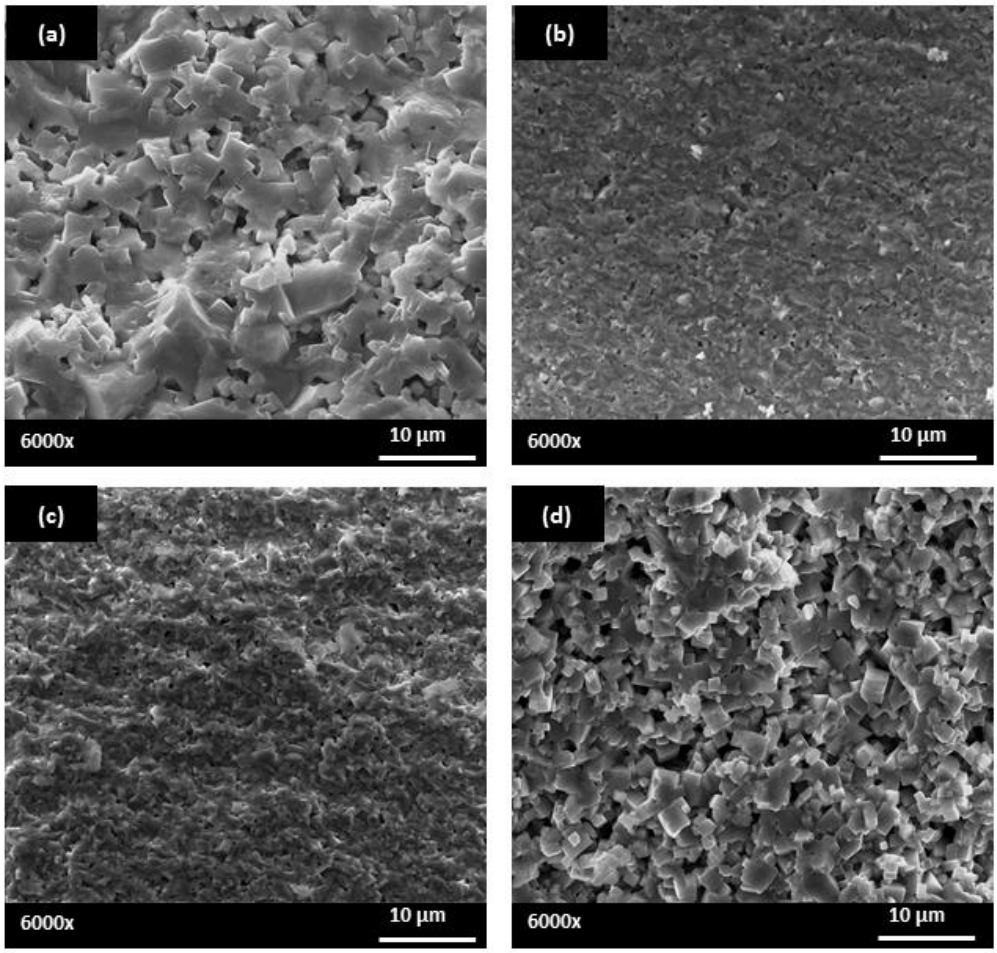

Figure 6.12. Fractured surface of KNN-BF pellets sintered at 1100°C prepared with different milling time. **(a)** 0h BM, **(b)** 6h BM, **(c)** 12h BM and **(d)** 24h BM.

However, the most interesting aspect concerns the effect of the milling on the densification process of KNN-BF ceramics. In **Figure 6.12** are shown the SEM images of the fractured surface of KNN-BF sintered pellets. The sintering temperature was kept fixed at 1100°C in order to evaluate any differences due to the milling process. The 6h and 12h milled samples **(Figure 6.12b-c)** have a dense microstructure characterized by fine grains and lower porosity compared to the un-milled sample which instead it has coarser particles and a high level of porosity **(Figure 6.12a)**. The 24 hours milled sample **(Figure 6.12d)** has a porous and inhomogeneous microstructure characterized by

predominant intergranular fracture. As expected, these microstructural differences lead to differences in terms of bulk density of the sintered ceramics (**Figure 6.13).**

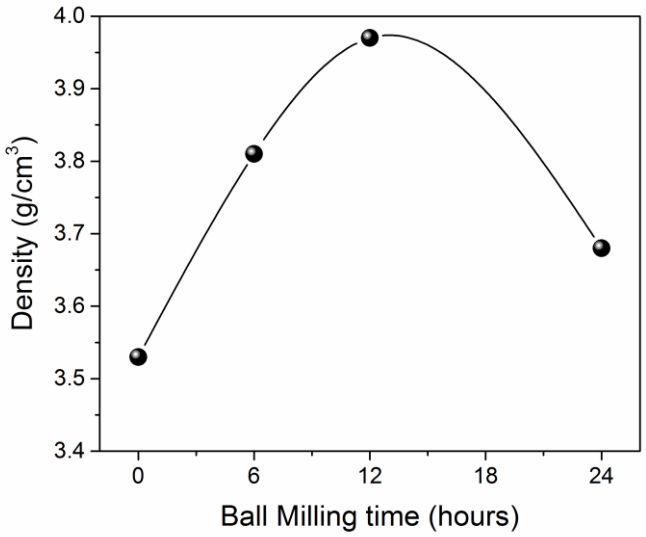

Figure 6.13. Geometric density Vs Ball Milling time of KNN-BF pellets prepared with different milling times.

With the increasing of the milling time, the density firstly increased from 3.53 g/cm^3 (0h BM) to 3.81 g/cm^3 (6h BM) until it reaches the optimum value of 3.97 g/cm^3 at 12 hours of milling. For longer milling time (24h BM) the density decreases to 3.61 g/cm^3. This different behaviour can be explained in terms of particle size and homogeneity of calcined KNN-BF powders after the milling process. It is widely accepted that reduced particle sizes provided larger driving forces for sintering. For instance, Zuo et al. found that the increasing of the attrition milling time up to 48 hours strongly decreases the mean particle size of the calcined KNN product from ~ 230 nm (6h BM) to ~70 nm.**[6]** This also determines a clear improvement in terms of densification of the material; the samples made from 48h attrition-milled powder reached a density of 98.5% TD at 1100°C, while the sample milled for just 6 hours and sintered at the same temperature shows lower density of ~ 95% of TD. In addition,

it is also necessary to consider the particle distribution. In general, a wide particle size distribution leads to higher density of the green pellet due to the gap filling ability of fine particles.**[7]** This promotes the sintering and the grain growth at the early stage of the process as the average coordination number of the particles increases. However, a broad particle size distribution may cause the sintering behaviour of the compact to deteriorate due to the low-sintering characteristic of the coarser particles. This usually lead to obtain large pores and size segregation both at macroscopic and microscopic level. These general observations, valid in principle for all ceramics, manage to explain very well the sintering behaviour that has been observed for this KNN-BF system. Considering the experimental evidence and the results obtained, we have set this milling step at 12 hours.

Summarizing, this preliminary work highlighted the effect of mechanical milling on the manufacturing process of a complex composition such as KNN-BF. Particular attention was paid to the pre- and post-calcination step. Milling for increasing milling times of the reaction mixture decrease the particle size, increase the reactivity and lowers the calcination temperature. The effect of milling is not very relevant for prolonged milling times (24 hours) therefore we set this milling step at 12 hours of milling, which represents a good compromise between the duration of the mechanical treatment and the increase in reactivity of the powders. The subsequent milling step (post-calcination) has an influence of density and microstructure of KNN-BF sintered pellets. Long milling times (24 hours) determines the formation of aggregates and widens the particle distribution, worsening the density and the microstructure, which instead is optimized for 12 hours of milling. However, the final density of the sintered product (3.97 g/cm^3; 88% of TD) prepared with 12 hours of milling is still low compared to the typical values commonly reported in literature (> 95% of TD).**[8]** Therefore, an accurate study is also necessary on the sintering temperature of this system. The first part of the next section will be devoted on this.

6.3 Sintering study of KNN-BF + xCuO ceramics

The density of the as prepared KNN-BF+xCuO ceramics sintered at different sintering temperatures are shown in **Figure 6.14**. The experimental results show that the addition of copper oxide helps the densification process by lowering the minimum sintering temperature required to obtain a dense product (> 4 g/cm^3). The KNN-BF composition shows density value larger than 4 g/cm^3 for sintering temperature >1100°C while for the compositions modified with CuO this temperature is reduced at 1075°C and 1050°C for 0.5 and 1 wt.% of CuO respectively. This behaviour could be related to the liquid-phase sintering (LPS) due to the addition CuO.**[9]** However, in all the three compositions, the maximum density reached a value close to 4.30 g/cm^3, which correspond to 95% of the theoretical density of KNN (4.51 g/cm^3). KNN-BF shows a maximum density of 4.34 g/cm^3 at 1150°C, which is very similar to the value of 4.32 g/cm^3 obtained at 1125°C. KNN-BF+0.5CuO has a maximum density of 4.30 g/cm^3 at 1125 °C while KNN-BF+CuO shows the highest density of 4.36 g/cm^3 at 1100°C. The experimental density measurements are consistent with the SEM observations of the fractured surfaces of the samples **(Figure 6.15)** which show a reduction in porosity and better welding of the grains as a function of the sintering temperature.

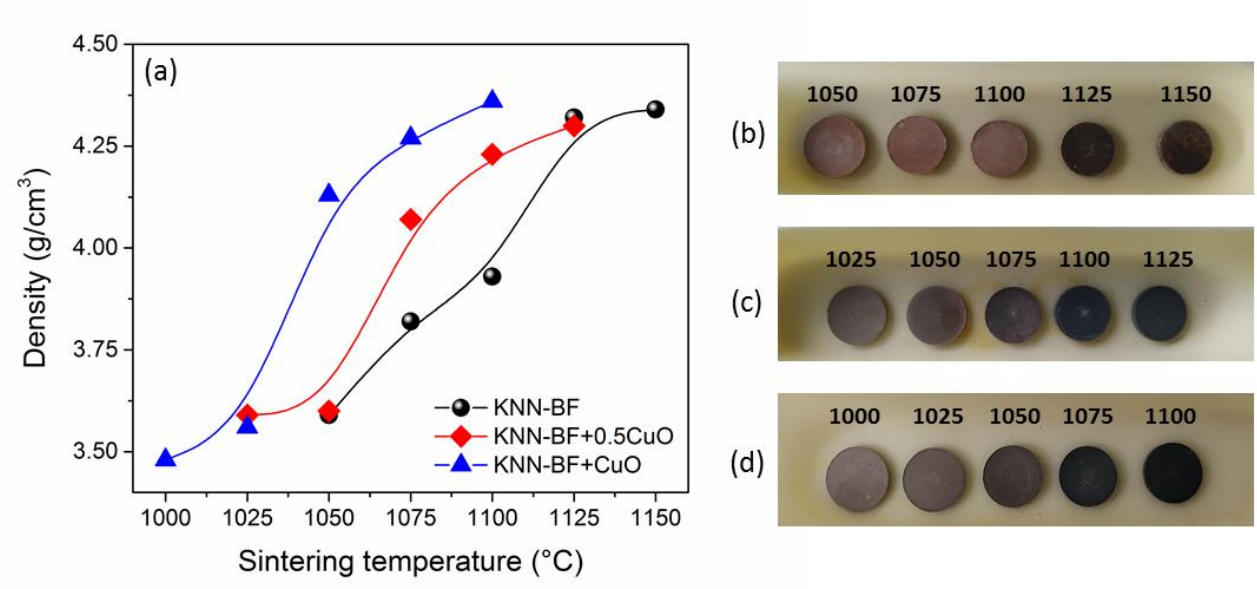

Figure 6.14. (a) Density Vs sintering temperature of KNN-BF+xCuO ceramics.(b-d) Photographs of KNN-BF+xCuO pellets sintered at different sintering temperatures: (b) KNN-BF, (c) KNN-BF+0.5CuO and (d) KNN-BF+CuO. Labels over the pellets indicate the sintering temperatures.

In **Figure 6.14(b)-(d)** the micrographs of the KNN-BF+xCuO pellets are shown. The densification process is accompanied by a change of the colour of the samples. Low density samples show light-brown colour which gradually becomes darker as the sintering temperature and density increases.**[10]** The KNN-BF 1150°C partially melted with the alumina crucible (**Figure 6.14b**), which is probably due to the high sintering temperature, pretty close to the solidus temperature of stoichiometric KNN.**[11]**

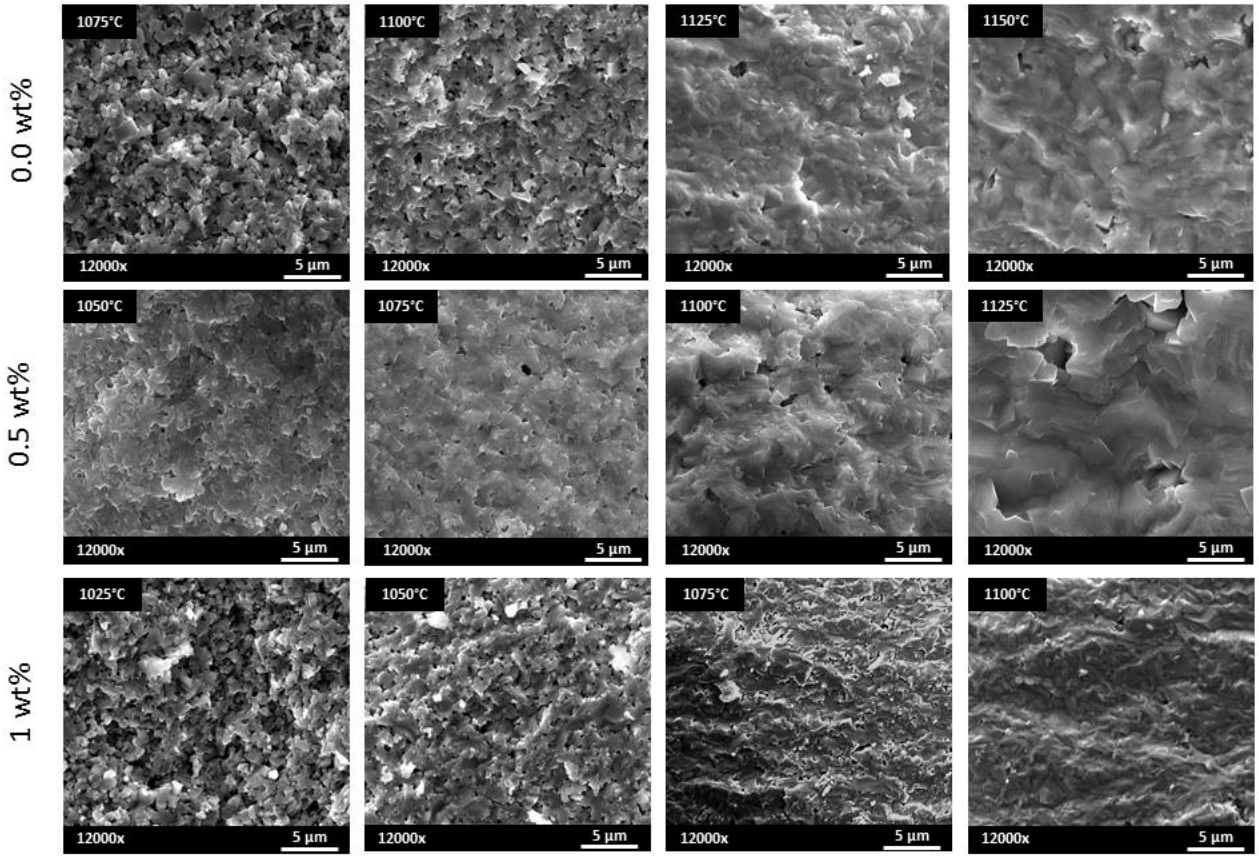

Figure 6.15. SEM images of fractured surface of KNN-BF+xCuO sintered at different sintering temperatures.

6.4 XRD study of KNN-BF+xCuO sintered pellet

The evolution of the crystalline structure of KNN-BF+xCuO as a function of the sintering temperature has been investigated with XRD. The Rietveld refinement were performed using as a starting model the correspondent orthorhombic Amm2, tetragonal P4mm and orthorhombic Pbcm CIF file phase structures. Considering first the KNN-BF composition (**Figure 6.16)**, the orthorhombic Pbcm progressively decreases as the sintering temperature increases until it disappears completely around 1150°C, while the orthorhombic Amm2 phase gradually becomes predominant. In particular, the KNN-BF 1050°C presents a percentage by weight of the orthorhombic Amm2, tetragonal P4mm

and orthorhombic Pbcm phases respectively of 39, 41 and 20% (**Table S1**); whose situation does not differ too much from the starting calcined product (**Table 1**), while the KNN-BF 1150°C shows the coexistence of just the orthorhombic Amm2 and tetragonal P4mm phases in percentage by weight of 70 and 30 % respectively.

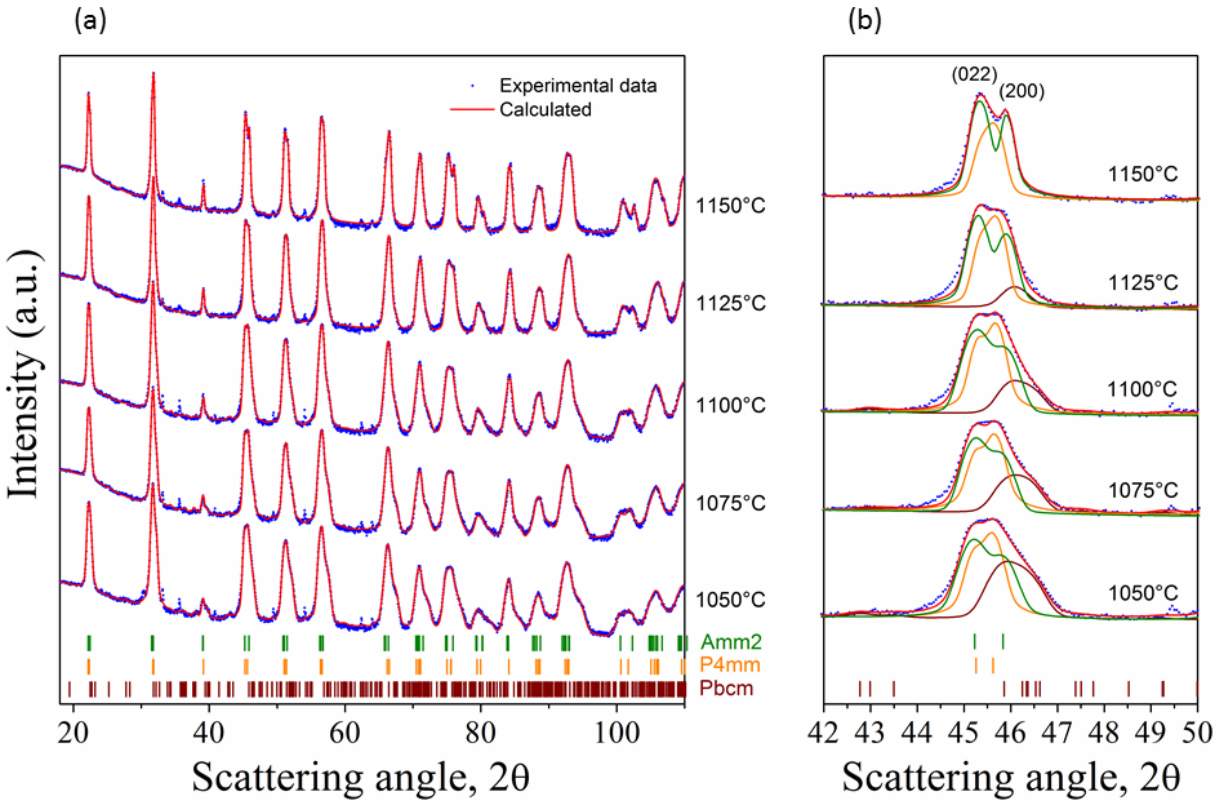

Figure 6.16. (a) XRD analysis and Rietveld refinement of KNN-BF Vs sintering temperature. (b) Magnification between 42 and 50° which shows the evolution of the phases as a function of the sintering temperature.

This transformation can also be evaluable from the progressive peak splitting around 46° **(Figure 6.16b)** and 104° which becomes more pronounced as the sintering temperature increases. According to Zhao et al., when the intensity of the (022) peak is more intense than the (200), then the orthorhombic Amm2 phase is prevalent.**[12]** This empirical approach can provide a good qualitative estimation of the phases that constitute the polymorphic phase boundary, however it cannot provide

structural information and quantitative evaluation as the Rietveld method does. Through an analysis of the cell parameters, it emerges that the Amm2 phase undergoes to a progressive decrease of the cell volume from 127.33 $Å^3$ for the KNN-BF 1050°C to 126.38 $Å^3$ of KNN-BF 1150°C, which is very close to the reference value of 126.42 $Å^3$ of the stoichiometric $K_{0.5}Na_{0.5}NbO_3$ (see **Table S6.1**).**[13]** This suggests that the Amm2 phase is progressively enriched of Na^+ ions at the expenses of the Pbcm phase. Also, the P4mm show a slight decrease of the cell volume from 63.36 $Å^3$ to 63.04 $Å^3$ along the studied temperatures; in any case, its presence at high sintering temperatures (>1100°C) suggests that BF has diffused into the KNN lattice, giving place to the orthorhombic and tetragonal symmetries coexistence, characteristic of the polymorphic phase boundary (PPB) composition.**[14]** From a comparison of the ionic radius, it is reasonable to expect that Bi^{3+} (103 pm) occupies the Na^+ (102 pm) and K^+ (138 pm) sites while Fe^{3+} (64.5 pm) occupies the Nb^{5+} (64 pm) sites. Therefore, the insertion of bismuth and iron ions inside the KNN matrix will produce defect dipoles. These defects generate polar nanoregion (PNRs) which are responsible of the frequency dependence of the dielectric permittivity vs. temperature curves, characteristic of the relaxor ferroelectric materials. This effect is related to the number of defects present in the crystal which depend on the amount of dopant added.**[15]** The presence of extra phases is negligible but the tungsten-bronze type phase, which is an undesired secondary phase frequently reported for KNN ceramics, is not detected.**[13]** The XRD patterns of KNN-BF modified with CuO are shown in **Figure 6.17** and **Figure 6.18**. Both compositions show similar behaviour to KNN-BF in terms of phase evolution (see **Table S6.2** and **S6.3** in the appendix at the end of the chapter). The orthorhombic Amm2 phase of KNN-BF+0.5CuO gradually becomes predominant and, at the same time, undergoes to a decrease of the cell volume from 127.21 $Å^3$ to 126.65 $Å^3$ in the sintering range between 1025 and 1125°C. The volume of the tetragonal P4mm phase decreases as well from 63.34 $Å^3$ to 63.06 $Å^3$, while the antiferroelectric Pbcm phase disappear completely at 1125°C.

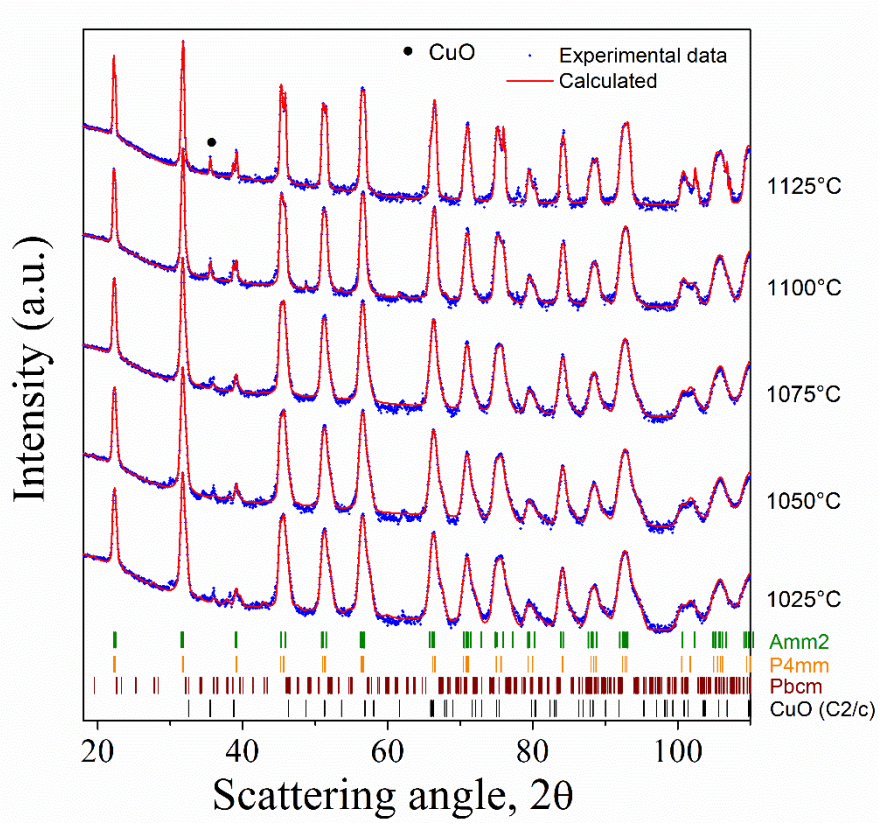

Figure 6.17. XRD patterns Vs sintering temperature of KNN-BF+0.5CuO.

The KNN-BF+CuO exhibit similar behaviour, however this effect is less pronounced since a lower sintering temperature range has been explored on this composition. KNN-BF+CuO sintered at 1000°C presents a percentage by weight of the Amm2, P4mm and Pbcm phases respectively of 37, 45 and 18%; while the sample sintered at 1100°C only shows a slight increase of the Amm2 phase (45 wt.%) and a residue of the Pbcm phase remains (4 wt.%). Furthermore, in both compositions we observed the presence of the monoclinic C2/c phase of CuO for the samples sintered at high sintering temperatures. As suggested by Takao et al., the sintering aid effect comes from the liquid phase generation of CuO at around 1050°C.**[16]** In any case, the presence of the monoclinic C2/c phase both in the KNN–BF+0.5CuO and KNN–BF + CuO suggests that the solubility limit of CuO in the KNN–BF matrix is below 0.5 wt.%.

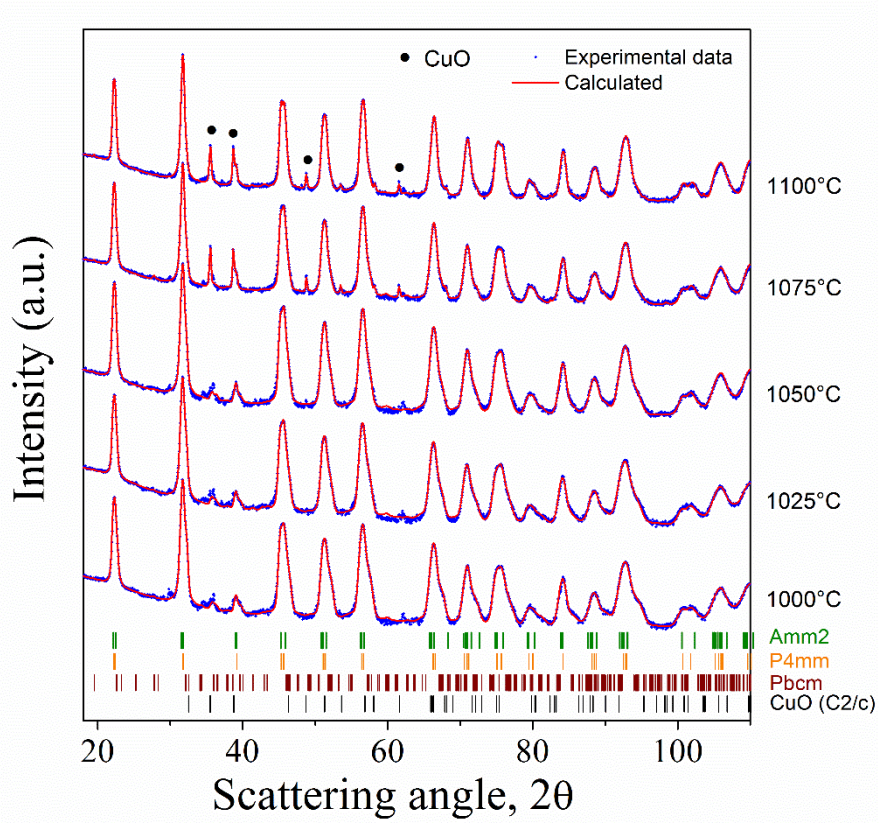

Figure 6.18. XRD patterns Vs sintering temperature of KNN-BF+CuO.

6.5 SEM/EDX characterisation

Based on the previous preliminary results, the three denser samples, one for each composition, were selected for the electromechanical characterisation which are the KNN-BF 1125°C, the KNN-BF+0.5CuO 1125°C and the KNN-BF+CuO 1100°C samples, respectively. The SEM micrograph of the as-sintered pellet surface and the fracture surface are shown in **Figure 6.19**. The fracture surface observation reveals a dense microstructure with predominant transgranular fracture, which is in good agreement with the high relative density measured experimentally (>95 %). Just some scattered porosity was detected in the KNN-BF+0.5CuO 1125°C sample (**Figure 6.19b**). The as-sintered surface morphology of the three samples reveals differences in terms of grain size; the KNN-BF

1125°C shows homogeneous and small grain size in the range of ~ 1 μm, while the KNN-BF+0.5CuO sintered at the same temperature presents larger grain size (~ 3 μm).

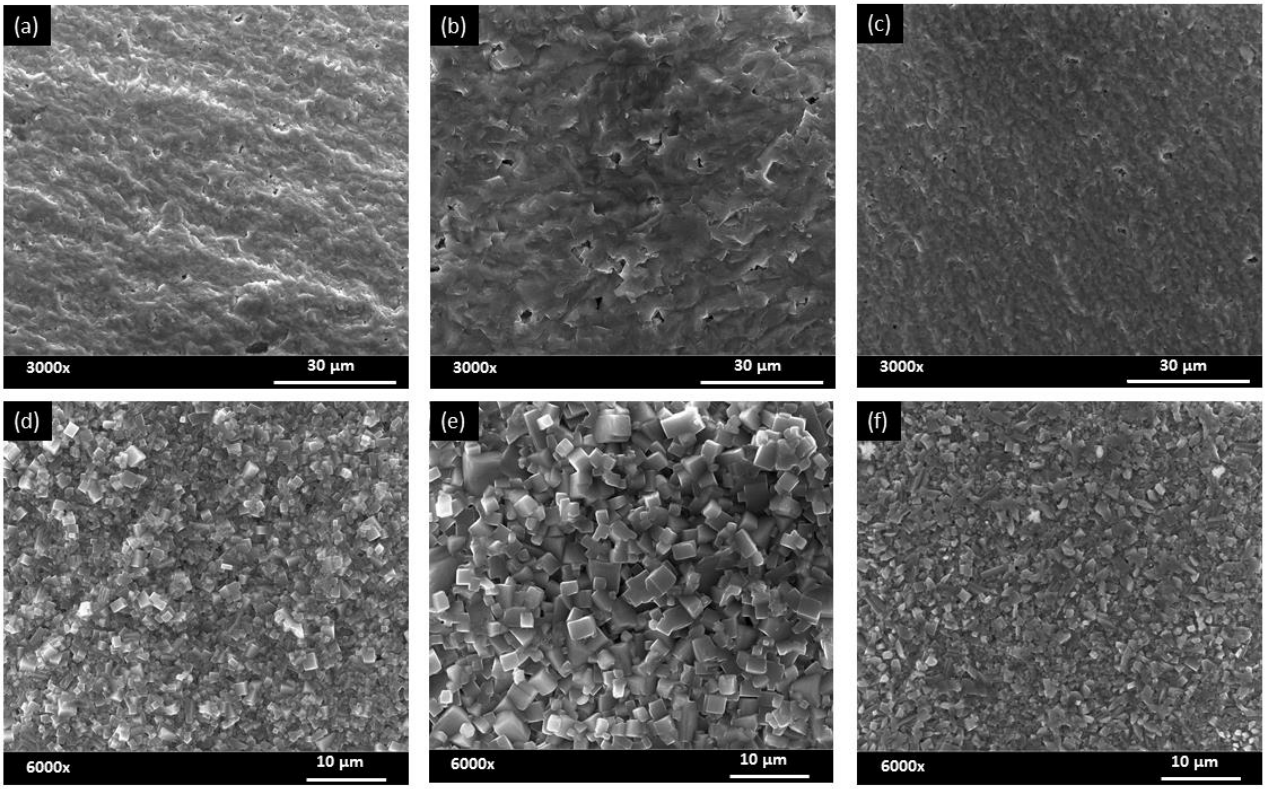

Figure 6.19. SEM micrographs of fractured surface (a-c) and pellet surface (d-f) of KNN-BF 1125°C (a,d), KNN-BF+0.5CuO 1125°C (b,e) and KNN-BF +CuO 1100°C (c,f).

This evidence is coherent with other works as the larger grain size is due to the liquid phase formation during sintering by the addition of the sintering aid.**[17]** However, in the case of KNN-BF+CuO the size of grains dramatically decreased (**Figure 6.19f**). This could be explained by the lower sintering temperature (1100°C) used for the sintering of this sample, but especially, it could be due to the excess of secondary phase at the surface which acts as a grain growth inhibitor in this case. As reported by Seo and co-workers, when the specimen contains large amount of liquid phase, the growth of grains is favoured at the early stage of sintering. Grains grow abnormally from the beginning and soon they collapse with each other, thereby preventing further grain growth and producing a fine-grained

microstructure.**[18]** The EDX spectroscopy performed on selected area of KNN-BF+0.5CuO and KNN-BF+CuO samples reveals a difference in terms of Cu concentration between the bulk and the pellet surface **(Figure 6.20)**. The pellet surface analysis show that Cu is present with a percentage by weight of 1.28 (0.64 at.%) and 4.06 (2.10 at.%) respectively for KNN-BF+0.5CuO and KNN-BF+CuO, which is consistent with XRD observation, while the bulk concentration of Cu is almost the same for both samples (~0.3 wt.%, 0.15 at.%). This evidence suggests that the solubility limit of CuO in KNN-BF systems is most probably around 0.3 wt.%, therefore any excess is expelled from the bulk. Moreover, a slight excess of Na has been observed for all samples (**Table S4**) which can be justified by the higher volatility of K.

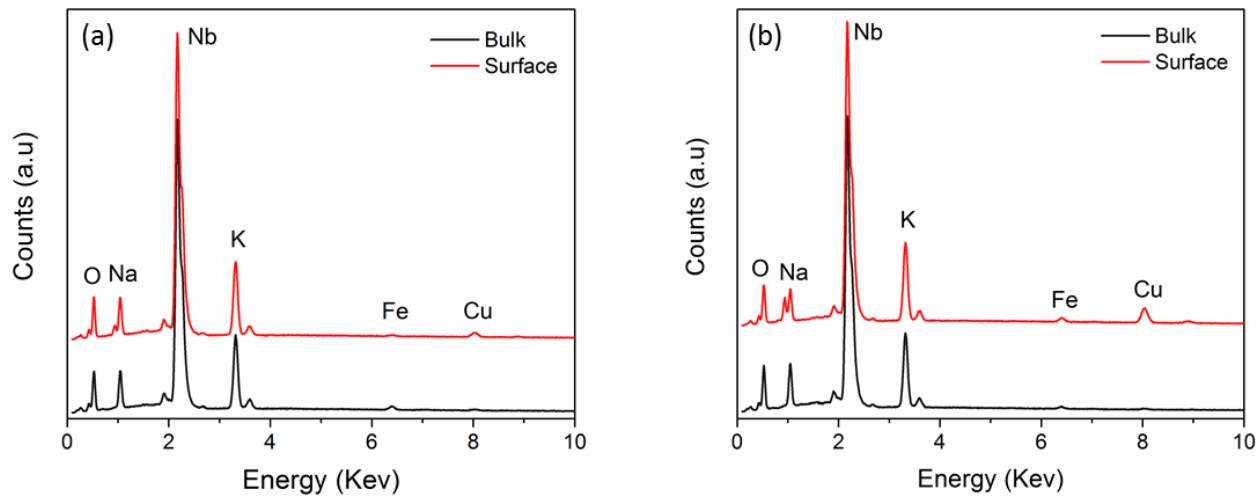

Figure 6.20. EDS spectra of pellet surface and bulk of (a) KNN-BF+0.5CuO and (b) KNN-BF+CuO. Note that bismuth is difficult to identify as its signals are overlapped with those of niobium.

6.6 Poling study, electric and dielectric characterisation

Figure 6.21 reports the current representation of the complex impedance (/Z/, red curves; θ, blue curves) at the fundamental radial mode of the above mentioned dense ceramic thin disks as a function of the poling electric field. It is well known that for a lossless resonator, the phase angle

approaches 90° in the frequency range between the resonance (/Z/ minimum) and antiresonance (/Z/ maximum).**[9]** We can see that the KNN-BF and KNN-BF+0.5CuO show a high degree of poling with a phase angle close to 90° at 25 kV/cm, while the KNN-BF+CuO sample was more difficult to pole and provided much lower phase angle, close to 60°.

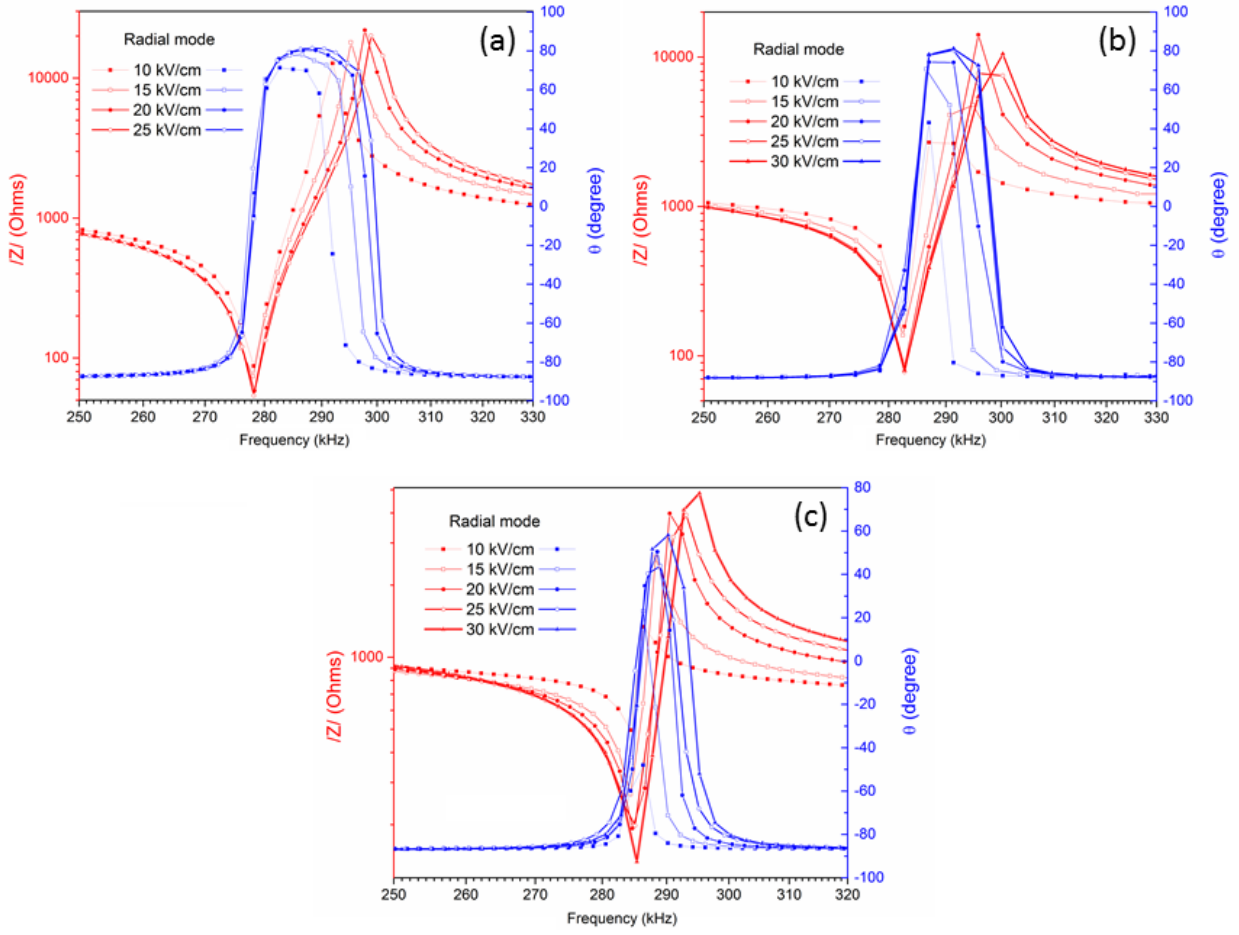

Figure 6.21. Modulus of impedance (red curve) and phase angle (blue curve) at Radial resonance as a function of the poling electric field of (a) KNN-BF 1125°C, (b) KNN-BF+0.5CuO 1125°C and KNN-BF+CuO 1100°C.

This observation is consistent with the evolution of the d_{33} piezo charge coefficient shown in **Figure 6.22**. The KNN-BF+CuO sample does not achieve d_{33} saturation at 30 kV/cm but keeps increasing with the increasing field as the impedance spectra (**Figure 6.21c**), while the KNN-BF and KNN-

BF+0.5CuO samples reach saturation at around 25 kV/cm. Also, the lower d_{33} for each applied field takes place for the KNN-BF+CuO sample. The piezoelectric response, thus, decrease as a function of the addition of CuO; the KNN-BF sample show d_{33} coefficient of 150 pC/N, while the KNN-BF+0.5CuO and KNN-BF+CuO have a maximum d_{33} coefficients of 125 and 105 pC/N, respectively.

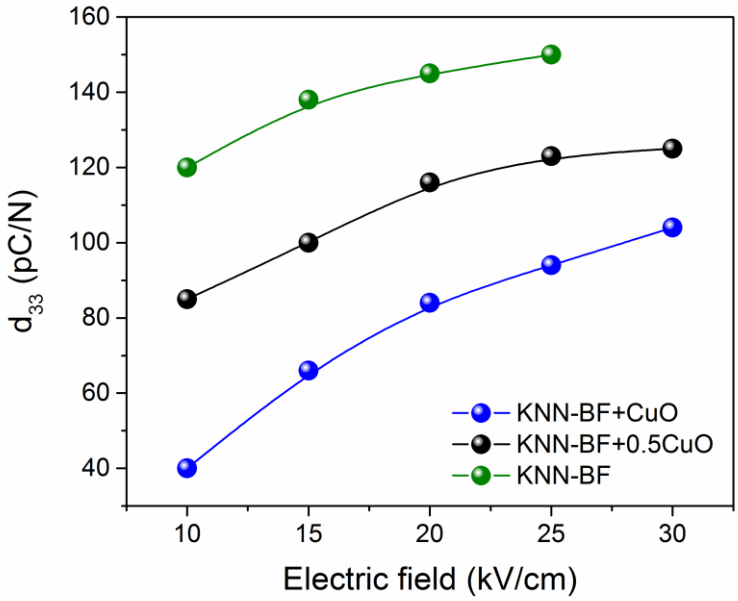

Figure 6.22. d_{33} Vs Electric field of KNN-BF+xCuO.

The determination of the piezoelectric, elastic and dielectric coefficients, their real part and losses, electromechanical coupling factor and frequency number, as well as the planar Poisson´s ratio, was also performed for each selected sample from their Radial mode (see **Figure 6.23**. The complete characterisation is reported in **Table S6.4)**. In **Figure 6.24** is reported the alternative representation of the complex impedance (Z*) at the fundamental Radial mode of resonance for the higher field applied at each sample. This consists of a plot of the peaks of the real part (R peak) of the complex impedance and the real part (G peak) of the complex admittance, the inverse of the impedance. According to Amarande et al., the calculation of the mechanical quality factor (Q_m) using the iterative

method of analysis of the impedance curve compared with standard methods is accurate for large variety of materials with a wide range of coupling factors and losses. It is expressed as the ratio between the real part and the imaginary part of the elastic constant C_{11}^{p}, as reported in the equation below (**Equation 6.1**).**[19]**

$$Q_m = \frac{C_{11}^{p\prime}}{C_{11}^{p\prime\prime}} \tag{6.1}$$

Where the single and double primes indicate respectively the real part and the imaginary part of C_{11}^{p}. Some relevant material coefficients obtained from the Radial mode are shown in **Table 6.2** together with the d_{33} coefficient.

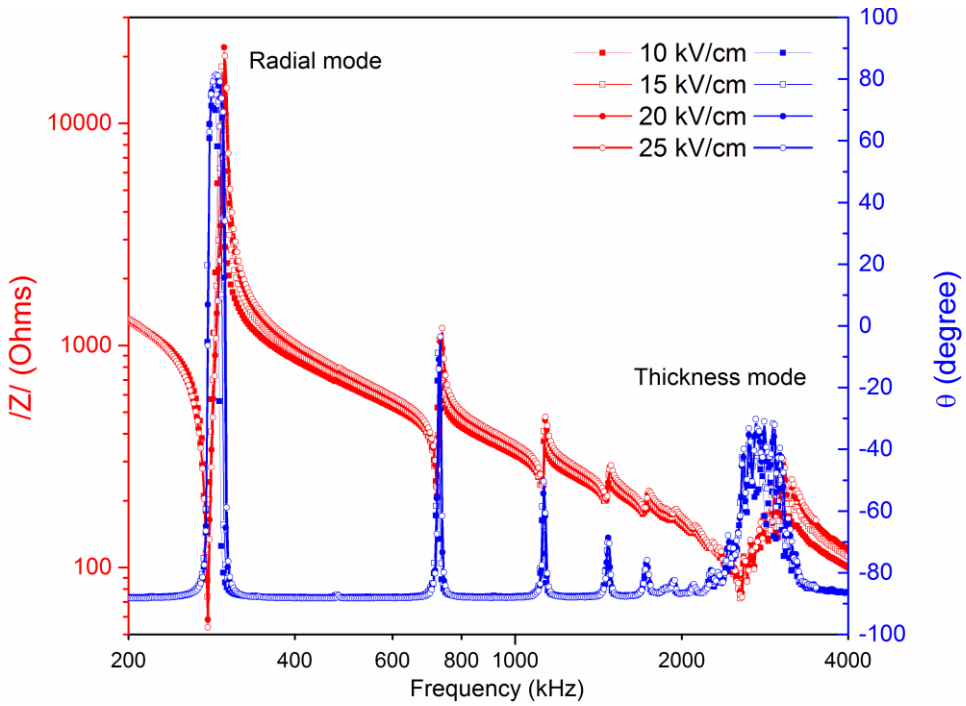

Figure 6.23. Impedance spectrum and phase angle between 200 kHz and 4MHz as a function of the poling electric field of KNN-BF 1125°C sample. In the selected frequency range are clearly visible the resonance (corresponding to /Z/ minimum) and anti-resonance (corresponding to /Z/ maximum) frequencies of the fundamental Radial mode, around 300 kHz, and its overtones, as well as for the Thickness mode, around 3MHz. The Thickness mode is overlaid with extra vibrational modes which disturb the signal.

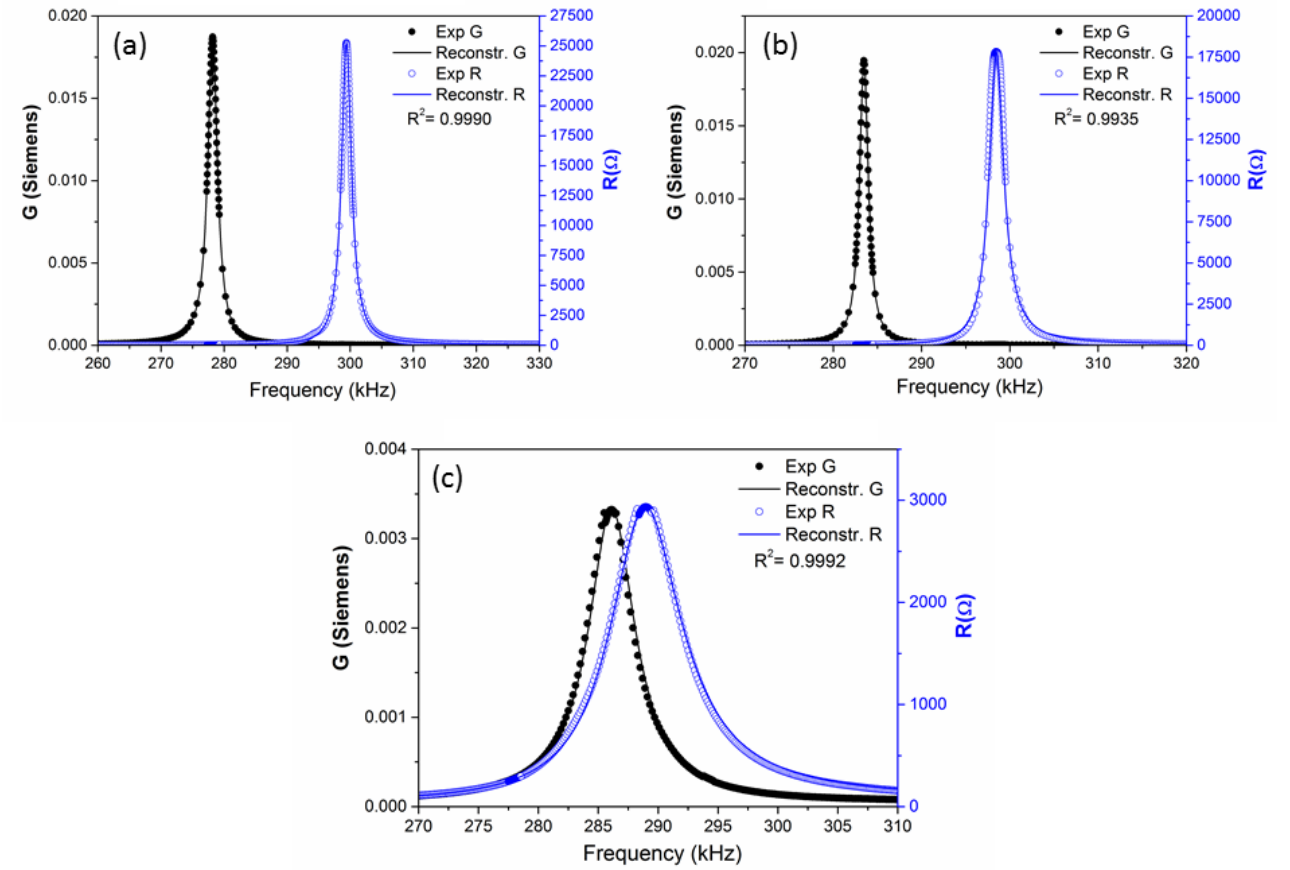

Figure 6.24 Representation of the complex impedance spectrum at the fundamental radial mode of resonance of a thin disk of (a) KNN-BF sintered at1125°C, (b) KNN-BF + 0.5CuO sintered at 1125°C and (c) KNN-BF+CuO sintered at 1100°C. The R and G plots were used for the iterative analysis. The symbols represent the experimental data and the lines the reconstructed peaks after material coefficients determination.

What clearly emerges from **Table 6.2** is that the KNN-BF shows the best piezoelectric response, i.e, higher piezoelectric coefficient (d_{33} = 150 pC/N; d_{31} = -56.84 pC/N) and higher coupling factors (k_p = 42% and k_{31} = 24%), however the KNN-BF+0.5CuO has better quality factors, both for the piezo coefficient ($Q(d_{31})$ = 207.35) and mechanical (Q_m = 235.52); furthermore this ceramic is more stiff, i.e, has higher elastic constant (C_{11}^{p} = 11.17).

Table 6.2. Some relevant material coefficients obtain from the radial mode characterisation of KNN-BF. +xCuO ceramics.

Properties /Sample	**KNN-BF**	**KNN-BF+0.5CuO**	**KNN-BF+CuO**
d_{33} (pC/N)	150	125	105
d_{31} (pC/N)	-56.84	-43.51	-38.47
$Q(d_{31})$	53.88	207.35	70.43
k_p (%)	42	35	26
k_{31} (%)	24	21	15
$\boldsymbol{\varepsilon_{33}^{T}}$	577.66	492.75	721.57
tanδ	0.028	0.029	0.049
$\mathbf{c_{11}^{p}}$ (10^{10}N m^{-2})	10.44	11.17	10.78
Q_m	149.79	235.52	60.31

Table 6.3. Comparison with some relevant KNN-based materials doped with ABO_3 and CuO based materials.

Sample	**d_{33} (pC/N)**	**k_p (%)**	$\boldsymbol{\varepsilon_{33}^{T}}$	**tanδ**	**Q_m**	**Ref**
KNN-BF	150	42	577.66	0.028	150	This work
KNN-BF + 0.5 wt% CuO	125	35	492.75	0.029	235	This work
KNSN + 1.5mol% CuO	150		525	0.011	206	**[23]**
KNLN-CZ + 0.5CTN	118	38	635	0.009	256	**[24]**
KNN-LS + 0.45 mol% CuO	175	46	551.23	0.014	41	**[25]**
KNN-LN + 1 mol% CuO	157	35	391		173	**[26]**
KNN-LNS + 0.8mol% CuO	207	44	340	0.0137	320	**[27]**

The KNN-BF+CuO shows a deterioration of the material coefficients but it possesses the higher dielectric permittivity at room temperature (ε_{33}^{T} = 721.57). In order to provide an insight into this behaviour, it is necessary to analyse the role of the CuO. Since the ionic radius of Cu^{2+} (73 pm) is close to the ionic radius of Nb^{5+} (64 pm), it is reasonable to expect that CuO could act as an acceptor dopant on KNN ceramics. Therefore, oxygen vacancies are created in order to compensate the charge unbalance. This phenomenon can be schematically described by the equation below (**Equation 6.2)**:**[20]**

$$2CuO \rightarrow 2Cu_{Nb}''' + 2O_O^X + 3V_O^{\circ\circ} \quad (6.2)$$

The creation of these defects leads to the formation of defect dipoles (P_d) made of positively charged O^{2-} vacancies and negatively charged Cu^{2+} which are preferentially oriented along the spontaneous polarization. The presence of these defect dipoles provides a restoring force which "pin" the motion of the ferroelectric dipoles. As a net result, this "pinning effect" provokes a ferroelectric "hardening" of the ceramic which is evidenced by the increase of the mechanical quality factors.**[21]** Among the samples examined, the KNN-BF+0.5CuO shows the highest Q_m and $Q(d_{31})$, which confirm the hardening effect as explained above; however, the sample with high content of CuO (1 wt.%) presents an obvious deterioration of the quality factors, both mechanical and electrical which is most probably due to inhomogeneity of the bulk composition and excess of the liquid phase, preventing saturation polarization.**[22]** Despite the good Q_m obtained for the KNN-BF+0.5CuO sample, the typical values reported for pure KNN modified with CuO are generally larger (Q_m > 500). Hu and co-workers have proposed an explanation for this behaviour. If Cu^{2+} is added together with another B-site atom (in this case Fe^{3+}) with ionic radius more similar to Nb^{5+}**,** then Cu^{2+} could occupy A-site as well; this leads to reducing the amount of oxygen vacancy, and thus reducing the hardening behaviour of the ceramics.**[23] Table 6.3** shows a comparison with some of the most relevant KNN-based materials

modified with ABO_3 and CuO.**[23-27]** The pure KNN-BF shows excellent values both in terms of piezoelectric response and Q_m, while the KNN-BF+0.5CuO composition, despite a slightly lower piezoelectric response, shows a relatively high Q_m, The temperature dependence of the dielectric permittivity and tanδ are shown in **Figure 6.25**. Experiments were performed from room temperature up to 500°C (heating ramp) on poled samples. The KNN-BF and KNN-BF+0.5CuO ceramics exhibit two well-defines anomalies.

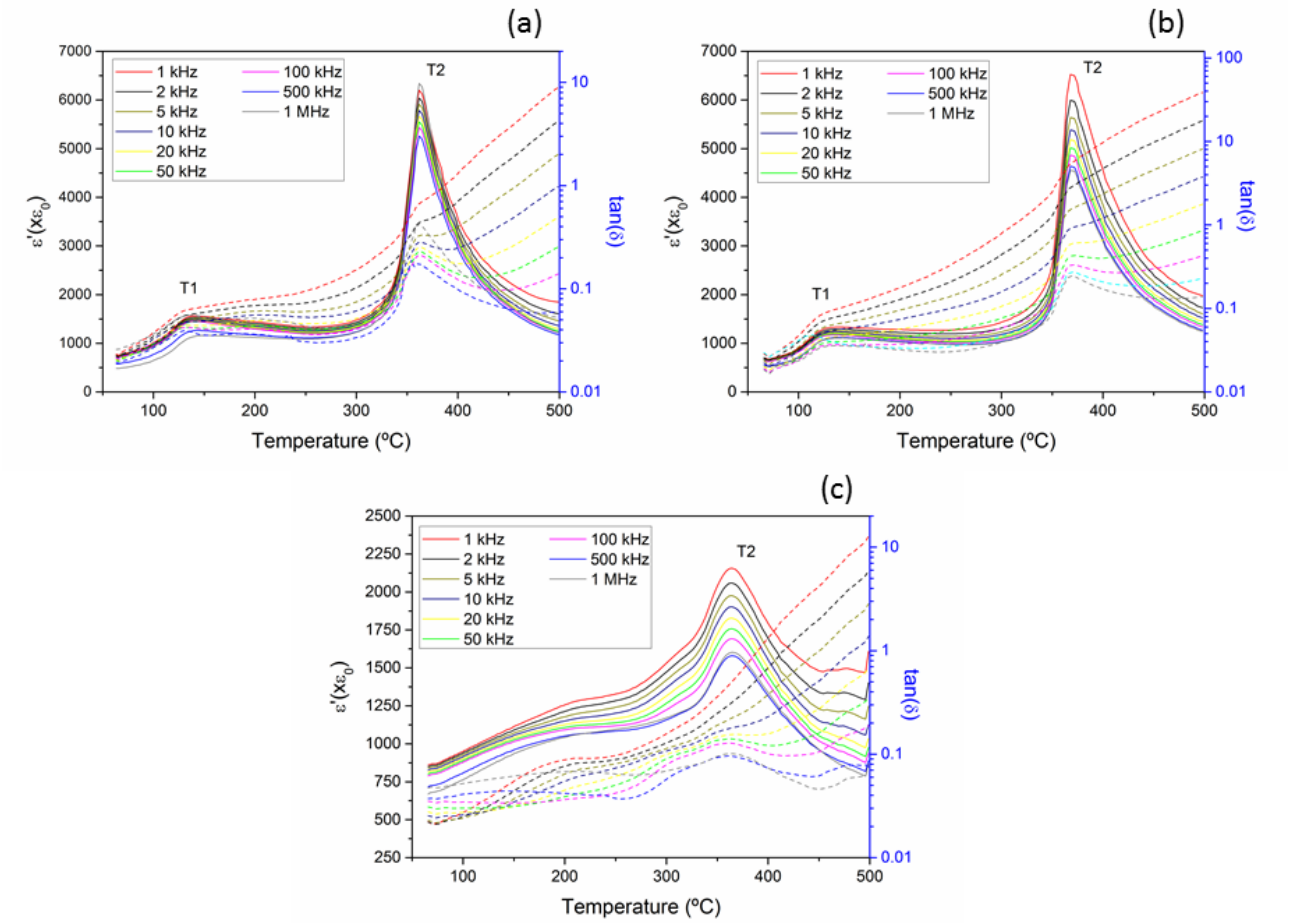

Figure 6.25 Dielectric permittivity vs. temperature of (a) KNN-BF, (b) KNN-BF+0.5CuO and (c) KNN-BF+CuO ceramics.

The low-temperature peaks correspond to the orthorhombic-tetragonal, ferroelectric-ferroelectric, phase transition (To-t), whereas the high temperature dielectric anomalies correspond to the

tetragonal-cubic, ferro- to para-electric, transition (T_c). For KNN-BF and KNN-BF+0.5CuO the first dielectric anomaly takes place around 130°C while the second is at 362 and 368°C respectively .In both cases, the transitions are shifted to lower temperature compared to pure KNN, which has the same dielectric anomalies at 195°C and 420°C.**[28]** Despite similar phase transition behaviour, the KNN-BF+0.5CuO shows much higher dielectric losses which could be related to the diffuse porosity observed with SEM investigation. The KNN-BF+CuO shows diffuse phase transition and strong frequency dependence, which suggest a relaxor behaviour of this sample. As a consequence, the orthorhombic-tetragonal phase transition is not well defined and the dielectric anomaly around the Curie point, which present a maximum at 364°C, is characterized by a very wide peak (**Figure 6.25c**). It is well known that the relative dielectric permittivity of ferroelectrics above the Curie temperature is governed by the Curie-Weiss law shown below (**Equation 6.3)**:**[29]**

$$\frac{1}{\varepsilon} = \frac{(T - T_0)}{C} \ (T > T_c) \tag{6.3}$$

Where ε is the permittivity, T_0 is the Curie Weiss temperature and C is the Curie Weiss constant. **Figure 6.26** shows the plots of inverse dielectric permittivity of KNN-BF+xCuO ceramics at 1 kHz versus temperature. The modified Curie-Weiss equation is proposed to describe the diffuseness of the phase transition (**Equation 6.4**):

$$\frac{1}{\varepsilon} - \frac{1}{\varepsilon_m} = \frac{(T - T_m)^\gamma}{C} \tag{6.4}$$

Where ε_m is the maximum value of the dielectric permittivity at the phase transition temperature T_m, C is the Curie-Weiss constant and γ ($1 \leq \gamma \leq 2$) is the degree of diffuseness. For normal ferroelectric material γ = 1; while for perfect relaxor γ = 2. Therefore, an intermediate behaviour between ferroelectric and relaxor is confirmed by an intermediate value of γ. The critical exponents γ, obtained by linear fit of the curves $\log(1/\varepsilon_r - 1/\varepsilon_m)$ versus $\log(T - T_m)$ where the γ coefficient represent

the slope of the curve are reported in **Figure 6.27**. All the sample shows a linear relationship above the Curie point. The results of the fitting parameters obtained from **Equation 6.3** and **6.4** are shown in **Table 6.4**. The KNN-BF sample shows γ = 1.20, while the KNN-BF+0.5CuO and KNN-BF+CuO have γ coefficients of 1.36 and 1.49 respectively. This means that the relaxor character increases with the addition of CuO, which provides crystal disorder.

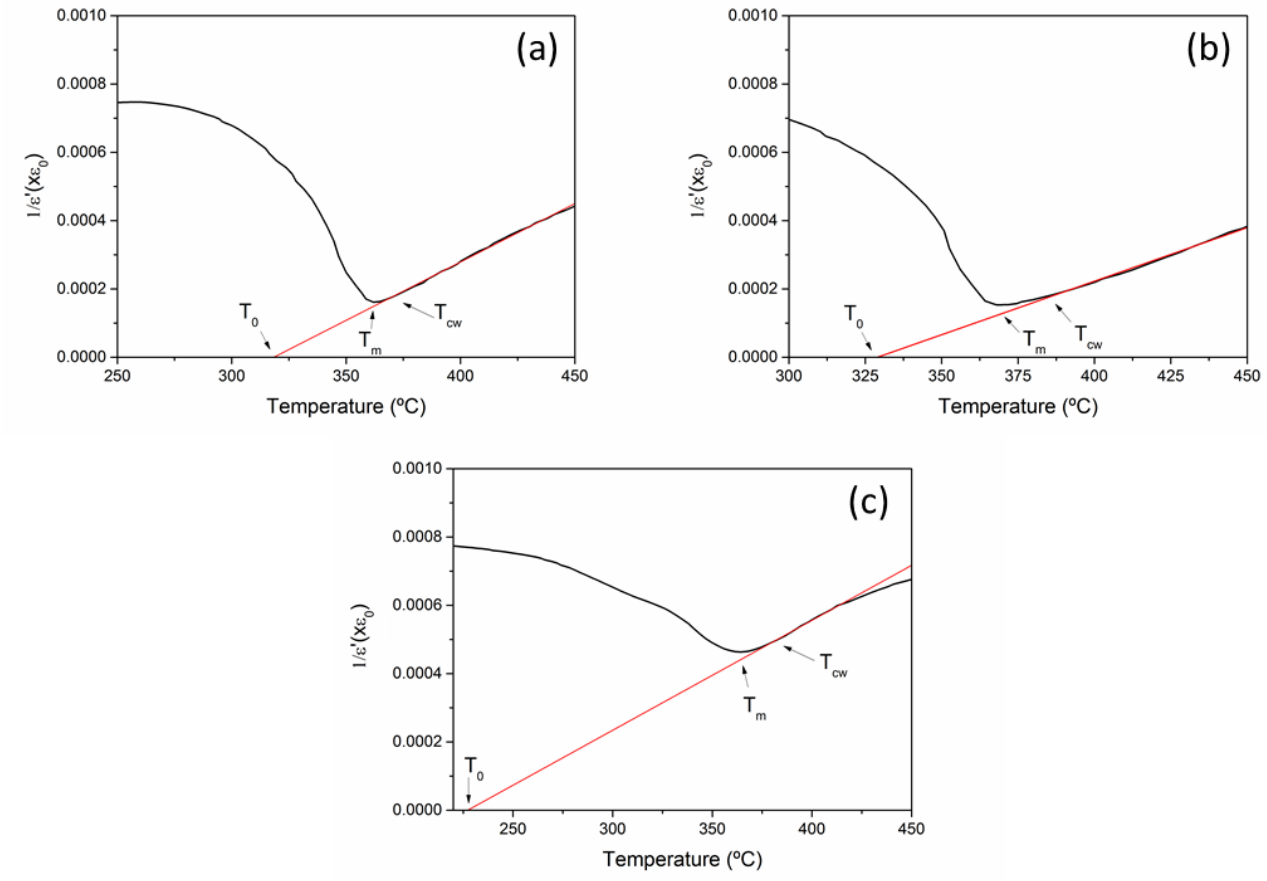

Figure 6.26. Inverse dielectric permittivity as a function of temperature at 1 kHz for (a) KNN-BF, (b) KNN-BF +0.5CuO and (c) KNN-BF+CuO.

As properly corroborated by the current literature, the relaxor state seems to be favoured by the grain size reduction, which contributes to enhance the local disorder.**[30]** This fact is consistent with the large diffusivity found in the sample with 1 wt.% of copper oxide; however, this does not explain

why γ increases with CuO. Most likely, this is due to semi conducting path in the ceramic caused by the addition of CuO. Dielectric relaxation behaviour due to conduction phenomena can be ascribable to the presence of oxygen vacancy generated by the introduction of Cu^{2+} into the crystal structure of the KNN.**[31]** The increase of crystalline defects should be the main reason for this behaviour. Moreover, copper oxide is a well-known semiconductor: its presence, confirmed by XRD investigation, determines a further increase of the ceramic conductivity.**[32]**

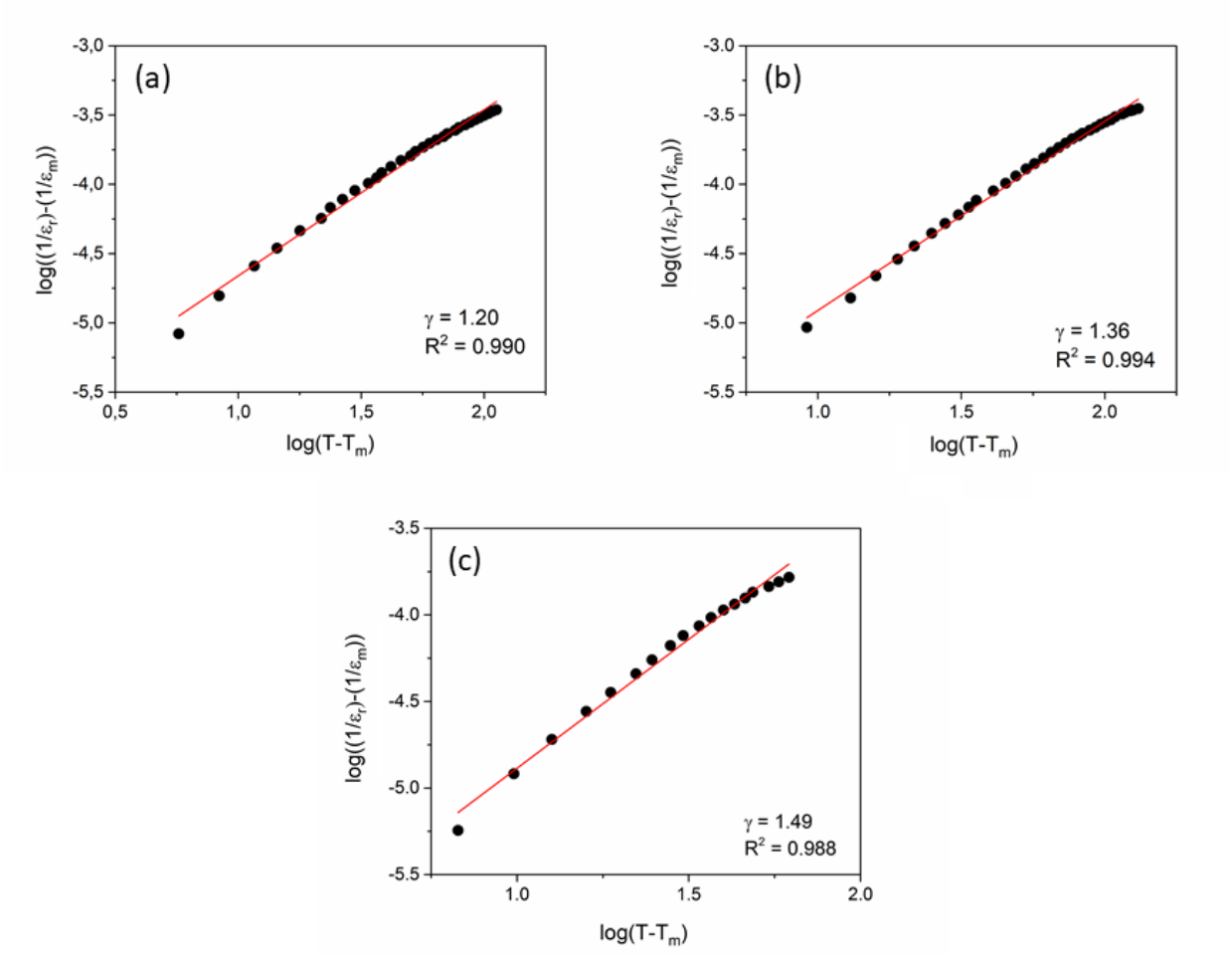

Figure 6.27. Plot of $\log(1/\varepsilon_r - 1/\varepsilon_m)$ *versus* $\log(T-T_m)$ for (a) KNN-BF, (b) KNN-BF+0.5CuO and (c) KNN-BF+CuO.

It is important to point out that also the unmodified KNN-BF has a certain degree of diffusivity (γ = 1.20). Pure KNN exhibits normal ferroelectric behaviour (γ ~1), therefore the diffusivity of KNN-BF

system should be attributed to crystal disorder generated by the introduction of iron and bismuth ions inside the KNN matrix.**[15]**

Table 6.4 Summary of fitting parameters for dielectric behaviour around the Curie point at 1 kHz for KNN-BF+xCuO ceramics.

Sample	**T_0 (°C)**	**T_{cw} (°C)**	**T_m**	**ΔT_m (°C)**	**γ**
KNN-BF	319	370	362	8	1.20
KNN-BF + 0.5 wt% CuO	329	385	369	16	1.36
KNN-BF + 1 wt% CuO	227	382	364	18	1.49

6.7 Conclusions

This work reports on the manufacturing process, microstructural and electrical properties of KNN-BF-xCuO (0, 0.5, 1 wt.%) ceramics. All the samples were prepared with the mechanically assisted (or mechano-activated) synthesis method followed by air sintering. The transient Pbcm phase decreases with the sintering temperature and is higher as the CuO content increases. The addition of CuO reduces the minimum sintering temperature required to obtain a relatively dense product (> 4 g/cm^3). All the three compositions show high density (> 95% of TD) at their optimized sintering temperature. SEM investigation reveals dense microstructure with predominant transgranular fracture. The addition of 0.5 wt.% of CuO determines an increase of the size of grains compared to undoped KNN-BF, however when CuO is added in excess (1 wt.%), a large amount of liquid phase is detected which acts as a grain growth inhibitor. The KNN-BF shows good electrical properties (d_{33} = 150 pC/N; k_p = 42%; ε_{33}^T = 577; Q_m = 150) attributable to the good microstructure achieved and to the coexistence of orthorhombic Amm2 and tetragonal P4mm symmetries characteristic of the PPB composition. The KNN-BF+0.5CuO sample shows an improvement of the quality factors, both

mechanical and electrical ($Q(d_{31}) = 207.35$; $Q_m = 235.52$) while maintaining good electromechanical properties ($d_{33} = 125$ pC/N; $k_p = 35\%$; $\varepsilon_{33}^{T} = 492$). Instead, the KNN-BF+CuO shows a deterioration of the electromechanical properties ($d_{33} = 105$ pC/N; $k_p = 26\%$; $Q_m = 60$) which is mainly attributable to the excess of liquid phase, fine-grained microstructure and crystal disorder that also cause frequency dependent dielectric permittivity vs. temperature and diffuse phase transitions.

6.8 Appendix

Table S6.1. Crystallographic information obtained from Rietveld refinement of KNN-BF sample sintered at different sintering temperature.

Sample	Phase (s.g)	a (Å)	b (Å)	c (Å)	V (Å^3)	Cryst. Size (Å)	r.m.s strain	wt. (%)	R_{wp} (%)
KNN-BF 1050	*Amm2*	3.9594	5.6632	5.6784	127.326	1204	$3.4*10^{-3}$	39	5.52
	P4mm	3.9767	3.9767	4.0071	63.364	1091	$2.3*10^{-3}$	41	
	Pbcm	5.6280	5.5654	15.6655	490.676	>2000	$5.1*10^{-3}$	20	
KNN-BF 1075	*Amm2*	3.9625	5.6539	5.6786	127.220	>2000	$3.9*10^{-3}$	44	6.07
	P4mm	3.9728	3.9728	4.0044	63.202	817	$1.9*10^{-3}$	44	
	Pbcm	5.5884	5.5824	15.6613	488.581	1429	$4.6*10^{-3}$	12	
KNN-BF 1100	*Amm2*	3.9558	5.6534	5.6723	126.854	>2000	$2.4*10^{-3}$	47	6.37
	P4mm	3.9708	3.9708	4.0000	63.069	1312	$1.9*10^{-3}$	46	
	Pbcm	5.5865	5.5697	15.6364	486.529	1226	$4.3*10^{-3}$	7	
KNN-BF 1125	*Amm2*	3.9526	5.6498	5.6689	126.594	>2000	$4.1*10^{-3}$	51	6.71
	P4mm	3.9702	3.9702	3.9939	62.953	>2000	$2.2*10^{-3}$	46	
	Pbcm	5.5674	5.5853	15.6994	488.182	744	$3.4*10^{-3}$	3	
KNN-BF 1150	*Amm2*	3.9513	5.6536	5.6574	126.381	>2000	$8.9*10^{-4}$	70	6.58
	P4mm	3.9728	3.9728	3.9941	63.039	>2000	$2.2*10^{-3}$	30	

Table S6.2. Crystallographic information obtained from Rietveld refinement of KNN-BF +0.5CuO sample sintered at different sintering temperature. The β angle of the monoclinic C2/c phase is 99.3°.

Sample	Phase (s.g)	a (Å)	b (Å)	c (Å)	V (Å^3)	Cryst. Size (Å)	r.m.s strain	wt. (%)	R_{wp} (%)
KNN-BF + 0.5CuO 1025	*Amm2*	3.9600	5.6572	5.6786	127.215	827	$3.9*10^{-3}$	38	7.67
	P4mm	3.9754	3.9754	4.0082	63.345	>2000	$2.8*10^{-3}$	44	
	Pbcm	5.5775	5.5869	15.7333	490.264	>2000	$5.5*10^{-3}$	18	
KNN-BF + 0.5CuO 1050	*Amm2*	3.9590	5.6587	5.6735	127.102	1230	$3.8*10^{-3}$	41	7.30
	P4mm	3.9739	3.9739	4.0059	63.261	1418	$2.4*10^{-3}$	46	
	Pbcm	5.5883	5.6010	15.6848	490.930	>2000	$5.8*10^{-3}$	13	
KNN-BF + 0.5CuO 1075	*Amm2*	3.9573	5.6610	5.6705	127.032	1966	$3.8*10^{-3}$	47	7.68
	P4mm	3.9741	3.9741	4.0023	63.210	1681	$2.2*10^{-3}$	44	
	Pbcm	5.5791	5.5827	15.8336	493.160	839	$5.4*10^{-3}$	9	
KNN-BF + 0.5CuO 1100	*Amm2*	3.9542	5.6550	5.6711	126.811	1987	$2.5*10^{-3}$	54	6.92
	P4mm	3.9737	3.9737	3.9965	63.109	>2000	$2.4*10^{-3}$	42	
	Pbcm	5.5625	5.5697	15.9329	493.624	587	$5.2*10^{-3}$	2	
	C2/c	4.7075	3.4185	5.1304	81.476	907	$6.1*10^{-4}$	2	
KNN-BF + 0.5CuO 1125	*Amm2*	3.9531	5.6563	5.6642	126.651	>2000	$5.6*10^{-3}$	64	8.40
	P4mm	3.9723	3.9723	3.9963	63.058	>2000	$2.3*10^{-3}$	34	
	C2/c	4.7045	3.4230	5.1279	81.492	974	$4.5*10^{-3}$	2	

Table S6.3. Crystallographic information obtained from Rietveld refinement of KNN-BF +CuO sample sintered at different sintering temperature. The β angle of the monoclinic C2/c phase is 99.3°.

Sample	**Phase (s.g)**	**a (Å)**	**b (Å)**	**c (Å)**	**V (Å^3)**	**Cryst. Size (Å)**	**r.m.s strain**	**wt. %**	**R_{wp} %**
KNN-BF+ CuO 1000	*Amm2*	3.9569	5.6597	5.6764	127.122	1388	$4.0*10^{-3}$	37	4.96
	P4mm	3.9743	3.9743	4.0045	63.251	1241	$2.7*10^{-3}$	45	
	Pbcm	5.6170	5.5616	15.6602	489.217	>2000	$5.2*10^{-3}$	18	
KNN-BF+ CuO 1025	*Amm2*	3.9585	5.6568	5.6753	127.111	1362	$4.3*10^{-3}$	35	5.40
	P4mm	3.9759	3.9759	4.0083	63.362	1215	$2.6*10^{-3}$	49	
	Pbcm	5.6260	5.5662	15.6824	491.101	>2000	$4.9*10^{-3}$	16	
KNN-BF+ CuO 1050	*Amm2*	3.9593	5.6535	5.6743	127.013	1396	$4.0*10^{-3}$	38	6.09
	P4mm	3.9736	3.9736	4.0045	63.229	1685	$2.5*10^{-3}$	49	
	Pbcm	5.6237	5.5639	15.7000	491.248	>2000	$4.8*10^{-3}$	13	
KNN-BF+ CuO 1075	*Amm2*	3.9564	5.6490	5.6783	126.908	1266	$3.4*10^{-3}$	41	5.59
	P4mm	3.9732	3.9732	4.0027	63.187	>2000	$2.6*10^{-3}$	46	
	Pbcm	5.5654	5.6292	15.6934	491.654	1605	$4.2*10^{-3}$	8	
	C2/c	4.6922	3.4235	5.1320	81.355	>2000	$6.1*10^{-4}$	5	
KNN-BF+ CuO 1100	*Amm2*	3.9554	5.6523	5.6711	126.789	1305	$2.6*10^{-3}$	45	5.75
	P4mm	3.9713	3.9713	3.9985	63.061	>2000	$2.2*10^{-3}$	46	
	Pbcm	5.5653	5.6288	15.7141	492.259	701	$3.0*10^{-3}$	4	
	C2/c	4.6905	3.4226	5.1337	81.331	>2000	$1.4*10^{-5}$	5	

Table S6.4. Room temperature piezoelectric, dielectric and elastic complex material properties, electromechanical coupling factors and frequency number, as well as the planar Poisson´s ratio, of KNN-BF + xCuO ceramics from the Radial resonance. The mechanical Q factors are also calculated as FWHM ($\Delta f/f$) for the G (Qs(calc)) and R (Qp(calc)) peaks.

Property\ Sample	KNN-BF	KNN-BF+0.5CuO	KNN-BF+CuO
d_{33} (pC N^{-1})	150	125	105
$\Re^2$	0.999	0.993	0.999
d_{31} (pC N^{-1})	-56.84	-43.51	-38.47
$Q_p(d_{31})$	53.88	207.35	70.43
d_{33}/d_{31}	2.78	2.87	2.73
g_{31} (10^{-3} mV N^{-1})	-11.11	-9.96	-6.01
$Q_p(g_{31})$	101.34	40.77	28.75
N_p (kHz mm)	3246	3297	3308
k_p	41.71	35.13	26.20
k_{31}	24.34	21.17	14.64
ε_{33}^T	577.66	492.75	721.57
Q_e	35.17	34.07	20.40
$\tan\delta_e$	0.028	0.029	0.049
s_{11}^E (pm^2 N^{-1})	10.66	9.68	10.80
$Q_m(s_{11}^E)$	149.65	235.51	60.33
s_{12}^E (pm^2 N^{-1})	-3.40	-2.65	-4.06
$Q_m(s_{12}^E)$	149.08	235.43	60.38
s_{11}^D (pm^2 N^{-1})	10.03	9.24	10.57

$Q_m(s_{11}^D)$	152.54	186.24	57.50
s_{12}^D ($pm^2\ N^{-1}$)	-4.03	-3.08	-4.29
$Q_m(s_{12}^D)$	142.49	1136.26	68.68
s_{66}^E ($pm^2\ N^{-1}$)	28.13	24.66	29.72
$Q_m(s_{66}^E)$	149.52	235.49	60.34
c_{11p}^E ($10^{10}\ N\ m^{-2}$)	10.44	11.17	10.78
$Q_m(c_{11p}^E)$	149.79	235.52	60.31
c_{11p}^D ($10^{10}\ N\ m^{-2}$)	11.89	12.17	11.32
$Q_m(c_{11p}^D)$	156.81	154.00	54.03
Poisson's ratio (σ^P)	0.32	0.27	0.37
Q_s(calc)	152.19	226.75	60.24
Q_p(calc)	163.80	146.92	53.49

6.9 References

[1] L.-Q. Cheng, J.-J. Zhou, K. Wang, J.-F. Li, Q.-M. Wang. *J Mater Sci.* **2012**, 47, 6908–6914.

[2] E. Hollenstein, *PhD thesis* (EPFL) **2007**.

[3] C. Suryanarayana. *Prog Mater Sci.* **2001** 46, 1-184.

[4] R. Singh, P. K.Patro, A.R.Kulkarni, C.S.Harendranath. *Ceram Int* **2014** 40,10641–10647.

[5] A. Iacomini, S. Garroni, N. Senes, G. Mulas, S. Enzo, M. Poddighe, Á. García, J. F. Bartolomé, L. Pardo. *ChemistryOpen* **2021**, 10, 798-805.

[6] R. Zuo, J. Rödel, R. Chen, L. Li. *J. Am. Ceram. Soc*. **2006**, 89(6), 2010–2015.

[7] J. Ma, L.C. Lim. *J Eur Ceram Soc* **2002** 22, 2197–2208.

[8] R. Zuo, C. Ye, X. Fang. *J Phys Chem Solids.* **2008**, 69, 230–235.

[9] H. Han, J. Koruza, E. A. Patterson, J. Schultheiß. E. Erdem, W. Jo, J. S. Lee, J. Rödel. *J Eur. Ceram Soc.* **2017**, 37(5), 2083-2089.

[10] M. Bah, F. Giovannelli, F. Schoenstein, G. Feuillard, E. LeClezio, I. Monot-Laffez. *Ceram. Int.* **2014**, 40(5), 7473–7480.

[11] E. Akçan, H. Yılmaz. *Ceram Int.* **2015** 41, 3659–3667.

[12] Y. Zhao, R. Huang, R. Liu, H. Zhou, W. Zhao. *Mater Res. Bull*. **2014** 49, 475–479.

[13] F. Hussain, I. Sterianou, A. Khesro, D. C. Sinclair, and I. M. Reaney. *J. Eur. Ceram. Soc.* **2018**, 38(9), 3118-3126.

[14] P. Xu, M. H. Jiang, X. Y. Liu. *Adv. Mater Res.* **2011** (335–336), 968–975.

[15] U. Nuraini, F. Fitriana, P. Kidkhunthod, M.A. Baqiya, S. Suasmoro, *Physica B*. **2021** 614, 413012.

[16] H. Takao, Y. Saito, Y. Aoki, K. Horibuchi. *J. Am. Ceram. Soc*. **2006** 89(6), 1951–1956.

[17] E. Mensur. A. M. Papila. *Ceram Int*. **2010** 36(6), 1921-1927.

[18] I.-T. Seo, K.-H. Cho, H.-Y. Park, S.-J. Park, M.-K. Choi, S. Nahmw. *J. Am. Ceram. Soc*. **2008**, 91(12). 3955–3960.

[19] L. Amarande , C. Miclea, C. Tanasoiu. *Ferroelectrics*. **2007** 350(1), 38-47.

[20] S. L. Yang, C.-C. Tsai, C. S. Hong, S. Y. Chu. *Mater. Res. Bull*. **2012** 47(4), 998–1003.

[21] D. Lin, K. W. Kwok, H. L. W. Chan. *J. Phys. D: Appl. Phys.* **2008**, 41, 045401.

[22] H. Wang, X. Zhai, J. Xu, X. Zhao, L. Yang. *J Mater Sci: Mater Electron*. **2016**, 27, 5016–5019.

[23] Q. Hu, H. Du, W. Feng, C. Chen, Y. Huang. *J. Alloy. Compd.* **2015** 640, 327–334.

[24] Bo Wang, F. Zhang, Y. Yang, F. Liu, Z. Liu, Z. Liu, Y. Li. *Ceram. Int.* **2021** 47 18886–18892.

[25] W. Hua, Z. Xia, J. Xu, C. Yuan, C. Zhou. *J. Mater. Sci. Mater. Electron*. **2013** 24, 2469–2472.

[26] R.X. Huang, Y.Z. Zhao, X.W. Zhang, Y.J. Zhao, R.Z. Liu, H.P. Zhou. *J. Am. Ceram. Soc*. **2010** 93, 4018–4021.

[27] Y. Zhao, Y. Zhao, R. Huang, R. Liu, H. Zhou. *J. Am. Ceram. Soc.* **2011** 94, 656–659.

[28] X. Li, M. Jiang, J. Liu, J. Zhu, X. Zhu, L. Li, Y. Zhou, J. Zhu, D. Xiao. *Phys. Status Solidi A*. **2009** 206(11), 2622–2626.

[29] A Reyes-Montero, L. Pardo, R. López-Juárez, A M González, S. O. Rea-López, M. P. Cruz, M E Villafuerte-Castrejón. *Smart Mater. Struct*. **2015** 24, 065033.

[30] C. Ciomaga, M. Viviani, M.T. Buscaglia, V. Buscaglia, L. Mitoseriu, A. Stancu, P. Nanni. J. *Eur. Ceram. Soc*., **2007** 27, 4061-4064.

[31] L. Liu, Y. Huang, Y. Li, M. Wu, L. Fang, C. Hu, Y. Wang. *Phys. B Condens. Matter* **2012** 407, 136-139.

[32] A. Rahnama, M. Gharagozlou. *Opt. Quant. Electron.*, **2012** 44, 313-322.

7 Spark Plasma Sintering (SPS) and electrical properties of KNN-BF system

7.1 Introduction

The Spark Plasma Sintering (SPS) is a highly efficient sintering technique which allows to obtain high density piezoceramics in a very short time and using relatively low sintering temperatures.**[1]** This technique is particularly attractive for KNN and KNN-based ceramics as they suffer from poor densification and high volatility of alkaline ion at the common sintering temperatures (~ 1125°C). However, due to the drastic conditions of the SPS process (high heating rate, high mechanical load, vacuum environment etc…) the resulting ceramic is generally characterized by inhomogeneity of the bulk composition (especially in the case of complex compositions), very small grain size and structural defects, like oxygen vacancy. In particular, the latter are responsible for the large conductivity found in the fresh SPS samples.**[2]** For these reasons, an air annealing treatment is usually necessary, after the SPS process, in order to increase the size of grains and to eliminate or, at least, decrease the oxygen vacancy concentration. Zhen et al. pointed out the importance of this treatment which also affects the piezoelectric properties of the ceramics.**[3]** In the light of these considerations, this chapter is focused on the synthesis and the electrical characterisation of the pseudo binary solid solution $0.99K_{0.5}Na_{0.5}NbO_3$-$0.01BiFeO_3$ (KNN-BF) obtained by SPS technique. The powder processing method is the same as the one used in the previous chapter (**Chapter 6**). The influence of the post annealing temperature on structure, microstructure and electrical properties of this “lead free” system was investigated. The results will be discussed and compared with the system obtained by air sintering.

7.2 Structural and microstructural characterisation

In **Figure 7.1** is reported the temperature time profile imposed during the sintering process. Two main phenomena can be recognized, which have been indicated as T1 and T2. The first shrinkage (T1) of about 0.8 mm occurs during the first minutes and is due to the application of the mechanical load (50 MPa). The second phenomenon (T2), which starts at around 320°C and it is completed at around 925°C, is due to the sintering process which causes an overall displacement of about 3.3 mm.

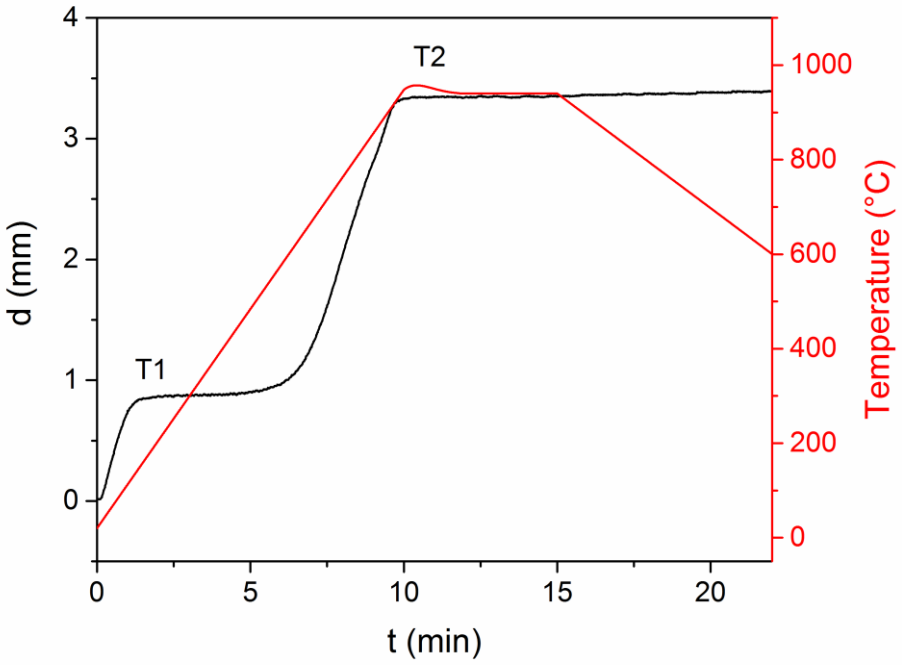

Figure 7.1. Temperature and sample displacement of KNN-BF sample during the SPS process

The densification is completed just before that the oven reaches the desired sintering temperatures (940°C), during the isotherm no more shrinkage is observed. In **Figure 7.2** is reported the photographs of the sintered pellet before **(a)** and after **(b)** the post-annealing treatment. All the SPS's replica shows a dark and homogeneous black colour, while the post annealing samples show a light brownish colour. As reported by Malic et al., the dark colour of the SPS samples it is related to the high concentration of oxygen vacancy and to the partial reduction of Nb^{5+} to Nb^{4+}.**[2]** This

observation will be discussed in more detail later. In **Figure 7.3** is reported the density of the samples. The post annealing treatment causes a clear decrease of the density of the samples. The Sh1 sample shows a high density of 4.51 g/cm^3, which correspond to the theoretical density of pure KNN. If we neglect the low concentration of bismuth and iron compounds, it is reasonable to say that the sample is full dense (~ 100% of TD).**[4]** The Sh2 and sh3 samples still maintain high density respectively of 4.48 g/cm^3 and 4.39 g/cm^3 while the Sh4 and Sh5 samples show lower density of about 4.19 g/cm^3. It is interesting to note that all the S1-5 samples exhibit very similar density values close to the theoretical one, which confirms the high reproducibility and efficiency of this sintering method. Furthermore, it is evident that the density deceases up to a certain temperature around 1050°C, a further increase of the post annealing temperature (1100°C) does not cause a substantial change of the bulk density.

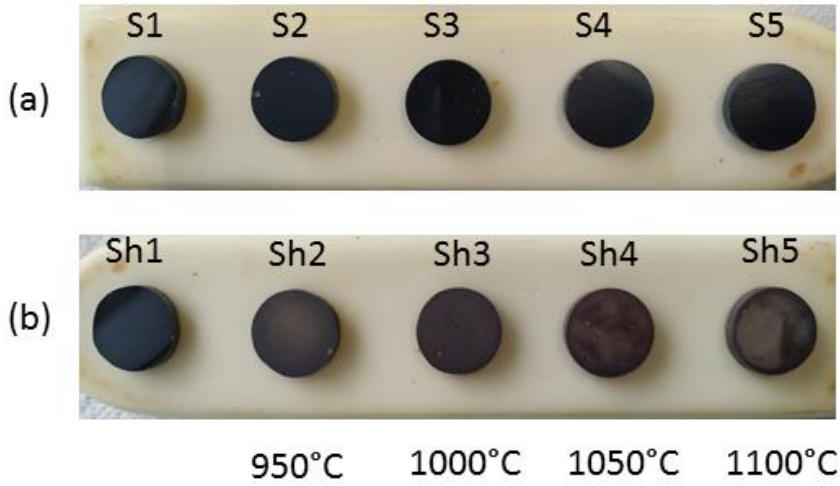

Figure 7.2. Photographs of KNN-BF pellets obtain through Spark Plasma Sintering (a) before and (b) after the post-annealing process. Labels under the post annealed samples indicated the post annealing temperatures. In Figure **2b**, the Sh1 sample, which is the fresh SPS sample, is reported for comparison purpose.

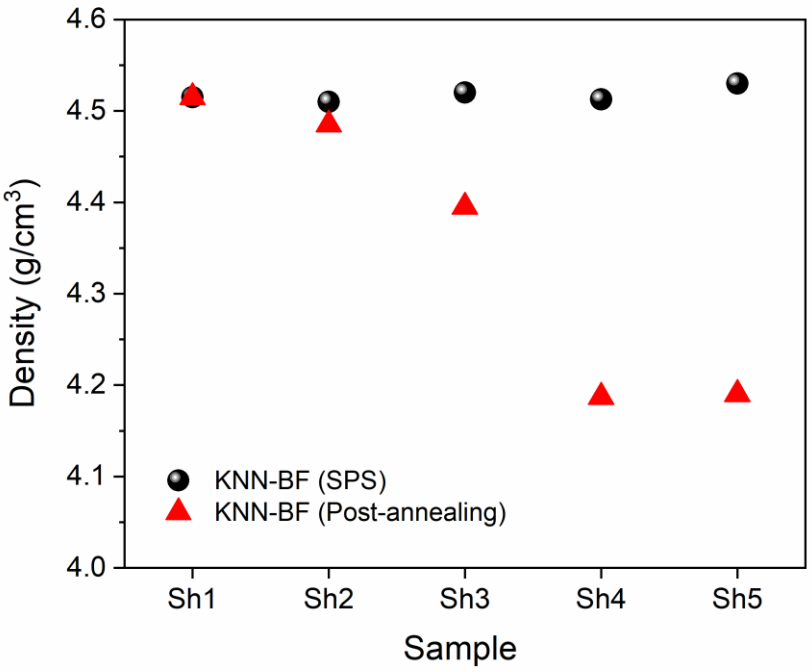

Figure 7.3. Density of the samples before (black) and after (red) the post annealing treatment.

In **Figure 7.4** are reported the full XRD patterns of the KNN-BF sintered samples. The analysis carried out with the Rietveld method highlighted several structural complexities, which can be appreciate in much more details in **Figure 7.5**. The convolution of the phases, that constitute the model used for the calculation, are indicated with different colour.

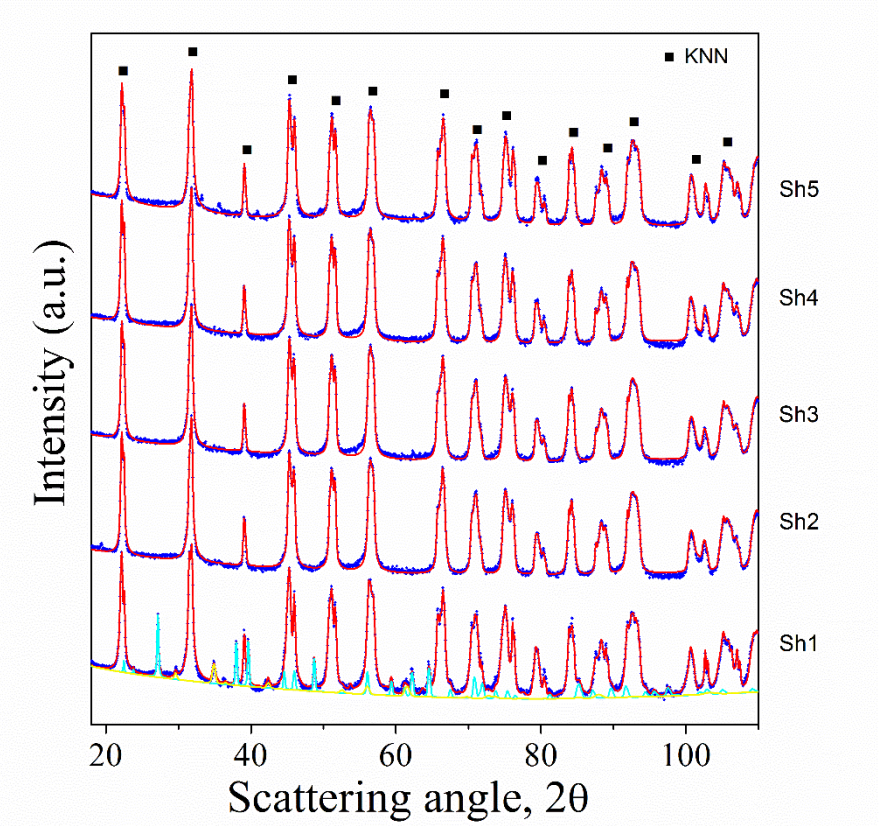

Figure 7.4. XRD patterns (log scale) of KNN-BF samples. Blue dots represent the experimental data. Red curve is the calculated fit obtain from the sum of the phases used as a model in the calculation. The Cyan and yellow curves belong to the secondary phases identified in the Sh1 samples, which are respectively bismuth and magnetite.

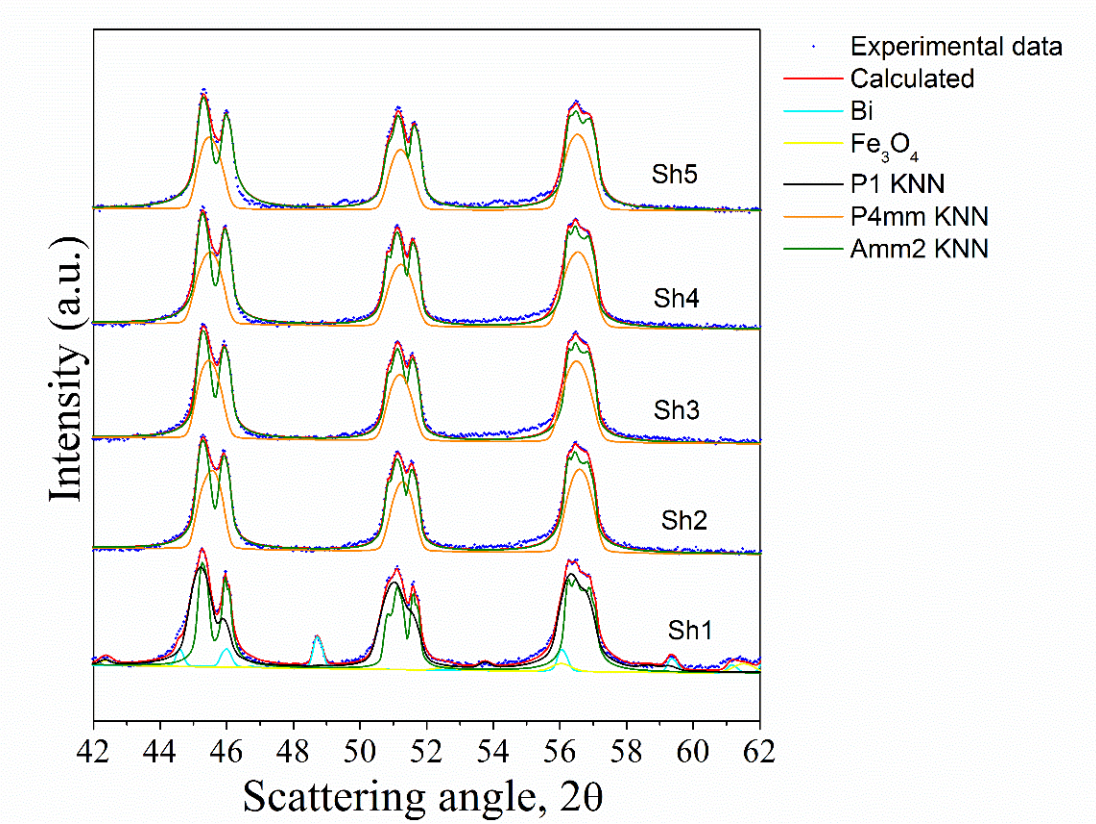

Figure 7.5. Magnification of some diagnostic peaks between 42 and 62°C. Different colour lines indicate the phases used in the model.

The Sh1 sample comes as a mixture mainly composed of an orthorhombic Amm2 phase and a monoclinic P1 phase. It is often reported that the crystal structure of KNN is purely orthorhombic (s.g Amm2), or purely monoclinic (s.g P1). However, a recent work by Thong and co-workers has highlighted that the use of a different niobia polymorph leads to obtaining slightly different crystalline product.**[5]** In particular, the use of the orthorhombic polymorph allows to obtain a homogeneous single-phase product, already in the calcination step. However, if the monoclinic polymorph is used, the calcined product results as a complex mixture of niobates.**[6,7]** A more homogeneous product is obtained in the subsequent sintering step which appears apparently as a single phase. However, the current density loops characterisation reveals the multiple ferroelectric phase coexistence of this system. In this case, we can observe a similar situation where the main diffraction peaks are a complex

mixture of two similar ferroelectric phases with most probably different Na/K ratio as the orthorhombic Amm2 phase and monoclinic P1 in percentage by weight respectively of 32 and 66 % (see **Table 1**). It is worth to point out that the fast-sintering rate and the shorter soaking time of SPS process does not facilitate the homogenization of the niobates.

Table 7.1. Crystallographic information obtained from Rietveld refinement of SPS's samples. The β angle of the monoclinic P1 cell of Sh1 sample is 90.04°.

Sample	**Phase (s.g)**	**a (Å)**	**b (Å)**	**c (Å)**	**V (Å^3)**	**Cryst. Size (Å)**	**wt. %**	**R_{wp} (%)**
Sh1	*Amm2*	3.9467	5.6447	5.6796	126.530	889	32	8.48
	P1	5.6687	3.9531	5.6729	127.124	1029	66	
	Fd-3m (Fe_3O_4)	8.5258	8.5258	8.5258	619.734	709	1	
	R-3m (Bi)	4.5462	4.5462	11.8600	245.122	1839	1	
Sh2	*Amm2*	3.9509	5.6471	5.6769	126.658	>2000	68	10.02
	P4mm	3.9771	3.9771	3.9994	63.260	>2000	32	
Sh3	*Amm2*	3.9502	5.6457	5.6762	126.588	>2000	69	9.50
	P4mm	3.9772	3.9772	3.9944	63.184	>2000	31	
Sh4	*Amm2*	3.9483	5.6471	5.6787	126.615	>2000	71	9.62
	P4mm	3.9806	3.9806	4.0025	63.420	>2000	29	
Sh5	*Amm2*	3.9452	5.6447	5.6752	126.384	>2000	71	14.69
	P4mm	3.9729	3.9729	3.9999	63.134	>2000	29	

The presence of the secondary phases suggests that the doping elements failed to settle within the crystal structure of KNN. Surprisingly, the secondary phases identified are bismuth metallic (Bi) and magnetite (Fe_3O_4). Most probably, the vacuum environment of the SPS chamber has favoured the reduction of iron and bismuth oxides used as starting reagents. The redox reaction may have involved

the graphite (C) which turns into carbon monoxide according to the following redox reactions (**Equation 7.1** and **Equation 7.2**):

$$Bi_2O_3 + 3C \rightarrow 2Bi + 3CO \quad (7.1)$$

$$3Fe_2O_3 + C \rightarrow 2Fe_3O_4 + CO \quad (7.2)$$

The Sh2 sample has no secondary phases. The best fit was obtained using the orthorhombic Amm2 and the tetragonal P4mm phases in percentage by weight respectively of 68 and 32%, in agreement with other works.**[8]** This evidence suggest that the post annealing treatment is effective for promoting the solid solution. From a comparison of the ionic radius, it is reasonable to expect that Bi^{3+} (103 pm) occupies the Na^+ (102 pm) and K^+ (138 pm) sites while Fe^{3+} (64.5 pm) occupies the Nb^{5+} (64 pm) sites. Both phases show large crystallinity (>2000 Å) which indicates that the post annealing treatment promotes the growth of grains. The samples treated at higher post annealing temperatures shows similar crystal structure (Sh3, Sh4 and Sh5), just only a slight increase of the Amm2 has been observed by increasing the post annealing temperature (**Table 7.1)**. Moreover, it should also be noted that the post-annealed samples do not contain any secondary phases, in particular the tungsten-bronze phase, which suggests that the volatility of the alkaline ions is negligible.

In **Figure 7.6** are reported the Raman spectrum of the SPS's samples. The wavenumbers range between 200-1000 cm^{-1} is attributable to internal vibrations, both stretching and bending modes, of the octahedral NbO_6 molecular group. Below 200 cm^{-1} all the signals are assigned to the translational modes of Na^+/K^+ cations and rotation of the NbO_6 group.**[9,10]** The NbO_6 octahedron shows a cubic O_h symmetry and six normal vibrations:

$$\Gamma_{vib} = 1A_{1g}(\nu_1) + 1E_g(\nu_2) + 2F_{1u}(\nu_3, \nu_4) + 1F_{2g}(\nu_5) + 1F_{2u}(\nu_6) \quad (7.3)$$

Where, ν_1, ν_2 and ν_3 are stretching modes that involves Nb-O and O-Nb-O bonds while ν_4, ν_5 and ν_6 are bending modes of O-Nb-O bond.**[11]** The Raman spectra consists of three main signals, an asymmetric broad band between 200 and 300 cm^{-1} which consists of three contributions, related with the bending vibrations ν_4, ν_5 and ν_6. The second signal centred around at 620 cm^{-1} is also formed by three bands which correspond to the stretching vibrations ν_1, ν_2 and ν_3. Finally, the isolated band at 860 cm^{-1} is due to the $\nu_1 + \nu_5$ vibrational mode. At first glance, it emerges that the Raman scattering intensity of the annealed samples (Sh2, Sh3, Sh4 and Sh5) are much more intense than the fresh SPS sample (Sh1). As reported in literature, the intensity of the Raman scattering is proportional to the grain size.**[12]** This evidence further confirms that the annealing treatment have caused an increase of the grain size.

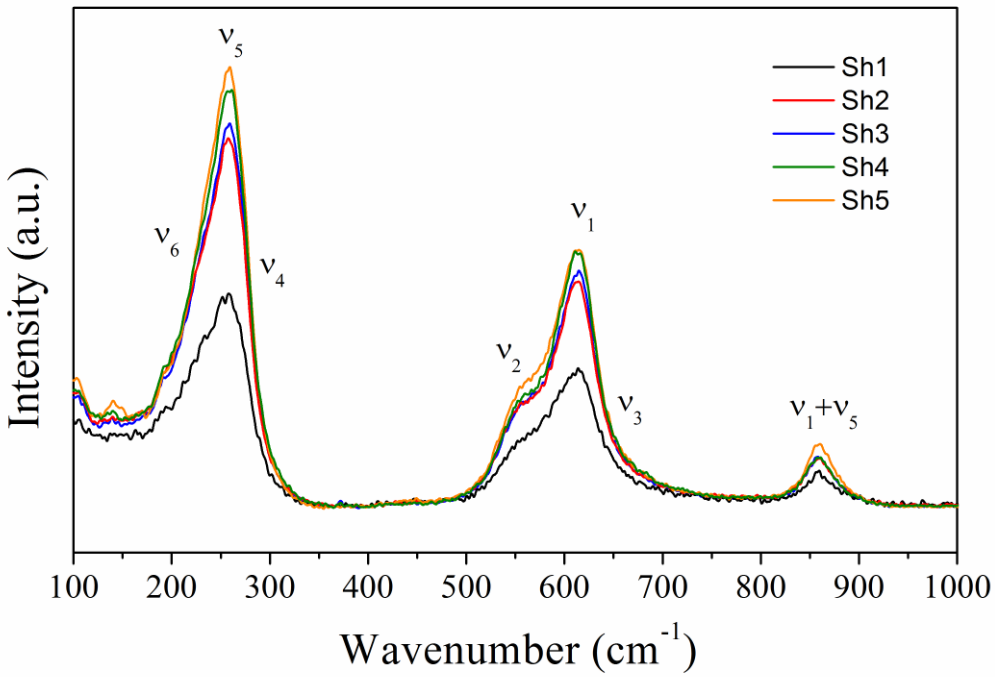

Figure 7.6. Room temperature Raman spectra of KNN-BF samples.

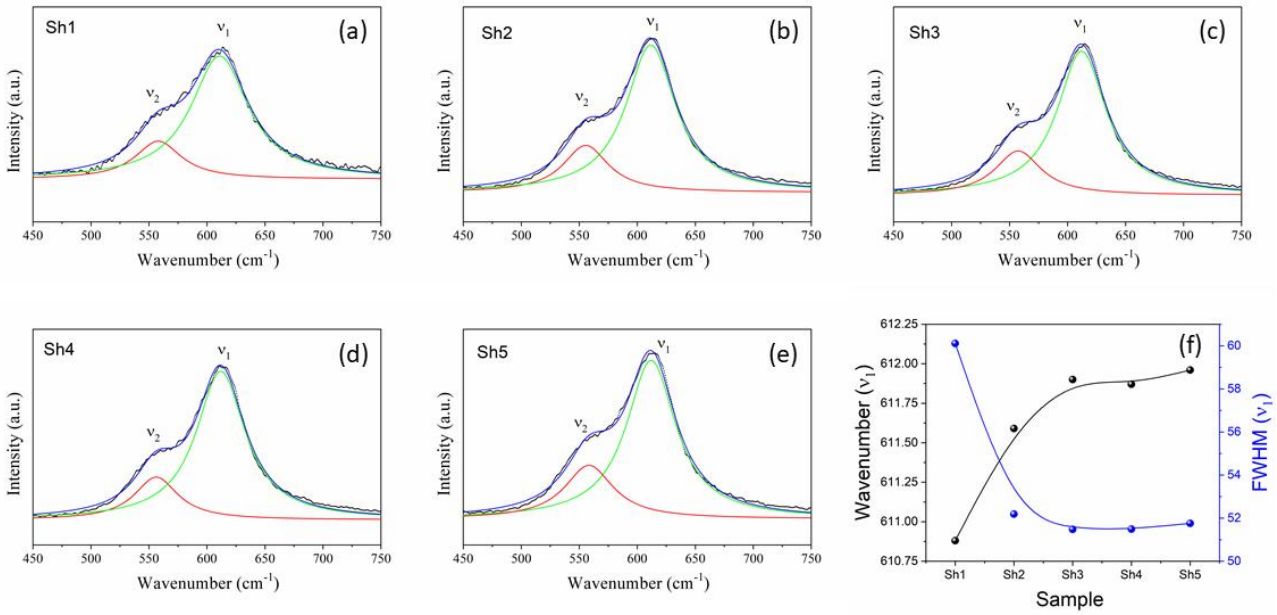

Figure 7.7. (a-e) Raman spectra of the SPS samples in the wavenumber range between 450 and 750 cm^{-1} and Lorenzian fit of the A1g(v1) (green lines) and Eg(v2) (red lines). (b) Evolution of the wavenumber and FWHM of A1g(v1) Raman modes as a function of the post annealing temperature, expressed here with the corresponding sample label.

In order to provide a precise identification and assignment of Raman modes, the Raman spectra in the diagnostic range between 450 and 750 cm^{-1} have been analysed. The spectra have been fitted with two Lorenzian peaks (**Figure 7.7a-e**) that correspond to A_{1g}(v1) and E_g(v2) Raman modes, in agreement with Rubio-Marcos et al.**[13]** The peak of A_{1g}(v1) slight shift toward higher wavenumbers (**Figure 7.7f**) as the post annealing temperature increases. This behaviour is generally attributed to the increase in the force constant due to the shortening of the distance between the B-site atom and their coordinated oxygen. Therefore, this effect could be associated with the reduction of the oxygen vacancy concentration. As reported by Ceo et al., the evaluation of the FWHM of A1g(v1) Raman mode can provide useful information as its reduction, which also determines the sharpening of the peak, is correlated with the alleviation of the large distortion of O-Nb-O angles and the increase in the interaction between Nb and O.**[14]** As shown in **Figure 7.7f,** it has been observed a strong

reduction of FWHM value, in particular between the Sh1 and Sh2 samples, which further confirm that the Raman shift towards higher wavenumber it is due to a greater interaction between Nb and O.

In **Figure 7.8** are shown the SEM images of the fractured surface of KNN-BF pellets. The Sh1 sample (**Figure 7.8a**) reveals a highly dense microstructure which agrees with the high experimental density measured. The annealed samples reveal a less dense microstructure characterized by an increase of porosity that seems to be related to the increase of the grain size with the annealing temperature. All the samples show a predominant transgranular fracture **(Figure 7.8a-d)** except the Sh5 **(Figure 7.8e)** which is characterized by an intergranular fracture. This type of fracture generally happens due to weak bonding of the grains; therefore, it is reasonable to conclude that the post annealing treatment influences the grain growth and the bond between the particles which determines the transition from a transgranular to a predominant intergranular fracture for high annealing temperatures (1100°C).**[15]**

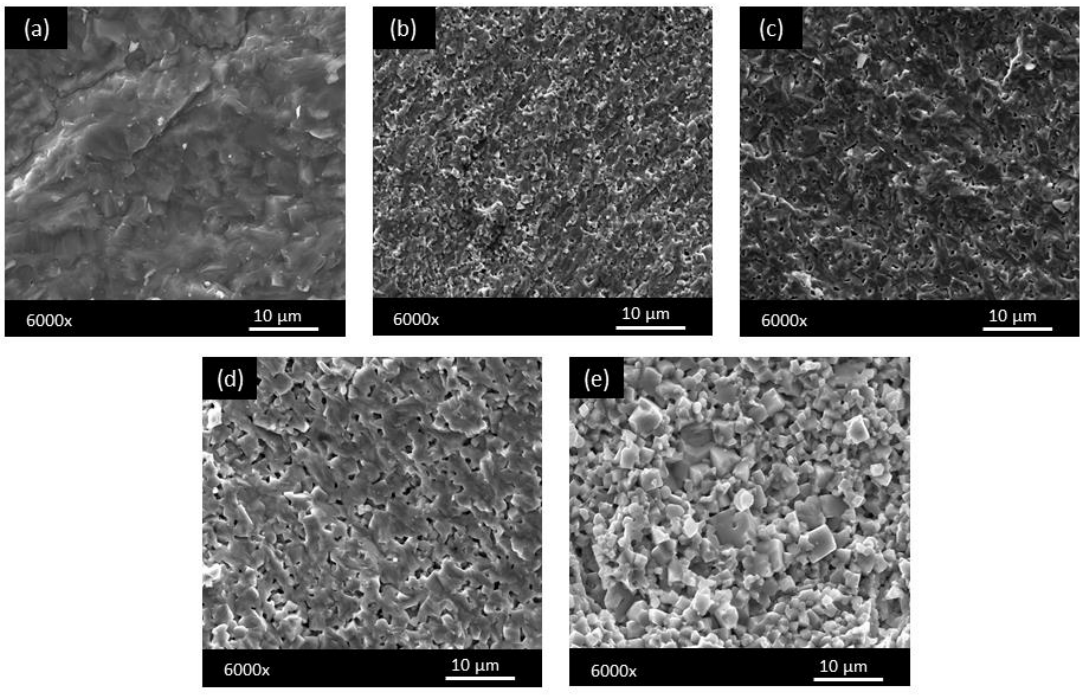

Figure 7.8. Fractured surface images of sintered pellets. **(a)** Sh1, **(b)** Sh2, **(c)** Sh3, **(d)** Sh4 and **(e)** Sh5.

7.3 Electrical characterisation

The resistance (ohm, Ω) between the two silver electrodes of the SPS samples was checked prior the electrical characterization. The Sh1 sample showed relatively low resistance, in the order of hundreds kΩ. As observed by other authors, this evidence can be explained by the high concentration of oxygen vacancy which make the ceramic highly conductive and thus, not suitable for poling and the electromechanical characterization.**[2,16]** In addition, should also be considered the presence in trace of bismuth metallic and magnetite (**Figure 7.4**) which could enhance this phenomenon. A clear improvement in terms of electrical resistance was achieved with the post-annealed samples. Sh2, Sh3 and sh4 showed similar values, in the order of tens MΩ, while the resistance of Sh5 was found to be out-of-scale. From a first glance, it seems that the annealing treatment have a positive effect on the insulating properties of KNN-BF which seems to be correlated with the annealing temperature. To further provide an insight on the dielectric behaviour of the samples, the temperature dependence of the permittivity and dielectric losses were measured at various frequencies and the results are shown in **Figure 7.9** and **7.10** respectively. Let us consider first the permittivity curves; all the ceramics presents two clear dielectric anomalies, indicated as T1 and T2, that correspond to the orthorhombic-tetragonal (T1) and the tetragonal-cubic (T2) phase transitions. A slight difference in terms of phase transitions has been detected. Sh2 and Sh3 exhibit similar dielectric behaviour and present T1 and T2 respectively at around 140 and 350 °C, while Sh4 and Sh5 show the same phase transitions at around 150 and 365°C respectively. Therefore, the increase of the annealing temperature determines a clear shift towards higher temperatures of the dielectric anomalies. However, the biggest differences concern the magnitude of permittivity at high temperatures and the shape of the dielectric peaks. Sh2 and Sh3 are characterized by broad dielectric peaks and large permittivity; on the contrary, Sh4 and Sh5 are characterized by lower permittivity and sharper dielectric peaks (**Figure 7.9**).

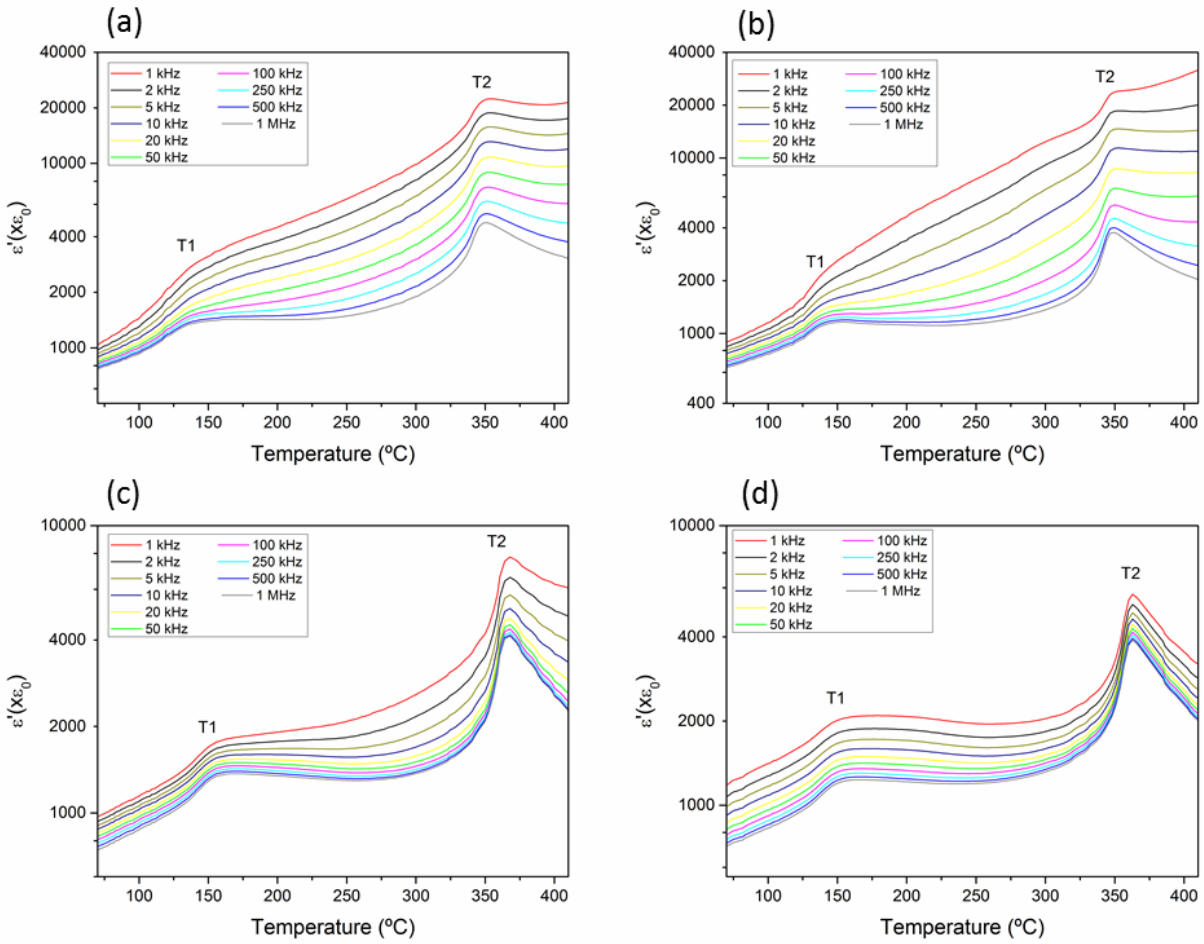

Figure 7.9. Dielectric permittivity (log scale) ε^{T}_{33} vs. temperature for (a) Sh2, (b) Sh3, (c) Sh4 and (d) Sh5.

Figure 7.10 shows the dielectric losses as a function of the temperature. The Sh2 sample shows very high losses at high temperature, as well as the Sh3 sample which presents slightly higher losses and an increased frequency dependence. However, a clear change in trend was observed for the Sh4 and Sh5 samples who they show a marked decrease in the high temperature dielectric losses with values comparable to those of "normal" dielectric material.**[17]** In order to explain this behaviour, it is necessary to consider two main contributions, which are the oxygen vacancy and the microstructural features of the materials. As reported by Buscaglia et al., the grain size strongly affects the dielectric behaviour of the ceramics.**[18]** In particular, ceramics characterized by small grain size typically show broad dielectric peaks which often causes a decrease of the Curie point. This observation perfectly fit

with our experimental evidence. Regarding the behaviour of the dielectric losses (**Figure 7.10**), it is widely accepted that oxygen vacancies are responsible to the conduction mechanism in dielectric ceramics which cause high dielectric losses, especially at high temperatures.**[19]**

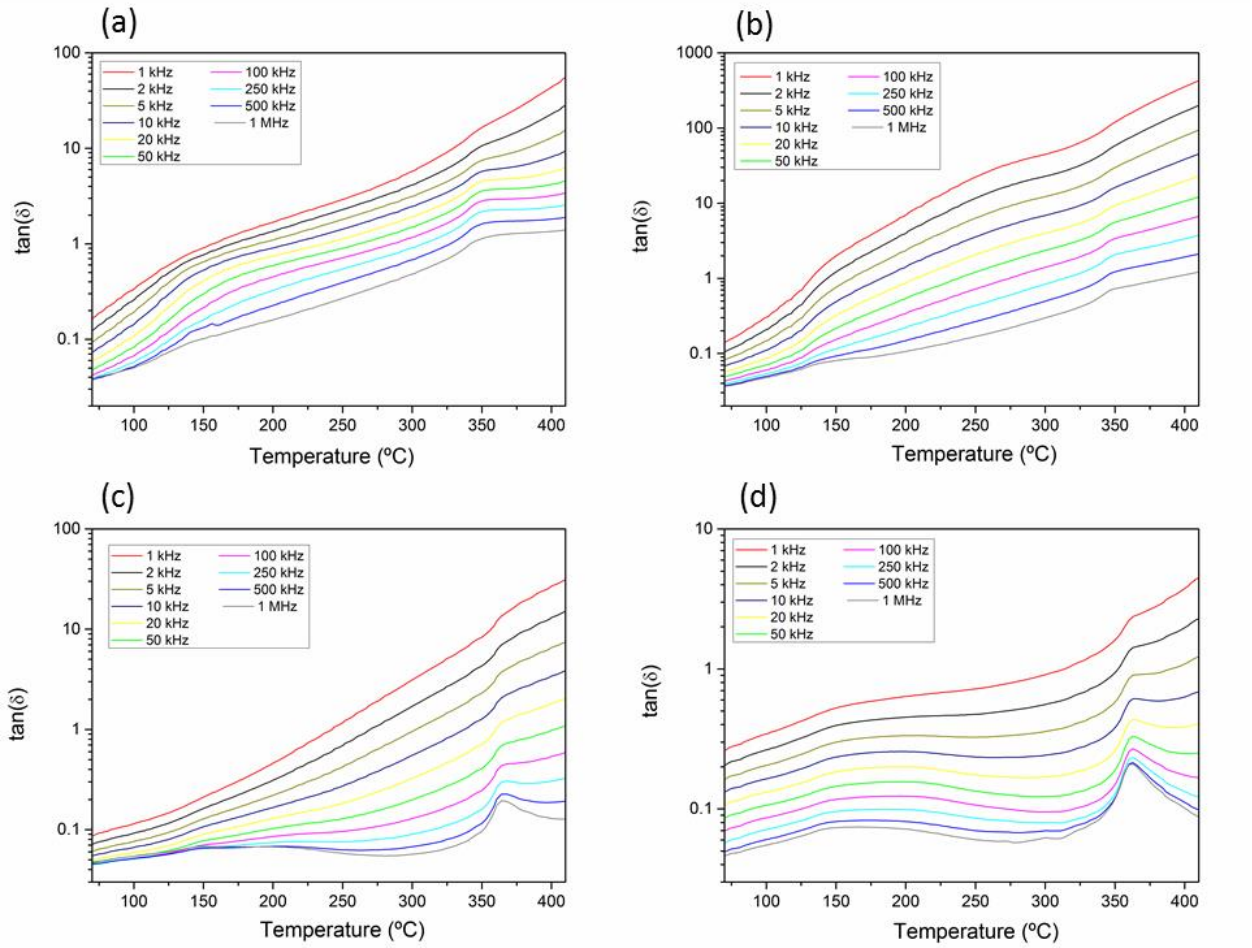

Figure 7.10. Dielectric losses (log scale) tanδ vs. temperature for (a) Sh2, (b) Sh3, (c) Sh4 and (d) Sh5.

The ionization of oxygen vacancy will create conducting electrons in perovskite structure oxides, written as follows:

$$V_o \leftrightarrow V_o^{\circ} + e' \tag{7.4}$$

$$V_o^{\circ} \leftrightarrow V_o^{\circ\circ} + e' \tag{7.5}$$

Where the two equations express the formation of single (**Equation 7.4**) and double (**Equation 7.5**) ionized oxygen vacancies. In order to explain the large dielectric permittivity (**Figure 7.9a-b**) and dielectric loss (**Figure 7.10a-b**) observed in the samples annealed at low temperatures (Sh2 and Sh3), it is necessary to consider the presence of the structural defects indicated in the equations expressed above. The generation of the double ionized oxygen vacancy is accompanied by the release of two electrons to keep the electric charge balance of the unit cell. When the external electric field and high temperature are applied, the electrons might deviate from the charge centre of $V_o^{\circ\circ}$. This phenomenon takes the name of *electron relaxation polarization* which determines the ultra-high dielectric constant and dielectric loss of the low-temperature annealed samples.**[20]** This behaviour is greatly reduced as the annealing temperature increases due to a better compensation of the oxygen vacancy. As a results, Sh4 and Sh5 presents lower permittivity and lower high-temperature dielectric losses. It is interesting to note that the Raman characterisation didn't shows remarkable differences between the air annealed samples (**Figure 7.7**). We can speculate that the oxygen vacancy compensation is much more difficult in the bulk than the surface of the pellet and the increasing of the annealing temperature guarantees a better oxygen bulk compensation and thus, better insulating properties.

In **Table 7.2** are reported the results of the electromechanical characterisation (Radial mode) of the samples poled at 20 kV/cm. For representative purpose, in **Figure 7.11** is reported the equivalent plot of R and G, both the experimental and reconstructed peaks, used for the calculation of parameters with the automatic iterative method of the Sh3 sample. Due to a not perfectly circular shape of the discs, the fundamental Radial mode is disturbed by another less intense vibrational mode which partially overlap with the main one. In any case, the regression factor ($\Re^2$), which measures the validity of the model for the resonance mode, is still quite high for all the samples analysed. From **Table 7.2** it clearly emerges that the best piezoelectric properties belong to the samples that have

undergone a post-annealing treatment at 1000 (Sh3) and 1050 °C (Sh4). In particular, Sh3 and Sh4 show similar piezoelectric coefficients (d_{33} ~ 110 pC/N; d_{31} ~ -33 pC/N), coupling factors (k_p ~ 26 %; k_{31} ~ 16 %) and permittivity at room temperature (ε_{33}^{T} ~ 480-500; tanδ ~ 0.06-0.07). The Sh5 sample shows a deterioration of the electrical properties, i.e, lower piezoelectric coefficients and lower coupling factors but it has the highest mechanical quality factor (Q_m = 100.43). In order to provide an explanation to this behaviour it is necessary to consider the different microstructural features of the samples. As observed in **Figure 7.8**, the increase of the post annealing temperatures is accompanied by an increase in the size of the grains.

Table 7.2. Some relevant material coefficients obtain from the Radial mode characterisation of KNN-BF ceramics obtained by Spark Plasma Sintering method. For comparison purpouse, the electromechanical characterisation of the KNN-BF obtained by air sintering (AS) is reported.

Properties /Sample	**Sh2**	**Sh3**	**Sh4**	**Sh5**	**KNN-BF (AS)**
$\Re^2$	0.968	0.987	0.995	0.999	0.999
d_{33} (pC/N)	73	110	109	55	150
d_{31} (pC/N)	-26.69	-32.27	-32.79	-19.56	-56.84
$Q(d_{31})$	45.53	93.84	416.41	25.24	53.88
k_p (%)	20	26	25	15	42
k_{31} (%)	12	16	16	9	24
$\boldsymbol{\varepsilon_{33}^{T}}$	573.39	477.95	506.20	532.20	577.66
tanδ	0.046	0.061	0.076	0.064	0.028
$\mathbf{c_{11}^{p}}$ (10^{10} N m^{-2})	11.35	11.34	11.52	10.43	10.44
Q_m	92.93	68.65	79.00	100.43	149.79

It is well-known that the poling process is easier when the sizes of grains are large. The more complex domain configuration and the higher surface pinning of domain walls, results in higher energy needed for their reorientation.**[7]** Therefore, the best piezo coefficients of the samples Sh3 and Sh4 could be related to the optimum grain size. A further increase of the post annealing temperature (1100°C) determines a worsening of the microstructure, that is, lower density, higher porosity and weaker bond between the grains, which leads to lower piezoelectric coefficients. Although the Sh3 and Sh4 samples show good properties, these are lower than the sample obtained by air sintering (**Table 7.2**).

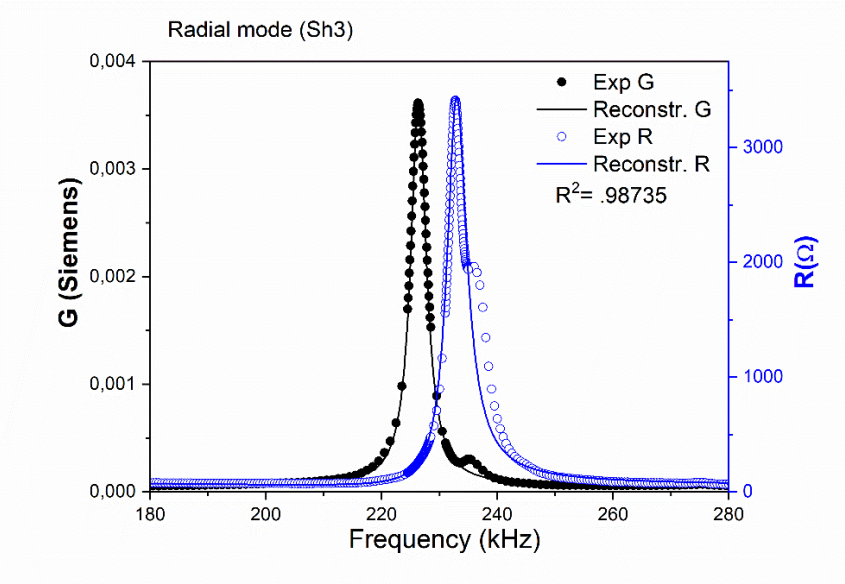

Figure 7.11. R and G plot that is used in the iterative analysis. Symbols represent the experimental data and lines the reconstructed peaks.

This difference can be traced back to the different insulating properties between the SPS's samples and the air sintered sample. As previously observed, Sh3 and Sh4 showed resistance values between the electrodes in the order of tens MΩ, which suggests a still high concentration of oxygen vacancies probably located in the bulk of the pellet. The presence of these defects determines a rather high electric current (in the order of few mA) during the poling process which affects the reorientation of the domains, and therefore, the electromechanical properties of the ceramics.

7.4 Conclusions

This work was dedicated to the synthesis and characterization of the "lead free" $0.99K_{0.5}Na_{0.5}NbO_3$-$0.01BiFeO_3$ (KNN-BF) ceramics prepared by a combination of mechanochemical activation method and Spark Plasma Sintering. Particular attention was paid to the post annealing treatment. Results show that the annealing treatment causes important microstructural and electrical changes to the fresh SPS sample. The annealing treatment proved effective to promote the formation of the solid solution between KNN and BF. Furthermore, an increase in the grain size and a decrease in the bulk density as a function of the annealing temperature has been observed. The fresh SPS sample is characterized by low electrical resistance, while the air annealed samples show better insulating properties due to a partial compensation of the oxygen vacancy. This effect would seem to improve as the annealing temperature increases. The best piezoelectric properties were found for the samples annealed at 1000 e 1050 °C due to the optimum grain size, however the electromechanical coefficients are lower than the KNN-BF prepared by air sintering due to a partial conductivity still present in the samples. With the aim of further improving the functional properties of the system, new heat treatments are planned in oxygen-rich atmosphere in order to ensure a better compensation of the oxygen vacancy and therefore better insulating and piezoelectric properties.

7.5 References

[1] R. Wang, R. Wang, R. Xie, T. Sekiya, Y. Shimojo. *Mater Res. Bull*. **2004**, 39, 1709–1715.

[2] D. Kuscer, A. Kocjan, M. Majcen, A. Meden, K. Radan, J. Kovač, B. Malič. *Ceram Int.* **2019**, 45, 10429–10437.

[3] Y. Zhen, J.F. Li, K. Wang, Y. Yan, L. Yu. *Mater Sci Eng B.* **2011** B 176, 1110–1114.

[4] H. Birol, D. Damjanovic, N. Setter, *J. Eur. Ceram. Soc*. **2006**, 26, 861–866.

[5] H.-C. Thong, C. Zhao, Z.-X. Zhu, X. Chen b, J.-F. Li, K. Wang. *Acta Mater.* **2019** 166, 551-559.

[6] J. Hrešcak, A. Bencan, T. Rojac, B. Malic. J. Eur. Ceram. Soc. **2013**, 33, 3065–3075.

[7] A. Iacomini, S. Garroni, N. Senes, G. Mulas, S. Enzo, M. Poddighe, Á. García, J. F. Bartolomé, L. Pardo. *ChemistryOpen*. **2021**, 10, 798-805.

[8] A. Khesro, D. Wang, F. Hussain, R. Muhammad, G. Wang, A. Feteira, and I. M. Reaney. *Front. Mater*. **2020**, 7, 140.

[9] M. Poomska, B. Hilczer, M. Kosec, & B. Malič. *Ferroelectrics*. **2008**, 369(1-3), 149–156.

[10] R. Singh, K. Kambale, A. R. Kulkarni, & C. S. Harendranath. *Mater. Chem. Phys.* **2013** 138(2–3), 905–908.

[11] W. L. Zhu, J. L. Zhu, Y. Meng, M. S. Wang, B. Zhu, X. H. Zhu, J. G. Zhu, D. Q. Xiao, G. Pezzotti. *J. Phys. D: Appl. Phys*. **2011**, 44, 505303.

[12] Y.L. Du, M. S. Zhang, Q. Chen, Z. Yin. *Appl. Phys. A* **2003**, 76, 1099–1103.

[13] F. Rubio-Marcos, M. A. Banares, J. J. Romero and J. F. Fernandez. *J. Raman Spectrosc*. **2011**, 42, 639–643

[14] Zhenyong Cen, X. Wang, Y. Huan, L. Li. *J Am Ceram Soc*. **2018**, 101, 2391–2407.

[15] D. Liu, H. Du, F. Tang, F. Luo, D. Zhu, W. Zhou. *J. Electroceram*. **2008**, 20, 107–111.

[16] M. Bah, F. Giovannelli, F. Schoenstein, G. Feuillard, E. LeClezio, I. Monot-Laffez. *Ceram. Int*. **2014**, 40(5), 7473–7480.

[17] R. Zuo, C. Ye, X. Fang *J. Phys. Chem. Sol*. **2008**, 69, 230–235.

[18] V. Buscaglia, M.T. Buscaglia, M. Viviani, L. Mitoseriu, P. Nanni, V. Trefiletti, P. Piaggio, I. Gregora, T. Ostapchuk, J. Pokorny´, J. Petzelt *J. Eur Ceram Soc*. **2006**, 26, 2889–2898.

[19] T.-F.Zhang, X.-G. Tang, Q.-X. Liu, Y.-P. Jiang, X.-X. Huang. *J. Am. Ceram. Soc*. **2015**, 98, 551-558.

[20] B. Wang, F. Liu, F. Zhang, G. Chen, Z. Liu, Y. Li. *Ceram. Int.* **2020**, 46(17), 27373-27380.

8 Development of a multifunctional device for *in-situ* poling/temperature experiments

8.1 Introduction

In-situ diffraction experiments of piezoceramics during the poling process are gaining a lot of interest due to the large amount of useful information that can be provide. For example, Li et al. employed this technique to study the effect of the field cooling (FC) on the domain reorientation of BCZT composition.**[1]** Other authors founds in textured KNN-based materials a new intermediate monoclinic phase that serving as a bridge facilitates the polarization rotation.**[2]** Relaxor ferroelectrics are extensively studied with this technique as their symmetry change with the application of an external electric field.**[3]** Furthermore, *in-situ* diffraction experiments are often employed in order to evaluate the percentage of the 90° domains reoriented during poling and to provide information about the relaxation effect that take place when the poling fields is cut-off.**[4,5]** The cases mentioned above are some of the several studies carried out using this technique; however, these kinds of experiments are particularly difficult to perform and are mostly carried out in synchrotron facilities, therefore, they are hardly carried out routinely. Furthermore, doesn't exist on the market a standard device to perform these measurements, and also, the "home made" cells described in some papers lacking in a heating system.**[6]** The heating system is certainly useful for investigating the effect of temperature in the poling process, but not only, as it can be exploited to investigate the evolution of the crystalline structure as a function of the applied temperature.**[7]** This is particularly useful for lead-free systems such as BT, BCZT and KNN-based materials which have phase transitions not far from room temperature.**[8-10]** For these reasons, we developed a patented cell, named X-poll, for standard *in-situ* diffraction poling/temperature experiments usable in a normal laboratory diffractometer. The development of the cell and the experimental conditions are described in detail. All the experiments

here reported were carried out on a well-known piezoceramics as the barium titanate. In order to demonstrate the potential of the cell, two simple experiments were carried out which are: 1) in-situ temperature experiment; 2) in-situ electric field experiment. We believe that this artifact can be a valuable tool to perform "homemade" diffraction experiments for piezoceramics materials and more.

8.2 Prior Art

In order to verify the concrete possibility of the novelty, the inventive contribution and the applications of this patent proposal, the anteriority analysis was carried out. The research produced 4 patent and 1 scientific paper with connotations reminiscent of the patent proposal in question and listed here below:

- CN 111912705 A (D1);
- US 2691111 A (D2);
- US 20070228874 A1 (D3);
- US 10888898 B2 (D4);
- *NEET In-Pile Ultrasonic Sensor Enablement-Final Report (Joshua Daw et al; United States: N. p., 2014. Web. doi:10.2172/1166037)*;

The patent that has similar characteristics to the invention here proposed is identified with the initials D1. In particular, this document describes an apparatus for measuring the electromechanical properties of a piezoelectric material. In paragraphs 10 and 11 of the aforementioned document is reported that this apparatus includes a piezoelectric test cavity which allows to carry out the measurements of the piezoelectric properties of the materials. The sectional view of the aforementioned piezoelectric test cavity of document D1 is reported in **Figure 8.1**. Inside this piezoelectric test cavity there are two cylindrical copper electrodes (207), between which the piezoelectric material to be measured is placed. It also identifies a heating rod (210) configured to

heat the inside of the cavity by heating the silicone oil contained in the external walls (214) of the cavity itself. The temperature inside the cavity is then controlled by a thermocouple (205). The cavity also includes a network cable interface (204) configured to connect the strain gauges to an external detection system, as specified in paragraph 26. The openings present in the aforementioned cavity are essentially two: an observation window (208) provided with a quartz plate, and a through hole defined in the upper part of the cell which acts as a channel for the insertion of heating silicone oil, as reported in paragraph 29 of document D1. Although not explicitly indicated in the text, this cavity is suitable for carrying out the passage of an electric current through a piezoelectric material and, at the same time, the heating.

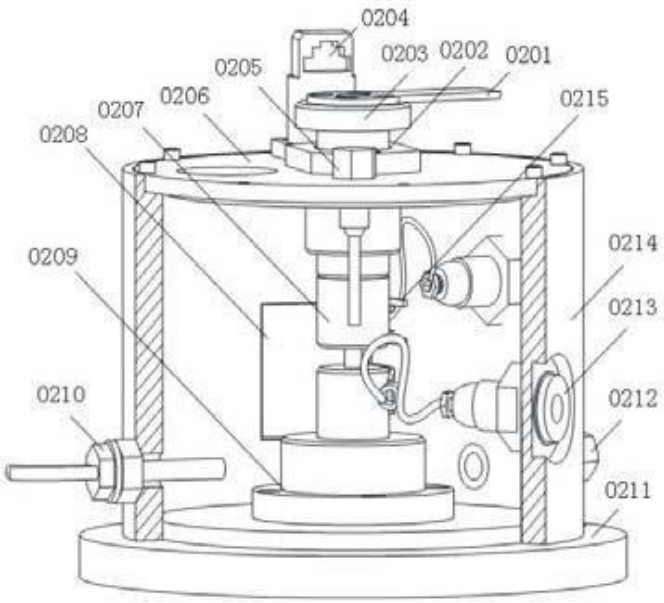

Figure 8.1 Scheme of the apparatus present in document D1.

The device illustrated in D1 is not suitable to perform diffraction experiments as schematically illustrated in **Figure 8.2**. Some papers report the use of "homemade" cells for *in-situ* diffraction experiments. In any case, the aforementioned devices do not have any integrated heating system.**[11]** From this anteriority analysis it emerges that:

- A measurement and polarization cell for piezoelectric materials that possesses one or more specific combined characteristics seems to possess both the novelty requirement and the inventive step requirement, allowing the obtaining the patent for industrial invention.

- None of the apparatuses described in the identified prior art documents seem to be suitable for allowing the simultaneous measurement and polarization of a piezoelectric material. Such simultaneity could be protected as an application.

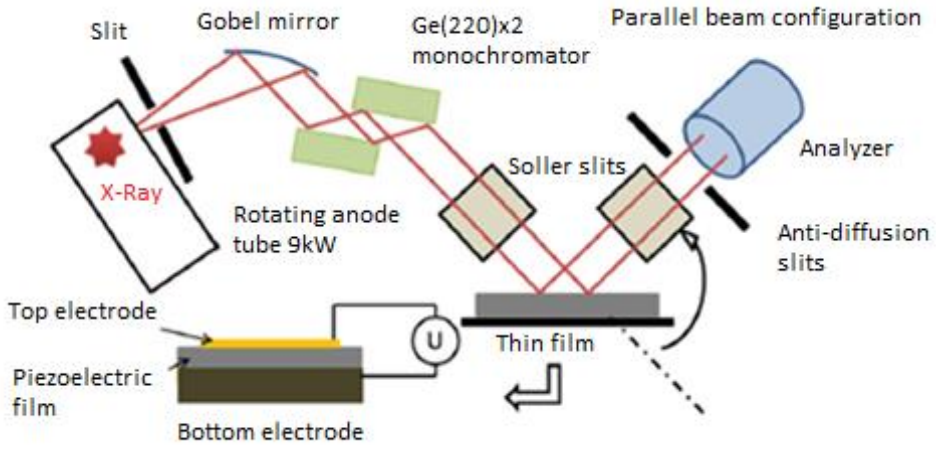

Figure 8.2. Parallel beam configuration for *in-situ* X-ray measurement of ceramic material during the application of an external electric field.**[6]**

8.3 Description of the invention

The present patent proposal describes the development of a cell prototype for polarization and measurement of massive and thin film piezoceramic materials. In summary, the invention that is the subject of this proposal, is based on an innovative device, capable of responding to both academic and industrial demands, for *in-operando* characterization of piezoceramics of any nature. The prototype shown in **Figure 8.3** has the following peculiarities:

- Small size (cube of about 3.5 cm per side).

- Modifiable dimensions using 3D printing techniques.
- Adaptability to different sample holder stages for laboratory analysis instruments.
- Controlled heating with temperature ramps having heating rates between 1-5 ° C / min with a range from room temperature up to 180 ° C.
- Polarization of the material through the application of an electric field.
- Extended angular range of diffraction analysis (up to 110 ° with copper wavelength). Control of temperature and external electric field.

Figure 8.3. 3D rendering of X-Poll device. The support (white) was printed using FDM 3D printing. The electric field is applied through a copper clip (orange colour) and a copper screw (red circle) which are connected to an external current generator. The temperature is generated with a resistance placed inside the copper screw. More details will be provided in the next section.

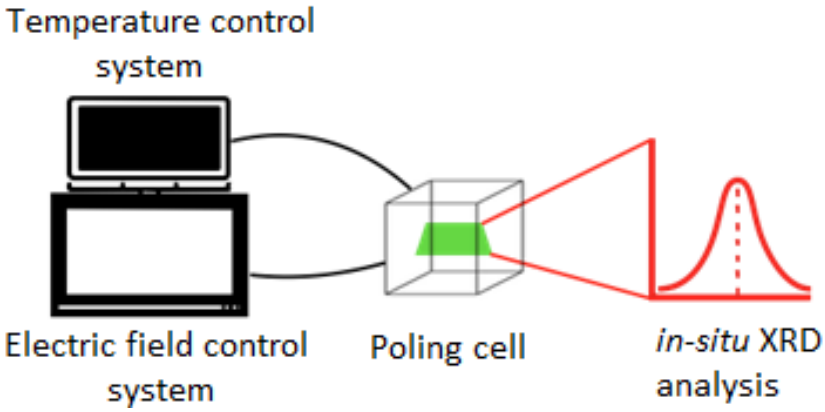

Figure 8.4. Schematic representation of the use of the cell for *in-situ* diffraction experiments.

The device allows to polarize the material by applying an adequate electric field at a certain temperature (25 °C - 140°C) and permit the analysis of the structure of the material by means of several techniques, including X-ray diffraction analysis (**Figure 8.4)**, but potentially extendable to other techniques as well as Raman spectroscopy, Scanning Electron Microscopy (SEM) and so on.

8.4 Cell Development

In **Figure 8.5** the images of the cell and its component are shown. **Figure 8.5a** shows the components of the cell before the assembly: (1) two electric cables; (2) U copper shape electrode (upper electrode). The U shape has been designed to ensure electrical contact at the same time to allow the beam to be intercepted by the sample. (3) The solid body is made of acrylonitrile styrene acrylate (ASA) (size around 5x5x3 cm). (4) Copper screw (lower electrode). (5) Copper screw block and (6) metal spring. The spring around the copper screw allows the optimal electrical contact between the pellet and the two copper electrodes by applying light pressure (Further details are shown in **Figure 8.6**), and (6) two cable (positive and negative) lugs. In **Figure 8.5b** and **8.5c** is shown the cell after the assembly. The removable drawer in **Figure 8.5b** was designed to facilitate the entry of the sample inside the cell; it also has the function of protecting the metal part, in this case the copper

screw, and therefore preventing it from being identified by the X-ray beam. In **Figure 1c** is shown the lower part of the cell. The cavities in the middle of the "feet" are used to house metal screws that guarantee the anchoring of the cell with the neodymium magnet of the sample holder of the diffractometer. The copper screw is empty in order to allow the heating cartridge to be accommodated inside, as reported in **Figure 8.5d**. The heating system is shown separately in **Figure 8.7** and consists of (1) a heating cartridge (cartridge diameter: 6 mm and length: 15 mm, 5.96 Ω, 12 V, 97 W, temperature range from R.T. up to 200 °C), (2) a thermistor for temperature reference, (2) an ARDUINO temperature controller circuit (12 V) and (3) the cartridge feed system (12-24 V). As mentioned above, the solid body of the cell is made of ASA, which is an amorphous thermoplastic polymer often used as an alternative to a similar polymer, namely acrylonitrile butadiene styrene (ABS). Compared to ABS, ASA has a better durability and a good resistance to weather conditions including tolerance to water and UV radiation.**[12]** Furthermore, it possesses fairly good mechanical properties which are due to the excellent adhesion between layers that guarantee high impact resistance, strength and the printing process.**[13]**

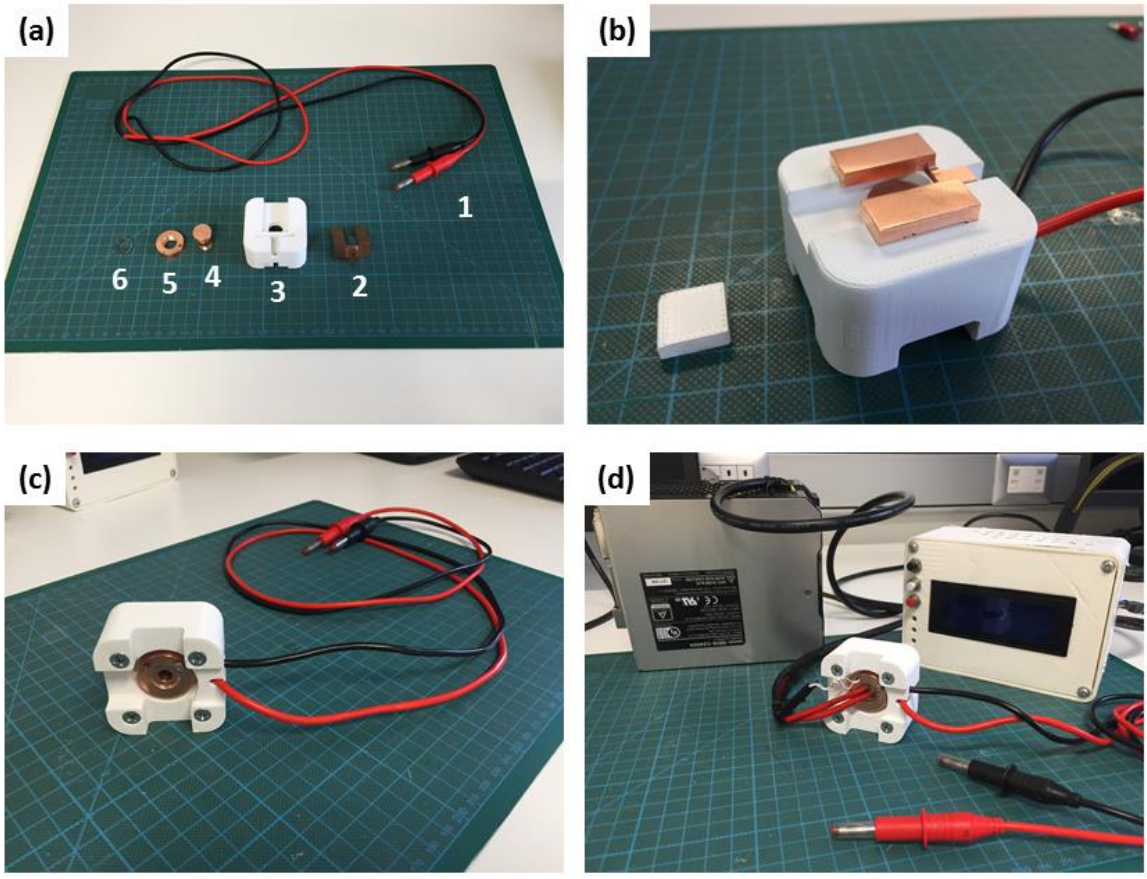

Figure 8.5. Images of X-Poll cell and its components. X-Poll before **(a)** and after **(b)** the assembly. **(c)** lower section of the cell and **(d)** X-Poll interfaced with the heating system.

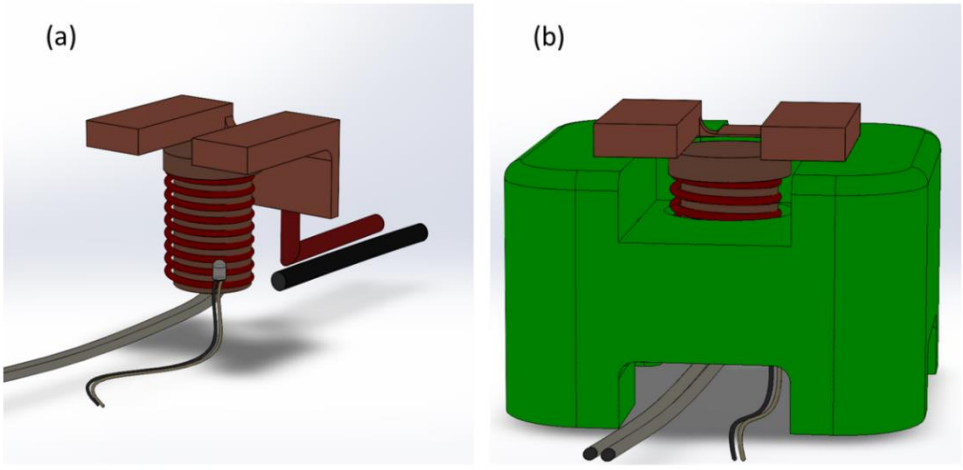

Figure 8.6. 3D rendering of (a) the copper screw system for the anchoring and the application of the electric field on the sample. (b) Front view of the cell

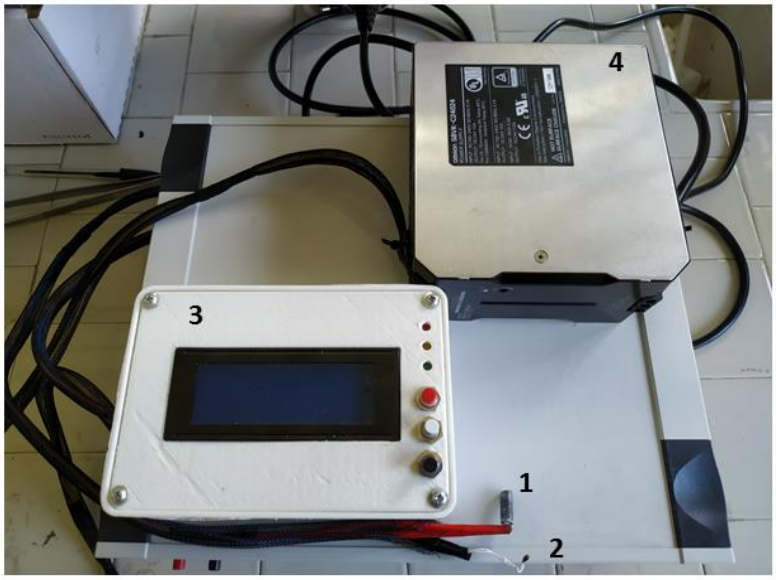

Figure 8.7. Heating system of the cell.

In order to assess the thermal and mechanical behaviour of ASA used in this prototype, differential scanning calorimeter (Tg/DSC) experiments and dynamic mechanical thermal analysis (DMTA) were performed. The results are shown in **Figure 8.8.** TGA/DSC experiment (**Figure 8.8a**) was conducted with a heating rate of 10°C/min from room temperature to 700°C under oxygen atmosphere. DMTA experiment (**Figure 8.8b**) was carried out on a rectangular 3D printed sample (1x4x0.3 cm), range temperature from R.T. to 150 °C with heating rate of 3°C/min, single cantilever clamp, fixed frequency 1Hz and fixed amplitude 100 um (optimized by LVR experiment).

The degradation process (**Figure 8.8a**) of ASA starts around at 300 °C and it is characterized by two steps probably derived from the 3D printed sample's structure. DMTA experiments shown the characteristic peaks for commercial ASA at 119°C, visible in the tanδ versus temperature plots for 3D printed ASA (**Figure 8.8b**). As can be seen, the storage modulus (green line) rapidly decease between 110-125° C which means that the mechanical properties deteriorate (the polymer become softer).

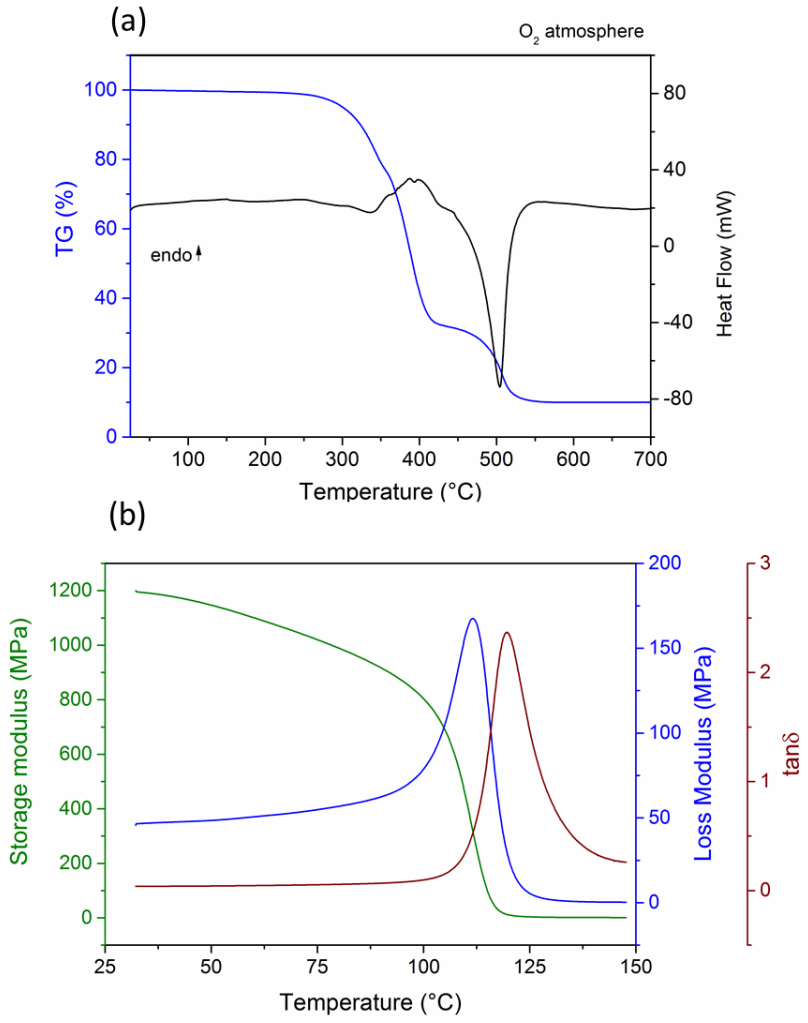

Figure 8.8 Thermal and mechanical behaviour of 3D printed Acrylonitrile Styrene Acrylate (ASA) used in the cell prototype. **(a)** Thermogravimetric analysis (TGA) and **(b)** dynamic mechanical analysis (DMA).

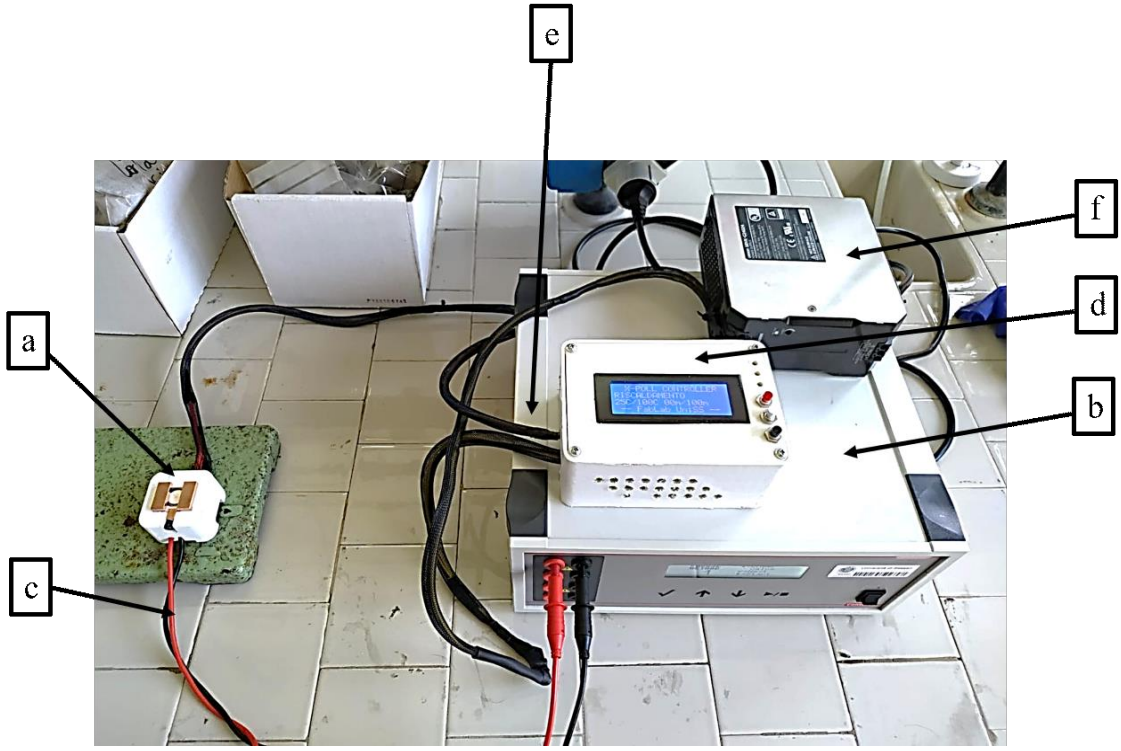

Figure 8.9. Complete setup assembled of X-Poll cell.

Figure 8.9 shows the entire assembled apparatus in which it is possible to identify:

- Poling cell (a)
- Current generator or power supply (b)
- Positive and negative connection cables (c) between X-poll cell and current generator
- ARDUINO temperature control circuit (d)
- Connection cables (e) for temperature control and poling cell
- Heating system power supply (f)

Current generator or power supply is provided by Consort BVBA, EV3330 model, voltage range from 30 V up to 3000 V. The EV3330 allows control of electric field speed application by programming an electric field gradient as a function of time, fixing the current (from 0 to 300 mA) and power (from 0 to 300 W) values. EV3330 permits programming different methods, each with 9

steps. Each step is able to recall a next one, providing a flexible multiple step function for special techniques. The method mode also permits to program a linear voltage gradient for any step provided the limiting current and/or power is not attained.

8.5 Preliminary test

Two poling experiments were carried out in order to assess the correct functioning of the electric and heating system of the cell. The material chosen for these tests is the 0.99KNN-0.01BF (KNN-BF) obtained by air sintering at 1125°C and widely studied along this thesis work. Details on sample preparation and its electrical properties have been extensively discussed in **Chapter 6**. Before each polarization, the pellet was covered with a thin layer of silicone oil in order to prevent the formation of electric arcs and short circuit. The sample were increased poled in thickness under 10-25 kV/cm for 15 minutes at room temperature and 100°C. At the end of each polarization, the piezoelectric coefficient (d_{33}) was measured with a Berlincourt d_{33} meter (**Figure 8.10** shows the evolution of the d_{33} coefficient as a function of the electric field and temperature. As can be seen, both curves converge towards the d_{33} value of 150 pC/N, which is in excellent agreement with the result obtained with similar poling conditions using a common poling apparatus (see **Figure 6.22**).

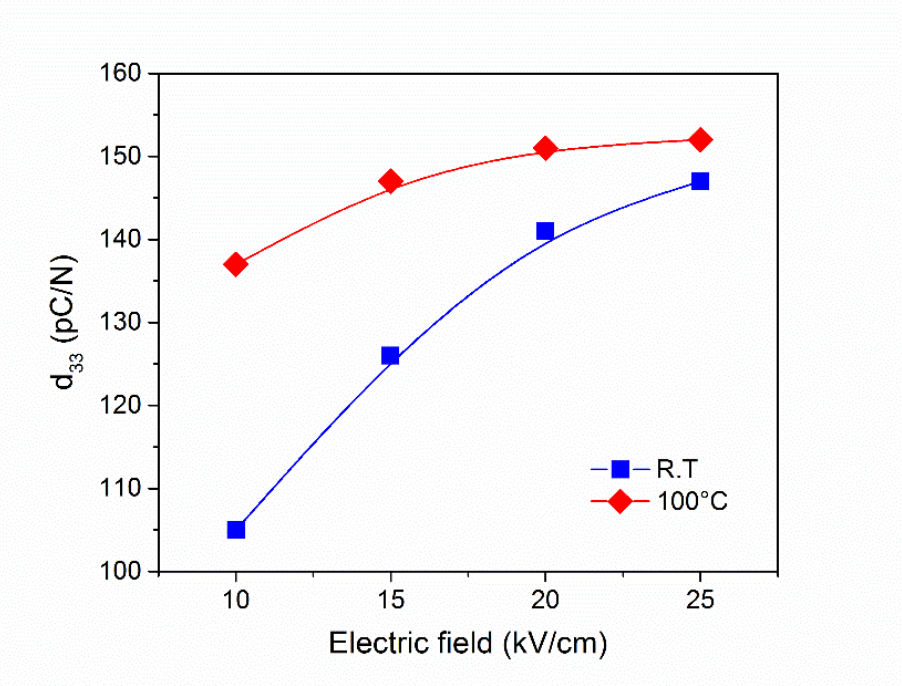

Figure 8.10. Piezoelectric coefficient (d_{33}) Vs poling electric field of KNN-BF sample poled with X-Poll cell.

8.6 Sample preparation and experimental setup

All the experiments presented here were performed on sintered barium titanate (BT). Sintered BT pellets were prepared using commercial barium titanate powders (Sigma Aldrich, 99.9% trace metals basis). The powders were finely ground in a mortar with few drops of a PVA binder solution (3 wt.%) and then were compacted with a hydraulic press at 220 kg/cm^2 for 30 minutes. Sintering was conducted at 1300°C for 2h in air. The sintered pellet has a final density of 5.58 g/cm^3 which corresponds to about 93% of the theoretical density (6.02 g/cm^3). **Figure 8.11** shows the XRD patterns of the raw BT powders and the sintered BT. All the samples show the typical tetragonal structure (P4mm s. g.), no secondary phases are detected. Cell parameters of BT powders (**a** = 3.997 Å; **b** = 4.034 Å) and the sintered products (**a** = 3.998 Å; **b** = 4.033 Å) are in good agreement with those found in literature for pure BT compound (**a** = 3.990 Å; **b** = 4.041 Å).**[14]**

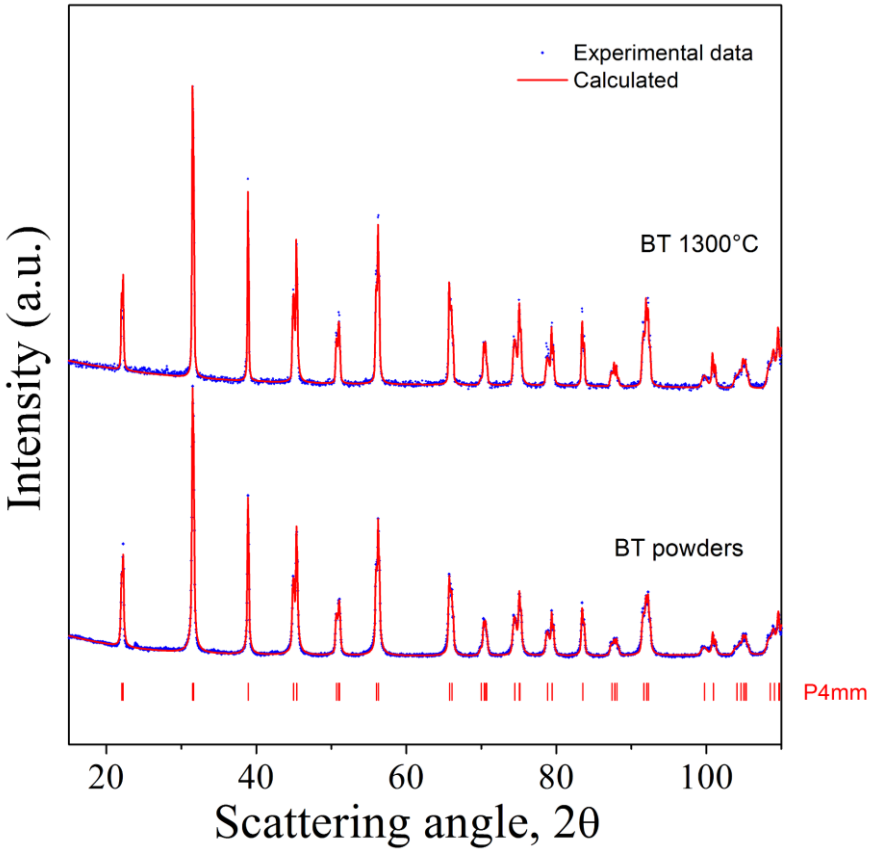

Figure 8.11. XRD patterns (intensity is expressed in square root scale) of BT powders and BT sintered at 1300°C.

The SEM micrographs of raw powders and the sintered products are shown in **Figure 8.11**. Commercial BT powders are characterized by fine and homogeneous particles with dimensions in the order of 1 μm. The sintered product (**Figure 8.11b)** shows a dense microstructure with predominant transgranular fracture, just some scattered porosity is detected along the surface, which justify the observed experimentally density.

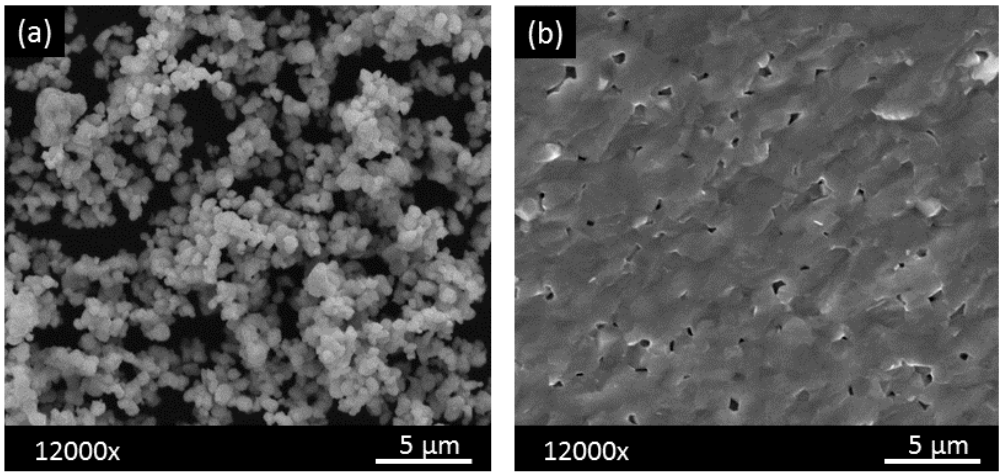

Figure 8.11. SEM micrograph of **(a)** commercial BT powders and **(b)** fractured surface of BT pellet sintered at 1300°C.

For *in-situ* electrical XRD experiments, sintered BT were polished on both surfaces and annealed at 1150°C to remove stress and preferential crystallographic orientation generated from sanding. A silver paste was welded at 400°C on the lower surface of BT while the upper surface was covered with a thin layer of graphite. The graphite does not interfere with the signals of BT (**Figure 8.12**) and with most of the perovskite-type structure of interest for this type of experiments. At the same time, it guarantees good electrical conductivity and it is cheap and easy to handle. A commercial spray graphite (Kontakt Chemie Graphit 33) was used as a precursor for the electrode deposition. In order to minimize the thickness of the graphite, the solution was deposited homogeneously with a glass capillary over the entire surface of the pellet. After few minutes, the solvent (2- propanol) is completely evaporated and the electrode takes on a dull black colour. After that, the electrode surface was lightly rubbed on absorbent paper; this process makes the black surface shiny and most importantly allows to break down the resistance from 15000 Ω to about 1000 Ω. The subsequent heat treatment at 250°C (heating rate and cooling rate of 2°C/min, isotherm 1h) further reduced the resistance of the electrode down to the final value of about 200 Ω.

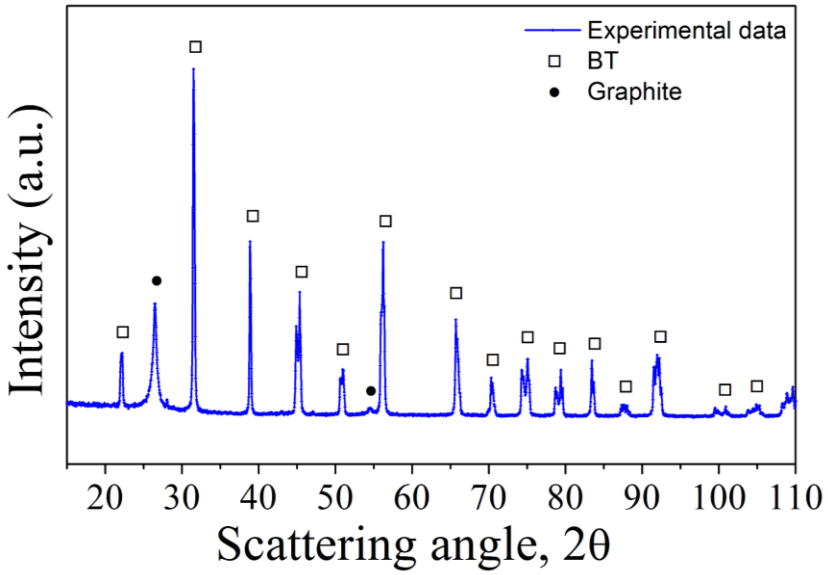

Figure 8.12. XRD pattern (intensity is expressed in square root scale) of sintered BT covered with a thin layer of graphite.

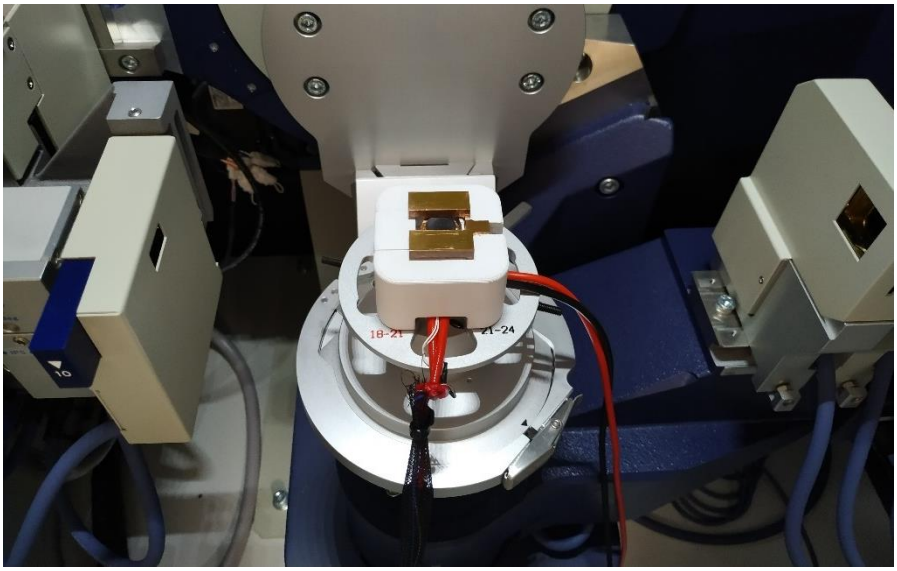

Figure 8.13 Set-up for the *in-situ* diffraction experiments.

Structural investigations were conducted using a SMARTLAB diffractometer with a rotating anode source of copper (l = 1.54178 Å) working at 40 kV and 100 mA. The spectrometer is equipped with a graphite monochromator and a scintillation tube in the diffracted beam. The diffractometer is

equipped with an automatic alignment system (Z-scan alignment) which allows to minimize the offset of the diffraction experiments. The cell is placed inside diffractometer's chamber as illustrated in **Figure 8.13**. For the *in-situ* temperature experiments, XRD patterns were recorded in the angular range of 15-90° using a step size of 0.05° and 1s of dwell time. The measurement started after about 5 minutes of reaching the selected temperature. For in situ electric field experiments, XRD patterns were collected on three diagnostic angular ranges (30-33°, 38-40° and 44-46.5°) using 4s of dwell time. The measurement is started after about 5 minutes from the application of the selected electric field. The automatic alignment procedure was performed before each measurement.

8.7 Results and discussion

In **Figure 8.14** are shown the diffraction patterns of the BT systems heat treated for increasing temperatures performed by using only the heating system of the X-poll cell. It is possible to appreciate the well-known tetragonal-cubic phase transition at around 100°C, which corresponds to the Curie point of this system. The common Curie temperature reported in literature for barium titanate is at around 120°C; however, deviation from this temperature could happen and may be due to structural defects generated by slight deviations from Ba/Ti ratio equal to 1.**[15,16]** The diffraction patterns were analyzed with the Rietveld method and the results are shown in **Table 8.1**. The goodness of fit (GOF) close to 1 highlights the good matching of the model with the experimental data. From room temperature to 90°C, the tetragonal structure undergoes a progressive increase of the cell volume from 64.367 $Å^3$ to 64.626 $Å^3$. This is mainly due to the modification of the **a** parameter (**a** is equal to **b** for tetragonal structures) which increases from 3.996 Å to 4.007 Å; at the same time, the **c** parameter slightly decreases from 4.031 Å to 4.025 Å. This behavior involves a progressive decrease of the c/a ratio which means that the structure turns from tetragonal, to pseudo-cubic to purely cubic at about 100°C.

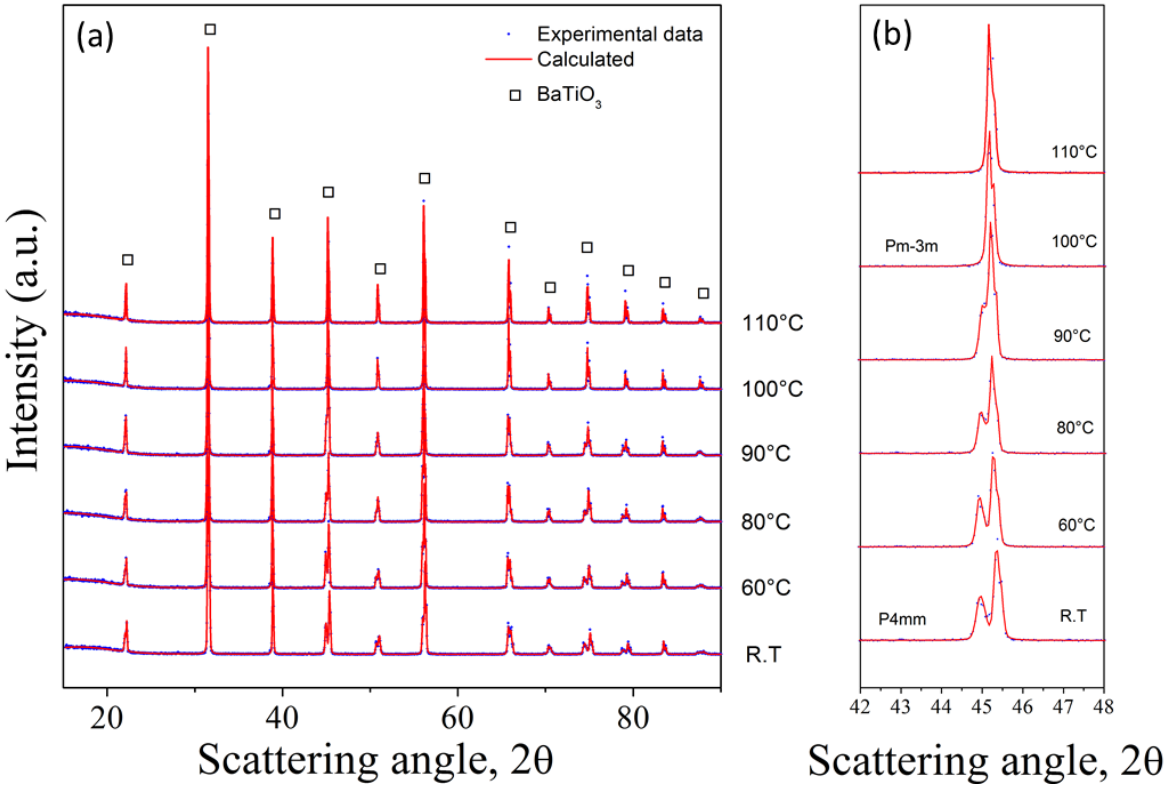

Figure 8.14 (a) Phase evolution as a function of temperature of sintered BT. Blue dots are experimental data while the red line is the calculated fit. (b) Magnification of the diagnostic peak at around 45°.

Table 8.1. Crystallographic information obtained from Rietveld refinement of sintered BT heat treated from 25°C (room temperature) up to 110°C.

T(°C)	**s. g**	**a** (Å)	**c** (Å)	**c/a**	**V** (Å^3)	**GOF** (χ^2)
25	*P4mm*	3.996	4.031	1.009	64.367	2.36
60	*P4mm*	4.002	4.031	1.007	64.560	2.26
80	*P4mm*	4.005	4.029	1.006	64.625	2.37
90	*P4mm*	4.007	4.025	1.004	64.626	2.18
100	*Pm-3m*	4.012	/	1.000	64.578	1.76
110	*Pm-3m*	4.011	/	1.000	64.529	1.75

It is interesting to note the discontinuity in the cell volume evolution around the phase transition. At first, the tetragonal volume cell increases and reaches a maximum of 64.626 $Å^3$ at around 110°C; after the phase transformation takes place, it is observed a shrinkage of the cubic cell which presents a cell volume of 64.578 $Å^3$. For a better view, all the crystallographic parameters collected and their evolution as a function of the temperature are shown in **Figure 8.15**.

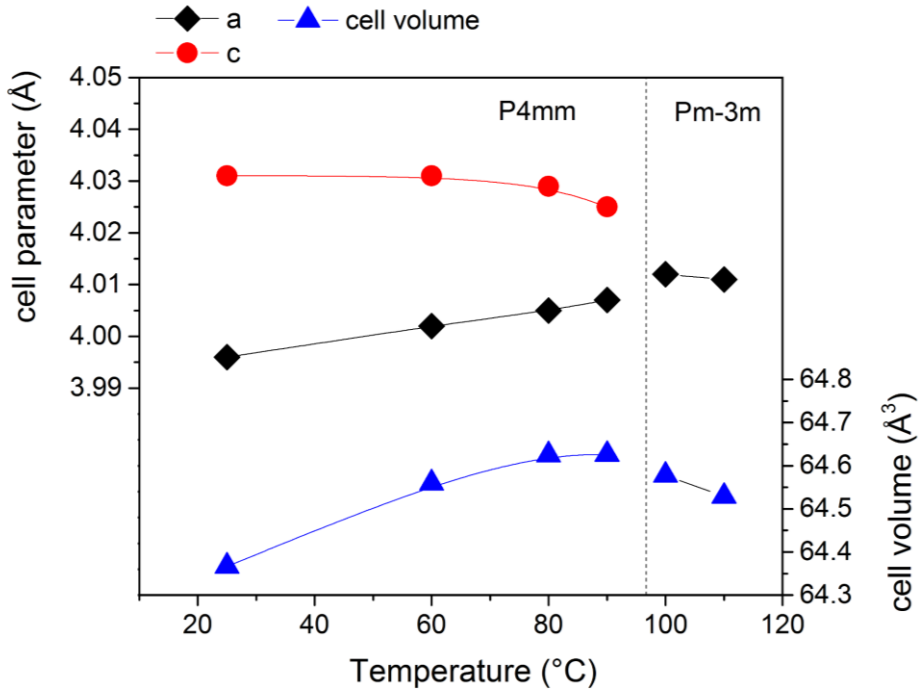

Figure 8.15. Cell parameters and cell volume evolution of sintered BT as a function of temperature.

In order to confirm the results obtained with the heating system of X-Poll cell, the phase transition is further investigated with dielectric permittivity measurements. **Figure 8.16a** shows the dielectric permittivity as a function of the temperature for increasing frequency (1, 10, 100 kHz). It is possible to appreciate the clear dielectric anomaly which presents the maximum of the permittivity at around 106°C, that confirms the ferroelectric-paraelectric phase transition. It is well-known that the dielectric behavior of a normal ferroelectric above the Curie temperature follows the Curie-Weiss law described by the following equation (**Equation 8.1**):**[17]**

$$\frac{1}{\varepsilon} = \frac{(T - T_0)}{C} \quad (T > T_c) \tag{8.1}$$

Where T_0 is the Curie-Weiss temperature, and C is the Curie-Weiss constant. For normal ferroelectric materials, T_0 and T_m, which represents the temperature at which the permittivity has its maximum, are very similar.

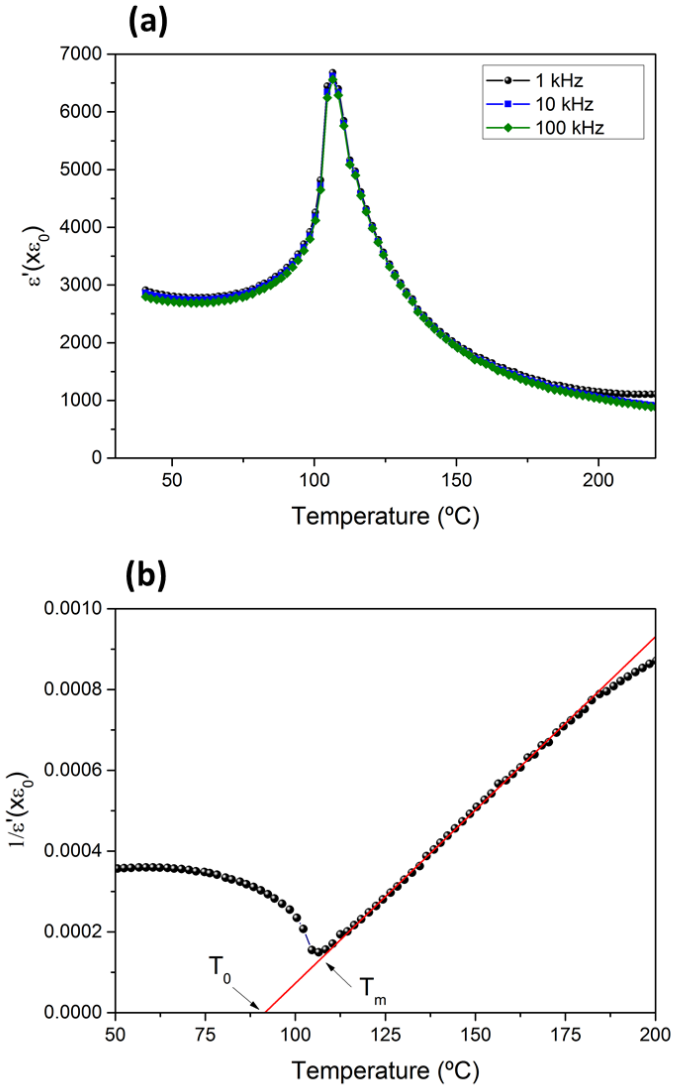

Figure 8.16 (a) Dielectric permittivity (1, 10, 100 kHz) Vs temperature and (b) inverse dielectric permittivity as a function of temperature at 1 kHz of sintered BT.

However, ferroelectric ceramics generally present a variable degree of diffusivity which mainly depends on grain size and crystalline defects that cause differences between these two parameters. In the specific case of the barium titanate under consideration, T_0 is at about at 93 °C (**Figure 8.16b**), which is consistent with the experimental evidence observed from XRD investigation.

Figure 8.17 shows the evolution, at room temperature, of some diagnostic peaks as a function of the poling electric field (0-16 kV/cm). Despite the application of the electric field, the sample maintain the tetragonal symmetry and the cell parameters do not vary appreciably. The main structural changes concern the change of the intensities of some reflection's peaks.

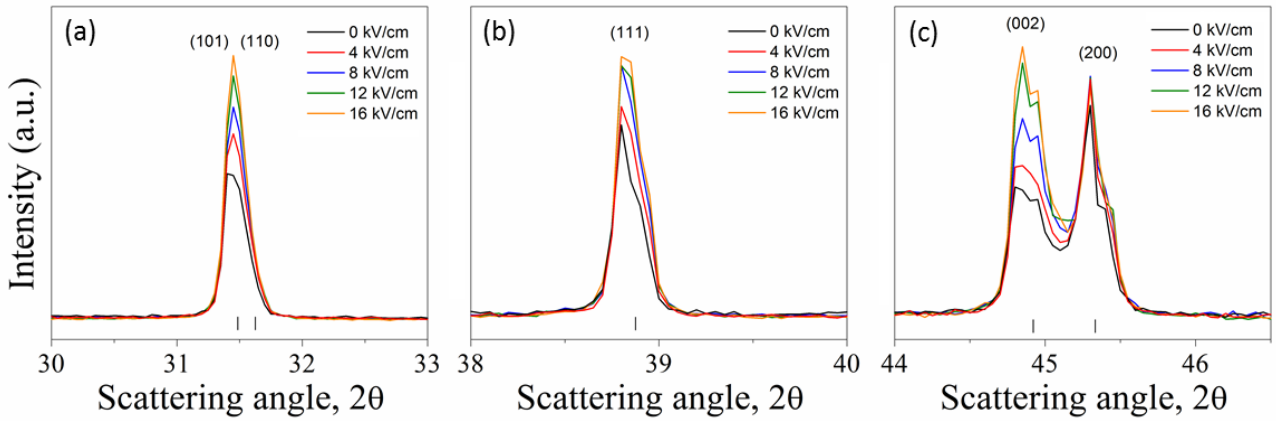

Figure 8.17. Room temperature *in-situ* electric field experiments of sintered BT. Magnification of some diagnostic peaks between (a) 30-33°, (b) 38-40 and (c) 44-46.5°.

As is well known, 180° domain reversal and 90° domain reorientation will occur in perovskite ferroelectrics with tetragonal symmetry during poling.**[18]** In particular, the latter (90° domain) are responsible for the change in intensity of the diffraction peaks. Let's consider the diagnostic peaks shown in **Figure 8.17c**. The 90° domain reorientation implies that **a-** and **c-**axis of the tetragonal structure are exchanged with the application of the field. Considering that the (200) reflection peak correspond to the family planes whose **a-**axis is vertical to the plane surface while the (002)

correspond to the family planes with pole axis (**c**-axis) vertical to the plane surface; thus, the (200) and (002) crystal planes are often associated with the **a** and **c** cell parameters, respectively. As observed in **Figure 8.17c**, the application of the electric field determines the preferential growth of the (002) domain, in agreement with the observations of other authors.**[19]** This phenomenon can be schematically appreciated in the figure below (**Figure 8.18**).

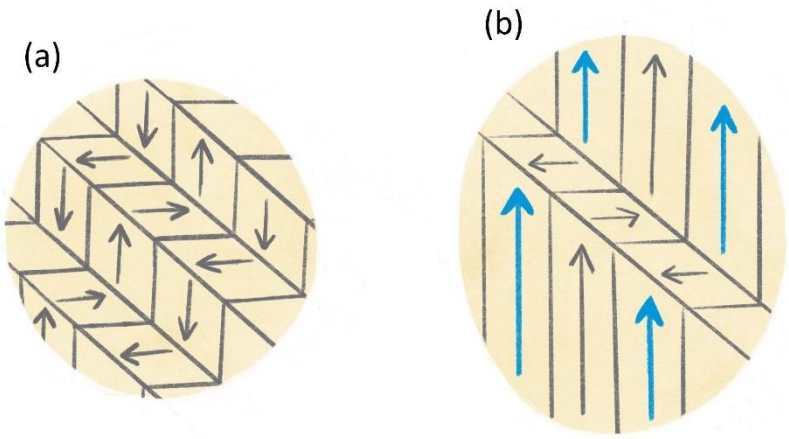

Figure 8.18. Schematic representation of the 90° domain reorientation due to the application of the poling electric field. (a) unpoled and (b) poled sample.

The amount of ferroelastic domain oriented when the field is applied is generally higher compared to those observed *ex-situ* with zero-field applied. The ferroelastic texture relaxation is a well-known phenomenon in ferroelectric materials which is called *ageing* effect.**[20]** This effect is mainly due to stress relief mechanisms that occurs as soon as the poling electric field is removed. **Figure 8.19** shows the difference between the sample measured during (*in-situ*) and after (*ex-situ*) the application of the higher electric field (16 kV/cm). The amount of oriented ferroelastic domain decreases when the poling electric field is cut-off in as much as (002) peak visibly decreases and, at the same time, the (200) gains intensity.

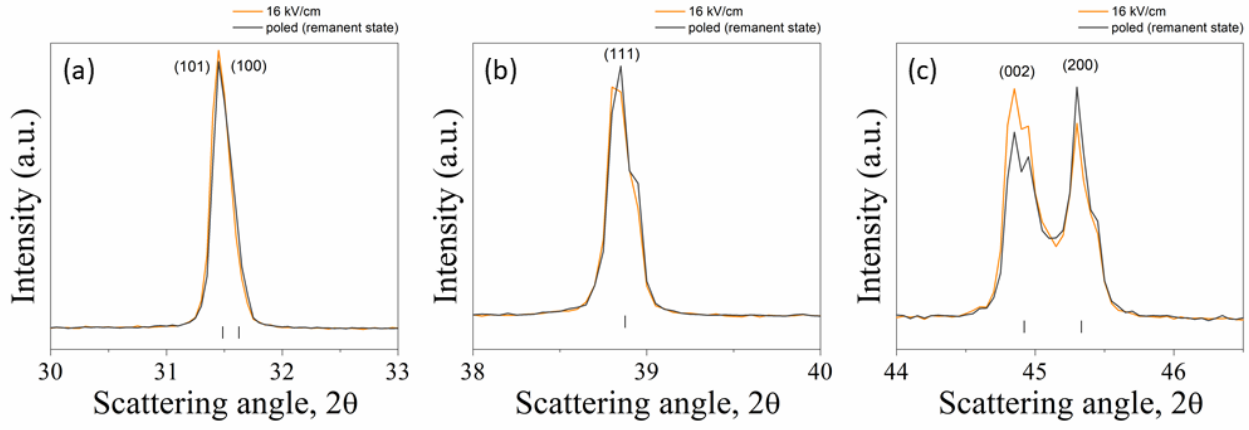

Figure 8.19. XRD measurements of some diagnostic peaks of sintered BT. Difference between *in-situ* (orange line) and *ex-situ* (black line) are due to the ferroelastic texture relaxation.

The study of the domain switching can be done by using different approaches. For example, some models consider the integrated intensity of the (002) and (200) peaks to evaluate the multiple random distribution (MRD) of tetragonal ferroelectric ceramic using the following equation:**[21]**

$$f_{MRD} = \frac{3 \times \frac{I^{E}_{002}}{I^{unpoled}_{002}}}{\frac{I^{E}_{002}}{I^{unpoled}_{002}} + 2 \times \frac{I^{E}_{200}}{I^{unpoled}_{200}}} \tag{8.2}$$

where I^{E} and $I^{unpoled}$ are the integrated intensity of the corresponding peaks under the electric field and unpoled state, respectively. Another model takes into account the maximum of the intensities of (002) and (200) peaks in order to evaluate the percentage of the 90° domains oriented with the field (**Equation 8.3**):

$$N = \frac{R - r}{(R + 1)(r + 1)} \times 100 \tag{8.3}$$

Where N is the percentage of the 90° domains reoriented, *R* and *r* are the ratio between I_{200} and I_{002} of the unpoled (R) and poled (r) state, respectively. The calculation of MRD is rather complicated

due to the presence of Kα2 (**Figure 8.17**); however, however, it can be roughly determinate measuring the area under each diffraction peak using a Lorentzian curves model (see details of the fit procedure in **Figure 8.20**).

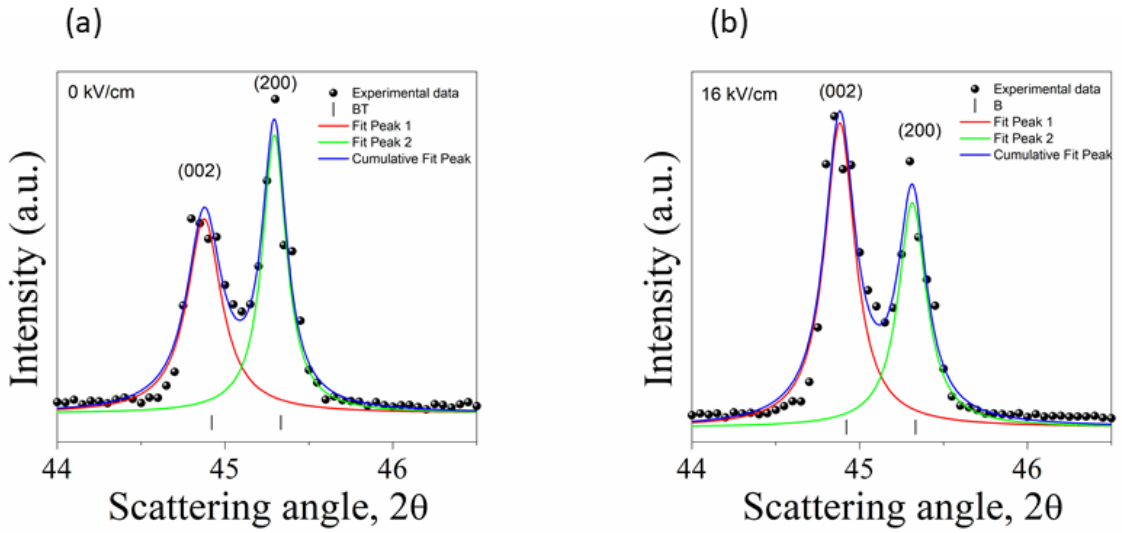

Figure 8.20. Peak fitting profile of (002) and (200) crystal planes of BT sample under (a) 0 kV/cm and (b) 16 kV/cm. Peak fitting has been done using a Lorentzian curve model.

The percentage of 90° domains oriented has been calculated using the **Equation 8.3**. The data collected from the *in-situ* investigation and the calculated 90° domains reoriented are reported in **Table 8.2**. As it clearly emerges, the ratio I_{200}/I_{002} progressively decreases as the electric field increase while percentage of the 90° domain-oriented, as well as the MRD, increase up to the final value of 15 % at 16 kV/cm. It is interesting to note that after the removal of the field, the poled sample (poled state) just shows 6% of oriented 90° domains which means that about 9% of 90° domains (about half) immediately return to a "random state". These values are in good agreement with those found by Subarrao et al. for polycrystalline barium titanate ceramics poled under similar poling conditions.**[22]**

Table 8.2. I_{200}/I_{002} ratio and percentage of 90° domains oriented (N) as a function of the poling electric field. The poling experiments were conducted at room temperature.

Electric field (kV/cm)	**I_{200}/I_{002}**	**MRD**	**N (%)**
0 (reference state)	1.60(R)	1	0
4	1.53(r_1)	1.01	1
8	1.20(r_2)	1.12	7
12	0.94(r_3)	1.24	13
16	0.86(r_4)	1.27	15
Poled state (no field)	1.23(r_4^*)	1.10	6

8.8 Conclusions

This work provides the "proof of concept" of a new device able to perform *in-situ* poling/temperature diffraction experiments for piezoceramics and more. The development and the engineering of the cell has been described in detail. In order to show the potentialities of the device, two basic experiments have been reported on a well-known piezoceramics as the polycrystalline barium titanate (BT). The reliability of the results was verified with auxiliary characterizations and by comparison with literature. We believe that the cell can be a useful tool to perform "homemade" *in-situ* diffraction experiments with common laboratory diffractometer. The room for improvement both the cell and the quality of experiments is very large. Some salient aspect which will be subject to further refinement in the near future are:

- **Improvement of the mechanical and thermal behavior of the solid body of the cell.** The acrylonitrile styrene acrylate (ASA) guarantees good printability but the working thermal range is quite limited due to the poor stability of the storage modulus with the temperature.

Therefore, we plan to create new prototypes based on PTFE (Teflon) or Nylon which guarantees better thermal and mechanical stability at high temperatures.

- **Improvement of the quality of the diffraction experiments.** The presence of Kα2 may affect the calculation of MRD. Therefore, we planned to perform new experiments using the *Johansson monochromator optics*, which allows to remove the contribution of Kα2.

- **Perform temperature-poling experiments.** It is possible to carry out *in-situ* poling diffraction experiments at various temperatures. This is particularly interesting for studying the effect of temperature on the polarization process.

- **Test the cell with other structural investigation tools**. The cell can theoretically be used with other structural or microstructural investigation tools as, for example, Raman spectroscopy or Scanning Electron Microscopy (SEM). The versatility of 3D printing allows to adapt the dimensions of the cell to the instrument concerned.

8.9 References

[1] B. Li, M. C. Ehmke, J. E. Blendell, K. J. Bowman. *J Eur. Ceram. Soc.* **2013** 33, 3037–3044.

[2] P. Li, J. Zhai, B. Shen, S. Zhang, X. Li, F. Zhu, X. Zhang. *Adv. Mater*. **2018**, 1705171.

[3] D. Hou, T.-M. Usher, L. Fulanovic, M. Vrabelj, M. Otonicar, H. Ursic, B. Malic, I. Levin, J. L. Jones. *Phys. Rev. B*. **2018** 97, 214102.

[4] J. Mendiola, L. Pardo. *Ferroelectrics*. **1984**, 54, 199-202.

[5] L. Pardo, F. Carmona, A. M. Gonzalez, C. Alemany, J. Mendiola. *Ferroelectrics*. **1992**. 126, 329-333.

[6] V. Thery, A. Bayart, J.-F. Blach, P. Roussel, S. Saitzek. *Appl. Surf. Sci*. **2015** 351, 480–486.

[7] M. Wegner, H. Gu, R. D. James, E. Quandt. *Sci. Rep*. **2020** 10, 3496.

[8] B.N. Ezealigo, R. Orrù, C. Elissalde, H. Debéda, U.-C. Chung, M. Maglione, G. Cao. *Ceram. Int*. **2021**, 47, 3, 3614–3625.

[9] D. A. Ochoa, A. Reyes-Montero, F. Suñol, M. E. Villafuerte-Castrejón, L. Pardo, J. E. García. *J. Alloys Compd*. **2019**, 774, 410-417

[10] A. Iacomini, S. Garroni, G. Mulas, S. Enzo, L. Cappai, M. Mureddu, C. Cau, Á. García, L. Pardo. *Open Ceramics*. **2022**, 100247

[11] M. Otonicar, A. Bradesko, S. Salmanov, C.C. Chung, J. L. Jones, T. Rojac. *OpenCeramics*. **2021**. 7, 100140.

[12] S. Guessasma, S. Belhabib, H. Nouri. *Macromol. Mater. Eng.* **2019**, 304, 1800793

[13] S.Raam Kumar, S.Sridhar, R.Venkatraman, M.Venkatesan. *Mater. Today: Proc.* **2021**, 39(4), 1316-1319.

[14] N. Yasuda, H. Murayama, Y. Fukuyama, J. E. Kim, S. Kimura, K. Toriumi, Y. Tanaka, Y. Moritomo, Y. Kuroiwa, K. Kato, H. Tanaka, M. Takata. *J. Synchrotron Rad.* **2009**, 16, 352-357.

[15] K. Sakayori, Y. Matsui, H. Abe, E. Nakamura, M. Kenmoku, T. Hara, D. Ishikawa, A. Kokubu, K. Hirota, T. Ikeda. *Jpn. J. Appl. Phys.* **1995**, 34, 5443.

[16] W.P.Chen, Z.J.Shen, S.S.Guo, K.Zhu, J.Q.Qi, Y.Wang, H.L.W.Chan. Physica B, **2008** 403, 660–663.

[17] A Reyes-Montero, L. Pardo, R. López-Juárez, A M González, S. O. Rea-López, M. P. Cruz, M E Villafuerte-Castrejón. *Smart Mater. Struct*. **2015** 24, 065033.

[18] X. Zhang, C. Lei, K. Chen. *J. Am. Ceram. Soc*. **2005** 88(2), 335–338.

[19] C. M. Valot , N. Floquet , P. Perriat , M. Mesnier & J. C. Niepce. *Ferroelectrics*. **1995**, 172(1), 235-241.

[20] C. Alemany, B. Jimenez, J. Mendiola, E. Maurer. *J. Mater. Sci.* **1984**, 19, 2555-2560.

[21] S. Sun, Y. Zhang, L. Fan, S. Deng, B. Gao, Y. Ren, H. Liu, J. Chen. *Scripta Materialia* **2021**, 194, 113627.

[22] C. Subarrao, M. C. McQuarrie, W. R. Buessem. *J. Appl. Phys.* **1957**, 28(10), 1194-1200.

9 Conclusions e future perspective

In the last decade, a tremendous effort has been dedicated to the development of lead-free systems with electrical properties comparable to PZT. Their introduction on the market is a matter of time. About KNN ceramics, a further effort is needed to make this material industrially palatable; in particular, about its processing method and reproducibility. Moreover, the cytotoxicity of the highly performing KNN based systems, analyzed in Chapter 3, is still unknown and they require careful study before they can be considered viable alternatives to the lead-based systems. This thesis work has provided a contribution on these aspects. The mechanochemical activation by High Energy Ball Milling proved to be an effective and easy-scalable technique for obtaining reproducible KNN systems with good electromechanical properties. A new approach was provided in order to optimize the reactivity of the starting powders by evaluating the evolution of the crystallite size of the main component (niobia) as a function of the ball-milling time (Chapter 5). Nevertheless, the second milling step, i.e post calcination, is equally important as it affects the sintering process (Chapter 6). Within a certain milling time (<12hBM), the mechanical processing guarantees a decrease in the average particle size which determines an improvement of the sinterability of the ceramics. However, prolonged milling times (>12hBM) determines the formation of large powder aggregates which worsen the densification process. Basically, what clearly emerges is that 12 hours of pre- and post-calcination milling are the optimal milling time.

Two modified KNN compositions, a binary (KNN-MN) and ternary (KNN-BF-CuO) systems, were prepared with the mechanochemical activation method. The effect of the modifying agents on the structure, microstructure and electrical properties of KNN has been evaluated. A small addition of MN causes an increase in density, a decrease in the grain size and an increase of the structural distortion (Chapter 5). The optimum composition (KNN-1MN) showed improved electromechanical

properties compared to pure KNN. Toxicological test performed on KNN-MN ceramics by exposing all the systems to two human and environmental cellular models, suggests that KNN-based materials are not cytotoxic and they do not have antifungal capacity. This novelty approach, first shown here, can be replicated in order to evaluate the cytotoxicity of new "lead-free" piezoceramic compositions. A small addition of CuO (0.5 wt.%) determines an increase in both mechanical and piezoelectric quality factors of the KNN-BF binary system. Further addition of CuO (1 wt.%) determines an increase in the dielectric permittivity and the "relaxation" behavior of the ceramic. This study proves that it is possible to modulate the electrical properties of KNN-BF by controlling the concentration of CuO.

The binary KNN-BF system was also prepared with the SPS technique (Chapter 7). The results showed that the post annealing temperature strongly influences the microstructure, the dielectric and piezoelectric properties of ceramics. The optimal post annealing temperature was found between 1000-1050 °C. In any case, further studies are needed to try to further decrease the oxygen vacancies concentration, which remains quite high despite the air annealing. A possible solution could be to carry out new experiments in oxygen flow atmosphere. Moreover, new tests have been planned in order to evaluate the toxicology of the KNN-BF binary system. Work is underway along this direction.

Finally, the last section of this thesis work (Chapter 8) describes the development of an innovative cell to perform *in-situ* diffraction experiments. The preliminary results provide the "proof of concept" of the device. The possibilities for improvement the cell and the quality of the experiments are very large and currently in progress. We believe that our device can be a useful tool to perform *in situ* diffraction experiments of piezoceramics and more.

10 Aknowledgments

I am thankful to my mentors, Prof. Stefano Enzo, Prof. Sebastiano Garroni and prof. Lorena Pardo for their precious guide throughout these unforgettable years.

I am thankful to my fellow “engineers”, dott. Davide Sanna, dott. Nicola Labate and dott. Andrea Melis (FabLab Uniss) for their availability and for the fruitful collaboration for the cell development.

I would like to thank prof. Gabriele Mulas for all the useful tips for my thesis work.

I would like to thank Prof. Roberto Orrù (University of Cagliari, Department of Mechanical, Chemical and Materials Engineering), Simone Barbarossa and dott. Ekaterina Pakhomova for hosting me in their laboratories and giving me the opportunity to perform the SPS experiments.

I am also really thankful to Prof. Luca Malfatti (Department of Chemistry and Pharmacy-Uniss), dott. Swapneel Thakkar and Matteo Poddighe for their invaluable help with Raman and thermogravimetric experiments.

I would like to thank Nina Senes, who started with me this incredible journey through the world of piezoceramics, and all of my lab colleagues during these years.

Finally, I wish to thank my family to whom I dedicate this thesis and without who it would have never been possible to achieve it.

At last, but not at least, Francesca, for your constant patience and love.

11 Appendix: Publication list and conferences

Publications:

1. A. Iacomini, J. A. Tamayo-Ramos, C. Rumbo, I. Urgen, M. Mureddu, G. Mulas, S. Enzo, S. Garroni. Processing Optimization and Toxicological Evaluation of "Lead-Free" Piezoceramics: A KNN-Based Case Study. *Materials*. 2021; 14(15):4337. https://doi.org/10.3390/ma14154337.

2. A. Iacomini, S. Garroni, N. Senes, G. Mulas, S. Enzo, M. Poddighe, Á. García, J. F. Bartolomé, L. Pardo. $MgNb_2O_6$ Modified $K_{0.5}Na_{0.5}NbO_3$ Eco-Piezoceramics: Scalable Processing, Structural Distortion and Complex Impedance at Resonance. *ChemistryOpen.* 2021, 10, 798. https://doi.org/10.1002/open.202100089

3. A. Iacomini, S. Garroni, G. Mulas, S. Enzo, L. Cappai, M. Mureddu, C. Cau, Á. García, L. Pardo. Processing, phase evolution and electrical properties of "lead free" KNN–BF–CuO eco-piezoceramic from mechanochemically activated precursors. *Open Ceramics*. 2022, 9, 100247. https://doi.org/10.1016/j.oceram.2022.100247

4. A. Iacomini, G. Mulas, S. Enzo, S. Garroni, L. Malfatti, S. Thakkar, G. Cao, R. Orrù, S. Barbarossa, E. Pakhomova, J. A. Tamayo-Ramos, C. Rumbo, J. F. Bartolomé', L. Pardo. Dielectric, piezoelectric and cytotoxic behaviour of "lead free" KNN-BF piezoceramics prepared through Spark Plasma Sintering (SPS). (in preparation).

5. A. Iacomini, D. Sanna, M. Mureddu, S. Garroni, G. Mulas, S. Enzo, N. Labate, A. Melis, L. Pardo. Development of a multifunctional device for in-situ poling/temperature experiments. (in preparation).

Conferences:

1. A. Iacomini, G. Mulas, S. Enzo, S. Garroni, M. Poddighe, J. F. Bartolomé, L. Pardo. Processing, sintering study and phase evolution of "lead free" potassium sodium niobate doped with bismuth ferrite (KNN-BF): effect of CuO addition on sintering behaviour and electrical properties. **Oral presentation**. PIEZO2021: Piezoelectrics for End Users XI Feb 21-24, 2021 | University of Sassari, Italy.

2. A. Iacomini, G. Mulas, S. Enzo, S. Garroni, L. Pardo. The effect of post annealing temperature on density and microstructure of "lead free" KNN-BF piezoceramics prepared through Spark Plasma Sintering technique. **Poster presentation.** XV Reunion Nacional de Electroceramica, Vitoria-Gasteiz (Spain) 07-09, 2021.